Spectroscopic Investigations of Laser-Produced Steel Plasmas in the Vacuum Ultraviolet

A Thesis Submitted to the Faculty of Science for the Degree of ***Doctor of Philosophy*** (PhD) in Physics

By

Mohamed Abbas Khater, MSc BSc

School of Physical Sciences
Dublin City University

Research Supervisor
Professor Eugene T. Kennedy

December 2001

Dedication:

This thesis is fully dedicated to my beloved

father

(1^{st} September 1935 – 21^{st} September 1999)

Declaration

I hereby certify that this material, which I now submit for assessment on the programme of study leading to the award of the degree of ***Doctor of Philosophy*** is entirely my own work and has not been taken from the work of others save and to the extent that such work has been cited and acknowledged within the text of my work.

Signed: Mohamed A. Khalil ID No.: **97971138**

(Candidate)

Date: 19 / 12 / 2001

Acknowledgments

I would like to take this opportunity in order to express my thanks and gratitude to ***Professor Eugene Kennedy***, my supervisor, for his highly and perfectly constant support and encouragement over the years. His great enthusiasm, discipline and experience as a scientist, and indeed as an individual, significantly eased up hard times, when things almost looked hopeless. In fact, I personally have no doubt that the work reported in this thesis would have never been done without Eugene. Many thanks Eugene, and may God bless you and your lovely family.

I would also like to extend my thanks to the other staff members of the Center for Laser Plasma Research (CLPR), my research group, *Dr John Costello*, *Dr Jean-Paul Mosnier* and *Dr Paul van Kampen* for the useful scientific (and sometimes non scientific!), arguments and discussions during almost the past four years. Their advice and assistance are highly appreciated. Special thanks are given to *John* for his support in writing the Qbasic code (Appendix H). To *Alan, Pat, Mark, John, Jonathan, Dr Andy Gray* (ex-DCU) and *Dr Oonagh Meighan* (ex-DCU), the postgrads in the group, I would like to acknowledge for the many laughs, chats and good times we had together.

I will always remember the continual assistance and support from our highly qualified and skilled technicians *Des Lavelle* (Mechanical Workshop) and *Pat Wogan* (electronic Workshop). They have been very helpful in many critical situations.

A special acknowledgment is given to *Professor Brian MacCraith* for providing the opportunity to continually read the "Applied Spectroscopy" journal. I will never forget his call, at the beginning of each month, telling me that a new issue has just been arrived!

Finally, I would like to thank the rest members of staff, postgrads, secretaries and technicians of both the National Center for Plasma Science and Technology (NCPST) and Physics department at Dublin City University.

Abstract

The analytical feasibility of *laser-produced plasmas* in the deep *vacuum ultraviolet* (VUV) spectral range (40 nm to 160 nm) for the *quantitative elemental characterization* of solid low-alloy *steels* is investigated, using time-integrated spatially-resolved *optical emission spectroscopy (OES)*. *Carbon* was chosen as a 'test' element in the present study. In this respect, six prominent carbon spectral lines, covering the spectral range mentioned, and representing three different ionization stages of II, III and IV, have been carefully selected and proved to be spectral-interference free.

It has been demonstrated that the spatially-resolved approach followed in this work resulted in significantly enhancing the emission intensity of the spectral lines studied with respect to that of the characteristic intense background continua given off by laser-produced plasmas. Furthermore, an extensive series of optimization studies for various experimental parameters and conditions, including the *laser-pulse focusing lens types (spherical* vs. *cylindrical), laser power density, laser harmonics, laser pulse energy,* as well *as ambient atmospheres and pressures,* has been carried out in order to further improve the spectral lines-to-background ratios achieved.

In this way, linear analytical calibration functions have been constructed for the different carbon spectral lines under consideration, in the concentration range 0.001% to 1.32%. Moreover, the ultimate sensitivity of the VUV-based laser-induced plasma spectroscopy *(LIPS)* technique developed has been considerably improved; an unprecedented limit of detection for carbon in steels of 1.2 μg/g ± 15% has been measured from the C III 97.70 nm spectral line.

Spectroscopic diagnostic techniques in the VUV for the determination of the laser-produced steel plasma physical parameters, namely the electron number density (n_e) as well as the excitation (T_{exc}) and ionization (T_{ion}) temperatures, have also been developed. In addition, criteria regarding the existence of local thermodynamic equilibrium (LTE) state in the plasmas investigated have been discussed.

Table of Contents

CHAPTER I

INTRODUCTION AND AIM OF THE WORK

This chapter begins with a general overview of the role of laser-induced plasma spectroscopy (LIPS) technique in the field of elemental composition analysis of solid materials, including its advantages over conventional techniques. The fundamental principle that LIPS is based upon, as well as its basic set-up, which applies in most applications, is briefly described. A short review of theoretical, as well as experimental studies carried out to investigate the nature and behaviour of laser-matter interactions and the consequent initiation and expansion of the plasma is also given. Analytical applications of LIPS for the quantitative elemental characterization of a wide variety of solid materials are briefly stated. The research problem to be undertaken in the thesis is explained, and the aim of the work is presented and summarized. Finally, the seven chapters constituting this thesis are briefly outlined.

1.1 Background and Overview

Soon after the introduction and development of the first ruby laser in 1960, Brech and Cross [1] demonstrated that when a pulsed, high-powered laser pulse is focused onto a solid surface, a short-lived high temperature and density plasma is generated on the surface, and that it can be used as a spectrochemical excitation source for the direct elemental composition analysis of solid materials using optical emission spectroscopy (OES). Such laser-generated plasmas, which contain a diversity of atomic and ionic species as well as free electrons, emit radiation over an extensive spectral range stretching from the infrared (IR) to the X-ray region. Although different solid materials have different breakdown thresholds, the plasma is typically produced when the laser irradiance (power density) exceeds several megawatts per centimeter squared [2]. Since then, the now well-established generic technique, usually termed laser-induced plasma spectroscopy (LIPS), has been successfully employed for the direct elemental characterization of almost every type of solid material and reviewed in the literature several times [see 3–15 and references therein].

LIPS has indeed proved to be the oldest spectroscopic technique employing high-power laser pulses [16]. However, until the end of the eighties, practical applications of the technique were very limited, mainly due to the relatively low performance and high cost of the instrumentation required. The most important developments and breakthroughs have only taken place in the last decade or so, as indicated by the number of papers published in the open literature. This is largely because of the substantial recent improvements in lasers, optics and, in particular, detector technologies. Furthermore, the intensive fundamental investigations carried out into laser-materials interactions and the subsequent initiation and expansion of plasmas produced, significantly revealed some important facts about the nature and behaviour of these processes. In addition, other very promising and challenging applications of laser-produced plasmas, created with approximately similar power densities to those used in LIPS, have flourished at the same period of time such as pulsed laser deposition (PLD) of thin solid films [17], and different types of laser-materials processing and fabrication [18].

In the context of spectrochemical analysis, laser-produced plasmas have in principle many advantages over other conventional spectroscopic sources [19] such as dc arcs, ac

sparks, glow discharge lamps (GD) and inductively coupled plasmas (ICP). These include the facts that almost little or no sample preparation is necessary, resulting in increasing throughput and reduction of tedious and time-consuming preparation procedures that can lead to serious contaminations. Also since optical, rather than thermal, energy is used for vaporization, excitation and ionization processes, the direct characterization of conducting, nonconducting, organic, inorganic, biological, radioactive and opaque, as well as transparent materials can be easily achieved. Moreover, a relatively small amount of the solid sample (in the range between 0.1 μg and 100 μg, depending on the laser characteristics as well as on the sample matrix properties) is required for performing the analysis. Therefore, the technique has been considered to be almost non-destructive and is recommended for some particular applications, for example cleaning of precious artworks [20–22]. Furthermore, the sample does not need to be transported to the plasma source; rather the plasma is formed on its surface by the aid of the incident laser beam. As a result, LIPS has shown a powerful capability in carrying out remote on-line and in-situ analytical applications, particularly those involved in hostile and harsh environments [23–39].

On the other hand, the main drawback of the LIPS technique has been its unsatisfactory quantification, and hence corresponding figures of merit [40]. The inferior analytical performance of laser-produced plasmas may be partly attributed to the differences in physical and chemical properties, and so vaporization behaviour, between the samples and reference standards used to calibrate the technique. In order to improve the analytical accomplishment of LIPS, many studies have been carried out to optimize the quite dependent several experimental conditions and parameters of the technique. These include the laser pulse characteristics (wavelength, energy, duration and repetition rate) [41–49], thermal-optical properties of the target [8–9, 43] and composition, as well as pressure of the ambient atmosphere [50–61]. Nonetheless, despite these considerable research efforts the mechanism of the vaporization of a solid target, and the consequent formation and expansion of the plasma by a laser beam is still at the present time neither fully understood nor clearly defined [62].

It is a well-known fundamental principle in spectrochemical analysis to physically separate the vaporization / atomization from the excitation / ionization process. In this way, each phase can be optimized independently and the maximum analytical power of

the relevant technique can be achieved. For this reason, laser-produced plasmas have been long investigated as possible atomization sources (atomic / ionic reservoirs) for different optical spectroscopic techniques [11, 15]; this method is usually given a generic name as "laser ablation" or "laser sampling". Examples for these hyphenated techniques include laser ablation-atomic absorption spectroscopy (LA-AAS) [63], laser ablation-laser induced fluorescence (LA-LIF) [64–65], laser ablation-microwave induced plasma-optical emission spectroscopy (LA-MIP-OES) [66], laser ablation-inductively coupled plasma-optical emission spectroscopy (LA-ICP-OES) [67–69] and finally laser ablation-inductively coupled plasma-mass spectroscopy (LA-ICP-MS) [70–71]. Better analytical performance in terms of sensitivity, selectivity, precision, accuracy and dynamic range, should be expected with these techniques in comparison with LIPS, at the expense, however, of increasing complexity and cost of instrumentation required.

1.2 LIPS Principles

The basic principle of LIPS is similar to that of conventional plasma-based methods of optical emission spectroscopy [16, 19]. When the light emitted from the excited / ionized sample is spectrally resolved, the individual neutral atoms and / or atomic ions in the plasma plume are identified and quantified by their unique wavelengths and line intensities, respectively. In practice, the technique can be calibrated through establishing a relationship between the observed spectral line intensities of a particular species and the corresponding concentrations in the sample material. The graph that corresponds to this relationship is called the analytical calibration curve, and can be used to determine the elemental contents of unknown samples by observations on reference samples of known concentrations, termed standards.

It is a well-recognized fact that laser-produced plasmas give off a strong broadband continuum background radiation, due to bremsstrahlung and recombination processes, extending between the infrared and X-ray region [72–74], along with different spectral lines superimposed on it. For many years, such bright continuum radiation has been used as background lighting sources for absorption spectroscopy in the VUV and soft X-ray [75–77], as well as in the UV-visible / infrared [73] regions. For emission spectroscopic studies, however, it is essential that this background continuum radiation

is shielded in such a way that the strength as well as contrast of the overlying spectral lines is maximized. Fortunately, a characteristic feature of this background continuum is that it only lasts for a much shorter time than the spectral line emission. Due to this inherent temporal structure of the emitting plasma, most work on applications of laser-generated plasmas to the elemental composition analysis of solid materials has made use of time-gated detector technology in order to discriminate against this early intense plasma emission. Various spectral lines, in this way, have been recorded after the decay of the background continuum, and their signal-to-background ratios have been greatly improved, leading to better precision and sensitivity of the analytical method [78–84, for example].

Line emission spectra from laser-produced plasmas also exhibit a strong space dependency, in which various excited atoms and atomic ions in the plasma volume are essentially distributed at different spatial distances from the target surface [2]. It has been long recognized that the very high level of background continuum is mostly emitted at a relatively short distance (0–3 mm, depending on the wavelength region observed and species of interest) from the sample surface [85–92]. Therefore, by applying simple spatial resolved measures to sample the emitted radiation from further out regions of the plasma it is possible to enhance both the spectral line contrast and sensitivity, and consequently obviate the need for more expensive time-resolved detector systems. In the present work we follow this approach, and develop, for the first time, a vacuum ultraviolet-based (40 nm to 160 nm), time-integrated and spatially-resolved laser-produced plasma optical emission spectroscopic technique for the quantitative elemental characterization of steel alloys [93]. The analytical capability of LIPS is explored in the vacuum ultraviolet by employing multiply charged atomic ions of carbon, as a test case. The technique developed in the present work can be extended to include other low atomic number elements, such as phosphorous, nitrogen and sulphur, which also have their strongest spectral line emission in the VUV. The aim of the work will be described in more details at the end of this chapter.

1.3 Basic Set-Up

A distinctive advantage of LIPS has been the versatility of its basic set-up. The instrumental set-up in all experiments performing LIPS principally consists of five

components: a Q-switched high-peak power laser for plasma ignition and creation; a relevant chamber for accommodating the target(s) under investigation; systems of lenses / mirrors for steering and focusing the laser beam onto the target surface, and for collecting the radiation emitted from the plasma produced; a detection system including a grating spectrometer and a suitable multichannel detector such as a photodiode array (PDA) or, alternatively, a charge-coupled device (CCD) and finally a PC for data acquisition and evaluation, as well as for controlling the timing of the whole experiment [94]. A brief account of some of these components is discussed in the following paragraphs. A full description of the experimental set-up and procedures performed in the present work is given in chapter III.

The laser system used for LIPS experiments must provide pulses of sufficient power to generate the plasma on the solid target. Commercially available lasers that meet this criterion include solid-state lasers such as Nd:YAG, and gas lasers such as CO_2 and excimer systems. Nd:YAG lasers with their ease of use and robust, as well as rugged performance characteristics are considered to be the workhorses for not only LIPS, but also for other applications utilizing high-powered lasers [17–18]. The YAG laser emits Q-switched, energetic and relatively short-duration (usually between 4 ns and 10 ns) pulses at its fundamental wavelength of 1064 nm, as well as at frequency doubled, tripled and quadrupled wavelengths of 532, 355 and 266 nm, respectively. On the other hand, the most frequent gas lasers used include the CO_2 (λ=10.6 μm and pulse length of about 100 ns), N_2 (λ=337 nm and pulse length between 30 ps and 10 ns) and excimers emitting at 308 nm (XeCl), 248 nm (KrF) and 193 nm (ArF) with a pulse width in the range of 10 ns to 20 ns. It is typical for any of these lasers to produce pulses of at least a few tens of millijoules in the time frames mentioned, and these correspond to peak powers on the order of several hundreds of megawatts. Depending on the laser properties as well as on the focusing lens used, power densities of the order of 10^8–10^{12} W/cm^2 can be achieved at the sample surface, which are sufficient to cause a breakdown of any solid material known and generate the plasma required. At these levels of power density, ejection of macroscopic particles from the target is minimal (or even does not happen) which implies that the composition of the vapour (plasma) produced by the relatively short, high-peak power laser pulses is representative of the sample material. This represents an ideal situation for spectrochemical analysis [95].

Some technical considerations regarding the design and construction of any target chamber include the following: (1) rapid, convenient, precise and reproducible mounting and positioning of the target(s); (2) existence of a sufficient number of ports for various purposes including spectroscopic, visual observations, gas inlet and outlet controls, as well as different electrical and gas pressure measurements; and (3) extending the spectral range in the VUV region, particularly to perform analysis of the light elements C, S, P, Cl, Fl, Br, I, O, N and H, since these elements have their strongest line emissions in the region below 200 nm. Target chambers are usually made up of various materials such as glass (quartz), polymers, aluminum and stainless steel. However, chambers usually used in various LIPS experiments have been mostly built using the latter two material types for better and precise control of the background atmosphere.

In spectroscopic terminology, a spectrometer is basically a monochromator with its exit slit replaced by a multichannel detector interface. For LIPS, as for all other spectroscopic techniques, a spectrometer with a sufficiently large focal length and narrow entrance slit width, as well as high-density grating is a necessity to efficiently resolve various emission wavelengths and obtain maximum signal-to-background ratios. Several optical configuration arrangements are used for spectrometers in various LIPS applications including Ebert-Fastie, Czerny-Turner, Echelle and Rowland mounts. The radiation dispersed by the grating is recorded using either an OMA / PDA detector or a CCD array, with or without time-resolution capability. Advantages of multichannel detectors include wide spectral range and response, low dark current and readout noise, large dynamic range, linear response and speed and ease of data acquisition. A particular advantage, compared to the more conventional photomultiplier tube (PMT), is the simultaneous recording of a fairly wide spectral range, obviating the need to perform measurements in the scanning mode. The multichannel detector used is usually connected to a PC (via a GPIB or RS-232 port) for data acquisition and controlling the synchronization of the experiment, which is usually performed through a suitable pulse / delay generator. Finally, direct photography, using streak or framing cameras, is also a very useful technique for providing information about the evolution of the shape, as well as physical dimensions of the plasma produced under different experimental conditions.

1.4 Fundamental Studies

In spite of the fact that the interaction of high-peak power laser radiation with solid materials and the fundamental properties of plasmas produced under various experimental conditions have been heavily investigated for a quite long time [11], the field is still active and growing not only because of the wide variety of possible applications in chemical analysis, engineering and materials processing, but also because of its great capacity in basic science. For example, the recent development of picosecond and femtosecond high-powered lasers have opened a gateway for new challenges in understanding the fundamental aspects of laser-matter interaction [97]. In fact, these lasers have been readily utilized for some practical applications concerning elemental analysis by LIPS [47, 48] and laser micro-machining and micro-fabrication [62], in which they demonstrated some advantages with respect to nanosecond laser systems.

The interaction of nanosecond laser radiation with solid materials involves heating, melting, vaporization, ejection of atoms, ions, molecular species and fragments, shock waves, plasma initiation and expansion, as well as other unspecified nonlinear processes [13]. It is a very complex phenomenon, not satisfactorily explained so far and still under intensive theoretical and experimental investigations in order to gain accurate knowledge of all the physical processes involved [97]. The complexity of the phenomenon originates from the fact that the mentioned physical processes are all strong functions of different experimental conditions including laser characteristics and thermo-physical properties of the solid material, as well as composition and pressure of the surrounding atmosphere. In this respect, many theoretical studies as well as experimental investigations have been carried out to describe the laser-matter interaction with its simultaneous material vaporization and the subsequent formation and expansion of the plasma plume.

1.4.1 Theoretical models

In the fundamental investigation of a laser-ablation process, it has been a common approach to assume the *adiabatic limiting case* description of the process, i.e. that laser light absorption and the resulting simultaneous target heating, vaporization and plasma

ignition occur much quicker than the expansion of the plasma formed (in reality, however, heating as well as expansion takes place almost simultaneously resulting in a complicated interaction between the laser beam and the expanding plume). Under this assumption, the laser-ablation process can be classified schematically into two stages: (1) heating and evaporation of the solid target, as well as formation of the laser plasma which, in turn, interacts with the incoming laser beam and (2) expansion of the ablated vapour plume in vacuum or into a background gas. In fact, relatively simple analytical and numerical models have been successfully developed in this way [62].

In the first regime, thermal approaches based on solution of the 1- and 2-dimensional time-dependent heat conduction differential equations have been developed to simulate the laser-target interaction and the simultaneous heating, evaporation, plasma formation and laser-plasma interactions [98–112]. These models have been mainly utilized to calculate the ablation depth, quantity of material ablated, vaporization threshold, rate of evaporation and the target surface temperature as functions of both the laser pulse energy density and wavelength. UV Laser pulses emitted in the nanosecond domain as well as various metallic targets, under both vacuum [102, 111] and background gases at low pressures, have been employed in the majority of these models. Both inverse bremsstrahlung [100, 106, 111] and photoionization [101, 109, 111] mechanisms have been considered for the absorption of the laser light in the plasma plume formed. Moreover, plasma kinetics including electron impact excitation and recombination processes, as well as energy transfer from electrons to ions and neutrals during and immediately after the laser pulse have also been taken into account [102, 109–110, 112]. General conclusions that can be drawn from these studies include the facts that all the laser-ablation parameters investigated are increasing functions of the laser fluence until a plateau is reached at relatively high values, and that thermal conduction into the solid target is regarded as an important source of energy loss [111]. In addition, laser-plasma interaction processes and their influence on plasma kinetics are of great importance during nanosecond laser ablation of metallic targets for power densities higher than 10^9 W/cm^2.

For the second regime, i.e. plasma expansion, time-dependent gas dynamic differential equations based on the special solution that describes the expansion of an ellipsoidal gas cloud into vacuum have been widely used [102, 113–121]. This modeling scheme is

frequently called the hydrodynamic approach, because in all cases the plasma density is so high that the number of collisions between the evaporated atoms is sufficient for hydrodynamics to be applied. In addition to nanosecond, the interaction between ultrashort (pico- and sub-picosecond) laser pulses and solids with the subsequent formation and expansion of a plasma plume have been already modelled [117, 121]. Time-dependent collisional-radiative (CR) models, in which excited levels are populated by a balance of both collisional and radiative rates have also been assumed [122–124]. Various issues of importance in the spectral analysis of laser-produced plasmas such as the partial local thermodynamic equilibrium approximation (PLTE), spectral line trapping and broadening, as well as time dependence have all been considered [122]. One advantage of the CR approach is that it provides an understanding for the deviation of excited states populations from those obtained under LTE conditions [124]. Finally, Monte Carlo simulations of plasma expansion in three dimensions have been proposed in a few studies [110, 125–126]. Considering these models, temperatures and densities of different species, as well as other fundamental parameters of the expanding plasma plume can be estimated, as a function of time and space, and compared to experiments.

Despite the considerable research efforts dealing with the different mechanisms occurred during laser-matter interaction and the consequent formation and expansion of the plasma produced, there has been no unified treatment applicable to all target materials, all laser characteristics and under all contact media conditions so far. This situation is due to the fact that each model developed refers only to a separate part of the interaction, and is appropriate only under specific assumptions and conditions.

1.4.2 Experimental studies

Several spectroscopic and non-spectroscopic techniques have been employed to study and characterize laser-produced plasmas in order to understand their behaviour and performance under the influence of a wide range of experimental conditions (laser characteristics such as wavelength, pulse duration and power density; material thermo-physical properties and composition and pressure of various ambient atmospheres), as well as to test and develop relevant theoretical models. Optical emission spectroscopy (OES) [127–144]; optical absorption spectroscopy (OAS) [133–134, 145]; laser-

induced fluorescence (LIF) [131, 145–146]; time-of-flight mass spectroscopy (TOFMS) [147]; photographic techniques including fast streak cameras [127], gated intensified charge-coupled device (ICCD) cameras [133–134, 148] and pinhole cameras [142–143]; various interferometric configurations [149–150] and electrostatic probes (including ion as well as Langmuir) [133, 136, 151–152] have been utilized.

The focus of these techniques has been the accurate investigation of the plasma physical parameters, including temperatures and densities of the several species constituting the plasma, i.e. ions, electrons and neutral atoms, as a function of space and time. In this respect, spectroscopic techniques (OES, OAS and LIF) are the most widely used because of their non-intrusive nature, relative simplicity and versatility, direct spatio-temporal resolved measurements (which are fundamental for the analysis of the laser-produced plume evolution), as well as the huge amount of information about the plasma characteristics carried by spectra. They offer the possibility for the analysis of atoms and atomic ions in their ground as well as excited states, allowing the characterization of the plasma temperatures and densities of different species in the plume. Of these techniques, OES is the simplest as far as instrumentation is concerned, while OAS and LIF have the particular advantage of monitoring ground state populations of various neutrals / ions in the plasma plume [134, 145].

Interferometric techniques, which are based on the analysis of fringe structures originated by a probe laser beam crossing the plasma plume, have the advantage that they provide a very accurate and absolute diagnosis for the electron number density even at the very first instant of plume expansion, when the strong background continuum emission from the plasma, for many spectral lines, makes it almost impossible to clearly detect the spectral lineshape by OES. A further important advantage of interferometry in laser-ablation experiments is the fact that it is insensitive to the intensity of the probing laser beam crossing chamber windows which may become coated with the plasma debris, thus reducing optical transmission. Ultra-fast photographic techniques allow one to directly follow, in space and time, the dynamics of the plasma expansion both in vacuum and ambient atmospheres.

On the other hand, mass spectroscopy and electrostatic probes are the most widely accepted techniques for the characterization of charged particles in laser-produced

plumes. The presence in the plasma plume of charged species with a considerable amount of kinetic energy is of paramount importance in some applications of laser-produced plasmas such as pulsed laser deposition (PLD). Due to its extraordinary capability of recording a complete mass spectrum from a single laser shot, time-of-flight mass spectroscopy (TOFMS) [147] allows one to observe plasma kinetics and to clarify the reaction dynamics of different species in the plume. This is of particular interest in the case of complex materials and for PLD process monitoring. In addition, ion as well as Langmuir electrostatic probes provide direct and useful information about the time-of-flight (TOF) and kinetic energy, as well as yield of the ablated charged particles, whose analysis is of great importance for the understanding of both the elementary and microscopic phenomena involved in the process.

All the above mentioned techniques show that there is no stand-alone experimental facility which can monitor and provide a detailed picture on all fundamental phenomena observed with laser-produced plasmas. Instead, a particular combination of some of these techniques is used to study the processes important for a specific application. For instance, OES in combination with a powerful imaging technique, such as ICCD, is often employed to characterize plasmas produced in a wide range of LIPS applications. Through extensive and detailed experimental investigations of laser-produced plasmas, the LIPS technique can evolve from uncontrolled and unpredictable explosion behaviour to a method that is routinely used not only for chemical analysis, but also for other useful applications.

1.5 Analytical Applications

Due to its great versatility and peculiar characteristics, the laser-induced plasma spectroscopy (LIPS) technique has been utilized for the elemental composition analysis of a wide range of solid materials including various environmental samples [22, 24, 27–29, 153–154]; geological and mineral samples [21, 80, 155–159]; different types of glass [160–163]; semiconductors [164–167]; polymers [168]; radioactive materials [169] and biological specimens [170].

In 1922, Meggers and co-workers reported on the first successful practical method for the composition analysis of metal alloys using a spark source. Since then the direct

quantitative elemental characterization of metals and alloys has always been a great challenge [171]. Accordingly, considerable research efforts in the field of spectrochemical analysis have been directed to achieve this task. In particular, the LIPS technique has been mainly developed to solve some relevant problems in metallurgical industries and related fields [15]. In this respect, the elemental analysis of steels and various ferrous specimens [23, 31, 172–178]; copper metal and alloys [79, 83, 179–182]; aluminum alloys [26, 183–187] and of zinc-based materials [188–190] have been the most important and popular applications. Due to the great industrial demands for improving production / process control and quality assurance for metallurgical products, particularly in the steel industry, many efforts have been recently devoted to develop rapid, in-situ and on-line LIPS systems to achieve this important aim [25, 30, 34, 35–36, 191–192]. However, further work is needed in this direction as the analytical figures of merit are still unsatisfactory for this type of application.

1.6 General Outlook on Steels

Steel is basically an alloy of iron and carbon with a wide variety of physical and mechanical properties required for a vast number of industrial and technological uses. Some few examples of steel products include motor engines, car bodies, computer cases, bicycle frames, central heat radiators, bridges, ships, machine tools, fencing wires, factory roofs and various cutting tools. These products and many others are classified under different categories according to the percentage content of carbon. For example, motor engines are made up of alloys that contain $\geq$ 2% carbon, while the carbon content in alloys that are used to manufacture car bodies and central heat radiators must not exceed 0.3% (known as low carbon steels). Moreover, bridges and ships use alloys that contain a medium concentration of carbon between 0.3% and 0.7%. In addition, high carbon steels are those that have carbon in the range from 0.7% up to about 1.3% and are used to make various cutting tools because of their hardness [261].

Steels are further divided according to the presence and content of some other alloying elements such as Al, Co, Cr, Cu, Mn, Mo, Ni, Si, Sn, Ti and V [261]. The combination of all or some of these elements, in different proportions, can have a great influence on the mechanical structures and physical properties of "carbon" steel alloys. As a result, there have been numerous alloys developed for particular applications, because they

have one or several specific properties. For instance, the effect of adding chromium during the stainless steel-making process is to create oxide thin films which prevent rusting of the alloy, and hence corrosion. A wide range of stainless steels are available with a Cr content between 12% and 30%, along with C and Ni, as well as some other low alloying elements. Examples of products that are made up of stainless steels are car exhausts, cutlery tools, valve and pump parts, ball and roller bearings, turbine parts, surgical tools and steam irons. Stainless steels can also have magnetic properties by adding some more alloying elements such as Co, Al, Cu and Si in different proportions. Examples of these "magnetic" stainless steel alloys include permanent magnets used in loudspeakers and electric motors, and temporary magnets used to produce electromagnets and transformer cores [261].

1.7 Formulation of the Problem

In connection with increasing industrial demands for process control and quality assurance of steel production, the rapid, precise and accurate chemical composition analysis of metals and non-metals during all steel-making processes, including the blast furnace products (molten steel) and the final casting pre-products, is of large practical importance. In this context, the LIPS technique has been developed to monitor the most common alloying metallic elements in steel samples, namely Al, Co, Cr, Cu, Mn, Mo, Ni, Si, Sn, Ti and V, both on-line and in-situ [25, 30, 33, 35–36, 39, 192–193], as well as in the laboratory [172, 174, 175–176, 178]. Other techniques used to quantify these elements in steel samples include spark ablation-inductively coupled plasma-mass spectroscopy (SA-ICP-MS) [194–197]; laser ablation-inductively coupled plasma-mass spectroscopy (LA-ICP-MS) [71, 198]; and laser ablation-inductively coupled plasma-optical emission spectroscopy (LA-ICP-OES) [198]. Although the analytical figures of merit of these "hyphenated" techniques are often superior to those obtained with LIPS, they can only be utilized at off-site laboratories due to their instrumentation cost and complexity, as mentioned earlier. However, a common feature for the LIPS technique as well as for other techniques is that the above-mentioned metallic elements were excited / ionized under standard conditions of air at atmospheric pressure, and determined using spectral lines in the UV / visible region with time-gated detectors.

On the other hand, light (low atomic number) elements such as C, N, P and S play an extremely important role in determining some of the mechanical and physical properties, such as stiffness and ductility, of almost all steel products [261]. For many applications, it is essential to keep the concentration of light elements, particularly N, P and S, as low as possible (around few parts per million). However, it has been long recognized that particular difficulties accompany the quantitative determination of light (low atomic number) elements, and there is very little published work concerning the direct characterization of steels for their light elements content. The difficulty arises from the well-known fact that the strongest spectral lines of these elements are emitted from their ions in the vacuum ultraviolet (VUV), which requires evacuating the section of the set-up through which the radiation emitted from the plasma passes. Nevertheless, determination of light elements in steels from spectral lines situated in the UV / visible region has been already investigated [198, 200], but produced very poor results in terms of sensitivity, as well as precision.

Despite these technical limitations, some studies concerning the quantitative determination of light elements in steels, using spectral lines in the far and / or vacuum UV have been performed. In an early application, Balloffet and Romand [199] utilized the sliding vacuum spark technique for the quantitative determination of the elements C, P and S in steel samples, using a 1-m normal incidence spectrograph equipped with a photographic plate as the detector. They employed VUV spectral lines in the region between 90 nm and 120 nm, and measured detection limits of 0.01%, 0.005% and 0.005% for the three elements under investigation, respectively. The authors suggested that by using photoelectric instead of photographic detection, the overall sensitivity of the technique might be improved.

Aguilera et al. [200] were the first to apply the laser-induced plasma emission spectroscopic technique to the quantitative determination of carbon content in solid steel samples. The emitting plasma, produced by a Q-switched Nd:YAG laser (1064 nm), was imaged onto the entrance slit of a 1-m nitrogen-purged spectrometer, which was equipped with a time-gated OMA detection system. The spectral range of the spectrometer was 185–700 nm with a typical resolution of 0.03 nm. The authors mentioned the particular technical difficulties associated with the analysis of carbon content arising from the small number of intense emission lines and their location at the

UV extreme of the spectral range covered by their instrument. Of the two most intense neutral carbon lines in the investigated spectral region, at 193.09 nm and 247.86 nm, they selected the former line because it proved to be interference-free. They also investigated the effect of different experimental conditions, such as the laser power, the laser beam focusing, the time resolution and the argon atmosphere, on the analytical signal. Excellent precision and detection limits, i.e. ~ 1.6% and 65 ppm (parts per million), respectively, which can be favourably compared to the most accurate direct emission techniques, were obtained. This research group later used the LIPS technique for the same purpose, but with employing molten steel samples produced in a laboratory induction furnace [201]. The neutral carbon line C I at 193.09 nm was again selected to identify and quantify the carbon content. The authors discussed the influence of matrix effects and the surrounding atmosphere on the spectral line characteristics. A precision of 10% and a detection limit of about 250 ppm were measured. The authors concluded that the technique is useful for the on-line analysis of molten metals and alloys.

González and co-workers [202] determined the total sulfur content in steel samples by Q-switch Nd:YAG laser-produced plasmas, using time-resolved optical emission spectroscopy. They obtained a detection limit of 70 ppm and a precision of 7%. Calibration curves were linear over the concentration range 0.008% to 0.28%, and the authors did not observe any noticeable matrix effects.

Recently, Sturm and co-authors [203] reported experiments on LIPS utilizing multiple laser pulse excitation, for the multielement (7 elements) analysis of low-alloy steel samples using time-gated detection. The Q-switched Nd:YAG laser emitted three equal-energy pulses of ~ 16 ns duration and with a time separation of 25 μs between the first and the second pulse and 40 μs between the second and the third pulse. A 0.75-m Rowland-based vacuum spectrometer, equipped with a holographic diffraction grating of 2400 grooves/mm was used to disperse the plasma radiation, while photomultiplier tubes were positioned across the Rowland circle to detect specific wavelengths. The authors concentrated on the light elements phosphorus, sulphur and carbon using emission wavelengths from 178.28 nm to 193.09 nm, i.e. in the far UV region. They achieved linear calibration curves, using the internal standard method, with limits of detection below 10 μg/g for all three elements, i.e. 9 μg/g for phosphorus, 8 μg/g for sulphur and 7 μg/g for carbon. One year later, the same research group [192] developed

a real time and in-situ LIPS system for production / process control and quality assurance in steel factories. They were able to quantify the same three elements for liquid steel in the molten bath. They have obtained detection limits of 3, 21 and 11 μg/g for C, P and S, respectively.

Most recently, Hemmerlin and co-authors [193] evaluated the LIPS technique as an on-site process control tool for the rapid analysis of the light elements C, N, P and S in steels, and compared their results with a spark discharge optical emission spectroscopy technique. The idea was to develop an industrial prototype elemental analyzer that has the capability to use either a spark or a laser source on the same optical mount to directly compare their analytical performances. The authors employed VUV spectral lines, namely 133.6 nm, 149.3 nm, 178.3 nm and 180.7 nm for C, N, P and S, respectively. They performed optimization studies including time-gated parameters (delay and width), the laser pulse energy and number of laser shots. Linear calibration curves were obtained over the concentration range investigated (2 ppm to 100 ppm). Limits of detection were measured by LIPS for these elements and valued at 5, 20, 6 and 4.5 μg/g, respectively. Noticeably better detection limits were obtained with the spark source. The authors suggested that further studies are needed in order to match the analytical performance exhibited by the spark source-OES.

1.8 Aim of the Work

In this work, we investigate the analytical feasibility in the deep VUV region (40 nm to 160 nm) for the quantitative determination of the element carbon in standard reference samples of low-alloy steels (carbon steels). Carbon was chosen as a test element. The carbon concentration range studied extends from 0.001% (10 μg/g) up to 1.32%; many important industrial and technological products are being manufactured from various steel alloys containing carbon in this range. To achieve this purpose, a VUV-based laser-induced plasma spectroscopic technique has been developed, using time-integrated space-resolved optical emission spectroscopy. We explore, for the first time, the effectiveness of employing spatially-resolved emission spectroscopy in the deep VUV in eliminating the need for more expensive time-gated detector systems. Six prominent ionic spectral lines of carbon, representing three ionization stages of 1^+, 2^+ and 3^+, have been carefully chosen and proved to be spectral interference-free.

Three modern Q-switched Nd:YAG lasers, operating at the fundamental wavelength of 1064 nm as well as at the second, third and fourth harmonics of 532 nm, 355 nm and 266 nm (for one of the lasers only), respectively have been employed. A 1-m normal incidence vacuum spectrometer, equipped with a concave reflective holographic grating of 1200 grooves/mm and reciprocal linear dispersion of 0.83 nm/mm in the first order was used to disperse the emitted radiation from the plasma. The VUV dispersed radiation was detected using two non-gated multichannel detectors (one at a time), namely a channel electron multiplier array / photodiode array (CEMA / PDA), and a backside-illuminated charge-coupled device (CCD).

The main objectives of the work are summarized in the following points:

1- To explore the analytical capability of the LIPS technique in the deep VUV region (40 nm to 160 nm) for the quantitative elemental characterization of steel alloys. Carbon was chosen as a test element.
2- To investigate the effectiveness in the VUV, for the first time, of space-resolved emission spectroscopy in obviating the need for time-gated detector systems.
3- To optimize various experimental parameters and conditions including the laser energy and power density, laser wavelength, focusing lens types and conditions, spatial distribution of the emitting species, as well as composition and pressure of different ambient atmospheres (air, argon and helium). The objective from these relatively extensive studies was to provide the best signal-to-background ratios for each case, and hence the best sensitivity.
4- To construct analytical calibration curves for carbon over a reasonable wide dynamic range, and to evaluate the analytical performance figures of merit for the developed LIPS technique (limits of detection, precision and accuracy).
5- To characterize the plasma in terms of its fundamental physical parameters such as electron densities and temperatures as a function of the axial distance from the target surface. The existence or absence of thermodynamic equilibrium in the plasmas investigated is also discussed.
6- Finally, to devise an industrial prototype of the technique capable of performing real-time, in-situ and on-line characterization of steels, in particular, and other metallurgical and solid materials, in general.

1.9 Thesis Organization

The thesis is divided into seven chapters. A brief account of each chapter is given in the following paragraphs:

Chapter I deals with an overview of the history and present state of the direct elemental composition analysis of solid materials, in general, and metals and alloys, in particular using laser-produced plasmas. Basic principles and instrumental set-ups of the laser-induced plasma spectroscopy (LIPS) technique are described, and variety of theoretical as well as experimental investigations into the nature of the interaction between lasers and solid materials and the subsequent plasma ignition and expansion are presented. Some selected analytical applications of the technique regarding different types of solid samples are also given. Then, the formulation of the research problem this thesis addresses is described, followed by a summary of the main objectives of the present work.

Chapter II introduces the theoretical basis of the interaction between nanosecond, high-powered lasers and solid materials, particularly metals and alloys, including heating, melting and vaporization processes encountered in such interactions. Also, the consequent formation and evolution of the plasma produced into vacuum and background gases are briefly described. Different atomic processes occurring in plasmas, as well as plasma thermodynamic equilibrium states are discussed. Fundamentals of quantitative spectroscopy for measuring the elemental constituents from plasmas with the subsequent construction of analytical calibration curves are outlined. Finally, various spectral line broadening mechanisms important for the plasmas investigated are discussed and summarized.

Chapter III presents a detailed description of the instrumentation and experimental procedures utilized in the present work, including lasers, target chamber and the vacuum system, the spectrometer and the multichannel detectors.

Chapter IV depicts the experimental feasibility and effectiveness of using the time-integrated spatially-resolved emission spectroscopic technique developed in this thesis for the quantitative characterization of steel alloys for their carbon content, using laser-

produced plasmas. The studies carried out in this chapter demonstrate the behaviour of each of the six different ionic carbon spectral lines selected in this work as a function of the distance in the plasma from the target surface in the wavelength range 40 nm to 160 nm. Also, a comparison between the non-gated CEMA / PDA and CCD detectors employed in this work is performed and evaluated in terms of spectral resolution, emission intensity and sensitivity of measurements.

Chapter V presents an extensive optimization study for the experimental parameters and conditions including the laser energy and power density, lens focusing types and conditions, spatial distribution of emitting species in the plasma as well as ambient atmospheres and pressure. A set of optimized parameters and conditions for this type of application is finally given and used for the rest of the work. Analytical calibration curves for carbon from one of the spectral lines under study, i.e. C III 97.7 nm, are constructed. The Limit of detection, obtained for the mentioned spectral line, of the developed LIPS technique is evaluated and compared with those from other previous studies. Also, a comparison of different methods to construct calibration curves such as the internal standardization method is discussed.

Chapter VI presents spectroscopic diagnostic methods in the VUV spectral range for the determination of the electron density, as well as excitation and ionization temperatures in the steel plasmas, using the time-integrated space-resolved emission spectroscopic technique developed in the present work. Furthermore, considerations of local thermal equilibrium (LTE) condition in the plasma are discussed, based-upon the results obtained.

Chapter VII A summary, as well as some general conclusions, drawn from the results obtained in this work are introduced. Moreover, prospects for future work regarding the improvement sought for the technique and new applications are discussed.

CHAPTER II

THEORETICAL PRINCIPLES

"Whatever is combustible flashes into flames at its torch, lead runs like water, it softens iron, cracks and melts glass, and when it falls upon water, in continently that explodes into steam"

H. G. Wells, The War of the Worlds (1896)

This chapter introduces the theoretical basis of the interaction between nanosecond, high-powered laser pulses and solid materials, particularly metals and alloys, including heating, melting and vaporization processes encountered in such interactions. Also, the consequent formation and evolution of the plasma produced into vacuum and background gases are briefly described. Different atomic processes occurring in plasmas, as well as plasma thermodynamic equilibrium states are discussed. Fundamentals of quantitative spectroscopy for measuring the elemental constituents from plasmas, with the subsequent construction of analytical calibration curves are also outlined. Finally, various spectral line broadening mechanisms are discussed and summarized.

2.1 Interaction of High Power Laser Radiation with Metals

The physical processes involved in the initial stages of generating a plasma by focusing a Q-switched, high-peak power laser pulse onto a solid metal surface are complex. For instance, initial populations of atoms, ions and electrons in the plasma and their subsequent dynamics considerably change with the laser pulse duration, energy, wavelength and irradiance (power density). In addition, the type of target material and the variation of its optical, thermal and mechanical properties with temperature and pressure greatly influence the generation and subsequent evolution of the plasma plume. Moreover, the composition as well as pressure of the surrounding atmosphere plays a significant role in the hydrodynamic expansion of the plasma plume formed.

Besides considering heating of the target while in the solid-state form, melting and vaporization, as well as thermal ionization of the vapour produced must also be taken into account. In this part of the present chapter, the focus will be towards nanosecond lasers producing power densities in the intermediate range of 10^{8}–10^{11} W cm^{-2}, that is the range usually used for almost all laser-induced plasma spectroscopy (LIPS) practical applications. However, a comparison with lower / higher power densities and with lasers emitting in the picosecond / femtosecond time regime is occasionally given.

2.1.1 Heating, melting and evaporation

Upon focusing a Q-switched laser pulse onto the surface of a metal target, a certain portion of the pulse is initially reflected off the surface. Photons constituting the rest of the radiation are absorbed by free electrons in the conduction band of the material, which are, in turn, raised to higher energy levels. The absorbed electromagnetic energy is converted, partially, into heat energy by collisions among the excited electrons and lattice phonons. Relaxation times between these collisions are on the order of 10^{-13} s, which is significantly short when compared to the nanosecond laser pulse employed. Consequently, the absorbed energy is effectively instantaneously transferred to the solid as heat causing a rapid rise in the surface temperature at a rate of about 10^{10} K s^{-1} [9].

The interaction between the laser beam and the solid material occurs over a very thin surface layer usually designated as the optical skin depth (sometimes called the optical

penetration depth), δ_{opt}. It is the inverse of the absorption coefficient of the metal surface, and describes the length along which the incident laser intensity drops to 37% of its initial value. The optical skin depth is given by [4]:

$$\delta_{opt} = \frac{1}{\sqrt{\pi \nu \mu_0 \sigma}} \qquad [2.1]$$

where μ_0 is the permeability of free space ($4\pi \times 10^{-7}$ Wb A^{-1} m^{-1}). For a Nd:YAG type laser emitting at its fundamental wavelength 1064 nm, the frequency, ν, is 2.82×10^{14} Hz, and irradiating an iron target (content of iron in the steel samples employed in the present work is $\geq$ 95%) having electrical conductivity, σ, of about 1×10^7 $mhos^{-1}$ m^{-1}, the corresponding optical skin depth is about 9.5 nm. On the other hand, the propagation length of heat energy into the metal because of thermal conduction is characterized by the heat penetration depth, δ_h, and is given by the following formula [4]:

$$\delta_h = \sqrt{2at_p} \qquad [2.2]$$

where a is the thermal diffusivity ($a = K/(\rho \, . \, C)$, where K is the thermal conductivity in W m^{-1} K^{-1}, ρ is the density in kg m^{-3} and C is the specific heat capacity in J K^{-1} kg^{-1}) and t_p is the laser pulse duration. The heat penetration depth for a Nd:YAG laser pulse of around 10 ns length in a steel target ($a = 0.23 \times 10^{-4}$ m^2 s^{-1}) is about 0.68 μm.

For very low power densities on the order of 10^6 W cm^{-2}, there is a rise in temperature by conduction and heating of the surface leading to a likely phase change in the metal. When employing higher power densities, i.e. in the range 10^7–10^8 W cm^{-2}, ejection of electrons, ions and neutral molecules by thermionic emission with the subsequent possible creation of low-density and temperature plasmas have all been observed [8]. This power density regime (10^6–10^8 W cm^{-2}) generally finds applications in different fields such as optical data storage, laser-materials treatment, cutting and welding. Thermal effects produced by the laser beam can be mainly determined by the thermal-optical properties of the metallic target under investigation. For instance, the largest heating effects should be expected with materials having the lowest thermal conductivity and reflectivity at the laser wavelength used [204]. As the laser spot size

on the metal surface is generally orders of magnitude greater than the heat penetration depth, effects of heat on a solid target can be predicted by solving the one-dimensional differential equation of heat conduction into a semi-infinite solid [205]:

$$K\frac{\partial^2 T}{\partial x^2}-\frac{K}{a}\frac{\partial T}{\partial t}=-E\alpha\exp(-\alpha x) \qquad [2.3]$$

where T is the temperature (K); x is the depth (m) developed on the surface after time t (s) of the laser pulse; K (W m^{-1} K^{-1}) and a (m^2 s^{-1}) are the thermal conductivity and diffusivity of the relevant material, respectively and α (m^{-1}) is the absorption coefficient. For the simple case of a constant power density, P (W cm^{-2}), and a material with large absorption coefficient the surface temperature, T_s, of the metal after a time t_b is given by:

$$T_s=\frac{2P}{K}\left[\frac{at_b}{\pi}\right]^{1/2} \qquad [2.4]$$

where t_b (s) is the time elapsed to reach the boiling point of the surface. For a steel target (iron content ≥ 95%), irradiated by a Q-switched nanosecond laser beam, a power density of about 1.1×10^8 W cm^{-2} is required to heat the surface to its boiling point of 3023 K. At this power density, the electric field strength imparted to the solid surface from the laser beam is estimated to be about 2.9×10^5 V cm^{-1} ($E = 27.45\sqrt{P}$ [204]). These simplified calculations assume that losses through re-radiation and convection are insignificant. They also neglect the dependence of reflectivity of the metallic surface on temperature. However, a model based on Drude-Zener free-electron theory for metals predicts a linear decrease in reflectivity of the metal as its temperature increases [8]. Consequently, more laser energy is expected to be absorbed by a hot metal surface than that predicted using room temperature reflectivity. In addition, experiments show that the fraction of the total energy reflected decreases with increasing the incident power density, hence enhancing the laser-metal coupling [9].

After heat is thermally conducted in the interior of the target, a thin molten layer forms below the surface. As the thermal energy deposited at the surface increases, a point is reached where the incident energy exceeds the latent heat of vaporization.

Consequently, heat can not be carried away from the point of irradiation fast enough to prevent the surface reaching its boiling temperature and evaporation occurs. It is of interest at this stage to estimate the laser power density, P_{th}, below which no evaporation from the target takes place. As mentioned, vaporization of the sample material begins when the energy deposited on the target surface equals to or exceeds the latent heat of vaporization, L_v, of the solid. The threshold power density, P_{th}, is given by [8]:

$$P_{th} = \rho L_v \left[a t_p \right]^{1/2} \qquad [2.5]$$

For an iron target having density, ρ, of 7.87 g cm^{-3}, latent heat of evaporation of 6095 J g^{-1} and diffusivity of 0.23 cm^2 s^{-1}, the threshold power density of vaporization is about 2.3×10^8 W cm^{-2}, with a laser pulse of 10 ns duration.

The maximum amount of material, m (g), that can be vaporized by a single laser pulse of energy E (J) is given by the following formula [208]:

$$m = \frac{E}{C(T_b - T_0) + L_v} \qquad [2.6]$$

where C is the specific heat capacity (J K^{-1} g^{-1}), T_b and T_0 (K) are the boiling and initial temperatures of the material under investigation and L_v is the latent heat of vaporization (J g^{-1}). Accordingly, for a single laser shot of 0.4 J, for example, the calculated maximum amount ablated from an iron target is about 55 μg. However, it was observed that the actual amount of vapourized material is significantly smaller than the calculated amount by almost one order of magnitude for most metals [86]. The initial reflection of the laser beam on the metal surface, as well as its absorption in the plasma produced during the pulse duration may well interpret this observation [86].

2.1.2 Picosecond / femtosecond laser pulses

For ultrashort laser pulses (in the picosecond and femtosecond regime), thermal conduction can be neglected leading to a heat penetration depth on the order of the

optical skin depth of the laser pulse, i.e. $\delta_h(t) \approx \delta_{opt}(t)$ [62]. To understand more this important phenomenon, let us consider the typical characteristic time scales of the different physical processes involved. These include free electron heating and thermalization, which takes approximately 100 fs; hot electron gas cooling and considerable energy transfer to the lattice lasts for a few ps; thermal diffusion in the bulk material takes place on a time scale of 10^{-11} s and the onset of thermal melting and vaporization occurs after 10^{-10} s [47].

An important conclusion can therefore be drawn: a laser pulse of duration longer than a few ps does not interact the whole time with the original thermodynamic state of the solid material. Instead, it interacts with different transient states and with the plasma of evaporated material, as well as with the buffer gas (if existing) above the sample surface. Particularly, this is extremely important in the course of spectrochemical analysis of brass samples (Zn / Cu alloys) where the main part of the sample is evaporated from the molten metal and preferential volatilization (fractionation) of different elements with different melting temperatures occurs [179]. In such a case the stoichiometric composition of the plasma produced does not adequately represent the composition of the bulk material and the accuracy of the analytical procedure deteriorates.

The situation dramatically changes if a laser pulse with a duration of approximately 100 fs or shorter is employed. Now the laser interacts only with the electron sub-system of the material. Before the material experiences any changes in thermodynamic state, the laser pulse is terminated and most of the energy is deposited into the sample; material removal takes place after the laser pulse. Also, the threshold power density for vaporization in the case of ultrashort laser pulses is much less than that for nanosecond pulses (about an order of magnitude less).

2.1.3 Plasma formation

For power densities of concern in the present work, i.e. 10^8–10^{11} W cm^{-2}, a variety of laser-matter interactions, as well as plasma effects such as phase change, vaporization, thermal ionization as well as shock waves occur during the first few cycles of the electric field associated with the incoming laser beam. In this respect, two mechanisms

of ionization predominate. Firstly, direct photoionization (PI) occurs when an incoming photon has sufficient energy to directly ionize an atom. Photoelectrons produced in this way may then proceed to ionize further atoms through collisions, thus resulting in a cascade effect (the electron concentration increases exponentially with time) [3]. Direct PI is dominant with UV laser pulses (such as the Nd:YAG fourth harmonic at 266 nm and KrF excimer at 248 nm) and target materials having photoelectric work functions of ≤ 5 eV (most metals have work functions in this range).

In the second mechanism, termed as multiphoton ionization (MPI), a number of laser photons are simultaneously absorbed permitting rather tightly bound electrons to be liberated. MPI process takes place very rapidly (within the first few cycles of the laser electric field) and predominates at such laser wavelengths where the probability of its occurrence is greatly increased. For example, at long wavelengths such as that of a CO_2 laser (10.6 μm), the simultaneous absorption of 50 laser photons each of energy of about 0.1 eV is required to overcome a 5 eV ionization potential; only 5 photons of a Nd:YAG laser (1.06 μm) are needed to perform the same process. It should be noted that a 50 simultaneous photon absorption process is a highly improbable event, except at very high power densities ($\geq 10^{16}$ W cm^{-2}) [206].

The rapid ionization of surface atoms provides a large free electron population, and this results in an increased efficiency of absorption of the incoming laser photons via the process of inverse bremsstrahlung (IB). In this process, free electrons accelerated by the electric field of the focused laser beam experience a momentum transfer with ions through their Coulomb interaction, thus leading to an increase of their kinetic energy. Collisions with atoms / ions in the solid target result in rapid melting and vaporization from the surface. The change in phase that takes place upon melting allows a significant decrease in the initial reflectivity of the metal surface, and the subsequent increase in coupling of the laser beam onto the target [205]. Figure 2.1 illustrates the interaction of a Q-switched, high-peak power laser with a metallic target and the subsequent production of a laser-produced plasma.

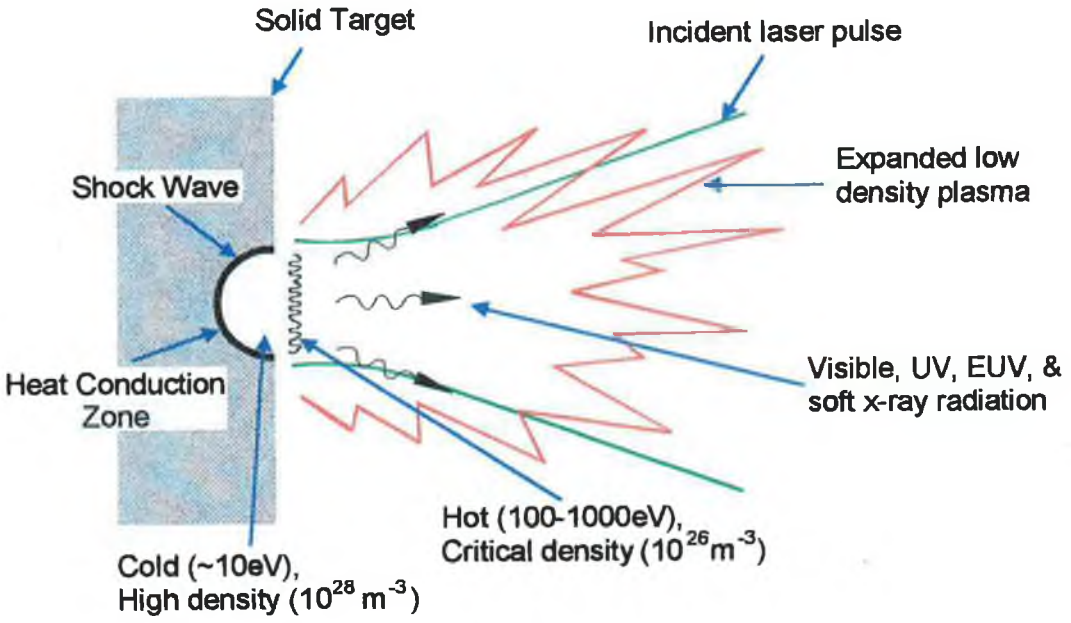

Fig. 2.1 Schematic representation of the creation of a typical laser-produced plasma [After Ref. 262].

Early during the incident laser pulse, the vapour formed in front of the target surface consists mainly of low electron and high neutral atom density [209]. Absorption of laser photons in the plasma generally begins via electron-neutral inverse bremsstrahlung (IB); direct photoionization (PI) of excited state neutrals plays an important rule for short laser wavelengths, as mentioned earlier. As the energy absorbed increases, the excitation temperature, T_{exc}, as well as ionization temperature, T_{ion}, increases and so too does the electron density of the plasma, n_e. As a result, the degree of ionization significantly enhances and the absorption of the laser beam by free-free electron transitions during collisions with positive ions becomes the dominant heating mechanism. Except near the threshold irradiance for creating the surface vapour plasma, vapour absorption and the subsequent temperature rise are so rapid that significant expansion of the hot vapour does not occur prior to the formation of a hot ionized vapour plasma at a pressure substantially above the ambient pressure (ablation pressure) [209].

When considering vaporization and the subsequent plasma initiation it is imperative to state that the boiling point of a solid material is pressure-dependent [204]. In this respect, two types of laser-induced pressure may be distinguished: radiation and ablation pressures. The radiation pressure, as the name implies, is due to the focused

high-peak power laser pulse on the target surface. To provide an estimation of the radiation pressure initiated on the target surface upon incidence of the laser radiation, a pulse of 100 MW peak power absorbed in an area of 10^{-4} cm^{-2} (1×10^{12} W cm^{-2} power density) exerts a peak radiation pressure of about 300 atmospheres. The ablation pressure, on the other hand, describes the momentum recoil exerted on the surface from the departing material. The ablation pressure is usually 4–5 orders of magnitude greater than the radiation pressure [204]. The combination of both ablation and radiation pressures results in the transmission of a compressive shock wave that propagates into the target [205]. Since the pressure is an increasing function of the power density [6], evaporation takes place at significantly higher power densities (it is as twice as big, as indicated by equation 2.5 for steel target and nanosecond laser pulses) than those required to heat the surface to its boiling temperature.

At very high laser power densities ($\geq 10^{12}$ W cm^{-2}), the physical processes usually occurring during initial stages of plasma formation, such as surface heating and thermal conduction as well as phase transformation and vaporization, are often ignored. The reason for that is partly due to the fact that the energy required to carry out these processes is negligible compared to that needed for ionization and plasma heating. For such irradiances, thermal ionization takes place early during the first few cycles of the incident electromagnetic radiation; plasmas produced in this way are assumed to be uniformly 'cold', with electron and ion densities equal to the solid atom density (10^{28} – 10^{29} m^{-3}) [204]. Because the thin plasma vapour formed is sufficiently dense and ionized, the laser light is significantly absorbed and completely shielded from the target surface. The continual absorption of the laser beam produces further ionization through collisions, thus increasing the electron density still further until it eventually reaches a critical value, n_{ec}, at some distance from the target surface. This critical electron density is defined by [7]:

$$n_{ec} = \omega^2 \frac{m_e \varepsilon_0}{e^2} \cong \frac{10^{15}}{\lambda^2} \qquad [2.7]$$

where ω is the laser angular frequency ($\omega = 2\pi\nu$; ν (Hz) = c / λ); e and m_e are the electron charge and mass, respectively and ε_0 is the permittivity of free space (8.854×10^{-12} F m^{-1}). Substituting these values in equation 2.7, one obtains a critical electron

density of 9.92×10^{26} m^{-3} at the fundamental wavelength (1064 nm) of the Nd:YAG laser. The thin layer or slab in the plasma at which $n_e \approx n_{cc}$ is termed as the deflagration zone. Radiation will propagate into the plasma until at some depth it reaches the layer of critical density, whereupon the absorption coefficient for inverse bremsstrahlung tends towards infinity, after which the wave becomes evanescent and is eventually reflected.

Due to light absorption in the plasma by IB, the vapour becomes hotter and expands leading to a reduction of the vapour density to the level which enables the laser beam to reach the target and evaporate more material, thereby increasing the density once more [6]. The process, which is usually known as the self-regulating regime, repeats itself with the critical density boundary moving towards the laser beam at velocities up to 10 km s^{-1}. After termination of the laser pulse, the plasma cools and decays. As the plasma expands, line emission dominates the radiation process, with average temperatures as high as 25×10^3 K (~ 2.16 eV) [6].

In summary, it is clear that plasmas created using power densities $\geq 10^8$ W cm^{-2} have many similar characteristics. However, plasmas produced in the power density range $10^8 < P < 10^{12}$ W cm^{-2} always have lower electron densities than the critical value and thus laser-target interaction is sustained throughout most the duration of the laser pulse. For this reason, laser-produced plasmas in this irradiance regime are useful for applications such as LIPS and PLD. In addition, the electron-ion inverse bremsstrahlung process may no longer be the sole mechanism by which laser radiation is absorbed by the plasma [109]. Other processes such as electron-atom inverse bremsstrahlung (IB) and direct photoionization (PI) must be accounted for [62, 109]. A short account on absorption mechanisms in laser-produced plasmas is discussed in Appendix A.

2.1.4 Laser-produced plasma expansion and evolution

As a consequence of thermally induced pressure gradients, the plasma plume produced when a Q-switched laser pulse is focused onto a metal target expands primarily along a direction perpendicular to the metal surface. Expansion continues long after the laser pulse is over, typically lasting on the order of microseconds. As the plasma expands, both the temperature and density rapidly decrease, with an adiabatic transfer of thermal energy into kinetic energy of expansion.

The expansion of laser-produced plasmas in vacuum fundamentally differs from that in higher-pressure ambient atmospheres, a situation that is highly important in terms of analytical applications of laser-produced plasmas. The nature and behaviour of the expansion of laser-produced plasmas in both vacuum and gaseous atmospheres will be briefly discussed in the following two sub-sections.

2.1.4.1 Plasma expansion in vacuum

In vacuum, the plasma up to the end of the laser pulse is optically thick throughout the entire spectral range from the X-ray to the IR [210]. Consequently, the spectrum observed is characterized by the surface temperature of the plasma, which is of the order of 10^4 to 10^5 K [210]. The strong radiation trapping, as well as high density and temperature state of the plasma makes the energy density content very high. This fuels the subsequent expansion and sustains the luminosity of the plasma for a long time after the expiration of the laser pulse. Depending on the laser, as well as on the background atmosphere characteristics, the plasma lifetime may be anywhere from about 300 ns up to around 40 μs [210].

For a solid-steel alloy target irradiated by a Q-switched, 1064 nm Nd:YAG laser pulses with a peak-power of 100 MW in about 0.1 mbar air, the expansion velocity of the luminous front is approximately 2.5×10^7 cm s^{-1}, and this corresponds to a mean kinetic energy of 18.2 keV of neutral and singly ionized iron atoms. This rapid expansion lasts for about 200–300 ns with respect to the laser pulse [210].

Higher ion stages, heated to higher temperatures and travelling at greater velocities than neutral and lower charged ions, lead the expanding plasma plume. These highly charged ions are essentially distributed within a narrow angular region about the normal to the target surface and the radii of such distributions increase with decreasing charge states. This spatial structure was observed experimentally by Irons et al. [211] for a laser produced carbon plasma, and is reproduced in Fig. 2.2. Also shown in Fig. 2.3 are the temporal and spatial distributions of peak intensities for different ion stages of carbon (I-VI) [212], which too support the behaviour observed in Fig. 2.2.

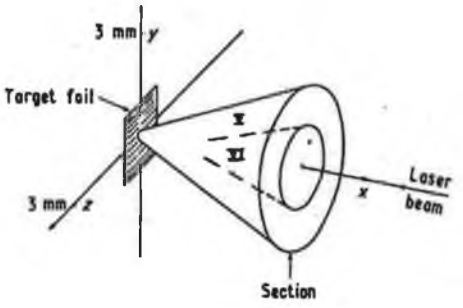

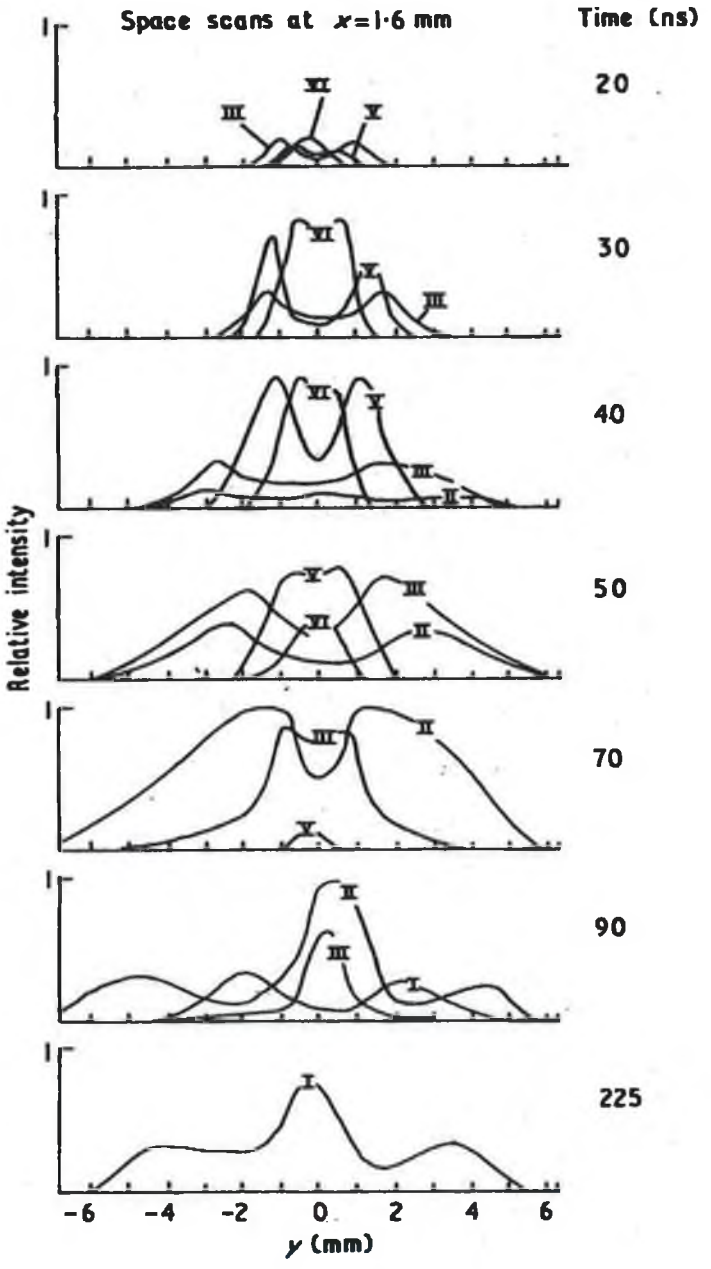

Fig. 2.2. A sequence in time showing the development of the spatial distribution of C I-VI (indicated by I-VI, respectively) at 1.6 mm from the target surface. The peak laser intensity occurs at 20 ns [After Ref. 211].

(A)

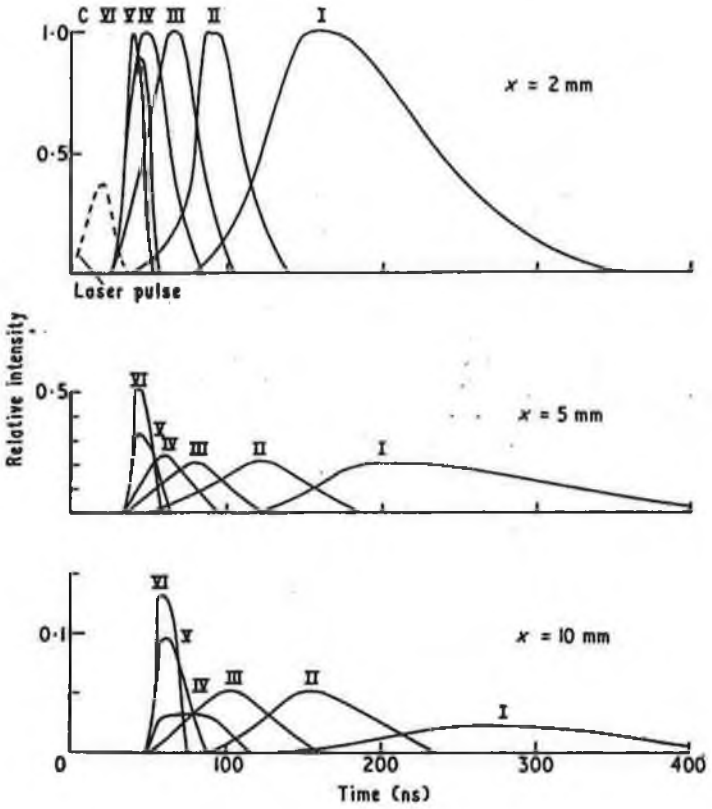

(B)

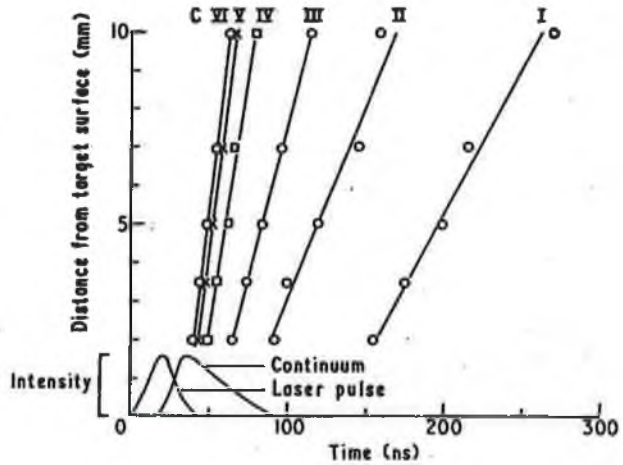

Fig. 2.3. Time variation (A) and axial distance against time (B) for the peak intensities of the lines C I-VI [After Ref. 212].

2.1.4.2 Plasma expansion in a gaseous atmosphere

When a hot, high-pressure laser-produced plasma expands with its supersonic velocity through a gas, the gas-dynamic theory predicts that a shock wavefront forms [209]. The wavefront is basically a discontinuity ahead of which is found undisturbed gas and behind which there is a region of high mass and energy density, as well as high pressure, temperature and momentum [50]. Energy is transferred to the gaseous atmosphere by a combination of thermal conduction, radiative transfer and heating by the shock wave [209]. The relative importance of these processes in determining the subsequent evolution of the vapour plasma depends on irradiance, vapour composition, ambient gas pressure and structure, as well as on the laser wavelength. For example, at low irradiance thermal conduction dominates the early stages of plasma development in the surrounding gas; the vapour plasma is too thin, both spatially and optically, to efficiently transport energy by radiation. On the other hand, shock wave heating dominates the energy transfer process at high irradiance [209]. The shock front velocity depends on the ambient gas pressure, and continually decreases with time. The maximum shock speed is approximately 2.4×10^6 cm s^{-1}, or one-tenth the velocity of the initial, fast expansion front that produced the shock wave [210].

Piepmeier and Osten [50] derived a formula for the fraction, f, of the laser beam energy that is absorbed by the plasma in the region just behind the wavefront:

$$f = \exp\left[\frac{-xk\gamma\left(1-\gamma^{-8}\right)}{s(\gamma-1)}\right] \qquad [2.8]$$

where x is the distance of the wavefront from the sample surface; k is the absorption coefficient of the laser beam in the gas behind the wavefront; γ is the adiabatic index (specific heat ratio) of the gas and $s = 4 + 4 / (\gamma-1)$. Calculations showed that even with a relatively transparent wavefront, most of the laser energy is absorbed in the region near its boundary. Therefore, all the absorbed laser energy is used to sustain the wave (laser-supported shock wave) and f is close to unity. At much lower laser energies and gas pressures, the wavefront is transparent enough to allow a significant fraction of the laser radiation to reach the extended regions behind the wavefront [50].

Once the atmosphere adjacent to the vapour plasma is heated, gases, which were initially transparent to the laser radiation when cold, start to absorb the incoming laser photons via the same absorption mechanisms discussed above, i.e. electron-atom and electron-ion IB (and PI for short wavelengths). Depending on the laser and surrounding gas characteristics, a strongly absorbing gas plasma is eventually created in front of the initial target vapour plasma, thus shielding the main bulk plasma from further direct interaction with the laser radiation. The absorbing gas plasma propagates towards the laser beam (it does so regardless the angle of incidence of the laser on the target surface; on the other hand, the target plasma almost always expands normal to the target surface) until the irradiation is either terminated or reduced to levels that can no longer support an absorption medium [209].

Sedov [213] derived, for a blast wave, a theoretical relationship between the propagation time, t, and the distance of the wavefront from the position of the source of explosion, r, as follows [175]:

$$r = \left[\frac{E_0}{\gamma\rho}\right]^{1/5} t^{2/5} \qquad [2.9]$$

where E_0 is the initial explosion energy (which is proportional to the laser pulse energy); γ is the adiabatic constant (the ratio of the specific heat capacities of the gas) and ρ is the density of the gas. From equation 2.9, one can easily derive the propagation velocity of the shock wavefront as:

$$\upsilon = \frac{2}{5}\left[\frac{E_0}{\gamma\rho}\right]^{1/2} r^{-3/2} \qquad [2.10]$$

Also, the temperature just behind the shock wavefront, T, can be expressed as follow [214]:

$$\frac{T}{T_0} = \left[\frac{2\gamma M^2}{(\gamma+1)} - \frac{(\gamma-1)}{(\gamma+1)}\right]\left[\frac{(\gamma-1)}{(\gamma+1)} + \frac{2}{(\gamma+1)M^2}\right] \qquad [2.11]$$

where T_0 is the room temperature and M is the Mach number of the shock wave. From the above equations, it can be seen that the temperature just behind the shock front increases with E_0. Thus, with increasing energy of the laser pulse, the speed of the luminous front of the plasma increases and so too does the plasma temperature. However, when the plasma temperature is high enough, it emits higher background continuum emission, thus decreasing the sensitivity of the spectral analysis.

Equations 2.10 and 2.11 can fairly well explain the experimental fact that the background emission intensity decreases with distance from the surface of the sample, because the intensity of the continuum emission decreases with decreasing temperature. By taking the spatial distribution of the emission intensity of the spectral line and that of the underlying background into account, the best position for the observation region must be carefully chosen so that the signal-to-background ratio is maximized [182].

Budi and co-authors [215] showed that a plasma having characteristics favorable to spectrochemical analysis can be generated by using a pulsed nanosecond laser pulses when the pressure of the surrounding atmosphere is reduced to around 1 Torr (~ 1.8 mbar). The authors demonstrated that the plasma produced consists of two distinct parts. The first part, usually termed the primary plasma, occupies a small region just above the target surface (0–1 mm), and mainly gives off a strong intense background continuum emission for a short time. The other part, called the secondary plasma, expands with time around the primary plasma and emits sharp and relatively intense spectral lines with very low background emission levels. It is in the secondary plasma that sensitive elemental composition analysis, as well as linear relationships between the emission line intensity of a specific spectral line and the content of its parent element in the target can be achieved. The main results from this study are shown in Fig. 2.4.

According to a model developed by the same group [61], the secondary plasma is excited by a shock wave created by the initially expanding primary plasma. Right after the termination of the laser pulse, particles constituting the primary plasma flow out at supersonic speed. It is strongly believed that the surrounding gas plays the role of damping material, obstructing the free expansion of the propelling particles, by forming something like a wall against which compression takes place. As a result of this compression, a shock wave is generated in the surrounding gas. The most important

point of the shock wave model is that the energy required to produce the secondary plasma is supplied in the form of kinetic energy from the moving particles; the kinetic energy of the moving particles is converted into thermal energy in the plasma by which the atoms / ions are further excited.

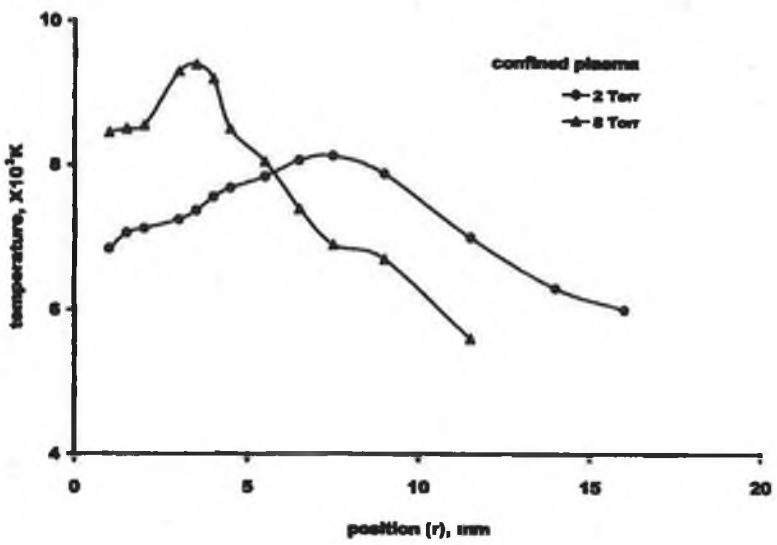

(A)

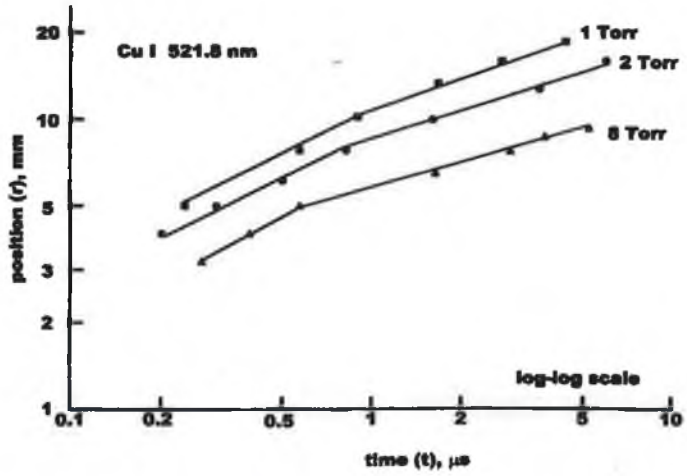

(B)

Fig. 2.4 Average temperature of confined plasmas as a function of position at a surrounding air pressure of 2 and 8 Torr (A), and relationship between the propagation length of the secondary plasma and time for confined plasmas at surrounding air pressures of 1, 2 and 8 Torr (B) [After Ref. 215].

2.2 General Characteristics of Plasmas

In its simplest terms, a plasma is considered to be the fourth phase of matter where a state of ionization, either partially or fully, is fulfilled. To generate and maintain the required assembly of electrons and ions, energy from some appropriate source must be supplied to the parent neutral matter. Throughout the duration of the plasma, overall electrical neutrality is sustained whereby the plasma electron number density, n_e, equates the summation over the total number of ions in all different charge stages, i.e.

$$n_e = \sum_z n_z z \qquad [2.12]$$

where n_z is the number density of ions of charge state z. In contrast to an ordinary gas, whereas the interactions taking place between neutral particles are both weak and short-ranged, the Coulomb forces between charged particles in a plasma are relatively strong and long-ranged. Because of the magnitude and breadth of the Coulomb field, significant numbers of charged particles in the plasma interact with one another and they tend to react together to any perturbing action caused by other neighbouring ions and electrons. In fact, it is this "collective" property of the plasma, which makes it so different and unique from its parent neutral gas. It has been well recognized that collective properties of plasmas significantly influence different radiation processes in many ways [216]. For instance, the long-range Coulomb interactions between the radiating atom or ion and the charged species control the population densities of bound states, shift and broaden energy levels (via Stark effect) and lower the ionization potentials of neutrals.

To quantify the concept of collective phenomena, a quantity known as the Debye length is employed as a measure of the spatial distance over which the long-range Coulomb force acts. In other words, each individual charged particle in the plasma will act on its immediate neighbours with a measurable Coulomb force within this distance; at greater distances, this effective interaction is shielded out by the other surrounding charged species, particularly those of the opposite sign. The Debye length is therefore inversely proportional to the electron number density (n_e) in the plasma and significantly

decreases in dense plasma regions where charge screening is highly prevailing. Debye length, λ_D, can be estimated as [2, 218]:

$$\lambda_D = \sqrt{\frac{\varepsilon_0 kT}{n_e e^2}} \qquad [2.13]$$

where ε_0 is the permittivity of free space; k is Boltzmann's constant; T (K) and e are the plasma temperature and electronic charge, respectively. It is only beyond the Debye length that charged particles in the plasma will respond collectively to external perturbing fields through the long-range Coulomb force. If collective phenomena are to dominate the plasma behaviour, the physical dimensions of the plasma, L, must satisfy the condition:

$$L \gg \lambda_D \qquad [2.14]$$

In plasmas where the condition in 2.14 holds, electrons are displaced collectively by a small distance in one direction with respect to positive ions [2]. As a result, the plasma will be momentarily polarized and the electrons will be inclined to move backwards towards their initial equilibrium positions. The oscillatory motion of electrons is called plasma oscillation or simply plasma frequency, ω_p, and is given by:

$$\omega_p = \left[\frac{n_e e^2}{m_e \varepsilon_0}\right]^{1/2} \qquad [2.15]$$

where m_e is the electron mass; other symbols were previously defined. Ionic oscillations can also occur at frequencies characterized by the ion charge. These frequencies can be obtained by simply replacing the electron mass, m_e, by the ionic mass, m_{ion}, in equation 2.15.

The above mentioned frequencies determine the response to electromagnetic radiation, such as laser beams, incident on the plasma. For example, if the angular frequency of the incoming wave matches that of the plasma a resonance interaction may take place and the transfer of energy from the electromagnetic radiation to the plasma is greatly

enhanced. The propagation of an electromagnetic wave, of frequency $\omega = 2\pi\nu$, through a plasma can be described by the dispersion relationship [217]:

$$\omega^2 = \omega_p^{\ 2} + c^2 k^2 \qquad [2.16]$$

where $k = 2\pi / \lambda$ is known as the propagation constant and c is the speed of light. If an electron density gradient exists, as in laser-produced plasmas, ω_p changes according to equation 2.15. For the case when $\omega_p < \omega$, k is real and the wave propagates through the plasma. On the other hand, when $\omega_p \geq \omega$, k is imaginary and the wave is not transmitted. In fact, the wave is eventually reflected at a specific plasma density, called the critical density, n_{ec}, and is given by equation 2.7. For this reason, lasers emitting in the UV part of the spectrum are ideally suited to heating denser plasma regions in comparison with visible and IR wavelengths [217].

The physics of plasmas is determined by several important atomic processes. The following section briefly summarizes these processes.

2.3 Atomic Processes in Plasmas

In order to improve the understanding of plasma behaviour under various conditions, it is important to identify the appropriate atomic processes (excitation mechanisms) through which energy is exchanged between various species in the plasma. The relative significance of these processes depends on the populations of different energy levels, as well as on the degree of ionization within the plasma. The degree of ionization, in turn, strongly depends on the electron temperature and density attained in the plasma [216].

The atomic processes taking place within a plasma are classified under three main headings: (i) bound-bound transitions, (ii) bound-free transitions and (iii) free-free transitions. Moreover, these processes are further divided according to the mechanism by which they occur, i.e. either collisional or radiative. In addition, for each of these three processes, excitation or ionization and their inverses, de-excitation or recombination, must also be taken into account. In the following sub-paragraphs, a brief

description of the atomic processes and their associated collisional and radiative mechanisms is presented. In addition, Table 2.1 summarizes these processes.

Table 2.1 Collisional and radiative events associated with the three atomic processes occurring in plasmas.

Atomic Process	Collisional		Radiative	
	Excitation	De-Excitation	Excitation	De-Excitation
Bound ↔ Bound	Collisional Excitation	Collisional De-Excitation	Photo Excitation	Photo De-Excitation
Bound ↔ Free	Collisional Ionization	Three-Body Recombination	Photo Ionization	Photo Recombination
Free ↔ Free		Bremsstrhlung	Inverse Bremsstrahlung	

2.3.1 Bound ↔ bound transitions

A bound ↔ bound excitation transition takes place when an atom / ion occupying a discrete atomic / ionic energy level is promoted to a higher level via absorption of a finite quantum of energy. A collision between the atom / ion and other atoms, ions or electrons within the plasma results in the conversion of kinetic energy into excitation energy (*Collisional Excitation*). It is worthwhile noting that collisional excitation and de-excitation processes are dominated by free electrons (rather than atoms or ions) because of their high mean velocity and the long-range nature of their interaction [216], and so collisions with electrons will only be considered here. In *Collisional De-Excitation*, the reverse process, excitation energy is converted into kinetic energy through a collision event between an atom / ion in an excited state and a free electron leading to a transition to a lower energy state. Collisional excitation and de-excitation processes are described by the following equation:

$$A + e_1 \rightleftharpoons A^* + e_2 \qquad [2.17]$$

where A and A^* are the atom / ion in its initial and excited state, respectively and e_1 and e_2 are the electrons involved in the collision event (K.E. of e_1 > K.E. of e_2).

On the other hand, a radiative bound-bound transition involves the absorption of a photon with a specific energy, hν, by an atom / ion, thus promoting to a higher discrete energy state (*Photo Excitation*). The converse process is *Photo De-Excitation,* in which a photon is emitted upon returning the atom / ion to its original energy state. The emission and absorption of a photon by an atom / ion in the plasma can be outlined by:

$$A + h\nu \rightleftharpoons A^* \qquad [2.18]$$

In terms of analytical applications of plasma spectroscopy, radiative de-excitation processes are the most important since they yield the characteristic line spectra used for spectrochemical analysis. Spectral line emission from partially ionized plasmas, i.e. plasmas having electron temperatures around 1 eV, occurs mainly in the UV / visible range. As the plasma temperature increases, atoms / ions are promoted to higher energy states and so, upon photo de-excitation, release line radiation at increasingly shorter wavelengths (in the far and vacuum UV spectral regions).

2.3.2 Bound ↔ free transitions

A bound ↔ free excitation transition takes place when an n times (n = 0, 1, 2, 3, ...) ionized atom obtains energy in excess of one of its ionization potentials, thus promoting an electron from a bound energy level to a 'free' continuum energy level. As a result, a free electron, e_1, and an (n+1) times ionized atom, A^{n+1} (normally in its ground state) are produced. Collisions with electrons in the plasma lead to such transitions (*Collisional Ionization*). Collisional recombination (*Three-Body Recombination*) can occur when two electrons (e_1 and e_2) encounter an (n+1) times ionized atom and one of them, say e_1, loses energy and returns to a bound energy level (recombines with the ion). The other electron, e_2, absorbs the surplus energy with a gain in the kinetic energy of the system. The production of a negative ion in the plasma is possible via the recombination

between an electron and an atom. The two collisional processes just described are represented in the following equation:

$$A^n + e_2(T_1) \rightleftharpoons A^{n+1} + e_1 + e_2(T_2) \qquad (T_1 > T_2) \qquad [2.19]$$

In a bound ↔ free radiative transition, a photon with a sufficient energy can remove an electron from a bound state in an atom / ion thus leaving it in a higher stage of ionization (*Photo Ionization*). The reverse process is called *Photo Recombination*, where an electron drops from a continuum energy level and recombines with an atom / ion with the emission of a photon. Both radiative processes are summarized in the following equation:

$$A^n + h\nu \rightleftharpoons A^{n+1} + e \qquad [2.20]$$

The optical spectrum associated with collisional and radiative recombination is a continuum emitted over a broad energy band and characterized by a low energy cut-off known as the recombination limit [204]. This limit coincides with the minimum energy required to remove an electron from the last atomic / ionic bound state. Consequently, the observed continuum emission is an integration of various recombination continua originating from numerous atomic / ionic bound states.

2.3.3 Free ↔ free transitions

Free-free radiative 'absorption' transitions occur when a free electron that is moving in the field of an ion absorbs a fixed energy photon. The electron is thus raised to a higher energy level in the continuum, and its kinetic energy is significantly increased. This process is called *Inverse Bremsstrahlung*. The latter process is considered to be the main mechanism of plasma heating by high-power lasers of all wavelengths [204]. *Bremsstrahlung*, the inverse process, involves an encounter between a free electron and another particle resulting in a transition to a lower continuum state of the system with the emission of a photon. Since the initial and final states are continuous, the spectrum observed is also continuous. Bremsstrahlung and its inverse processes are outlined in the following equation:

$$A^n + e(T_1) + h\nu \rightleftharpoons A^n + e(T_2) \quad (T_2 > T_1) \qquad [2.21]$$

Although electron-ion and electron-atom collisions can result in Bremsstrahlung radiation, the majority of the observed emission continuum is due to the former type.

2.4 Thermodynamic Equilibrium in Plasmas

One of the most important applications of plasma spectroscopy has been the determination of the fundamental physical parameters of the plasma such as electron temperature and density. These, in turn, strongly depend on the thermodynamic equilibrium state of the plasma; if the thermal state of the plasma is known, all parameters of interest can be derived. In order to achieve this aim, spectra observed should be interpreted in terms of a fully consistent theoretical plasma radiation model.

If the plasma is contained in an ideal thermodynamic enclosure at a constant temperature, then its thermal state can be fully characterized by a finite number of thermodynamic macroscopic variables. These are the temperature, the pressure and, in case many elements are present, the concentration of these elements. In such a system, usually termed complete thermodynamic equilibrium (CTE), the following conditions are satisfied [218]: (i) the intensity distribution of the radiation as a function of frequency and temperature is governed by Planck's radiation distribution function (black body radiator); (ii) all particles, electrons, neutral species and ions obey the Maxwell velocity distribution law (kinetic temperature); (iii) population distributions over bound energy states of any atom or ion are given by the Boltzmann formula (excitation temperature) and (iv) the number of ions in an ionization stage z relative to that in a stage (z-1) is given by the Saha distribution equation (ionization temperature) [219]. The equations describing various distribution functions are given in Appendix B.

In CTE plasmas, the temperature used to describe the above four distributions has a unique value. Moreover, every atomic process described in the previous section is directly balanced by its opposite process, i.e. various atomic processes in the plasma follow the principle of detailed balance [216]. For example, for every photon emitted, a photon of the same frequency must be absorbed, and for every excitation by electron collision, there must be a deexcitation between the same two energy levels. In most

laboratory plasmas, however, the CTE condition rarely exists because of the fact that these plasmas are optically thin at most frequencies and thus radiation originated in the interior of the plasma passes through without being re-absorbed.

For this reason, a number of approximate thermodynamic equilibrium models have been developed in order to better interpret the plasma conditions, as well as emission spectra observed [216]. The requirement for a range of various models has arisen from the highly diverse nature of laboratory-based plasmas. These models are mainly characterized by the value of electron number density, n_e, which largely affects the relative importance of the different atomic excitation and de-excitation processes [219]. In the following sub-sections, plasma state models satisfying this requirement are briefly discussed.

2.4.1 Local thermodynamic equilibrium (LTE)

For sufficiently high electron density plasmas, collisional events, particularly those involving electrons, play a more important role than radiative processes in determining the behaviour of the system. For instance, the excited state of an atom / ion must have a much larger probability of deexcitation by an inelastic collision with a free electron than by spontaneous emission of radiation. Plasmas in which equilibrium is maintained for all CTE distribution functions (with the exception of Planck distribution law) at any instant and spatial point are said to be in LTE state. Consequently, an electron temperature, T_e, is defined and in terms of this temperature the electron velocity distribution, the populations in excited states and various stages of ionization are given by the Maxwell velocity distribution, the Boltzmann formula and the Saha equation, respectively [219]. The kinetic temperature, which characterizes the velocity distribution of ions and neutral species, as well as the atomic / ionic excitation temperature has no significance and they are not necessarily to be the same as the electron temperature [2]. This is because the atom-ion interactions are much less important than electron-atom and electron-ion interactions, and thus do not normally influence the LTE condition. It is worthwhile noting that in LTE plasmas, the principle of detailed balance exists amongst the collisional processes alone.

For plasmas in which collision transition rates are at least ten times more probable than radiative decay rates, McWhirter [219] derived a criterion for the minimum electron number density, n_e (cm^{-3}), above which the LTE condition applies:

$$n_e \geq 1.6 \times 10^{12} T^{1/2} \chi^3 \qquad [2.22]$$

where T is in Kelvin and χ is the excitation energy difference (in eV) between terms of the atomic / ionic transitions under consideration. The inequality in 2.22 is least likely to be satisfied for the largest energy gaps. For hydrogen, for example, this is the 1s-2p (resonance) transition that corresponds to an energy difference of 10.2 eV. At such conditions, a laser-produced hydrogen plasma would have a temperature of 4 eV [221]. Substituting these values in 2.22, the electron density must exceed 2×10^{17} cm^{-3} for LTE to hold in the plasma.

2.4.2 Coronal equilibrium (CE)

At much lower electron densities, such as those found in the solar corona (~ 10^6–10^{10} cm^{-3}), the LTE condition does not exist and another category of equilibrium, referred to as corona equilibrium (CE), may become applicable. It is used in situations when the electron collisional excitation and ionization processes are no longer balanced by their inverse collisional processes (as in LTE), but instead are balanced by radiative de-excitation and recombination events. In such plasmas, the velocity distribution function of free electrons is still Maxwellian (Appendix B), but since the populations of various ion species are independent of electron density, the Saha distribution is no longer valid and replaced by the corona equation [221]:

$$\frac{N_z}{N_{z-1}} = \frac{S(z-1,T)}{\alpha_r(z,T)} \qquad [2.23]$$

where S(z-1, T) is the collisional ionization coefficient (cm^3 s^{-1}); α_r(z, T) is the radiative recombination coefficient (cm^3 s^{-1}) and z is the stage of ionization (z = 0, 1, 2, ...). Unlike the LTE model, quantitative interpretation of the CE model depends strongly on the details of the atomic processes involved and their cross-sections.

2.4.3 Collisional radiative equilibrium (CRE)

The collisional radiative equilibrium (CRE) was mainly developed to be applied in the intermediate electron density regimes, where neither the LTE nor the CE model is valid. The CRE model is basically based upon making some modifications to the coronal model in order to take into account collisional de-excitation and three-body recombination processes that are more important for transitions between upper energy levels at these density regimes [219]. Radiative recombination and spontaneous radiative decay processes continue to be important in the CRE model for lower energy levels (as they are for the CE model). For laser-produced plasmas, Colombant and Tonon [222] extended the CE model and derived a formula describing steady-state equilibrium populations of various ion species:

$$\frac{N_z}{N_{z-1}} = \frac{S(z-1,T)}{\alpha_r(z,T)+n_e\alpha_{3b}(z,T)} \qquad [2.23]$$

where $\alpha_{3b}(z, T)$ is the three-body recombination rate (s^{-1}) and other terms have been defined in the previous section. For low electron density plasmas, i.e. $n_e\alpha_{3b} << 1$, the CR model depicted in 2.23 reduces to the CE model discussed in the last section. In the case of high densities, the model approaches the LTE approximation. The three rate coefficients in equation 2.23 can be determined using the following relations [222]:

$$S = \frac{9\times10^{-6}\xi_z(T/\chi_z)^{1/2}}{\chi_z^{3/2}(4.88+T/\chi_z)}\exp(-\chi_z/T) \qquad \text{cm}^3\ \text{s}^{-1} \qquad [2.24]$$

$$\alpha_r = 5.2\times10^{-14}(\chi_z/T)^{1/2}z\left[0.429+\frac{1}{2}\log(\chi_z/T)+0.469(T/\chi_z)^{1/2}\right] \qquad \text{cm}^3\ \text{s}^{-1} \qquad [2.25]$$

$$\alpha_{3b} = 2.97\times10^{-27}\xi_z/T\,\chi_z^{\,2}(4.88+T/\chi_z) \qquad \text{s}^{-1} \qquad [2.26]$$

where T is in eV units; χ_z (eV) is the ionization potential of an ion of charge state z and ξ_z is the number of electrons in the outmost subshell of an ion of charge state z. If these parameters appeared in the last three equations were calculated and replaced in equation

2.23, the fractional ion density for a given element can be computed and its evolution as a function of the plasma electron temperature, T_e, can also be determined. This relationship is reproduced in figure 2.5 for carbon after Colombant and Tonon [222].

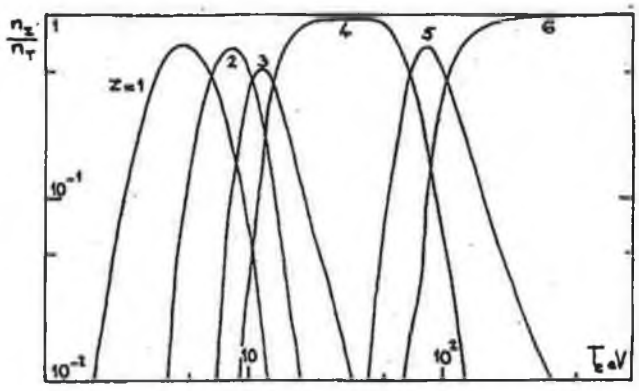

Fig. 2.5 State of charge densities as a function of electron temperature for carbon at $n_e = 10^{21}$ cm^{-3} [After Ref. 222].

An approximation to equation 2.23 was obtained by considering that $n_e\alpha_{3b} << \alpha_r$, thus the dependence on electron density is removed. This approximation relates an average charge state, z, to the plasma electron temperature, T_e (eV) alone [222]:

$$z \approx \frac{2}{3}(ZT_e)^{1/3} \qquad [2.27]$$

where Z is the atomic number for the element under consideration. This simplification is valid only for $T_e \geq 30$ eV and applies better in case of heavy (high-Z number) elements than light ones [222]. However, using a hydrodynamic expansion model, Colombant and Tonon related T_e (eV) to the incident laser power density, ϕ (W cm^{-2}) such that:

$$T_e \approx 5.2\times10^{-6} Z^{1/5}\left[\lambda^2\phi\right]^{3/5} \qquad [2.28]$$

Substituting the different parameters in equation 2.28 for an iron target (Z = 26) and for Nd:YAG laser (λ = 1.06 μm and $\phi \approx 2 \times 10^9$ W cm^{-2}), one obtains a temperature in the laser-produced steel plasma under investigation of about 4 eV. Using this value in equation 2.27, an average charge state of iron ions in the plasma has a value of ~ 3.

2.5 Quantitative Spectroscopy

Optical emission spectra are observed when light emitted from a hot gas (plasma) is dispersed by wavelength, so that photons of different frequencies appear in the focal plane of the spectroscopic apparatus as an array of monochromatic images of the entrance slit. The so-produced spectrum is found to consist of spectral lines superimposed on a background continuum; each spectral line is characteristic of a particular atom or ion, and once it is observed in the spectrum the presence of the relevant species is established in the plasma. This may be performed quantitatively by measuring relative line intensities produced when standard reference samples are introduced to the plasma source. In the present thesis, an emission spectroscopic technique is developed for the quantitative elemental determination of solid steel samples using laser-produced plasmas (chapters IV–V).

Another important application of atomic spectroscopy has been plasma diagnostics. Here, the fundamental physical properties (such as temperatures and particle densities) of the plasma containing the emitting species strongly influence the intensity and wavelength distribution in various ways. The study of the intensities and widths of spectral lines, as well as the intensity and spectral distribution of continuous radiation leads to the knowledge about abundances, temperatures and electron densities prevailing in the plasma. Spectroscopic diagnosis of laser-produced steel plasmas for the determination of electron densities and temperatures will be the subject of chapter VI of the present thesis.

2.5.1 Spectral line intensity relations

Determination of the elemental constituents of a condensed-phase matter by means of laser-produced plasmas requires the measurement of spectral lines intensities that are characteristic of the individual species present in the solid sample. These intensities must then be related to the number densities of the corresponding species in the plasma. Indeed, this relationship turns out to depend on the temperature of the plasma as it is shown in the following treatment.

Consider a plasma of depth D in LTE at temperature T. The specific intensity of an emission spectral line of frequency ν is defined as the energy emitted from the plasma per unit time, unit surface area, unit solid angle and unit frequency (Appendix C). The change in the specific intensity, I(ν), along the line of sight is given by the equation of radiative transfer [223] as follows:

$$\frac{dI(\nu)}{dx} = K(\nu)[B(\nu,T) - I(\nu)] \qquad [2.29]$$

where x is the coordinate axis along the line of sight normal to the surface area of the plasma; B(ν, T) is the Planck blackbody function (Appendix B) and K(ν) is the absorption coefficient of the spectral line including a correction for the induced emission (Appendix C). Equation 2.29 can readily be integrated with respect to x between the two limiting planes of the plasma separated by D to obtain:

$$I(\nu) = B(\nu,T)[1 - \exp(-K(\nu)D)] \qquad [2.30]$$

The constant of integration has been set to zero since there is no external source of radiation outside the plasma. The quantity K(ν)D is simply a measure of the optical thickness of the plasma; the plasma is considered optically thin if this value is small in comparison to unity and optically thick if it is large. If the K(ν)D value is very large, then the specific intensity in equation 2.30 is entirely given by the Planck function reducing the plasma to a blackbody radiator at temperature T.

Instead of the specific intensity, it is more common and convenient to measure the integrated intensity of an emission line with center frequency, ν_0,:

$$I = \int_{\nu_0-\infty}^{\nu_0+\infty} I(\nu)d\nu \qquad [2.31]$$

which is simply equivalent to the area under the spectral line profile. By combining equations 2.30 and 2.31, one obtains:

$$I \cong B(\nu_0, T) \int_{\nu_0 - \infty}^{\nu_0 + \infty} [1 - \exp(-K(\nu)D)] d\nu \qquad [2.32]$$

The blackbody function, $B(\nu_0, T)$, was taken out of the integral because it remains essentially constant over the width of a single emission line, over which the integration with respect to the frequency occurs. The integrated spectral line intensity as given in equation 2.32 grows with the concentration of the corresponding species in the plasma through the number density, N_p, of the species populating the lower energy level of the transition as contained in the expression of $K(\nu)$ (Appendix C).

The concentration dependence of the integrated intensity is generally nonlinear. This is because the optical depth of the plasma effectively decreases with increasing concentration, thus reducing the number of radiators participating in the observable emission intensity. In the low concentration range where the plasma becomes optically thin (larger optical depth), the observed integrated intensity linearly increases with the number density (concentration).

In order to carry out successful elemental analysis of solid phase materials by laser-produced plasmas, it is of great importance to select an appropriate domain both in time and space of the plasma for quantitative spectroscopic measurements [210]. In other words, regions in time and space must be carefully selected where the plasma is as optically thin as possible at the transition under consideration in order to increase the dynamic range of measurements, with no or little influence on the signal-to-background ratio and hence the sensitivity of the analytical method. Once the selection is made, there are three methods for implementing the quantitative analysis. The first method is to determine each elemental abundance independently by working with those elemental emission lines of accurately known transition probabilities and by making absolute measurements of the integrated intensities.

A second approach is to measure the integrated intensities of the elemental emission lines with respect to that of a line of the major abundant element of the sample; this method is known as internal standardization. In this case, the transition probabilities of emission lines need to be known only relatively. In the third method, the line emission intensities are measured relatively and their relationships to the respective elemental

abundances are calibrated by working with samples of known elemental composition, i.e. reference standards. The last two methods are widely employed in spectrochemical analysis, and hence they are briefly discussed in the following sub-section.

2.5.2 Line emission measurements

The total intensity of a spectral line, I, emitted from an excited atom or ion, in a homogeneous and optically thin plasma, with a frequency ν is defined as the energy emitted per unit time per unit solid angle at this frequency (Appendix C). In other words, it is the number of transitions per unit time multiplied by the energy of the emitted photon. Accordingly, if N_q is the population of the upper level, then the number of transitions taking place per unit time to the lower level p equals $A_{qp}\, N_q$, where A_{qp} is the Einstein coefficient for spontaneous emission (Appendix C). According to the above definition, the intensity of the spectral line, integrated over the line profile, corresponding to the transition q → p is given by:

$$I = \int_{Line} \varepsilon_{\nu,L}\, d\nu = \frac{h\nu_{pq}}{4\pi} A_{qp} N_q \qquad [2.33]$$

where ε is the emission coefficient of the spectral line undergoing the transition and h is Planck's constant. If the energy levels concerned are in local thermodynamic equilibrium (LTE), then the population density of the upper level, N_q, is related to the ground level number density, N_T, by the Boltzmann equation (Appendix B):

$$\frac{N_q}{N_T} = \frac{g_q}{Q(T_{exc})} \exp\left(-\frac{E_q}{k_B T_{exc}}\right) \qquad [2.34]$$

where g_q and E_q are the statistical weight and energy of the upper level q, respectively; Q is the partition function of the relevant species; k_B is Boltzmann's constant and T_{exc} is the plasma excitation temperature. From the above two equations, we have:

$$I = \frac{h\nu_{pq}}{4\pi} A_{qp} \frac{N_T g_q}{Q(T_{exc})} \exp\left(-\frac{E_q}{k_B T_{exc}}\right) \qquad [2.35]$$

This equation is the fundamental equation for emission spectroscopy. According to this equation, one can determine the population density of the relevant species (atoms or ions) for an element in the plasma from a measurement of the absolute line intensity of the corresponding transition and knowledge of the excitation temperature and other atomic constants. However, it is not possible to derive a theoretical expression relating (N) and the concentration of that element in the solid sample under investigation. In practice, an empirical relationship is sought between the observed line intensity, I_x, and its corresponding concentration, C. This relationship can be written as:

$$I_x = F(C) \qquad [2.36]$$

and is called the analytical calibration function; the graph that corresponds to it is called the analytical calibration curve. This curve can be established experimentally by observations on reference samples of known concentrations termed standards, and can be used to determine the elemental contents in unknown samples.

By considering equation 2.35, the intensity ratio of a spectral line emitted by a trace element (denoted a) to that emitted by the major constituent in the sample (denoted b) can be written as follow:

$$\frac{I_a}{I_b} = \frac{\left(\nu_0 A_{qp} g_q\right)_a}{\left(\nu_0 A_{qp} g_q\right)_b} \frac{N_{a,q} Q_b}{N_{b,q} Q_a} \exp\left[-\frac{E_{a,q} - E_{b,q}}{k_B T_{exc}}\right] \qquad [2.37]$$

Consequently, a plot of the intensity ratio against "fractional" concentration of the trace element should demonstrate a linear relationship. It is apparent from equation 2.37 that it is desirable to use transitions having as similar upper level energies as possible, so the intensity ratio will then be independent, or only a weak function of the plasma temperature.

2.6 Spectral Line Broadening and Profiles

In general, the spectral lines emitted from plasmas are observed to have a finite breadth that is directly proportional to the width of the spectrometer entrance slit. The intensity

distribution (profile) of the spectral line, therefore, exhibits a maximum at the central frequency, ν_0, and then falls to a minimum on both sides and can be represented by equation 2.31. Even when the highest resolution spectrometric system is available, each spectral line still shows a characteristic shape, which is strongly related to the conditions prevailing in the plasma.

When discussing spectral line broadening and shapes, one conveniently distinguishes between the physical (source) and the instrumental profiles. The former profile type is a result of the physical conditions occurring in the plasma before any interference from the spectrometric system takes place. The instrumental profile, on the other hand, arises from the influence of the spectroscopic equipment on a uniform intensity distribution. Spectral line profiles observed are simply a convolution of both instrumental and physical effects. In this case, the width of the spectral line distribution is represented by the full-width at half maximum (FWHM) of the line, which is defined as the distance between two points on the profile where the maximum line intensity drops to one-half of its value.

Measurements of intensities of spectral lines, as well as of some fundamental physical parameters of the plasma, such as the electron number density, require specific knowledge of the spectral line shapes and widths. In the ensuing sub-sections, the two broadening mechanisms that are mainly responsible for broadening of spectral lines emitted from laser-produced plasmas studied in the present work are briefly described. These are Doppler and Stark (collisional) broadening. A third mechanism known as the natural broadening, resulting from the fact that the quantum states of an atom / ion do not have a single energy but rather a small spread of energies that can be represented by Heisenberg's uncertainty principle [224], has an insignificant effect in comparison with the other two mechanisms and can be generally ignored.

2.6.1 Doppler broadening

Doppler broadening is a result of the well-known 'Doppler effect' which is the apparent shift in frequency (wavelength) of the signal emitted from a source moving towards or away from an observer. In the plasma, these shifts arise from thermally random motions of the radiating atomic / ionic species [225]. The Doppler shift can be represented in

terms of the velocity component of a radiating species parallel to the direction of observation, v_x, and is given by:

$$\frac{\Delta\lambda}{\lambda_0} = \frac{\Delta\nu}{\nu_0} = \frac{v_x}{c} \qquad [2.38]$$

where c is the speed of light. If the radiating species gave a Maxwellian velocity distribution, then the superposition of the resultant emitted photons yields:

$$I(\nu) = I_0 \exp\left[-\frac{c^2(\nu_0 - \nu)^2}{\nu_0^2 \delta^2}\right] \qquad [2.39]$$

where I_0 is the intensity at ν_0. Equation 2.39 represents a Gaussian distribution around the central frequency ν_0 with a width determined by the parameter δ, the most probable velocity, which can be given by the following formula:

$$\delta = \left(\frac{2k_B T}{M}\right)^{1/2} = \left(\frac{2RT}{\mu}\right)^{1/2} \qquad [2.40]$$

where M is the actual mass of the relevant species (kg); μ is the atomic mass (amu) of the species = M / m_u, where $m_u = 1.66\times10^{-27}$ kg and R is the universal gas constant. For $I = I_0 / 2$, the FWHM due to Doppler effect, $\Delta\nu_D$, is given by:

$$\Delta\nu_D = \frac{2\nu_0\delta\sqrt{\ln 2}}{c} = \frac{2\nu_0}{c}\sqrt{\frac{2RT\ln 2}{\mu}} \qquad [2.41]$$

Equation 2.41 can conveniently be expressed in the dimensionless form:

$$\frac{\Delta\nu_D}{\nu_0} = \frac{\Delta\lambda_D}{\lambda_0} = 7.16\times10^{-7}\sqrt{\frac{T}{\mu}} \qquad [2.42]$$

If λ_0 and T are in units of angstrom and Kelvin, respectively, then $\Delta\lambda_D$ is also expressed in units of angstrom. Equation 2.42 shows that thermal Doppler broadening is most

pronounced for spectral lines of light elements at relatively high temperatures [225]. For example, consider the hydrogen H_β spectral line at 4861 Å and a plasma temperature of 5000°K, it follows that $\Delta\lambda_{D1/2} \cong 0.25$ Å. This is a substantial broadening and it is almost equivalent to that due to the Stark effect in a plasma having an electron density of 10^{14} cm^{-3} [221].

Doppler broadening can also occur in non-thermal plasmas due to the fact that the radiating species may not be distributed according to Maxwellian velocity distribution. In addition, there may be a large turbulent velocity component superimposed on the thermal components thus broadening the spectral line further [221]. Finally, there may be mass motion of the entire plasma or large clumps in it.

2.6.2 Stark broadening

In plasmas with sufficiently high number density of ions and electrons (such as laser-produced plasmas) — say, at least 1% of the total plasma density — the long-range Coulomb forces are dominant and the spectral line profiles will be predominantly determined by interactions between the emitting atoms / ions and the surrounding charged particles. This broadening effect is usually termed Stark broadening. In laser-produced plasmas, broadening of spectral lines by the Stark effect dominates in regions very close to the target surface where the plasma density is very high. Unlike Doppler broadening which remains fairly constant, Stark broadening decreases with increasing distance from the target surface [221]. Stark broadening is a powerful diagnostic technique for the determination of electron number density in plasmas, as will be presented in chapter VI of this thesis.

Stark broadening theory has been developed from two very different points of view, which are contained in a general theory as two extreme approximations. These are the impact and quasi-static approximations, and briefly introduced here.

2.6.2.1 The quasi-static theory

In the quasi-static approximation, which was initially developed by Holtsmark in 1919, the atom / ion is considered to be continuously subjected to the influence of the charged

perturbers during the whole emission process. Furthermore, the perturbing species are assumed to move so slowly during the time of emission that the perturbing electric field may be thought of as quasi-static. Hydrogen atoms and hydrogen-like ions (singly-ionized helium, doubly-ionized lithium, etc.) exhibit the linear Stark effect in which the interaction is proportional to the electric field strength. The linear Stark effect splits the energy levels of the perturbed species symmetrically, and thus yields a symmetrical line profile. By assuming the plasma is electrically neutral, i.e. $N_p = n_e / Z_p$ where N_p is the number density of the perturbers (ions, in this case), the FWHM (in Å units) produced by the quasi-static Stark broadening for these species is expressed by [221]:

$$\Delta\lambda_{1/2} = 8.16\times10^{-19}\left(1-0.7N_D^{-1/3}\right)\lambda_0^{\,2}\left(n_q^{\,2}-n_p^{\,2}\right)\left(\frac{Z_p^{\,1/3}}{Z_e}\right)n_e^{\,2/3} \qquad [2.43]$$

where λ_0 is the central wavelength (in Å), n_q and n_p are the upper and lower principal quantum numbers of the relevant transition, respectively; Z_p is the ionic charge; Z_e is the electronic charge; n_e is the electron density (cm^{-3}) and N_D, the number of perturbing particles in the Debye sphere, is given by the following equation [221]:

$$N_D = 1.72\times10^{12}\frac{\left[T\,(eV)\right]^{3/2}}{\left[n_e\left(m^{-3}\right)\right]^{1/2}} \qquad [2.44]$$

As may be seen from equation 2.43, the Stark broadening due to the quasi-state approximation is independent of the plasma temperature, and increases as the principal quantum number of the transition upper energy level. Taking as an example the H_β line with $n_e = 10^{16}$ cm^{-3} and T = 4 eV (46,400 K), $\Delta\lambda_{1/2} \cong 9.3$ Å is obtained. A modification to Holtsmark's theory involved the introduction of ion-ion correlation and shielding effects due to the presence of surrounding ions and electrons, as well as the introduction of a time dependence of the ion microfields. In general, the ionic contribution to the widths of Stark broadened lines is usually less than ~ 20% [226].

2.6.2.2 The electron impact theory

The impact theory was first developed by Lorentz in 1906 and further modified in 1958

by Kolb and Griem [225]. In this approximation a wave train of light emitted from an atom / ion is perturbed by fast electron impacts and cut it up into a number of smaller independent wave trains. Statistical averaging over all possible times between collisions followed by a Fourier analysis provides the required spectral line intensity distribution. The spectral profile produced that way can be represented by the well-known Lorentzian distribution function, i.e.:

$$I(\Delta\lambda) \propto \left[1 + \left(\frac{\Delta\lambda}{\Delta\lambda_{1/2}}\right)^2\right]^{-1} \qquad [2.45]$$

Despite the fact that the detailed features of the line profile are very dependent on the contribution from electron impacts, the half-widths are often insensitive to their influence. This is notably the case for the L_β, L_δ, H_β and H_δ hydrogenic spectral lines, and their half-widths can be fairly represented by the quasi-static approximation (equation 2.43). However, other lines such as L_α and H_α are strongly affected and sometimes even completely dominated by the electron collisional broadening. The FWHM (Å) of such lines can be represented by the following formula [221]:

$$\Delta\lambda_{1/2}(impact) \cong 1.62\times10^{-17}\frac{n_e}{T_e^{1/2}}\left[13.76 - \ln\left(\frac{n_e^{1/2}}{T_e}\right)\right] \qquad [2.46]$$

where the plasma electron temperature, T_e, and number density, n_e, are given in K and cm^{-3} units, respectively. Unlike ion broadening, the FWHM due to electrons impact is strongly dependent on temperature. Unless T_e is known at least approximately, it is advisable to chose one of those spectral lines whose width is ion-dependent, such as the hydrogen H_β.

Electron impact broadening also dominates isolated spectral lines of neutral and singly ionised non-hydrogenic atoms (e.g., singly-ionized lithium and barium) [226]. Accordingly, one can calculate the FWHM of these lines using the impact approximation, and then correct for the relatively unimportant quasi-static neutral or ion broadening contribution. In addition to the broadening, there is also a shift (usually towards increasing wavelength) of the spectral line center away from the position it has

in the limit as the perturbers number density approaches zero. To a good approximation (~ 20 to 30%), the FWHM (Å), $\Delta\lambda_{1/2}$, and the line shift (Å), $\Delta\lambda_{shift}$, are given by [226]:

$$\Delta\lambda_{1/2} = 2W\left(\frac{n_e}{10^{16}}\right) + 3.5A\left(\frac{n_e}{10^{16}}\right)^{1/4}\left[1-\frac{3}{4}N_D^{-1/3}\right]W\left(\frac{n_e}{10^{16}}\right) \qquad [2.47]$$

Electron contribution *Ion correction*

$$\Delta\lambda_{shift} = D\left(\frac{n_e}{10^{16}}\right) \pm 2A\left(\frac{n_e}{10^{16}}\right)^{1/4}\left[1-\frac{3}{4}N_D^{-1/3}\right]W\left(\frac{n_e}{10^{16}}\right) \qquad [2.48]$$

Electron contribution *Ion correction*

where n_e is expressed in units of cm^{-3}. The coefficients W, A and D are independent on the electron density and slowly varying functions of the electron temperature, and called the broadening and shift parameters. The two above formulas apply to neutrals. However, to make them applicable also to singly-ionized atoms, the numerical coefficient ¾ is replaced by 1.2. A comprehensive list of the width and shift parameters is given in [226] for numerous spectral lines of different neutrals and singly-ionized atoms. Generally, the ion contribution to the FWHM is significantly small and therefore $\Delta\lambda_{1/2}$ varies almost linearly with electron density (equation 2.47). For a given n_e, the widths are usually much smaller than are the Stark widths of one-electron, hydrogen and hydrogen-like atoms. Accordingly, equations 2.47 and 2.48 are only useful in the diagnostics of relatively dense plasmas, $10^{16} \leq n_e \leq 10^{19}$, where the one-electron spectral lines may be considerably broad [221].

Line shift measurements are also a possible alternative method for determination of the electron density. However, the parameters D of equation 2.48 are much more dependent on the electron temperature than are the corresponding width parameters W. In addition, the theoretical values of D are somewhat inferior. For these reasons, it is not recommended to use spectral line shifts in plasma diagnostics [221].

2.6.3 Convolution of spectral line profiles: the Voigt function

In many practical situations, Doppler (Gaussian profile) as well as Stark (Lorentzian profile) broadening mechanisms contribute to the observed width of the relevant

spectral line. In this case, the observed profile should be corrected for the nonrelevant broadening mechanism; in other words, it must be "unfolded" or "deconvoluted". The deconvolution process is possible since the two mechanisms are independent so that they may be considered as superimposed.

Consider that the spectral line profiles of the two mentioned broadening types can be represented by functions of the type $I(x)=f(x)$ and $I(x)=\phi(x)$, where x is defined in terms of the central wavelength of the profile, λ_0, as $x=\lambda-\lambda_0$. If both functions act at a point on the profile where $x=\lambda'$, the resultant intensity at this point is given by:

$$I(\lambda')=\int_{-\infty}^{+\infty} f(x)\phi(\lambda'-x)dx = F(\lambda') \qquad [2.49]$$

The process described above can be repeated for any number of broadening effects. The difficulty arises from the fact that an exact integration of the complex functions (analytical solutions) represented by f, ϕ and F is almost impossible, and approximate numerical methods must be proposed. The latter are greatly simplified if the functions can be combined in some way before attempting to carry out the integration. To do so, the functions representing the individual broadening factors are placed into two classes:

(a) Gaussian functions which are of the type:

$$f(x)=C\exp\left(-\frac{x^2}{B_1^2}\right) \qquad [2.50]$$

where C and B_1 are constants. Doppler broadening results of a function of this type.

(b) Lorentzian functions which are of the type:

$$f(x)=\frac{C}{1+\frac{x^2}{B_2^2}} \qquad [2.51]$$

where B_2 is a constant. Natural and Stark (collisional) broadening result in functions of

this type. If ϕ and f in equation 2.49 are both Gaussian and have the constants B_1' and B_1'', then F is also a Gaussian and has a constant given by:

$$B_1^2 = B_1'^2 + B_1''^2 \qquad [2.52]$$

On the other hand, If ϕ and f are both Lorentzian functions, a constant for the resultant Lorentzian function F is obtained as:

$$B_2 = B_2' + B_2'' \qquad [2.52]$$

However, if f is Gaussian and ϕ Lorentzian or vice versa, F then is known as a Voigt function and has both the constants B_1 and B_2, and is given by the following formula:

$$F(x) = \frac{\left[C \exp\left(-\frac{x^2}{B_1^2}\right)\right]}{\left[1 + \frac{x^2}{B_2^2}\right]} \qquad [2.53]$$

Another type of spectral line broadening which is often encountered in plasma spectroscopy and significantly contribute to the width of the line is due to the finite spectral resolution of the spectroscopic apparatus, and usually termed instrumental broadening. Like other types of broadening, instrumental broadening may be treated by another "folding" process in the same way as described above. But first the apparatus function must be measured experimentally using spectral lines of a negligibly small physical width compared to the apparatus width. In this respect, spectral line emission from low-pressure gas discharges is well suited; alternatively, spectral line emission from a He-Ne laser would be sufficient. After that, some simple analytical function must be applied to fit the profile of the spectral line used and permits a half-width correction via the convolution integral in equation 2.49.

CHAPTER III

EXPERIMENTAL SET-UP AND PROCEDURES

This chapter describes in some detail the characteristics of the instrumental set-ups and experimental procedures utilized. A typical LIPS set-up consists of a high power laser, focusing lens, target chamber and the spectrometric system. Three Q-switched, high-peak power Nd:YAG laser systems were used to produce the steel plasmas under investigation during the course of the present work. The laser beam was focused by spherical or cylindrical plano-convex lenses onto the steel targets within an aluminium chamber under vacuum or background gases. Methods of samples manipulation and control are also discussed. VUV radiation emitted from the steel plasmas were dispersed using a 1 m near normal incidence vacuum spectrometer equipped with 1200 grooves/mm diffraction grating. Steel spectra in the vacuum ultraviolet were detected by two VUV-sensitive multichannel photodetectors (CEMA / PDA and CCD detector arrays).

3.1 An Overview

In the present work, emission spectroscopic characteristics of laser-produced steel plasmas in the vacuum ultraviolet (VUV) are investigated. The experimental arrangement employed to perform this task is almost similar to that used for various laser-induced plasma spectroscopy (LIPS) applications in the UV / visible region, and mainly consists of five parts. These are a Q-switched, high-peak power Nd:YAG laser for plasma ignition; an aluminium chamber for accommodating the steel target(s) under investigation; a system of lenses / mirrors for steering and focusing the laser beam onto the target surface; a 1-m vacuum spectrometer equipped with VUV diffraction holographic grating; two multichannel detector systems including a CEMA / PDA combination, as well as a VUV-sensitive CCD array. Synchronization of laser pulses with the relevant detection system used is achieved via a suitable pulse / delay generator; data acquisition and evaluation, as well as control of the experimental sequence is carried out by an ordinary PC. Schematic representations of the two set-ups employed in all experiments are illustrated in figures 3.1 and 3.2. The first arrangement (Fig. 3.1) has been used for preliminary investigations, while the other set-up (Fig. 3.2) has been applied for the rest of the experiments. Furthermore, each of the above components is described in some details in the following sections and sub-sections.

3.2 Laser Systems

Steel plasmas investigated were generated by three Q-switched, nanosecond Nd:YAG laser systems. The first laser was used for the initial experiments (Fig. 3.1), whereas the rest of the work was carried out using the other two lasers (Fig. 3.2). The first laser (Spectron, Model SL803) is a two-stage amplifier-oscillator system, operating at its fundamental wavelength (1064 nm) and has a typical pulse energy of about 850 mJ and duration (FWHM) of about 15 ns. Pulse-to-pulse energy fluctuation was found to be $\leq 1\%$; moreover, the pulse energy does not significantly change even after several working hours. A simple schematic diagram of this laser is shown in Fig. 3.3 as a representative example of Q-switched Nd:YAG type laser systems.

The laser cavity is defined by the ~ 100% reflecting rear coupler and the partially transmitting front mirror. The opposite surface of the output front mirror has an

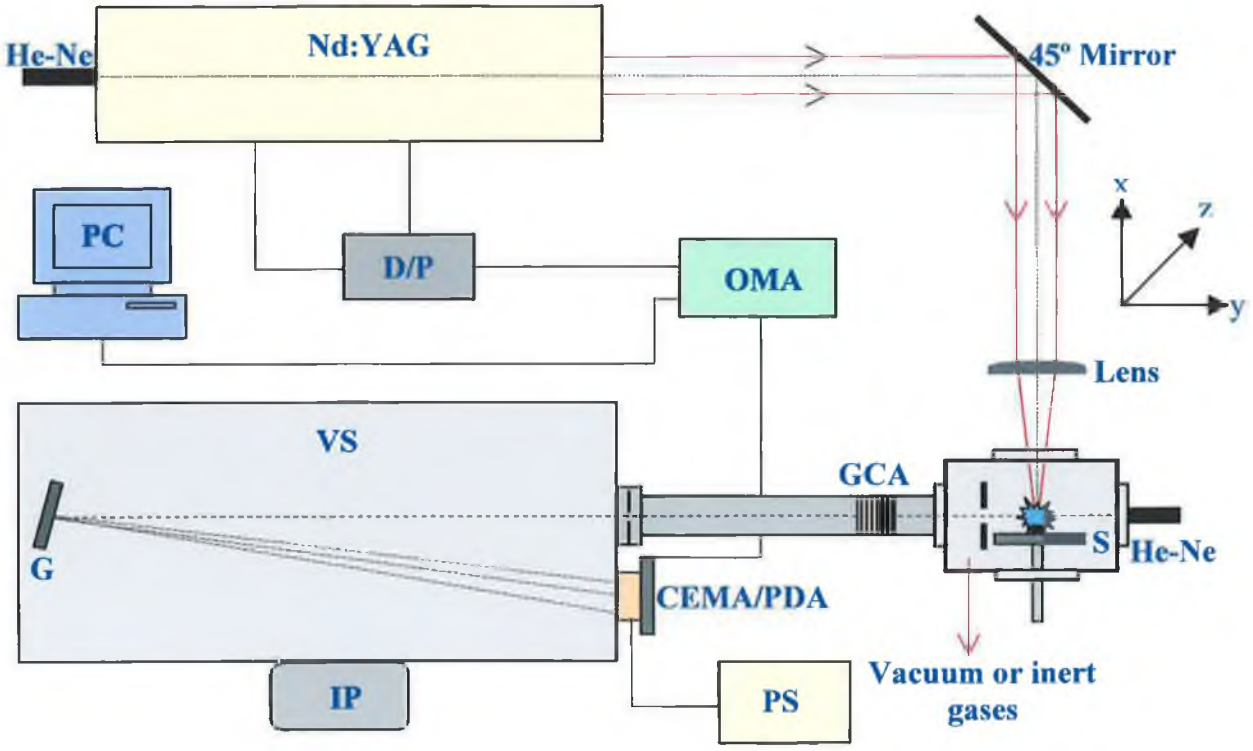

Fig. 3.1 Schematic illustration of the set-up utilized for preliminary studies. S is a steel sample; GCA is a glass capillary array; CEMA/PDA is the channel electron multiplier array/photodiode array detector combination; PS is the detector power supply; VS is 1-m, normal incidence vacuum spectrometer; G is a VUV-sensitive grating; IP is an ion vacuum pump; OMA is an optical multichannel analyzer; D/P is a delay / pulse generator and PC is a personal computer. Note the position of the pre-slit in the target chamber.

antireflection coating (AR). Both front and rear mirrors are housed in x-y centering mounts for fine adjustment of the oscillator. Furthermore, an intra-cavity shutter (electro-mechanical) is installed in the rear mirror housing in order to prevent the formation of a laser resonator, if desired. The active lasing medium is a 103 mm long, 6.35 mm diameter yttrium aluminium garnet (Y_2 A_{l5} O_{12}) crystal rod doped with neodymium ions (Nd^{3+}). Population inversion in the lasing medium is achieved via light absorption from a nearby linear flashlamp. Both the Nd:YAG rod and linear flashlamp are contained in the oscillator pumping chamber (Fig. 3.3), and sealed into their respective housing with O'rings. They are also surrounded by two ceramic reflectors (one is located beneath the rod and the other is placed above the flashlamp) for efficient

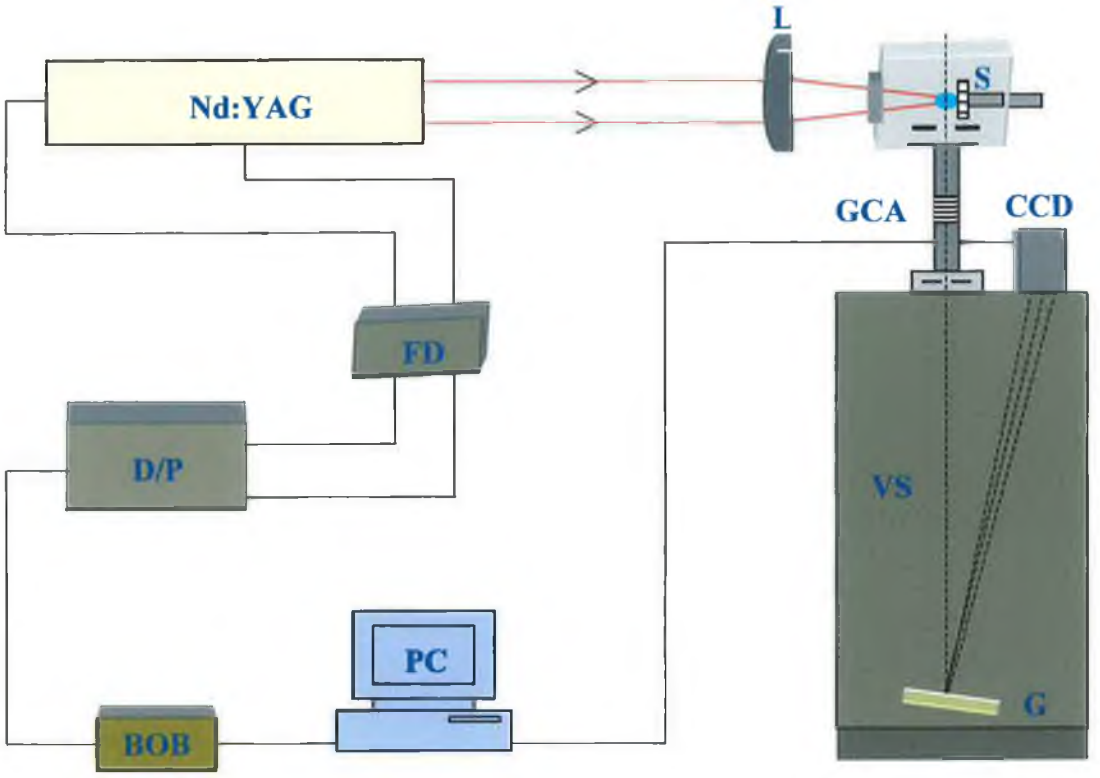

Fig. 3.2 Schematic representation of the second set-up. L is a plano-convex spherical or cylindrical lens; CCD is a VUV-sensitive charge-coupled device array; BOB is a breakout box and FD (Appendix F) is a frequency divider unit. Other abbreviations used are as in Fig. 3.1.

and uniform pumping of the rod. Furthermore, a glass filter is located between the flashlamp and the rod in order to protect the latter from permanent damage caused by the UV radiation emitted from the lamp. Two intra-cavity telescopes (Fig. 3.3) serve to collimate the laser beam, hence reducing beam divergence; the final beam divergence, following traversal through all optical components within the laser head, lies between 0.8 and 2 mrad. The telescopes also compensate for thermal lensing action that can take place in the laser rod when it heats up during operation. The inter-lens distance in the telescope is adjusted in terms of a specific repetition rate value in such a way that the optimum laser performance is obtained. The combination of a linear polarizer and temperature-stabilized Pockels cell crystal within the Q-switch unit is used to prevent oscillations in the laser cavity until a sufficient level of population inversion has been accomplished. When the flashlamp is triggered, a voltage (usually termed the ¼ wave voltage) of about 915 V is applied to the Pockels cell crystal. This induces birefringence

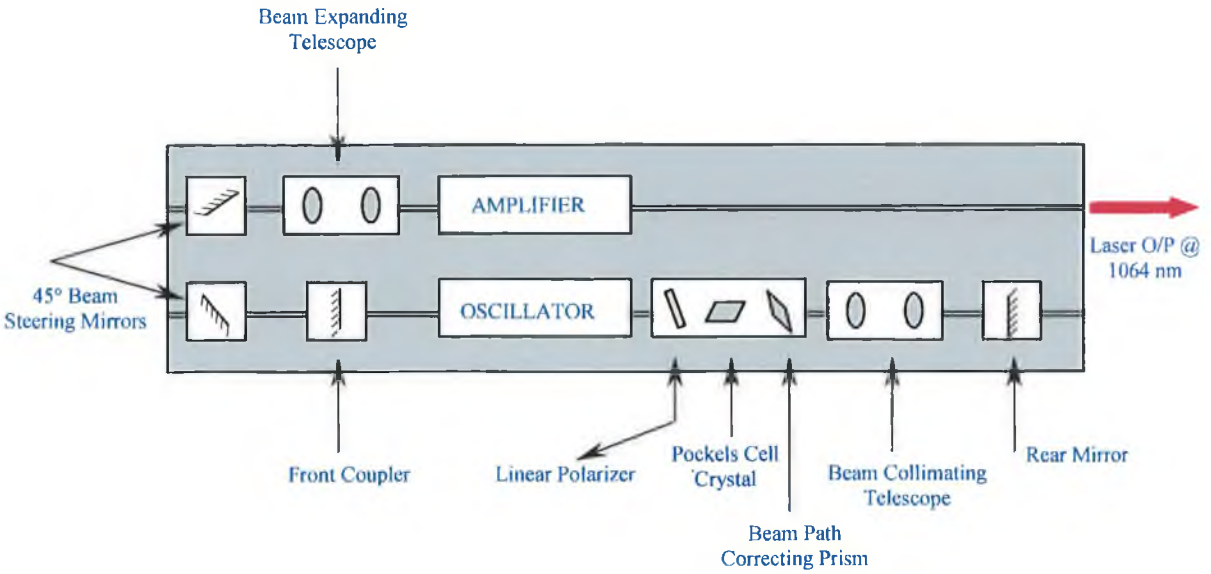

Fig. 3.3 Representative illustration of the components of a typical Q-switched, two stage amplifier-oscillator Nd:YAG Laser head.

in the crystal and makes it act as a quarter wave, i.e. the position of the two optical axes of the birefringent crystal are at 45° with respect to the horizontal plane of polarization of light transmitted by the linear dielectric polarizer. Accordingly, the linearly polarized light incident on the front (facing the polarizer) crystal face can be resolved into two components each of which is parallel to a birefringent axis. On passing through the crystal, one component suffers a phase retardation of 45° with respect to the other component and on emerging the exit face the light is circularly polarized. Upon reflection from the rear mirror, the light passes through the crystal for a second time and the same component suffers a further phase retardation of 45°, resulting in a vertically polarized light, which is rejected by the polarizer. Therefore, there is no light feedback and the laser cavity has no oscillations. When the stored energy in the laser rod reaches a maximum, the ¼ wave voltage is removed, hence no polarization change will occur. Oscillations within the laser cavity are resumed and the Nd:YAG gain medium is depleted in the order of ten nanoseconds. The beam is then steered in the head by two 45°, 1064 nm dielectric mirrors before it enters the second telescope (Fig. 3.3). The latter expands the laser beam to fully illuminate Nd:YAG crystal located in the flashlamp-pumped amplifier unit. The final output of the pulse has a typical energy of 850 mJ and duration of about 15 ns at the fundamental wavelength.

The other two Nd:YAG lasers utilized in the present work are oscillator-only systems, and were manufactured by Continuum, USA. One of them (Surelite, Model III-10) is working only at the fundamental wavelength (1064 nm), and can deliver a relatively energetic pulse of around 800 mJ in 5–7 ns duration. The other laser (Surelite, Model I-10) emits radiation at either the fundamental wavelength, second, third or fourth harmonic (532, 355 or 266 nm, respectively). The corresponding pulse energies recorded at the exit aperture of the laser bench were 400, 250, 100 and 55 mJ for the four wavelengths, respectively. The pulse duration was between 5–7 ns for the fundamental radiation and its second harmonic, and 4–6 ns for the third and fourth harmonics. The divergence of the resulting beam amounts to about 0.6 mrad.

Except for the amplifier pumping chamber, telescopes and the 45° beam steering mirrors (Fig. 3.3), the basic structure of the two Surelite lasers is similar to that of the SL803 system previously described, and the final pulse can be extracted at the front coupler following amplification in the oscillator Nd:YAG crystal. A further difference is that the Surelite lasers use double linear flashlamps (200 μs FWHM pulses) in the oscillator pumping chamber, resulting in high pumping efficiency and homogeneity required for producing high gain and superior quality beams. Moreover, this configuration minimizes thermal loading and reduces power consumption.

Q-switching of the laser radiation is performed in a completely different way (indeed opposite) to that carried out in the SL803 laser. A quarter wave plate is introduced in the laser head between the linear dielectric polarizer and the Pockels cell crystal, in such a way that the beam propagating within the oscillator makes a double pass through the Pockels cell and the ¼ wave plate. This configuration is shown in Fig. 3.4. At 0 volts, the ¼ wave plate adds 45° to the beam with each pass, giving a total of 90°. Thus, the horizontal beam that is transmitted through the plate polarizer is rotated to vertical and is eventually rejected and oscillations within the cavity stop. On the other hand, when 3600 V is applied to the Pockels cell, the beam undergoes a total of 180° rotation (90° due to the ¼ wave plate and 90° due to the Pockels cell). Accordingly, the horizontal beam is rotated to vertical and back to horizontal, so that it is transmitted by the polarizer and the cavity is open again, which permits lasing (see Fig. 3.4 for more explanation).

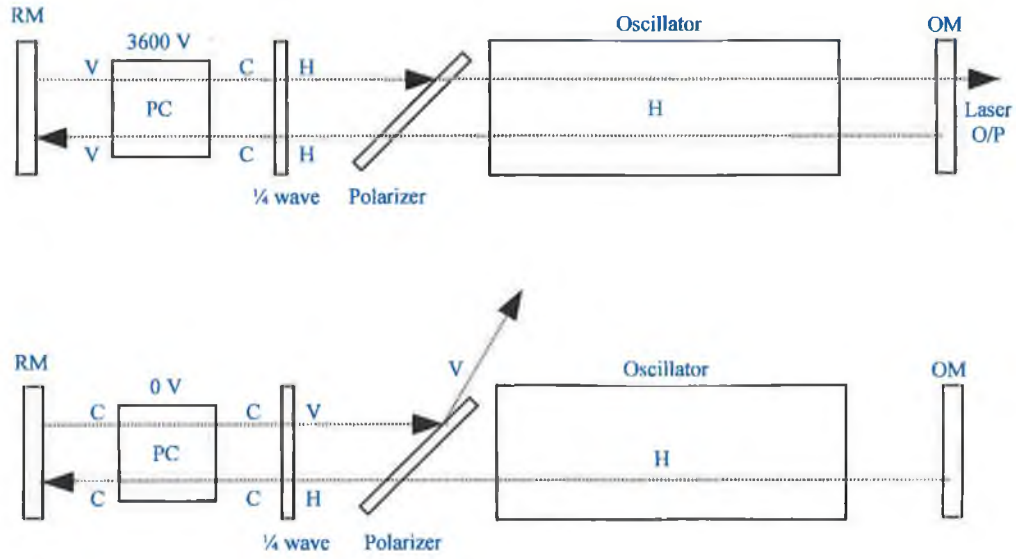

Fig. 3.4 Q-switching mechanisms in Surelite lasers. PC is the Pockels cell; RM is the rear mirror; V, C and H indicate the vertical, circular and horizontal polarization of the laser beam and OM is the output mirror.

The generation of the three harmonics (Model I-10) was achieved via passing the fundamental radiation through non-linear crystals, located at the end of the laser bench and could be adjusted by knobs from outside the laser head. Creation of harmonics will only occur when the non-linear crystal is oriented such that the direction of propagation of the original pump beam is at a specific angle to the crystal axis. This condition is known as *phase matching*. The actual phase matching angle is essentially determined by the refractive indices of the crystal. Due to the fact that the refractive index changes with the ambient temperature, the crystal mounts are temperature stabilized to ensure stable harmonic generation efficiencies. As most crystals used are *hygroscopic*, i.e. significantly absorb water, the temperature is often stabilized at 40° C to protect the crystal surface from moisture. It is of interest here to mention that the generation of the third or fourth harmonic takes place after that of the second harmonic, since it is based on mixing the 532 nm and residual 1064 nm radiation. Isolation, as well as increasing the spectral purity of the third and fourth generated harmonics is usually achieved through inserting two dichroic mirrors in the path of the final beam.

For the SL803 laser system, the total energy per laser pulse was recorded during experimental procedures using a Radiant Dyes Chemie™ thermopile-based energy

meter. Depending on the sensitivity scale chosen, a voltage output (displayed on an oscilloscope) with a conversion ratio of either 0.65 V or 1.15 V per 1 Joule of incident laser energy was measured. In the case of the Surelite III-10 and I-10 systems, a volume-absorbing power meter (Molectron, Model PowerMax 500A) was instead employed. The meter, which has a power scale, measures the energy per pulse indirectly by averaging the power of laser pulses over a certain given period of time. For some cases, especially those involved with measurements of laser power densities, the laser pulse duration (FWHM) was monitored by detecting the laser light reflected off the glass entrance window of the target chamber. This was done by coupling a fibre optic cable (600 μm core diameter, and 660 μm cladding diameter) directly placed somewhere in front of the entrance target window to a BPX-65 fast photodiode, which is connected to Hewlett Packard™ HP54510A digital oscilloscope via a BNC connector. Characteristics of the three laser systems used in the present work are summarized in appendix E, at the end of this thesis.

3.2.1 Laser steering and focusing optics

Focusing of the 1064 nm Nd:YAG laser radiation was achieved by two plano-convex spherical and cylindrical lenses, one at a time, with relatively long focal lengths of 125 mm and 150 mm, respectively. In the preliminary experiments (Fig. 3.1 and chapter IV), the laser output pulses were directed to the position of the steel samples in the target chamber by simply translating a 45° dielectric steering mirror (optimized for the fundamental radiation) along optical rails external to the laser head. For the rest of experiments, the Surelite laser III-10 (working at 1064 nm only) was located in such a way that its radiation was focused directly onto the target surface (see Fig. 3.2). To accommodate the two Surelite lasers together in one set up (Fig. 3.2), the Surelite I-10 (which can emit at the 4 Nd:YAG wavelengths) was placed in a perpendicular position to the III-10 model. Accordingly, four sets of dielectric steering mirrors (each set is specified to one laser wavelength and consists of three mirrors) were employed to adjust the height, as well as to direct the laser output to the target area. Furthermore, the laser beam was focused onto the sample by using 4 plano-convex spherical lenses, with nominal focal lengths of 125 mm, each of which has a maximum transmittance at the corresponding wavelength.

Each focusing lens used was mounted on a precision x-y-z translation stage for accurate positioning of the lens. All holders were provided with micrometer heads, which permit translation up to a distance of 6 mm in any of the three directions with an accuracy of ± 5 μm. In this way, accurate three-dimensional positioning of the laser focal spot on the target surface was achieved. Each lens holder was mounted on an optical rail (250 mm long), which was in turn attached to an optical breadboard (250 mm × 200 mm). The optical rail allows coarse adjustment (in the x-direction, which is parallel to the incident laser beam) of the lens holder in order to position the lens from the target surface at a distance approximately equal to its focal length. Figure 3.5 shows a photograph of the optical system described above.

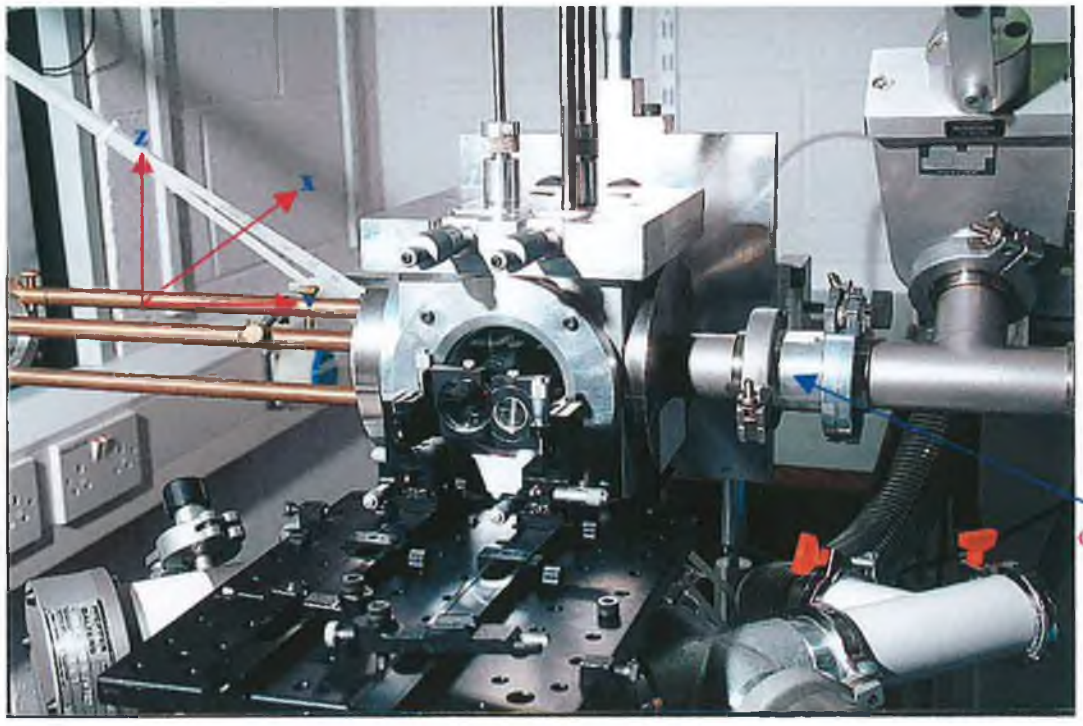

Fig. 3.5 Photograph of the optical layout used to focus laser pulses onto the steel samples. The second lens holder (to the right) is included in the photo to indicate the capability of the system for carrying out absorption experiments, using two laser sources. Shown also is the aluminum target chamber used.

3.3 Target Chamber and Samples

Laser-produced steel plasmas under consideration were generated inside a custom-made, vacuum-tight aluminium cube of internal volume of about 750 cm^3 (see Fig. 3.5).

The cubic chamber was provided with 70 mm diameter holes (which connect to form a hollow central area) drilled into each of its six faces. Custom-built flanges were then attached to each face of the cube to integrate the chamber into the set-up (Fig. 3.5). A photograph that illustrates such integration is shown in Fig. 3.6. The laser beam was admitted to the target(s) via the front face of the cube by using a glass window (quartz window was instead used for admission of the 355 nm and 266 nm harmonics). A He-Ne laser holder for alignment purposes with respect to the optic axis of the spectrometer was attached to one of the side faces. The flange affixed to the other side of the cube was used to connect the target chamber to the entrance arm of the 1 m vacuum spectrometer chamber through a NW-40 steel tube, thus facilitating an efficient vacuum coupling of both chambers (Fig. 3.6).

In this respect, a Galileo^{TM} glass capillary array (GCA), mounted within its own housing, was inserted into the steel tube (KF-40 size) connecting the two chambers (see Fig. 3.5). The GCA is nothing other than a circular disk of 25 mm diameter, a thickness of 3 mm, and a pore diameter of 50 μm. It serves to significantly reduce the amount of plasma debris entering the spectrometer chamber, and also permits differential pumping between the spectrometer and target chamber. Accordingly, experiments at higher ambient atmosphere pressures in the target chamber can be carried out while maintaining relatively low pressure in the spectrometer chamber. For example, at atmospheric pressure in the target chamber, the pressure in the other side of the experiment was maintained in the order of about 10^{-3} mbar. The target chamber can be evacuated to a pressure of about 1×10^{-5} mbar via a small capacity turbo-molecular

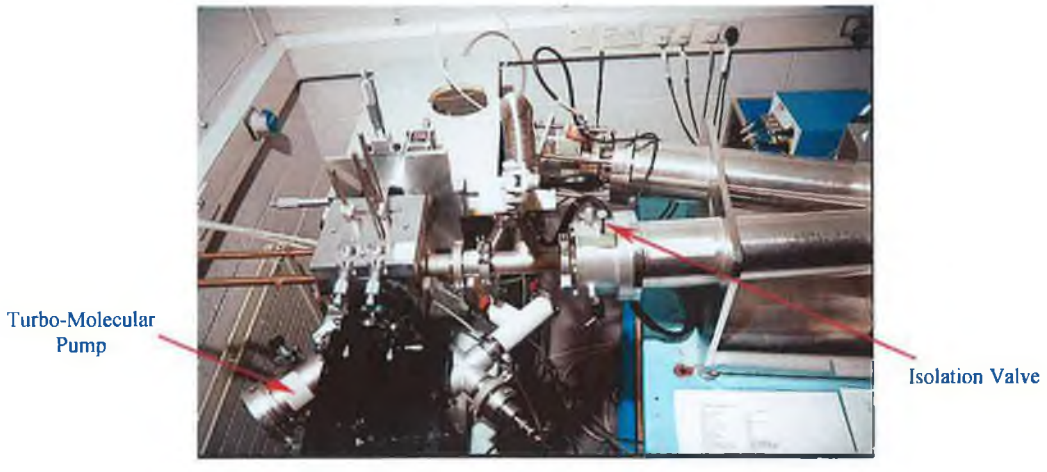

Fig. 3.6 Integration of the target chamber in the experiment. Shown also is the CEMA / PDA detector mounted on the exit arm of the spectrometer.

pump, which is backed with a double-stage rotary pump.

A slit isolation valve (Fig. 3.6) mounted on the entrance arm of the vacuum spectrometer (within the entrance slit housing) permits venting of the target chamber without changing the vacuum environment in the spectrometer chamber. This significantly reduced the turn-round time for replacement of the target samples. The time interval taken between venting the target chamber, changing the samples over and resuming measurements was valued at around 15 minutes.

The target chamber employed in the present work has the possibility of accommodating up to three target holders, two of which are mounted on the top of the chamber (Figs. 3.5 and 3.6) and a third is attached to the backside of it (Fig. 3.7).

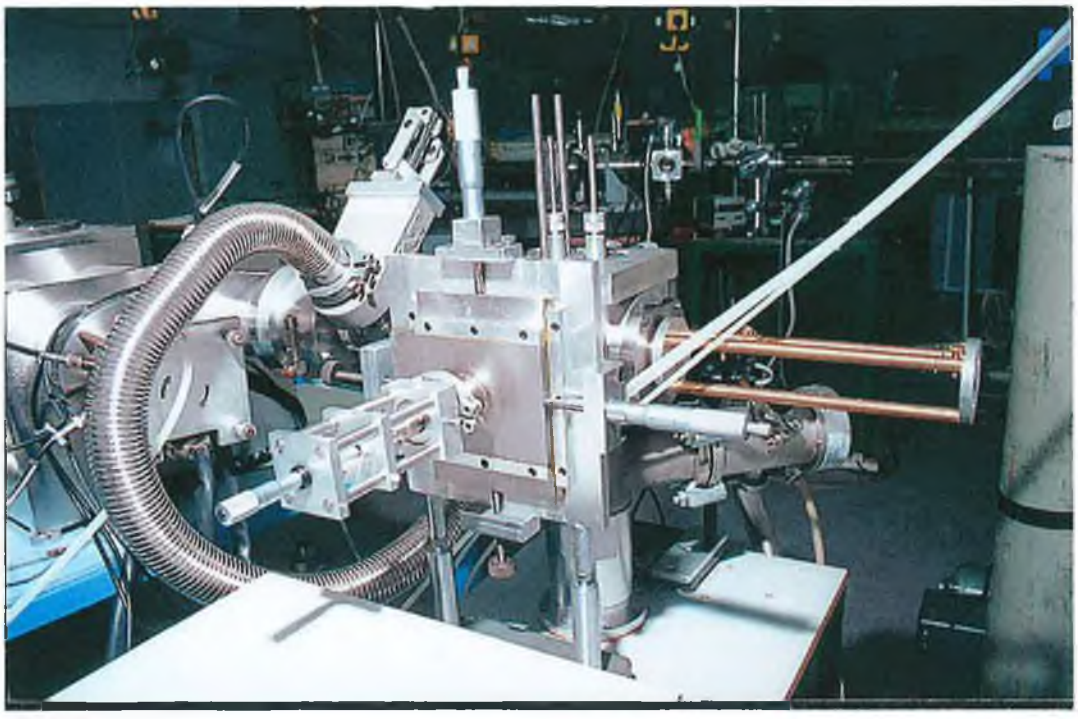

Fig. 3.7 The third target holder mounted on the back of the target chamber. Also shown are the other two holders placed on top of it. Details are in the text.

Both target holders mounted on the top of the target chamber comprise a stainless steel rod (200 mm long, 6 mm diameter) passing through a Wilson vacuum seal that is fixed to an aluminium supporting block. Both aluminium blocks are then inserted into

specially machined grooves in a custom-built flange attached to the top of the target chamber (Fig. 3.5). Sitting on O-rings seals, these blocks are free to move in one dimension without affecting the vacuum environment in the chamber. Translation of the target holders in the x-direction (parallel to the laser beam, perpendicular to the optic axis) was achieved using two micrometer heads attached to the side of the flange (see Fig. 3.5). The 90 mm length of the grooves, combined with the 70 mm length of the aluminium blocks confine the motion of the target to a maximum displacement of 20 mm in the x-direction. Movement of the target in the vertical z-direction (see Fig. 3.5) is also possible by extension and retraction of the stainless steel rod through its Wilson seal. In the present work, the target holder to the left in Fig. 3.5 was used to mount the cylindrically-shaped BeO (Beryllium Oxide) target employed to calibrate various spectral lines in the VUV region studied (40–160 nm). A vertical fore-slit (in the z-direction), of ~ 250 μm width, mounted in the target chamber using the right-hand side target holder illustrated in Fig. 3.5, provided spatially-resolved observations of different regions (in the y-direction) in the laser-produced steel plasmas that expanding in the axial direction, i.e. the x-direction (see Fig. 3.1).

The steel samples investigated in the present work were mounted in the target chamber using the third target holder shown in Fig. 3.7. It permits x-y-z movement of the target, along with rotation about the x-axis (4 degrees of freedom). Like the two holders on the top of the chamber, the backside target is attached to a 6 mm stainless steel rod that is extended into and retracted from the target chamber through a Wilson seal. A bracket mounted on top of the Wilson seal supports a micrometer head that translates the rod in the x-direction (see Fig. 3.7). The Wilson seal / micrometer arrangement is centered on a stainless steel plate, which in turn is driven by two additional micrometer heads in the y- and z-directions. Accordingly, a total displacement of 50 mm (5 μm increments) of the target in all three directions was achieved. Moving this target holder in the x-direction with respect to the fixed-position fore-slit could sequentially access different horizontal regions of the plasma produced (in the y-direction). The ~ 250 μm width fore-slit was positioned about 40 mm away from the plasma, so that only about 0.3 mm of the plasma (in the axial direction) was viewed by the spectrometer entrance slit (see Fig. 3.1). Moreover, the lens used to focus the laser beam was moved in conjunction with the target in order to keep the pre-set focusing conditions constant.

3.3.1 The samples

A set of 12 certified carbon-steel standard reference samples were employed in the present work. These samples were chosen so that the carbon content covers a relatively wide concentration range (from 0.001% to 1.32%), a range that is important in industrial steel alloys. Appendix E includes a list of the reference steel samples used in this work, along with their certified concentration levels for carbon and iron. The samples were on the form of cylindrical discs of ~ 40 mm in diameter, ~ 20 mm in thickness, and supplied by Glen Spectra Reference Materials™. For the purpose of constructing the calibration curves (chapters IV and V), each sample was turned down on a lathe to 15 mm in diameter and the 12 samples were fitted into corresponding holes in two circular target holders of 60 mm in diameter and 1 cm in thickness. Both target holders were then sequentially mounted in the target chamber, and measurements were carried out with a turn-round time of about 15 minutes, as mentioned earlier. In this way, emission spectra recorded from plasmas produced for all 12 targets under exactly the same operating conditions were obtained. It is worth mentioning that the only cleaning process on the surface of each target, apart from prior washing with an organic solvent, was firing a number of laser shots (10-50 shots, depending on the nature of the experiment), so that undesired surface contaminants were removed before further carrying out the experiment. Furthermore, the samples were rotated around the x-axis in order to ensure that a fresh area of the target surface was exposed to the incident laser pulse each time a new measurement was undertaken.

3.4 The Spectrometric System

The spectrometric system employed in the present work comprises a 1 m near normal incidence vacuum spectrometer, equipped with a 1200 grooves/mm spherical concave reflective grating and either a 1- or 2-dimensional detector array. The holographic-ruled grating operates in an off-Rowland circle type configuration. The radiation dispersed were monitored using either a Galileo™ Channel Electron Multiplier Array (CEMA) coupled to an EG&G™ linear Photodiode Array (PDA), or a 2-dimensional CCD detector array. The various parts of the spectrometric system under consideration are described in more details in the following sub-sections. Furthermore, technical specifications of the spectrometer and detectors used are summarized in appendix E.

3.4.1 The 1 m normal incidence vacuum spectrometer

A 1 m near normal incidence vacuum spectrometer (Acton Research Corporation™, USA, Model VM-521), provided with fixed entrance and exit arms, was used to disperse the VUV radiation emitted from laser-produced steel plasmas under investigation. The entrance slit, housed into a custom-made flange attached to one arm of the spectrometer (Fig. 3.8), can be adjusted to a width between 5 and 3000 μm, whereas the exit slit compartment was replaced by a 1- or 2-D multichannel detector array system. The spectrometer accommodates a 1200 grooves/mm spherical concave reflective (Al + MgF_2 coating) grating (Bausch & Lomb™) operating in an off-Rowland circle type configuration. In this configuration, wavelength scanning is achieved via rotation of the grating about an axis parallel to its vertical grooves and tangent to its centre. In addition, the linear translation of the grating along the bisector of the angle subtended (15° in the present instrument) by the slits at the grating centre provides focusing onto its focal plane [227]. The entrance and exit slits, as well as the concave grating all lie on the Rowland circle whose diameter equals to the radius of curvature of the concave surface (1000 mm in the present case). A photograph, as well as schematic drawing of the spectrometer is given in Figs 3.8 and 3.9, respectively.

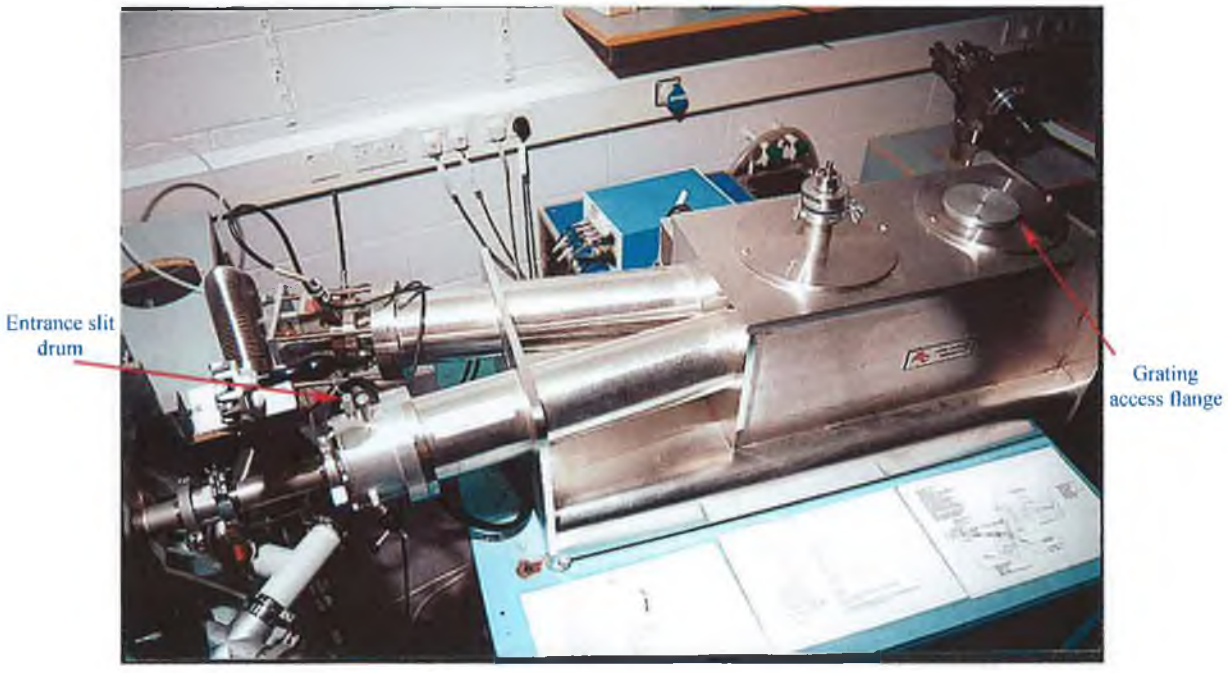

Fig. 3.8 Photograph of the VM-521 vacuum spectrometer. Also shown is the CEMA / PDA detector mounted on the far-side arm of the instrument.

The spectrometer in conjunction with the holographic concave grating can, in theory, disperse optical radiation in the wavelength range from 30 nm up to 325 nm. However, the actual wavelength coverage of the instrument is mostly determined by the reflection efficiency of the grating coating as well as by the spectral sensitivity of the detector used. For example, the detection efficiency of the CEMA detector employed significantly drops below 10% outside its spectral response range between 20 and 180 nm. Generally, when combined with either detector type utilized, the present instrument captures a wavelength interval of around 20 nm.

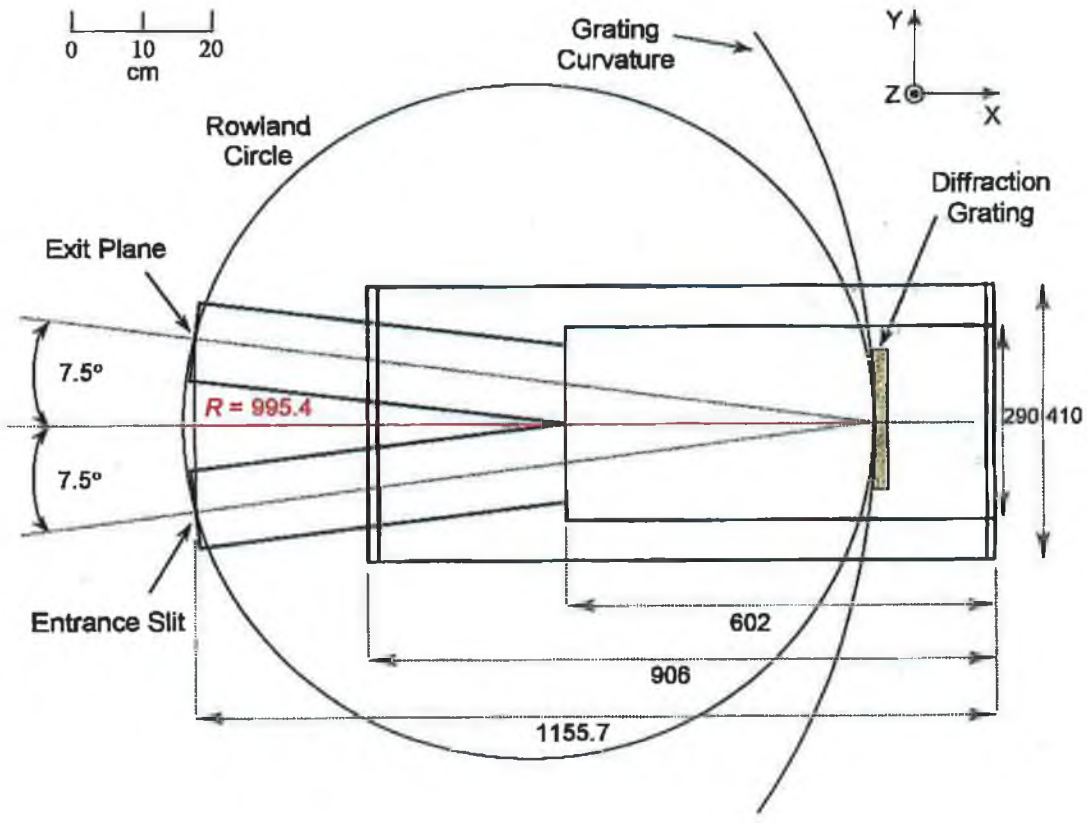

Fig. 3.9 Top view of positions of the spherical concave diffraction grating, the entrance slit as well as the exit plane on a Rowland circle whose diameter equals the radius of curvature (R) of the grating (~ 1000 mm). All dimensions are in mm units [After Ref. 263].

3.4.1.1 The grating and its off-Rowland mount

Since the grating is carried by a kinematic mount, the removal and the subsequent replacement within the spectrometer chamber are greatly facilitated without the need for re-alignment. The grooves of the grating are blazed at an angle of 2.75° with respect to the normal of the grating, which results in maximizing conversion efficiency of incident radiant flux to first order light at 80 nm.

The spherical concave diffraction grating, first developed by Rowland in 1882, combines the dispersive properties of a ruled grating surface with the focusing capability of a concave mirror [227]. The positions of the horizontal (primary) and vertical (secondary) foci of the spherical concave grating differ and their relative positions dramatically change according to the region in which the grating is operated. For instance, in the near normal incidence regime where angles of incidence (α) and diffraction (β) are relatively small and equal ($\alpha = \beta = 7.5°$ for the present instrument), the grating is in its zero order position and acts like a reflection mirror producing a *stigmatic* focus at its focal plane. In other words, a point source on the entrance slit is focused to a point image at the exit slit of the spectrometer. This situation arises from the fact that the geometrical location of both the vertical focus (which lies on a tangent to the Rowland circle perpendicular to the grating normal) and the horizontal focus (which lies on the Rowland circle itself) begin to coincide for small angles of incidence and diffraction.

As the angle of incidence (and accordingly diffraction) is increased, the horizontal focus moves upwards along the Rowland circle towards the grating whereas the vertical focus displaces outward along the tangent to the Rowland circle perpendicular to the grating normal (Fig. 3.10). This increasing separation between both foci results in more severe *astigmatism*, whereby a point source at the entrance slit is focused to a vertical line on a detector placed on the Rowland circle. In spectroscopic applications, astigmatism can be tolerated since only horizontal focusing is required to separate the various wavelengths [227]. However, it reduces the light intensity per unit area (radiant flux) of the image and demands strict focusing conditions to produce maximum spatial as well as spectral resolution. In the present work, astigmatism is minimum and quasi-stigmatic images are produced due to the near normal incidence nature of the instrument employed.

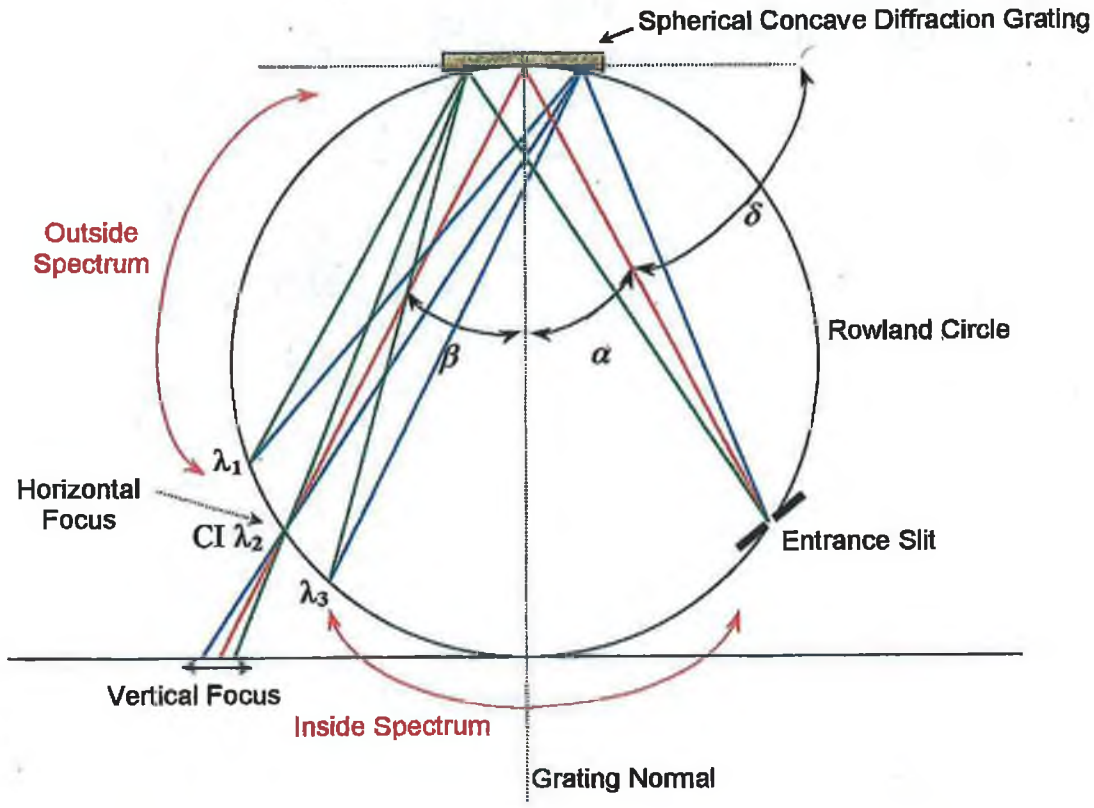

Fig. 3.10 Diffraction and focusing characteristics of the spherical concave grating of different wavelengths constituting a point source located at the entrance slit. δ is the grazing angle of incidence (90°–α), and CI refers to as the central image [After Ref. 263].

Diffraction by the spherical concave grating of the constituent wavelengths of light emerging from the entrance slit is described by the same formula that is used for a plane diffraction grating, i.e.

$$\pm m\lambda = d(\sin\alpha + \sin\beta) \qquad [3.1]$$

where m (= 1, 2, 3, ...) is the spectral order, λ is the wavelength, and d is the intergroove spacing (d = 8.33×10^{-4} mm for the 1200 grooves/mm used). The negative sign in equation 3.1 describes the outside spectrum that lies along the Rowland circle between the zero order position or the central image (CI) and the tangent to the grating (see Fig. 3.10). On the other hand, the positive sign outlines the inside spectrum positioned along the Rowland circle between the CI and the entrance slit (Fig. 3.10). Due to the configuration of the VM-521 spectrometer system (Fig. 3.9), the inside

spectrum is only recorded and so equation 3.1 becomes:

$$m\lambda = d(\sin\alpha - \sin\beta) \qquad [3.2]$$

where α and β lie on opposite sides of the grating normal, and hence have an opposite sign. The spectral region from ~ 35 nm to 70 nm is predominantly first order light due to the lower efficiency of the grating for short wavelengths. Outside this region, higher spectral orders, of wavelength λ / m that satisfy equation 3.2, overlap first order spectral light. For example, oxygen spectral lines, emitted from laser-produced beryllium oxide plasmas, of up to 3rd order have been observed and used in the present work for calibration of various VUV spectral regions under consideration.

As previously mentioned, when the angles of incidence and diffraction are equal (α = β), the grating is in its zero order position and specular reflection resulting in the formation of a "white light" image known as the central image or zero order image (see Fig. 3.10). When the grating is rotated through an angle ϑ about an axis lying in the z-direction that passes through the centre of the grating's front face, α and β change accordingly and thus dispersed light is scanned across the fixed detector array placed at the focal plane of the grating (Fig. 3.11). In order to maintain a good focus for each angle of rotation, ϑ, the grating is linearly translated a certain distance *l* in the y-direction along the bisector of the angle subtended by the entrance slit and the centre of the detector at the centre of the grating (see Fig. 3.11). The need for this linear translation arises from the fact that both the entrance slit and detector are fixed in position. The linear translation of the grating results in a mounting known as off-Rowland configuration, as described in § 3.3.1.

Upon rotation of the grating, both the entrance slit and the detector no longer lie on the circumference of the Rowland circle, which has also undergone rotation. The entrance slit is now located a distance, s, beyond the newly rotated Rowland circle, and the centre of the detector plane is located a distance, s`, inside it (see Fig. 3.11). For near normal incidence, where s` ≈ s [227]:

$$s = R\sin\alpha_0 \sin\vartheta \qquad [3.3]$$

where α_0 is the angle of incidence before rotation of the grating and R is the diameter of Rowland circle.

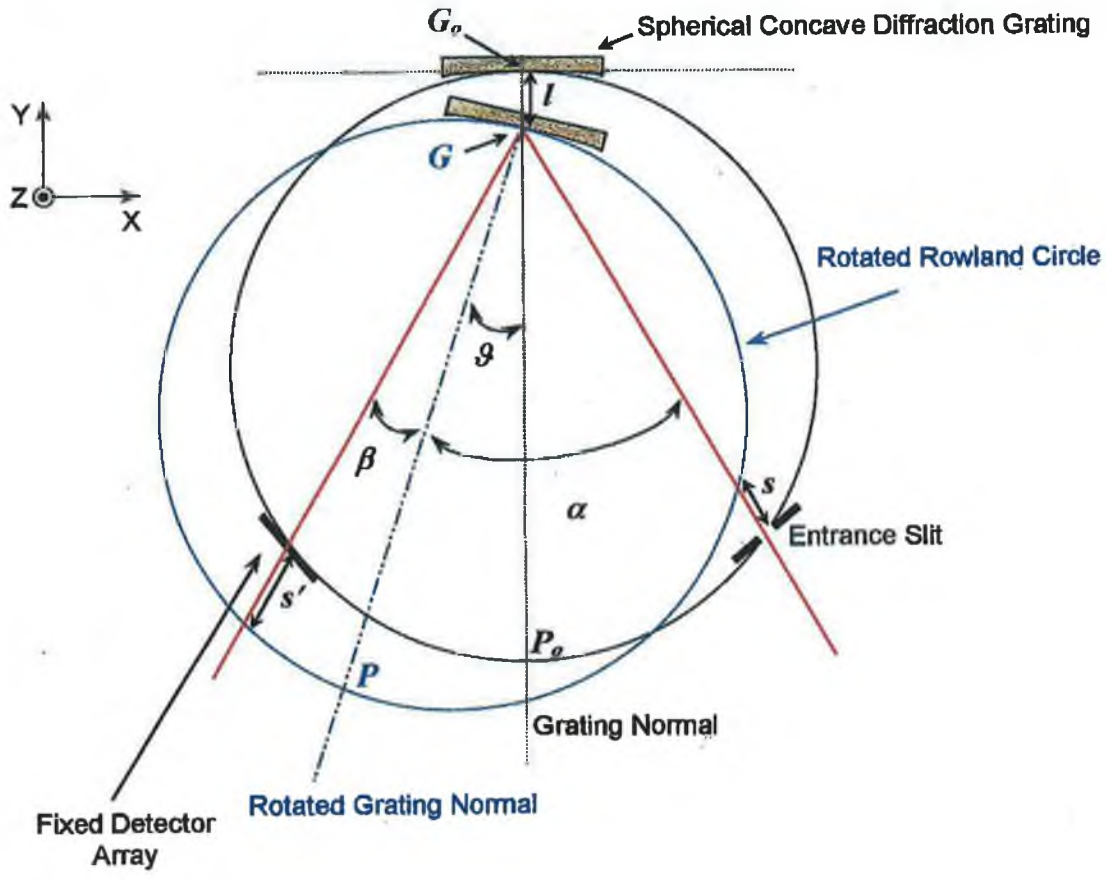

Fig. 3.11 Rotational and translational motion of the spherical concave grating within an off-Rowland circle type mount in order to achieve a simultaneous scanning and focusing of dispersed spectra at the detector plane [After Ref. 263].

Now, the relationship between the linear displacement of the grating, l, and its angle of rotation, ϑ, can be expressed following Fig. 3.11 and using simple geometrical relations:

$$l + GP_0 = R$$

$$\Rightarrow l + R\cos\vartheta \cong R \qquad (\text{As } GP_0 \cong R\cos\vartheta)$$

$$\therefore l \cong R(1 - \cos\vartheta) \qquad [3.4]$$

According to the manufacturer manual, in order to scan the 30 to 325 nm wavelength range over which the grating disperses light, the grating is rotated through an angle ranging from 0 to 20°. Accordingly, the corresponding linear translation (Eqn. 3.4) of the grating is calculated to be in the range from 0 to 20 mm.

Accurate positioning of the grating is achieved via a cam driven stage that is machined to give the correct combination of both movements (rotational and linear) for each wavelength setting. A precision lead screw located outside the vacuum spectrometer chamber drives the cam. The screw is connected to a stepper motor and this, in turn, is connected to electronic SpectraDrive™ controller that allows either manual or computer control (via an electronic interface) of the grating positions. A single revolution of the stepper motor changes the central wavelength on the detector by 1 nm when the 1200 grooves/mm grating is used.

The VM-521 vacuum spectrometer is evacuated, through a flange (ISO NW-160 size) attached to its base, to a pressure as low as 7×10^{-7} mbar using an ion pump connected to turbo-molecular / rotary pumps. This relatively low pressure represents a necessary environment for the CEMA device, which does not operate at pressures higher than 2×10^{-6} mbar. However, towards the second part of the present work when different background gases were introduced into the target chamber and the CEMA / PDA detector array was replaced by the relatively pressure-independent CCD detector, it became necessary to remove the ion pump. The pressure achieved by using the turbo-molecular pump backed with a double-stage rotary pump was about 2×10^{-6} mbar.

3.4.2 Performance of the VM-521 vacuum spectrometer

Because of its location as the first optical component in the path of the light emitted from the plasma plume, the length (= 3 mm) to diameter (= 50 μm) ratio of the pores within the glass capillary array (GCA) structure ultimately determines the solid angle over which the spectrometer can collect light. The maximum acceptance angle, Φ, of the GCA can be calculated from the following formula (Fig. 3.12):

$$\Phi = Tan^{-1}\left[\frac{50}{3000}\right] \cong 17 mrad \qquad [3.5]$$

Equation 3.5 means that the VUV radiation incident on the GCA at angles higher than 17 mrad will not be further transmitted to the grating. Consequently, the GCA characteristics in conjunction with the GCA-slit-grating distances will determine the dimensions of the footprint image of the plasma source on the grating surface.

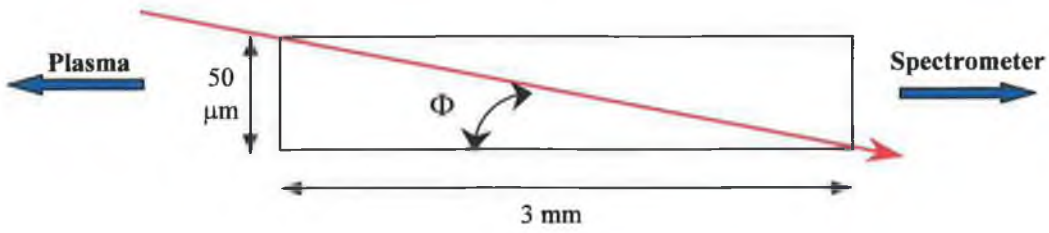

Fig. 3.12 Maximum acceptance angle (Φ) for light transmitted through one pore within the GCA.

The GCA-slit separation valued at 212 mm and the slit-grating distance is ~ 1000 mm, which results in the illumination of about 34 mm (W) of the 96 mm width of the grating employed in the present work. The resolving power of any plane diffraction grating can be expressed by the following well-known formula [227]:

$$\Re = \frac{\lambda}{\Delta\lambda} = mN \qquad [3.6]$$

where m is an integer (1, 2, 3, ...) representing the spectral order, and N is the total number of grooves that is illuminated (N = W / d, where d is the intergroove spacing). Equation 3.6 is also true for concave gratings provided that the illuminated width of the grating, W, is less than or equal a specific optimum width, W_{opt}, multiplied by 0.85 [227]. An expression for W_{opt} has been derived by Namioka [228] using geometrical optics:

$$W_{opt} = 2.38\left[R^3\lambda\frac{\cos\alpha\cos\beta}{\sin^2\alpha\cos\beta+\sin^2\beta\cos\alpha}\right]^{1/4} \qquad [3.7]$$

where R is the radius of curvature of the grating, and α and β are the angles of incidence and diffraction, respectively. Expression 3.7 was based on a modified Rayleigh's

criterion for resolution of spectral lines dispersed by plane diffraction gratings. Two spectral lines of equal intensity will be resolved if the wavelength separation between them is such that the ratio of the minimum intensity of the composite structure (between the two lines) to the intensity of either maximum remains the same as in the Rayleigh definition, namely, $8/\pi^2$. $\Re(\lambda)$ can then be determined from table 3.1 depending on the value of W with respect to $W_{opt}(\lambda)$.

Table 3.1 Resolving power ($\Re$) of the concave grating as a function of the illuminated width (W) [After Ref. 227].

Width of grating illuminated, W	Resolving power, $\Re$
$W \leq 0.85\ W_{opt}$	mN or W (m / d)
$W = W_{opt}$	$0.92\ W_{opt}$ (m / d)
$W \geq W_{opt}$	$0.75\ W_{opt}$ (m / d)

For the VM-521 spectrometer under investigation, W_{opt} lies between 55 mm and 95 mm across the wavelength interval covered by the instrument. As W is limited by the GCA aperture to only 34 mm, it is always less than 0.85 W_{opt} and so the theoretical resolving power is estimated at 40,800 (34 × 1200) as suggested by table 3.1. However, in practice this value is significantly reduced due to considerations such as the quality of the grating surface, entrance slit width and more importantly the pixel size of the detector at the spectrometer focal plane. The resolving power of the present grating is quoted by the manufacturer at a value of 5,700 at 80 nm for 10 μm entrance slit width.

The reciprocal linear dispersion of the grating is another important characteristic of grating spectrographs, and describes the spatial separation between two adjacent wavelengths. For the present instrument, the reciprocal linear dispersion varies between 0.830 (first order) and 0.816 nm/mm over the spectral range covered by the grating. For

a particular entrance slit width, W_s, the corresponding image on the focal curve of a concave grating in a Rowland mount has a width identical to a wavelength interval $\Delta\lambda$, determined as [228]:

$$\Delta\lambda = \frac{W_s d}{R} \qquad [3.8]$$

Accordingly, for a slit width of 50 μm the corresponding instrumental width is 0.042 nm. The spatial resolution capabilities of the multichannel detectors utilized in the present work and its influence on determining the spectral resolution of the system will be discussed in the following sub-sections.

3.4.3 Multichannel photo detectors

During the last ten years or so many spectroscopic applications, including LIPS, have benefited from substantial improvements in solid-state, multichannel detector technologies, such as those involved with the photodiode array (PDA) and charge-coupled device (CCD) [181]. Advantages of PDA and CCD detectors include wide spectral range and response, low dark current and readout noise, large dynamic range, linear response and speed and ease of data acquisition [229].

In the present work two classes of multichannel radiation detectors were utilized. These are channel electron multiplier array / photodiode array (CEMA / PDA) combination, and charge-coupled device (CCD) detector.

3.4.3.1 CEMA / PDA detector

A diagram illustrating the structure and operation of the CEMA / PDA detector is schematically shown in Fig. 3.13. The CEMA detector (Galileo^{TM}, Model 6025-FM) is basically an image intensifier consisting of a microchannel plate (MCP) input stage followed by a phosphor coated fibre-optic faceplate. The MCP employs both fibre optic and photomultiplier technologies to convert charged particles or energetic photons into an electronic signal, which is subsequently amplified. It finds applications in the sensing of VUV / XUV (extreme UV) radiation, soft X-rays, neutron and charged particles in

scanning electron microscopes, residual gas analyzers, image tubes and time-of-flight mass spectrometers.

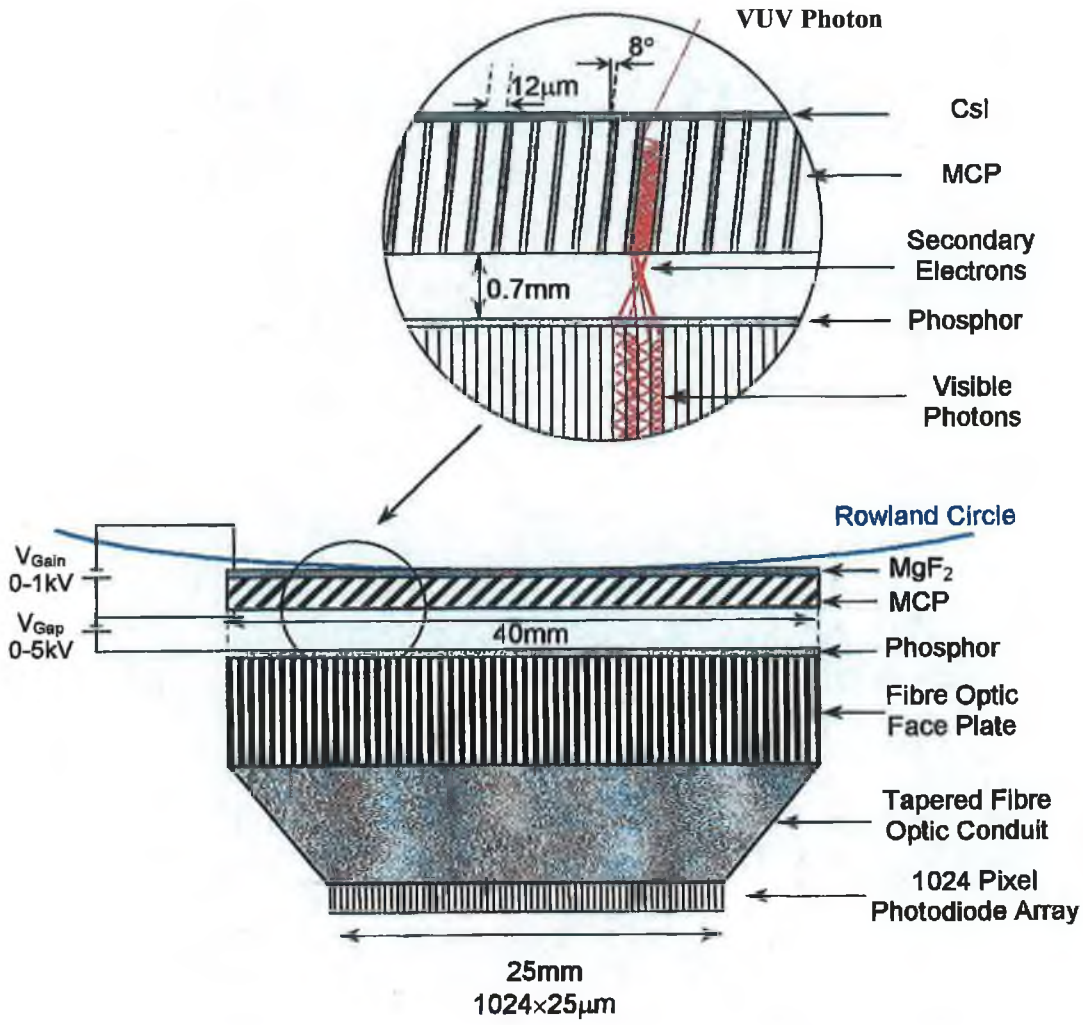

Fig. 3.13 Schematic representation of the structure and operation of the Galileo™ CEMA image intensifier incorporating an MCP and phosphor-coated fibre optic faceplate that butt coupled to a 1024 pixels linear photodiode array (PDA) detector [After Ref. 263].

The MCP consists of an array of lead glass fibre optic bundles that are fused together and chemically etched to form a porous structure. Each glass pore has a diameter of 12 μm, and a centre-to-centre spacing of 15 μm. The total MCP "disc" has a diameter of 40 mm, a thickness of 0.5 mm and an electron gain of ~ 3×10^4. The quoted quantum efficiency (QE) of the MCP lies in the region between 10 and 20% for normal incidence photons over its wavelength response range from 20 to 180 nm. A bias angle of 8°, with

respect to the vertical axis of the MCP surface was applied to each microchannel. According to the manufacturer, the choice of this angle was based on various considerations such as maximizing the detection efficiency of radiation and prevention of incident particles from passing through the channels creating undesired ionic currents. In order to enhance the detection efficiency of VUV and XUV photons, CsI (cesium iodide) layer (1000–3500 Å thick) has been coated over the MCP input surface (underneath the protective MgF_2 coating). The CsI layer acts in the same way as the photocathode material in a typical photomultiplier tube does. Thin metallic layers (mostly Ni-Cr) vacuum-evaporated on both the front and back faces of the MCP serve as electrodes across which a negative bias, V_{gain}, (0–1 kV) is applied. As can be seen in Fig. 3.13, the MCP front face is tangentially positioned onto the Rowland circle of the 1-m normal incidence vacuum spectrometer used.

The internal walls of each microchannel within the MCP structure are covered with a silicon dioxide-rich secondary electron emissive coating. The incident VUV photons cause electrons to be photoelectrically emitted at the entrance to the microchannel plate (at the CsI layer). These electrons collide with the electron emissive coating on the pore walls, resulting in emission of secondary electrons which, in turn, collide with other surrounding electrons causing amplification of the electronic signal down the continuum dynode structure of the pore walls. Simultaneously, a negative voltage (V_{gain}) of the order of about -900 V is applied across the microchannel, causing these electrons to accelerate and multiply in number. As the final electron bunches leave the microchannel plate they are further accelerated across a vacuum gap of almost 1 mm, by a potential difference, V_{gap}, of +2500 V, before they interact with the phosphor-coated fibre optic faceplate. The phosphor fluoresces in the visible region causing visible photons to propagate down a tapered fibre optic bundle, which de-magnifies the initial 40 mm image by a factor of about 1.6 in order to fill the 25 mm length photodiode array (PDA). The PDA is butt-coupled to the optic fibre bundle by an optical index matching cement.

The PDA is an EG&G^{TM} (Model 1453A) silicon linear array with 1024 photodiodes (40 pixels/mm) and 25.6 × 2.5 mm^2 overall size. The wavelength range of the array covers the 180–1100 nm spectral range, and its quoted quantum efficiency is ~ 70% at 650 nm. The photodiode array operates on the well-known phenomenon of the p-n junction. Visible photons incident on the p-n junction of each photodiode generate electron-hole

pairs which are proportional to the incident amount of light. Each photodiode is connected in parallel with a storage capacitor which, in turn, is attached to the common video line of the chip through a transistor switch. The switches are sequentially turned on and off by the shift register circuit, thereby periodically recharging each photodiode element to 5 V (reverse bias) and storing the resultant charge on the capacitor. During the scanning (readout) time, the charge on each capacitor is gradually removed, by the reverse current flowing in the associated photodiode, to an amplifier through the common video line. The analogue video signal is digitized by a 12 bit analogue-to-digital converter (0 to 2048 dynamic range) within an optical multichannel analyzer (EG&G^{TM}, Model 1471A). The digitized signal is then sent to a PC via a GPIB (General Purpose Interface Bus) card for further treatment.

A thermoelectric cooler (Peltier type) is attached to the PDA head to reduce the dark current contribution to the output signal. Furthermore, water is circulated through the PDA head in order to assist the thermoelectric cooler to bring the temperature down to 5° C. Nitrogen gas, set to a flow rate of about 2.5 l/min, is also circulated through the PDA head in order to prevent formation of condensation on the PDA surface, and oxidation of the aluminium heat sink that the PDA rests upon when operating at temperatures lower than room temperature. The vacuum in the spectrometer chamber was maintained at about 7×10^{-7} mbar, as mentioned previously, in order to prevent arcing (generation of ions within the microchannels) of the CEMA detector. A photograph of the CEMA / PDA detector is shown in Fig. 3.14. Spectral resolution of the CEMA / PDA detector combination, as well as procedures for synchronization and control of the experiment and data acquisition will be discussed in § 3.4.3.3, as well as in chapter IV.

3.4.3.2 CCD arrays

Two VUV-sensitive, backside-illuminated CCD detectors were utilized in the present work. The first array (Photometrics^{TM}, Model SI003-AB) was on loan from the DESY synchrotron facility in Hamburg, Germany, and used for comparison with the CEMA / PDA detector towards the end of the preliminary studies (chapter IV). The other CCD detector (Andor Technology^{TM}, Model DV420-BN) was employed for the rest of the experiments (chapters V & VI).

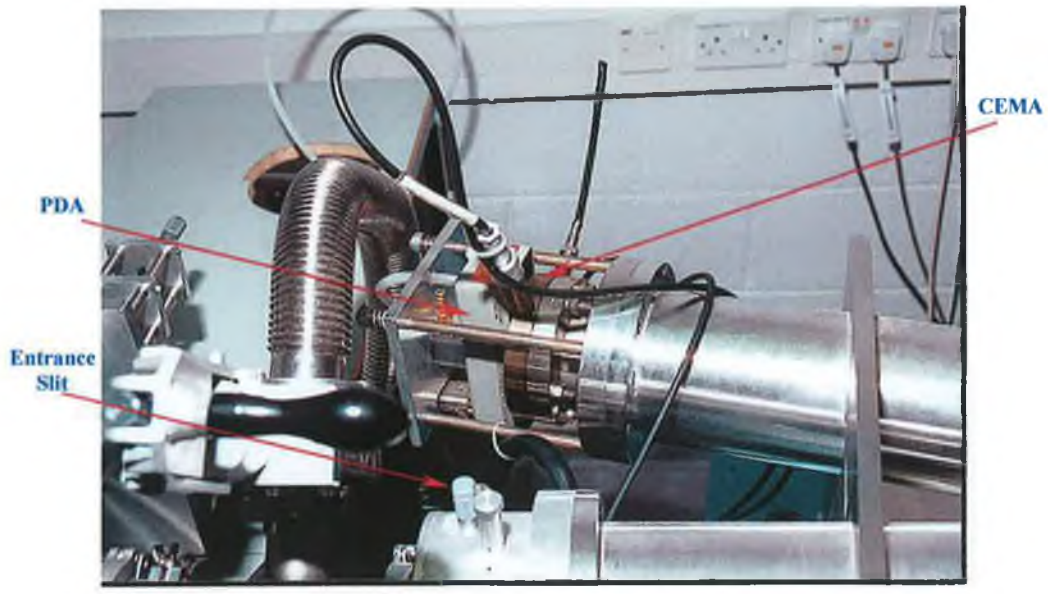

Fig. 3.14 CEMA / PDA detector mounted on the exit arm of the 1 m vacuum spectrometer.

Basically, the CCD (charge-coupled device) is a device designed for electronic charge accumulation and transfer. Its essential building block is based on a two-dimensional array of metal-oxide-semiconductor (MOS) capacitors. The MOS capacitor is formed by growing a layer of silicon dioxide (SiO_2) on a silicon substrate (mostly p-type); a metal electrode is then evaporated on top of the oxide layer (see Fig. 3.15). The metal electrode is known as the gate and is biased positively with respect to the silicon substrate.

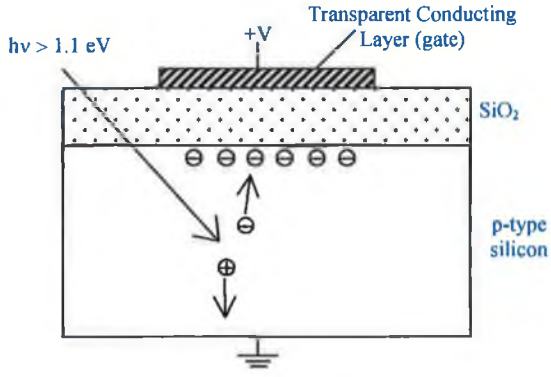

Fig. 3.15 MOS capacitor structure. When the gate is biased positively, photogenerated electron-hole pairs become separated and the electrons then trapped at the SiO_2-Si boundary beneath the gate electrode.

Photogenerated electron-hole pairs within the silicon will be separated, with the electrons being attracted to the surface of the silicon under the gate, where they will remain whilst the gate voltage is positive. In other words, the electrons are effectively trapped within a potential well formed under the gate contact (it is also called the depletion region, because it depletes the majority carriers, which are holes in a p-type silicon). The amount of trapped charge will be proportional to the total integrated light flux falling onto the device during the measurement period.

When a quantity of charge is available in the depletion layer under the gate, it may be transferred or "coupled" into an adjacent capacitor (pixel) by applying a repeated sequence of potentials to the gate supply lines. This process simply involves changing the gate voltage periodically between low and high values. Firstly, the gate voltage on the adjacent electrode (denoted as P_2) must be raised to the same value as that for the first electrode (denoted as P_1). This routine has the effect of lowering the floor of the potential well that belonging to the second electrode (P_2), thus allowing the transfer of charge from one pixel to the other. The quantity of charge becomes now shared between the two pixels. Secondly, the gate voltage on the original electrode (P_1) is reduced to zero volts, thus allowing a complete transfer of the charge to the second pixel. If a third pixel, P_3, exists, then the charge accumulated in P_2 will eventually completely transferred to P_3 before a new cycle takes place in the next three pixels. Continuing this cycle of lowering and raising the gate voltages (known as clocking) will progressively move the charge along the line of MOS capacitor line. At the end of that line, the amount of charge arriving as a function of time then provides a sequential scan of the 'P_1' detector output. It is obvious from the above that three voltage clocking lines are required to define the process of moving the charge accumulated in one pixel along the array. This is known as the three-phase scheme.

One problem encountered with the just described one-dimensional array is that a new light scan can not be carried out until all of the charge has been transferred along the array. With the introduction of two-dimensional arrays, faster scanning rates can be achieved. Here, a second CCD array, usually termed the output or shift register, which is shielded from incident radiation, runs below and parallel to the original CCD array as illustrated in Fig. 3.16. At the end of each clocking cycle, the charge built up at the end of all columns of the CCD is transferred to the corresponding pixel of the second CCD

array underneath it, thus delivering a 'row' of charge to the output register. A clocking system, similar to that of the main CCD array, horizontally transfers the charge accumulated in the pixels of the shift register, one pixel at a time, to the output amplifier where it is detected and converted into an electrical signal. The above process is repeated until all the rows in the CCD are delivered to the output amplifier through the shift register.

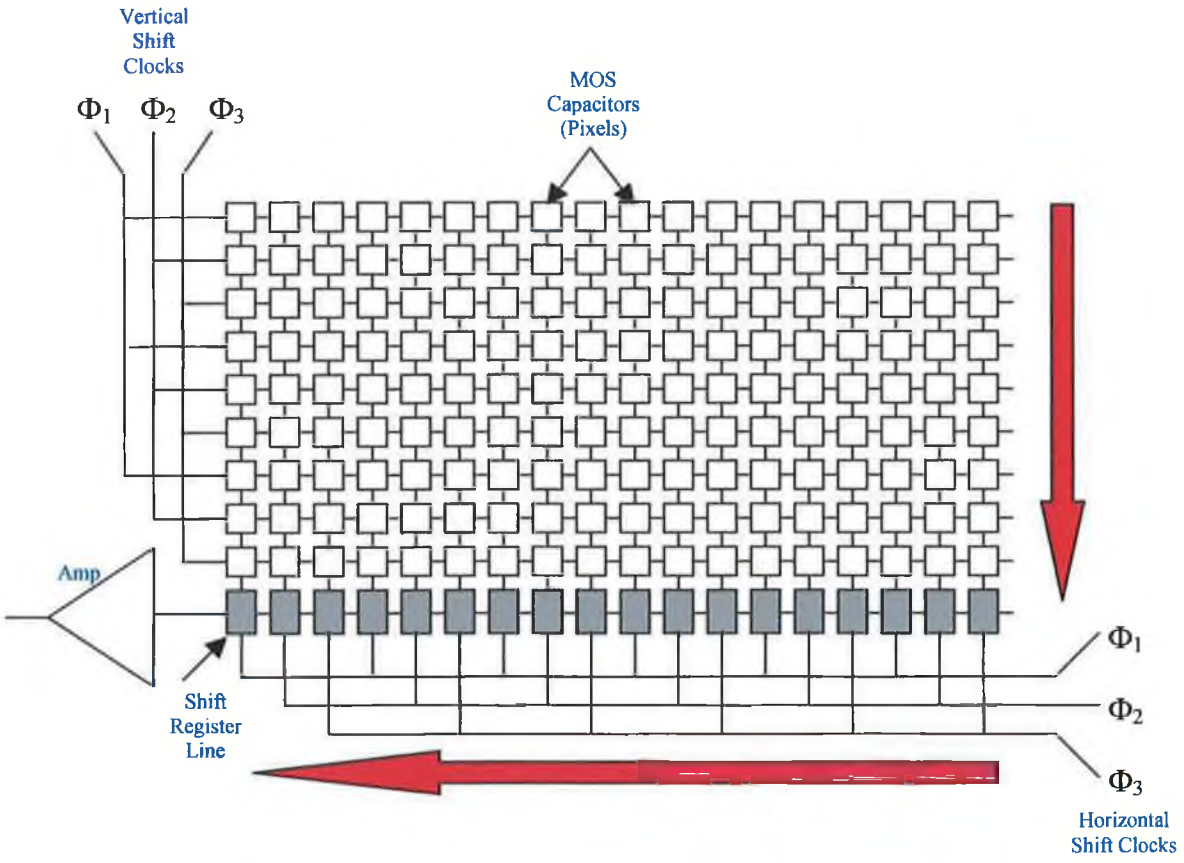

Fig. 3.16 Basic structure and operation of two-dimensional CCD arrays. Φ_1, Φ_2 and Φ_3 are the gate potentials required for clocking different pixels in the two shown directions. Red block arrows show the direction of charge transfer to the output amplifier, one pixel at a time. See text for more details.

Unlike the PDA, there are no electronic switches required to access each element, resulting in very low levels of readout noise. Another factor that contributes to further decreasing the readout noise is through "binning" the chip pixels. Binning is a process that allows charge from two or more pixels to be added on the CCD chip before readout

can really take place. Summing charge on the chip and doing a single readout results in better noise performance than reading out several pixels and then summing them in the external circuit attached. It is worthwhile noting here that binning could cause some deterioration in the spectral resolution of the system if the detector is tilted in any way.

The CCDs just described are sometimes called surface channel CCDs because the electronic charge are stored and transferred at the surface of the silicon substrate immediately under the insulating oxide layer. However, the inherent crystal irregularities and lattice defects in the surface layer of silicon semiconductors significantly contribute to the phenomenon of charge trapping, which results in poor charge coupling and severe image blemishing. One way to avoid the surface trapping phenomenon is to grow a higher n-doped layer of silicon on the existing p-type substrate in order to separate it from the insulating oxide. These CCDs detectors are usually termed buried channel devices because the depletion region formed is now completely buried within the silicon bulk, away from the surface region. Most modern "front-illuminated" CCD devices are making use of the buried channel technology to enhance the quantum efficiency and gain of the detector.

Generally, CCDs that are illuminated from the front side have very low quantum efficiency (< 5%) for radiation in the ultraviolet and beyond regions. This is due to the fact that the relatively thick (500 to 1200 Å) polysilicon gate electrodes overlying on the front side (Fig. 3.15) of the chip is opaque to wavelengths shorter than 400 nm. One solution to this problem is to phosphor coat the surface of the array at specific positions, so that shorter wavelength photons are stepped down in energy to the visible region (blue-green) in which they can be detected. This simple method, however, has its own limitations because phosphor scatters almost half of the downconverted photons before they really arrive at the silicon substrate. Accordingly, the UV quantum efficiency (QE) of phosphor-coated devices is thus limited to half of the QE of the CCD in the blue-green band of visible wavelengths, or ~ 15% [230].

A more effective solution to the problem was achieved by thinning the silicon substrate layer to a thickness of ~ 10 to 20 μm, and illuminating the array from the back side; CCDs manufactured in that way are usually referred to as thinned, backside illuminated detectors [231]. The absorption coefficient of silicon increases with decreasing

wavelength and so short wavelength light is absorbed close to the surface of the illuminated area [231]. The thickness of the silicon substrate produced should not exceed 20 μm so that the electrons (holes) produced are able to travel to the depletion region underneath the oxide layer with little or no recombination and / or capture. The most important feedback of such a practice has been the extension of the sensitivity range of these CCDs to the far- and vacuum-ultraviolet, as well as the x-ray spectral regimes. Quantum efficiencies over the extended range from near IR down to the x-ray spectral region (1100 nm to 0.1 nm) for a typical thinned, backside-illuminated CCD array were recently demonstrated by Poletto and co-authors [232], and are shown in Fig. 3.17.

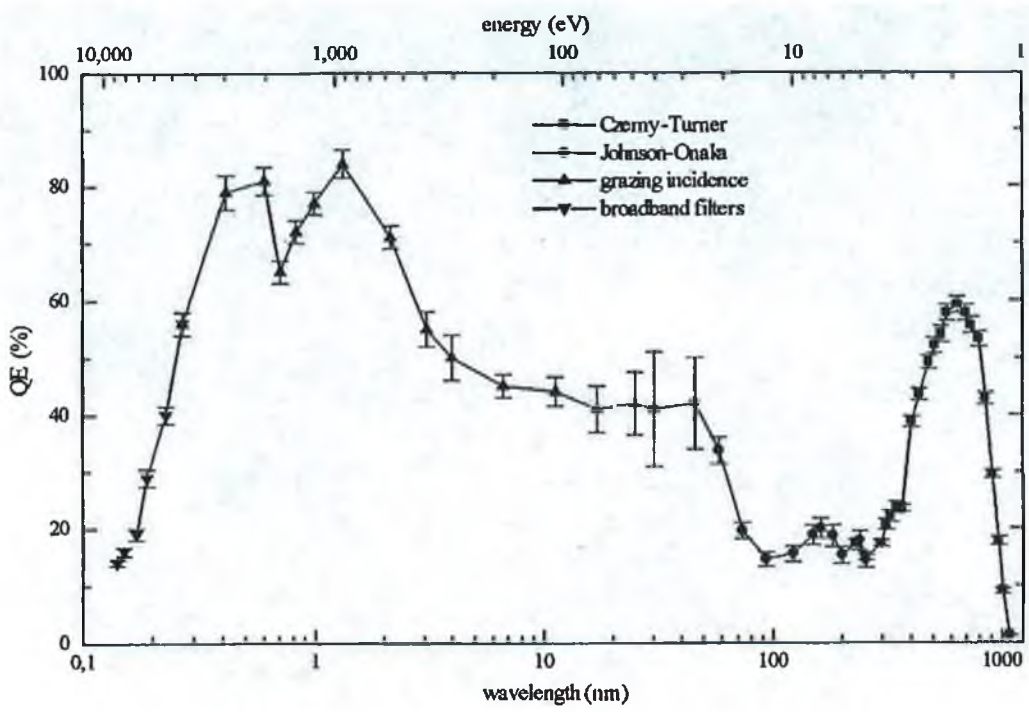

Fig. 3.17 Effective quantum efficiency in the 1 eV to 10 keV spectral range for a thinned, backside-illuminated CCD array [After Ref. 232].

3.4.3.2.1 Photometrics™ CCD

The thinned, backside illuminated CCD consisted of a two-dimensional array, 1024 pixels high × 1024 pixels wide, with a pixel size of 24 × 24 μm corresponding to an active imaging area of 24.6 × 24.6 mm. The CCD chip operates at 200 kHz readout frequency. Analog video signals from the amplifier are digitized in a 16-bit analog-to-

digital converter (ADC) in the camera control unit before being relayed to the computer for display as a two dimensional image. The quantum efficiency of the CCD quoted by the manufacturer to be in the range between 15 and 40% over the wavelength range 20–220 nm. The quantum efficiency values for the present CCD compare well with those illustrated in Fig. 3.17 for the same spectral range.

Various UV and visible anti-reflection coatings can be applied to both front- and backside-illuminated CCDs to improve the quantum efficiency in the corresponding spectral regions. However, the SI003AB CCD was uncoated due to the fact that UV and visible coatings absorb VUV radiation. Accordingly, the backside of the CCD was placed tangential to the Rowland circle of the VM-521 vacuum spectrometer, with its silicon substrate directly exposing to the dispersed VUV radiation.

The CCD array was thermoelectrically cooled to a temperature of -35° C using a Peltier cooler, in order to reduce the thermally generated dark current, which is not a part of the incident photon flux. The dark current, as measured by the manufacturer, was valued at 0.5 electrons / pixel / second.

3.4.3.2.2 Andor Technology™ CCD

The two-dimensional, thinned, backside-illuminated, and anti-reflection coated CCD array (Model DV420-BN) had 1024 (high) × 256 (wide) pixels corresponding to an active imaging area of 26.6 × 6.7 mm (26 μm^2 pixel size). The CCD controller operated at readout frequency of 1 MHz, and the analog video signal was digitized using a 16-bit analog-to-digital converter. The gain of the CCD array was estimated by the manufacturer at 10 electrons per analog-to-digital count. Also, the quoted dark current valued at 0.01 counts / pixel / sec. A Peltier type cooler was used to cool the CCD down to about -45° C.

Both the readout noise and dark current associated with the present CCD were measured in the present work by recording the counts obtained at the central pixel of the CCD (pixel number 512) over various exposure times, and up to the time interval at which the output signal became saturated. Figure 3.18 illustrates this relationship when the temperature of the CCD was set at -20° C, for example, and readout mode was adjusted

to full-vertical binning (single pixel). The pressure inside the vacuum spectrometer was maintained at 2×10^{-6} mbar during this experiment. The slope of the perfect straight line obtained represented the dark current (integrated over the 1024 pixels of the array), while the intercept with the counts axis provided an estimation of the inherent readout

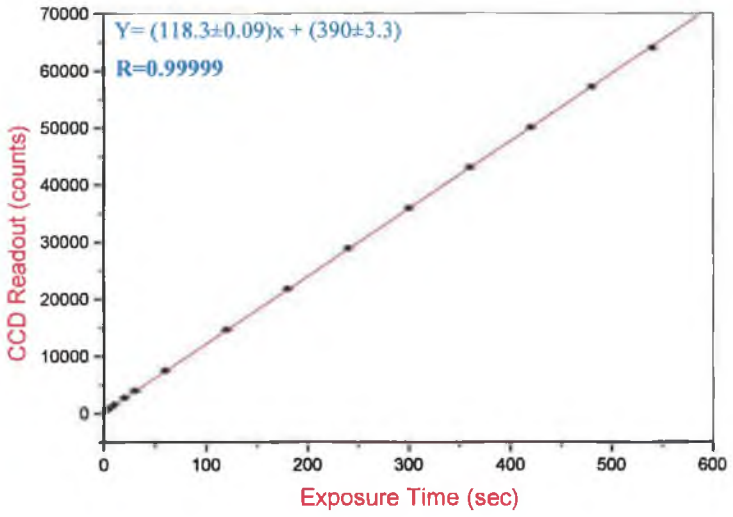

Fig. 3.18 The output counts of the Andor CCD as functions of exposure time for measuring the dark current and readout noise of the detector.

noise of the detector. As can be concluded from Fig. 3.18, the dark current valued at 0.12 counts / pixel / sec at -20° C, while the readout noise of the detector was 390 counts. It should be mentioned that at -40° C (the highest temperature achieved with no water-cooling assistance) the dark current was better than 0.01 counts / pixel / sec, which compares very favourably with the value quoted by the manufacturer. Similar curves to that produced in Fig. 3.18 were obtained for the five other temperatures employed, i.e. -40, -10, 0, 10 and 20° C. Figure 3.19 shows the variation of both the readout noise and dark current with the CCD temperature. As illustrated in Fig. 3.19, the thermally-generated dark current monotonically increased with increasing temperature up to room temperature, while the readout noise was almost constant up to about -10° C when it starts a dramatic increase with temperature. Therefore, except when otherwise stated, all the experiments to follow (chapters IV-VI) that employing the Andor CCD camera are carried out at -40° C. The spectral resolution exhibited by the spectrometric system used is discussed in the following section, as well as in chapter IV.

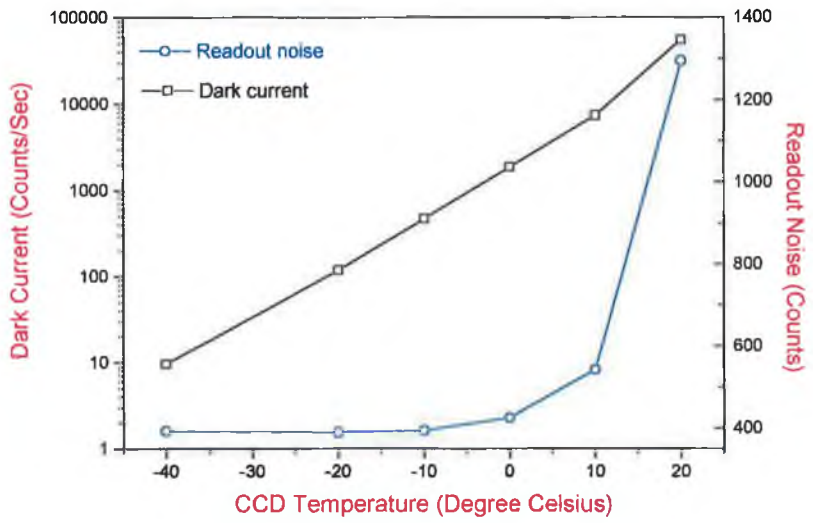

Fig. 3.19 Variation of dark current and readout noise with the Andor CCD temperature. Dark current values were plotted on $\log_{10}$ scale for more clarity. The saturation level (not shown) of the CCD used valued at 65536 counts/sec.

3.4.3.3 Spectral resolution of the system (spectrometer + detector)

Due to the presence of the tapered fibre optic reducer in the structure of the CEMA / PDA detection system (see Fig. 3.13), the 25 μm size of each PDA pixel records light accumulated over a 40 μm interval at the front face of the MCP. Accordingly, the effective spatial sampling interval at the Rowland circle is 40 μm. For an entrance-slit width of 50 μm, the instrument function has a typical FWHM of 5 pixels (corresponding to 0.1 nm). This value was obtained using the first order O V spectral line at 77.45 nm, which was emitted from a laser-produced beryllium oxide plasma. The corresponding best resolving power (λ / $\Delta\lambda$) of the spectrometric system (spectrometer + CEMA / PDA) is therefore about 800 at 80 nm. Deconvolution of the instrumental function from the raw spectrum is an effective technique for improving the spectral resolution of the system. However it is usually combined with some limitations, which will be discussed in more details in the following chapter (chapter IV).

The Andor CCD array records VUV radiation directly on its 26.6 × 6.7 mm backside surface, the centre of which is mounted tangentially to the Rowland circle of the vacuum spectrometer used. The associated broadening of the system instrument

function encountered with the CEMA detector is therefore absent, resulting in higher spatial and hence spectral resolution.

In order to estimate the instrumental FWHM of the spectrometer in conjunction with the Andor CCD detector, low-pressure helium and argon gas discharges were employed. It is a well known fact that the physical contributions to the broadening of spectral lines emitted from these sources are negligibly small, so that the observed broadening of a spectral line can be approximated by the instrument function itself of the spectrometric system. Figure 3.20 shows typical VUV spectra emitted from the He and Ar discharges when the central wavelength of the grating was adjusted at 90 and 80 nm, respectively. Spectra shown in Fig. 3.20 were recorded at entrance slit width of 50 μm.

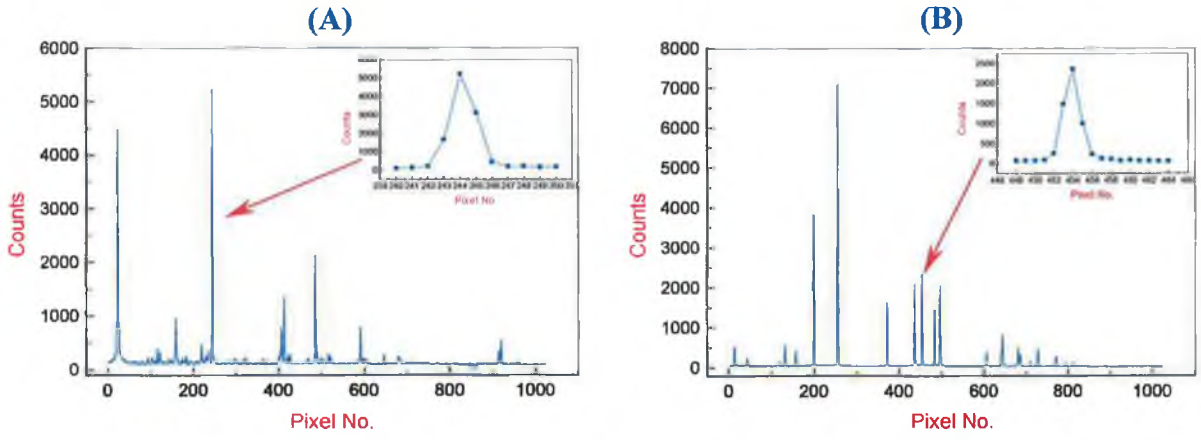

Fig. 3.20 VUV He (A) and Ar (B) spectral lines emitted from low-pressure gas discharges at central wavelengths of 90 (A) and 80 (B) nm, respectively. Insets show the typical instrumental FWHM obtained in each case. For more details see the text.

These measurements were carried out when the whole instrument was brought to the Synchrotron radiation facility (L.U.R.E.) in Orsay, France. The He and Ar discharge lamps operated at 12.8 and 8.6 W, respectively, and the pressure in both sources was kept at 1×10^{-4} mbar using a small turbo-molecular pump backed by a double-stage rotary pump. Radiation emitted from each discharge was integrated for 1 s, and the CCD readout mode was set to full-vertical binning.

Careful observations of insets shown in Fig. 3.20 yielded that the FWHM of both spectral lines under consideration has a typical value of about 2 pixels. The reciprocal linear dispersion of the present spectrometer, as mentioned earlier, has a value of 0.83 nm/mm at 80 nm. Combining this with the 38.5 pixels/mm (1024 pixels divided by the 26.6 mm total width of the array) of the Andor CCD produced a spectral resolution of about 0.0216 nm/pixels. Now simply multiply this value by the 2 pixels spectral line wide obtained from Fig. 3.20 to get the instrumental FWHM of the present system of about 0.045 nm. This value compares very well with the theoretical value (0.042 nm) obtained from equation 3.8 for a 50 μm entrance slit width. Accordingly, the resolving power of the system (λ / $\Delta\lambda$) has a value of about 1800 at 80 nm, approximately 2.25 times that obtained with the CEMA / PDA detection system.

3.5 Laser Synchronization and Procedure for Spectral Data Acquisition

Laser firing and subsequent plasma production must be accurately timed so as to coincide with detector integration period. In this section, the timing scheme used to control the sequence of events required to achieve the above criterion, as well as the method of spectral data acquisition are described in detail for the system illustrated in Fig. 3.1. Synchronization of the other system used in this work (Fig. 3.2) was simply performed by sending a master TTL (Transistor-Transistor Logic) pulse from the PC, via the CCD detector controller, to a delay / pulse generator, which in turn sends two triggering pulses to both the flash lamps and Q-switch of the laser system, at the required delay times.

Various experimental parameters such as the number of laser shots fired, the duration over which the detector integrates (exposure time) at each laser shot and the repetition rate of laser shots are entered and stored on the PC via the *Omasoft* software package. The read / reset time of each pixel in the PDA detector is 28 μs and so an exposure time of 30 ms was chosen to read all 1024 pixels. Exposure times longer than 30 ms result in a build-up of dark current and the subsequent decrease in the dynamic range.

A master TTL pulse is sent from the PC to the OMA controller via a GPIB parallel interface. The OMA controller in turn generates and sends a TTL signal to the BNC

input channel of the Stanford™ digital delay / pulse generator (Model DG535) upon initiation of detector integration. This pulse is 30 ms long and its rising edge is defined as time T_0 (see Fig. 3.21). The delay / pulse generator has 4 other output channels termed as A, B, C and D; the delay on each one is programmable with respect to T_0 and can be varied between 0 to 1000 s with a minimum of 5 ps increment. The amplitude (~ 5 V) of each output TTL signal from the delay generator is insufficient to trigger neither the flashlamp nor the Q-switch circuitry of the Spectron Nd:YAG laser system; the laser flashlamp triggers on the rising edge of a 0 → +15 V pulse, while the Q-switch triggers on the falling edge of a 0 → -15 V. Therefore, the output pulse from any of the 4 channels is amplified to ~ +/- 15 V using a custom-built amplifier circuit.

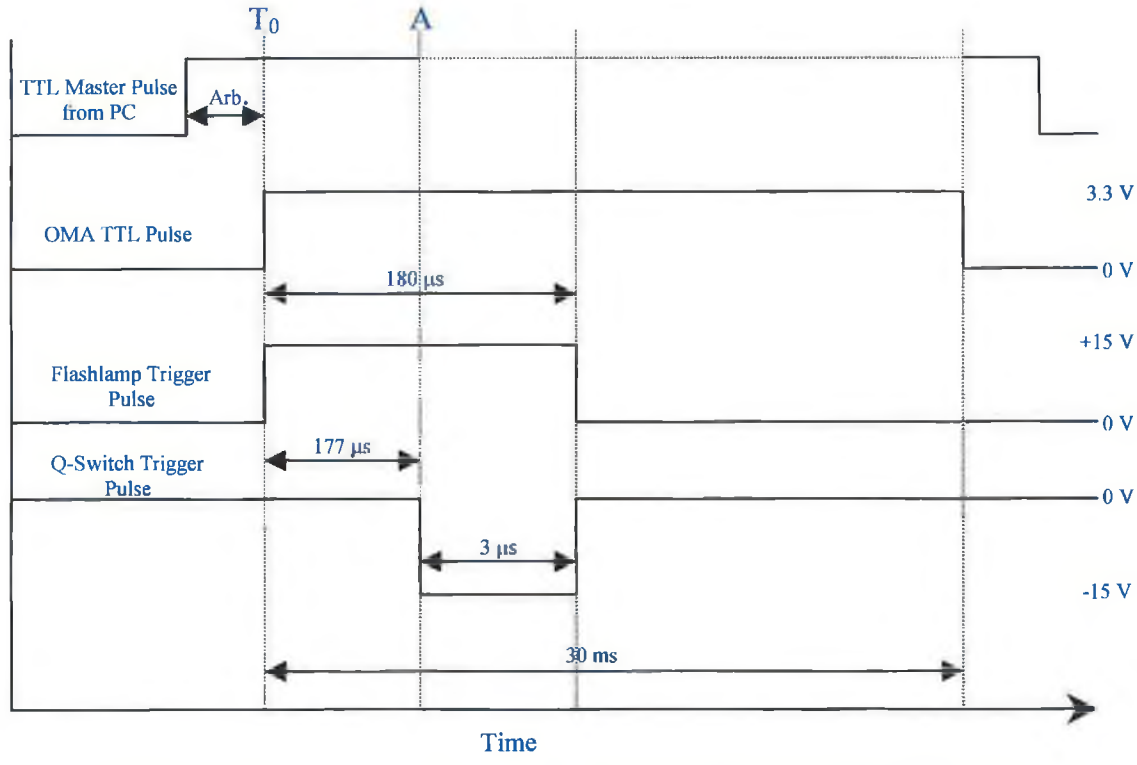

Fig. 3.21 Timing diagram used to synchronize firing the SL803 Nd:YAG laser with starting the integration period (exposure time) of the PDA detector.

When the OMA TTL pulse arrives, the delay generator instantly sends a pulse from T_0 to trigger the flashlamp of the SL803 laser. The Q-switch of the laser is then triggered by a pulse form channel A, which is appropriately delayed by 177 µs (at this time delay, the laser operation is optimum) with respect to T_0. The laser fires and the PDA integrates the light emitted from the plasma produced over the rest (30 ms–180µs) of the OMA TTL pulse. The resultant video signal is digitized via a 15-bit ADC and then sent to the PC for further acquisition and treatment of the spectral data.

CHAPTER IV

VUV Investigations of Laser-Induced Plasma Spectroscopy for the Quantitative Elemental Characterization of Steel Alloys: Preliminary Results

This chapter presents preliminary results obtained from the laser-induced plasma spectroscopy (LIPS) technique in the vacuum ultraviolet (VUV) for the quantitative determination of the carbon content in steel alloys. Six carbon spectral lines, representing different ionic stages and covering a wide spectral range in the VUV (40–160 nm), were employed in this work. The results obtained demonstrate that when combined with deep VUV spectroscopy to detect emission lines from ionic species, the time-integrated, space-resolved LIPS is a useful and effective technique, eliminating the need for more expensive time-gated detectors. Linear analytical calibration curves were constructed for the six carbon spectral lines under investigation in the concentration range 0.041–1.32%. A limit of detection of 87 ± 10 ppm (parts per million) was obtained from the C III 97.70 nm spectral line. Also, the CCD array is advantageous over the CEMA / PDA detector in terms of spectral resolution, relative intensity, as well as sensitivity of measurements.

4.1 Overview

For the first time, the analytical capability of laser-produced plasmas in combination with time-integrated, spatially-resolved emission spectroscopy (TISR-OES) in the vacuum ultraviolet (VUV) for the quantitative elemental characterization of standard reference steel alloys is investigated. Carbon was chosen as a test element since that the strongest emission spectra of carbon, as well as other low atomic number elements such as N, P and S, are often obtained from their ions and appear in the VUV region of the electromagnetic spectrum. In addition, many physical and mechanical properties of final steel products, such as stiffness and ductility, are strongly dependent on the total content of these light elements during all steel-making processes.

In this chapter, the advantages of using high-powered lasers as the excitation source combined with modern electronic detection of VUV radiation is demonstrated to compare the reliability of various ionic spectral lines of carbon content of solid steel samples in the 0.04–1.32% concentration range. The samples used, along with their corresponding iron as well as carbon concentrations are included in Appendix E.

4.2 Space-Resolved Spectroscopy

It is well known that the high-temperature, high-density core of a laser-produced plasma lying close to the target surface emits a strong background continuum stretching throughout the visible and VUV spectral regimes. For emission spectroscopic studies, therefore, it is essential that this continuum radiation is in some way screened out in order to maximize the contrast of the overlying spectral lines. Fortunately, a characteristic feature of the background continuum is that it lasts for a much shorter time than the spectral line emission. Accordingly, most studies on applications of laser-produced plasmas to the elemental charactrization of solid samples discriminate against this continuum emission by using time-gated detector technology to detect the spectral lines after decay of the strong background radiation [see 78–84, for example]. Nevertheless, this option is usually relatively expensive, is not easily extended to the VUV spectral range and its suitability depends on the relevant application and various experimental parameters and conditions [15, 198].

It is shown, in the present work, that an alternative and effective method of discriminating against the continuum emission is to exploit the space dependence of the laser-produced plasma emission (see Figs. 2.2 and 2.3 in chapter II). In the VUV regime, the very high level of background continuum is mostly emitted from a region of about 0–1 mm above the target surface, after which it starts a dramatic decrease permitting the overlying spectral line intensity of various species in the plasma to maximize. Table 4.1 provides details of the carbon spectral lines chosen in the present work together with their corresponding energy levels, transition probabilities and electronic configurations. Moreover, the partial energy level diagram for the various carbon ionic spectral lines under investigation is shown in Fig. 4.1.

Table 4.1 Wavelengths, ion stages, energy levels, transition probabilities, as well as electronic configurations for carbon spectral lines under investigation [from Kelly's tables, Ref. 233].

λ (nm)	Ion stage	Energy levels, lower–upper (eV)	Transition Probability (s^{-1})	Corresponding electronic configuration
(1) 45.96	III	6.503–33.477	1.06×10^{10}	$1s^2 2s2p\ ^3P_2$–$1s^2 2s3d\ ^3D_3$
(2) 68.73	II	0.0079–18.045	2.84×10^{9}	$1s^2 2s^2 2p^2 P_{3/2}$-$1s^2 2s^2 3d\ ^2D_{5/2}$
(3) 90.41	II	0.0079–13.721	3.42×10^{9}	$1s^2 2s^2 2p\ ^2P_{3/2}$-$1s^2 2s2p^2\ ^2P_{3/2}$
(4) 97.70	III	0.000–12.689	1.77×10^{9}	$1s^2 2s^2\ ^1S_0$-$1s^2 2s2p\ ^1P_1$
(5) 117.57	III	6.503–17.047	9.86×10^{8}	$1s^2 2s2p\ ^3P_2$-$1s^2 2p^2\ ^3P_2$
(6) 154.82	IV	0.000–8.01	2.65×10^{8}	$1s^2 2s\ ^2S_{1/2}$-$1s^2 2p\ ^2P_{3/2}$

To achieve this aim, a simple, inexpensive and effective method was applied in the present work. A fore-slit, of approximately 250 μm width and ~ 1.5 cm height, which was vertically mounted in the target chamber on the spectrometer side of the sample (see Fig. 3.1), provided the required spatial discrimination in the plasma viewed by the vertical spectrometer entrance slit. In this way, the emission was selected from a narrow 'slice' of the plasma parallel to the target surface (y-direction in Fig. 3.1). The fore-slit was positioned 40 mm from the plasma produced, so that only about 0.3 mm of the

plasma (x-direction in Fig. 3.1) was viewed by the spectrometer entrance slit. While the fore-slit was kept fixed in position on the optical axis of the spectrometer, different spatial regions of the plasma could be sequentially examined by carefully moving the backside target holder (Fig. 3.7) through its micrometer screw. In addition, the lens used to focus the laser beam onto the target surface was displaced in conjunction with the target in order to keep the focusing conditions constant.

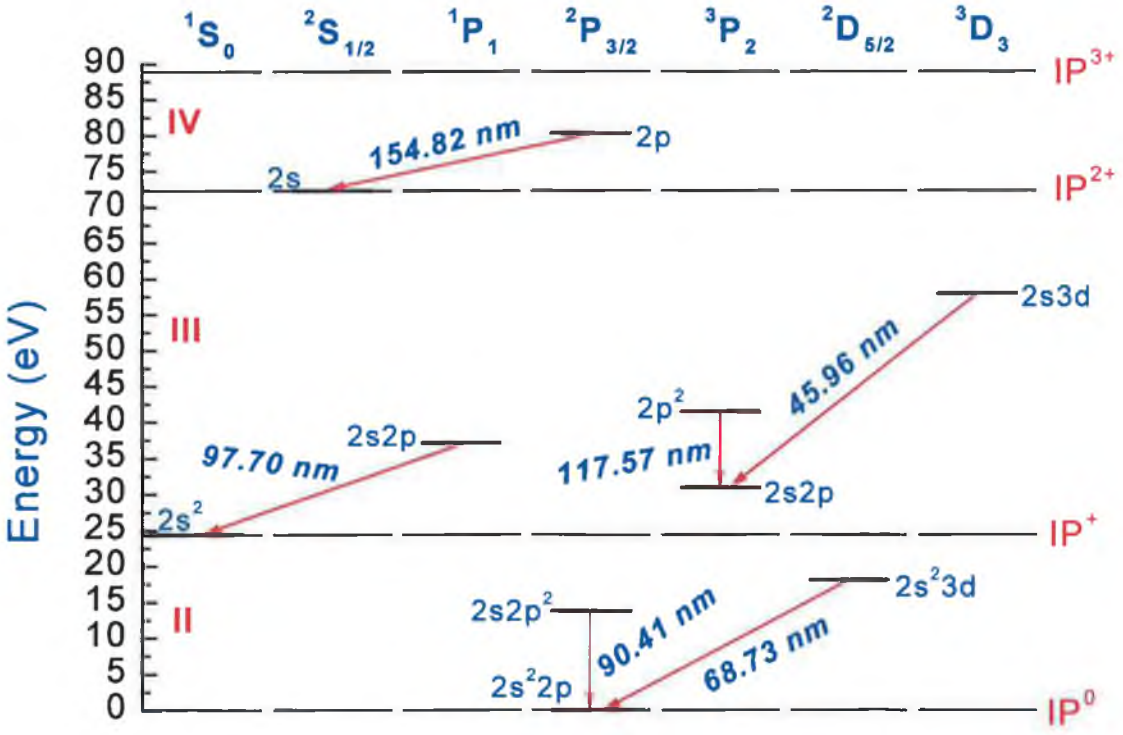

Fig. 4.1 Partial energy level diagram for different carbon spectral lines employed in this work. Note that energy values are measured with respect to the C II ground state $2s^22p$.

Figure 4.2 presents an example of laser-produced steel plasma emission spectra taken at different spatial distances from the target surface. The spectra shown in the figure were produced when the plasma emission was integrated after firing the laser 10 times (at 5 Hz repetition rate) onto the steel target that contains 0.91% carbon. The plano-convex spherical lens (125 mm focal length and 30 mm diameter) was used to focus the 850 mJ pulses of the SL803 Nd:YAG laser system described in the previous chapter (Fig. 3.1). The focusing lens was slightly defocused 0–5 mm behind the target surface. Figure 4.3 illustrates the dependence of the net line intensity for the C III 45.96 nm spectral line on

the displacement of the spherical lens from the best focus position with respect to the target surface. The best focus position was determined by displacing the lens a few millimetres from its nominated focal length in each direction, and measuring the diameter of the pit formed on the target surface for each case (average of 5 laser shots) by an optical microscope.

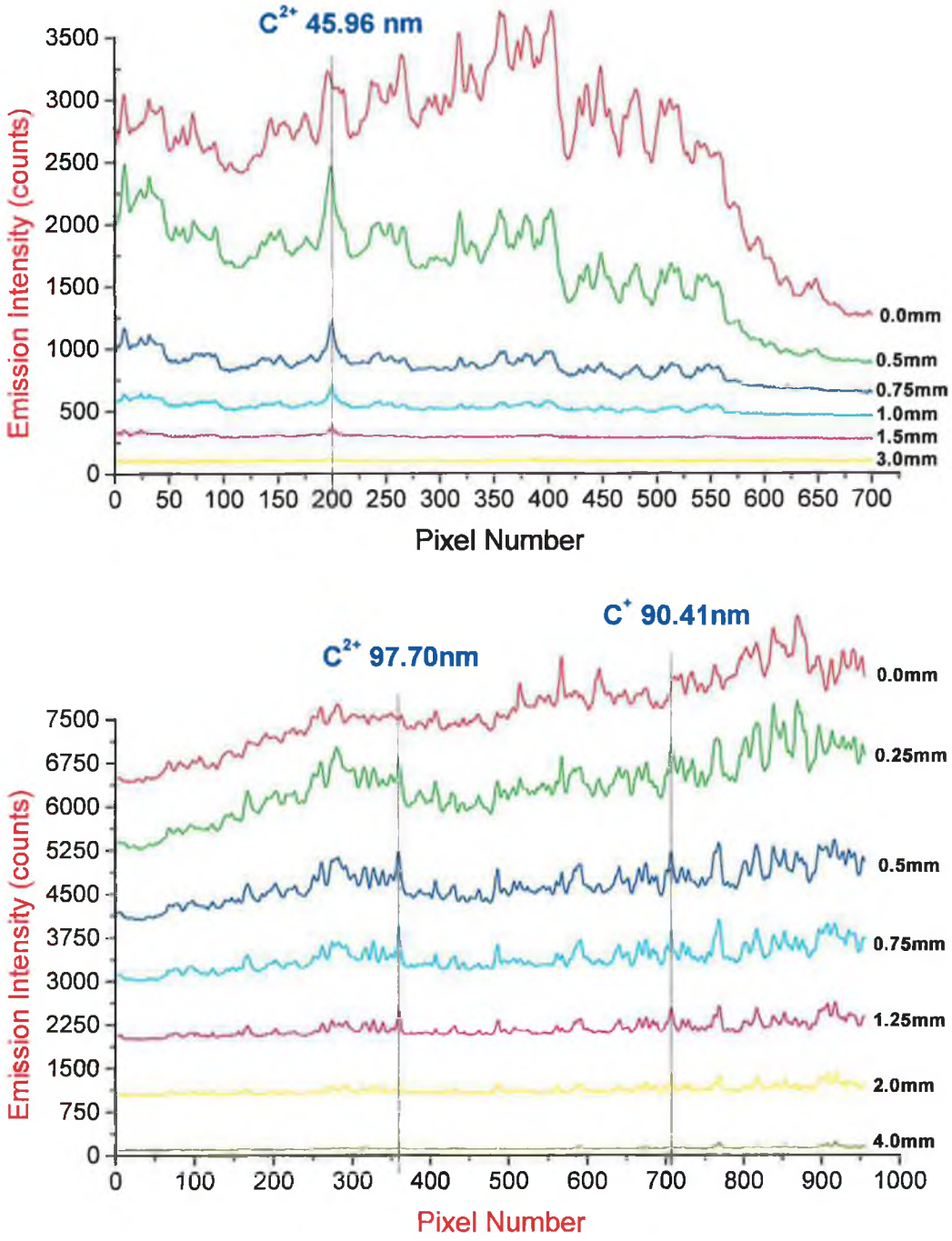

Fig. 4.2 Spatial evolution of the emission intensity for three carbon spectral lines at 45.96, 90.41 and 97.70 from laser-produced steel plasmas under investigation. For clarity purposes, all spectra shown were set to an offset of 75%. See text for more details.

As can be seen in Fig. 4.3 the highest 'net' spectral line intensity was obtained when the focusing lens was displaced from its best focus position up to a distance of 5 mm towards the target surface, i.e. the focus was located 0–5 mm behind the target surface. In addition, more stable and reproducible emission from the plasma was obtained when the lens was located at these positions, as demonstrated by the error bars in the figure. Note the dramatic decrease in the spectral line intensity for defocusing distances in the negative direction (away from the target surface) compared to a smooth decline on the other direction (towards the target surface). Similar results were obtained with the other spectral lines under study (Table 4.1). Lens displacements behind -7.5 mm results in a permanent damage of the lens due to reflections of laser radiation from the glass window of the target chamber. The results obtained from this simple experiment indicate that the focusing of the laser beam onto the sample surface is insensitive to the position of the focusing lens within approximately +5 mm from the best focus position, towards the target surface. The comparison between spherical and cylindrical lenses in focusing the laser beam will be studied in more details in the following chapter.

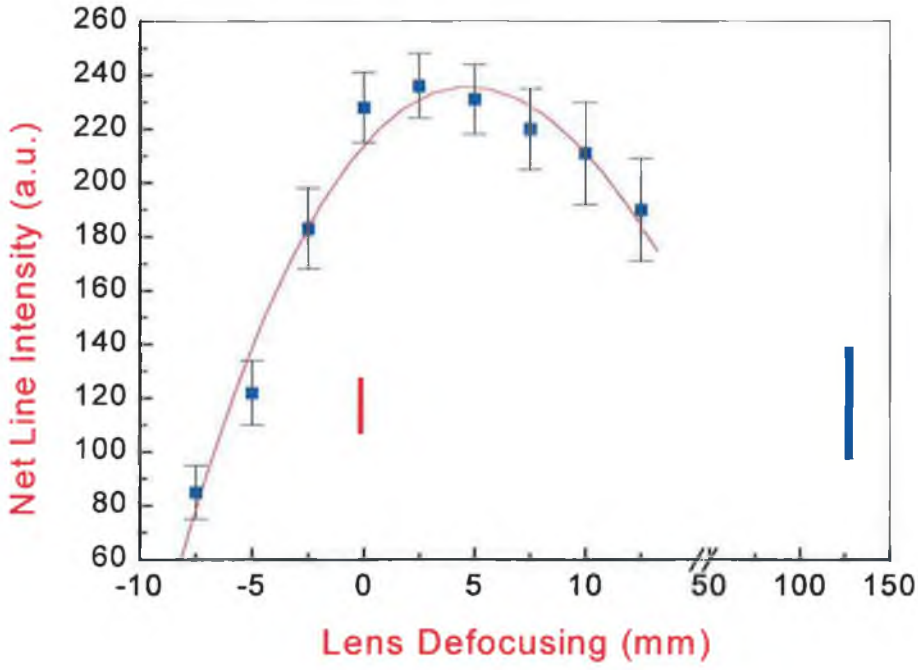

Fig. 4.3 Dependence of the net emission intensity for the C III 45.96 nm spectral line on defocusing the spherical lens (125 mm FL) used. The blue line represents the position of the best focus of the lens with respect to the location of the target surface (red line).

Now returning to Fig. 4.2, it can be seen that levels of the underlying continuum radiation are unacceptably high at axial distances less than 1 mm from the target surface. The best results are therefore obtained at 1–2 mm from the surface, where the background continuum is low and the spectral lines emitted are relatively strong and narrow, resulting in a significant enhancement of the spectral line-to-background intensity ratios. It is also evident from the figure that the intensities of these lines dramatically decrease at distances greater than about 2 mm above the target surface, due to the rapid expansion and cooling of the plasma and different recombination processes. At the +5 mm defocusing of the lens used, the diameter of the pit formed on the target surface was approximately 1 mm. Accordingly, the laser power density (irradiance) deposited on the target surface was about 5 GW/cm^2. The entrance slit width of the VM-521 vacuum spectrometer was set to 50 μm (~ 10 mm height) in all experiments carried out in this part. Also, the voltages of the MCP plate and MCP-phosphor gap were optimized for different spectral regions studied and set to 0.95 and 3 kV, respectively.

Laser-produced steel emission spectra obtained at an axial distance of 1.5 mm from the target surface for the six carbon spectral lines under investigation (Table 4.1) are shown in Figs. 4.4 and 4.5. All the spectra shown were produced when the instrumental function of the spectrometric system was deconvoluted from the raw spectra, resulting in spectral resolution of approximately 0.05 nm. This value was adequate for all spectral lines investigated in this part of the work; the six carbon lines shown in Figs. 4.4 and 4.5 proved to be spectral interference-free from neighbouring lines originating from other elements constituting the steel samples, particularly iron. In addition, these spectral lines were the most prominent among all carbon lines tested in the spectral range studied, i.e. 40–160 nm. Spectral lines originating from neutral carbon species were not observed in the plasmas generated, even at the farthest distance (~ 7 mm) from the target surface observed with the CEMA / PDA detection system.

All the spectra in Figs. 4.4 and 4.5 were obtained by integrating the emission produced by firing 20 consecutive laser shots at 5 Hz onto the target surface of the highest carbon concentration, i.e. 1.32%. Although further increasing the number of shots would improve somewhat the signal-to-noise ratios (SNRs) of the spectral lines, it was found that 20 shots produced an acceptable SNR while at the same time providing adequate reproducibility and data acquisition rates. The spectra recorded are dark subtracted and

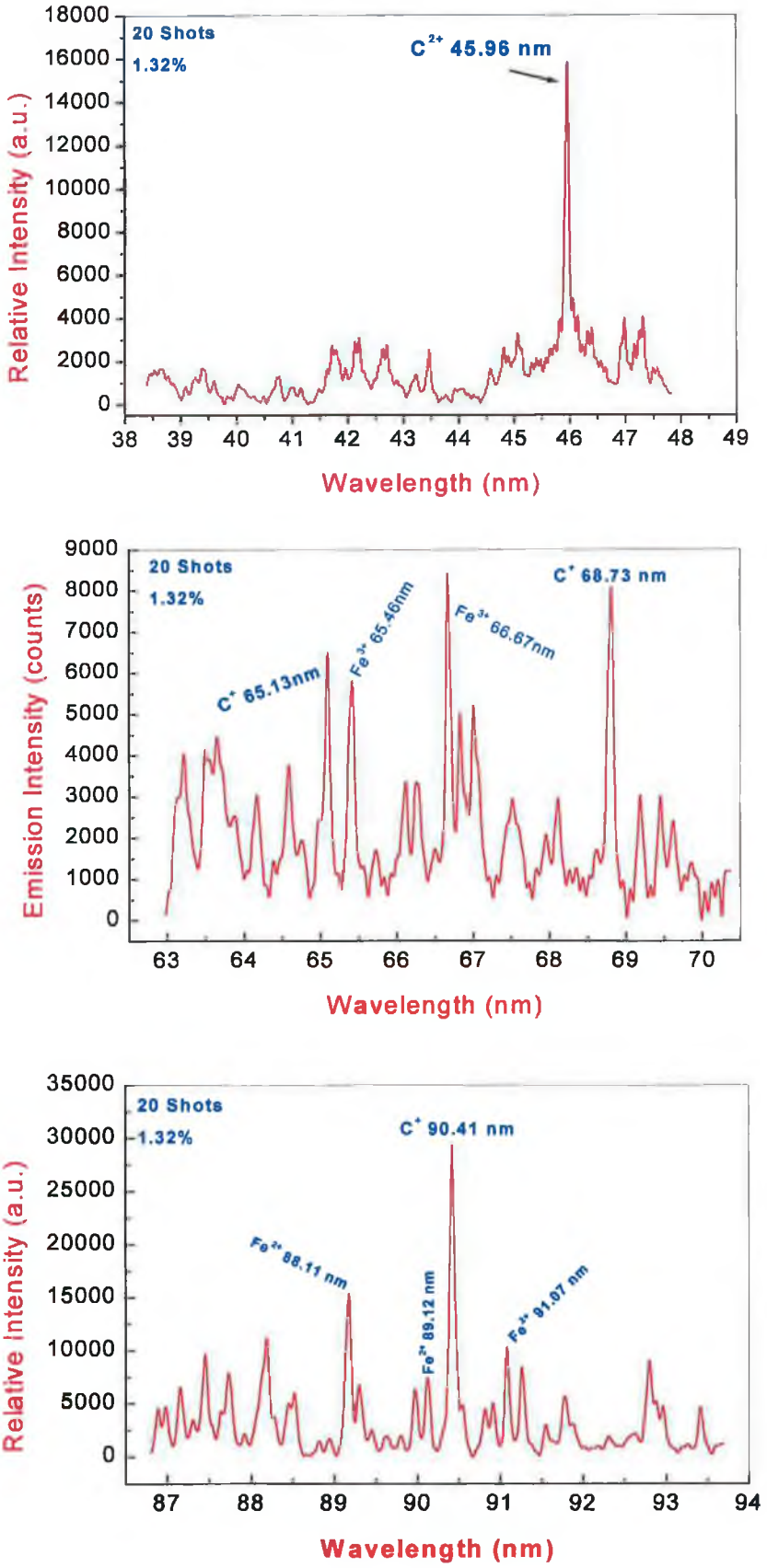

Fig. 4.4 Emission spectra obtained from laser-produced steel plasmas in the VUV. Shown also are the doubly- and singly-ionized carbon spectral lines at 45.96, 68.73 and 90.41 nm, respectively.

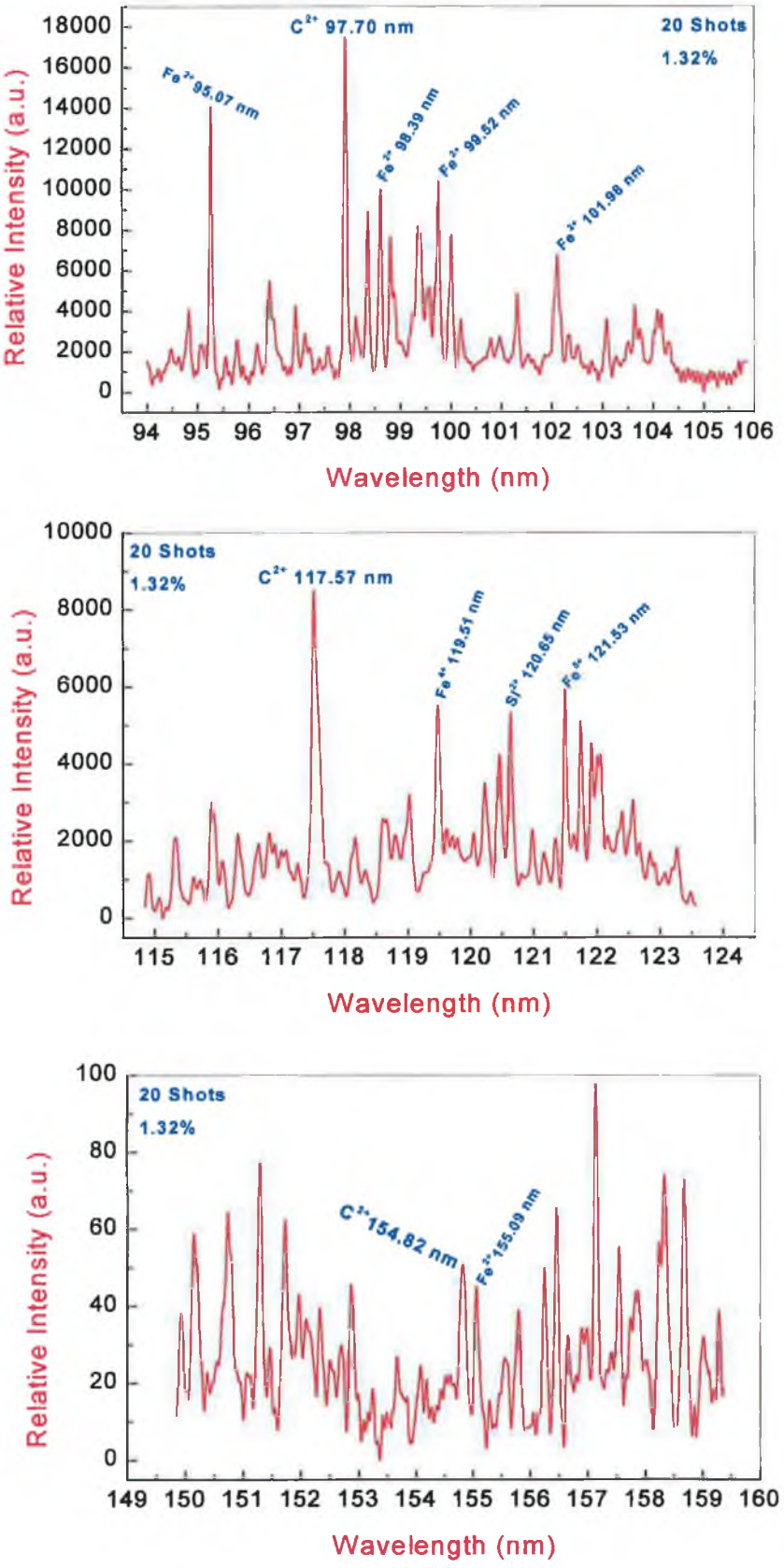

Fig. 4.5 Emission spectra obtained from laser-produced steel plasmas in the VUV. Shown also are the doubly- and trebly-ionized carbon spectral lines at 97.70, 117.57 and 154.82 nm, respectively.

background corrected. The background correction was carried out by subtracting the emission signal produced from an iron sample, containing a relatively very low carbon concentration of 0.001%, from that obtained with the other targets. In this way, again, any possible spectral line interference due to the presence of the major elemental constituent (Iron) in the target matrix was avoided.

Of the six selected spectral lines, the highest relative emission intensity was obtained with the C II 90.41 nm line, while the lowest was obtained with the C IV 154.82 nm line. The differences in the line intensities are due to a combination of several factors that may vary in relative magnitude, depending on the particular transition and ion stage. These include the relative population of each ion stage, the excitation and spontaneous decay rates for the different excited states, the grating efficiency at each wavelength (the present grating is blazed at 80nm) and the detector performance as a function of incident photon energy, i.e. its quantum efficiency (QE). The quantum efficiency of the CEMA detector used in the present work lies between 10 and 20% over the spectral region 20–180 nm, as stated in the previous chapter.

The most important result to be inferred from the spectra presented in Figs. 4.2, 4.4 and 4.5 is the effectiveness of the manner in which unwanted light contributions from other parts of the plasma can be blocked from reaching the spectrometer, enabling the use of a non time-gated detection system, while still maintaining discrimination against the background continuum emission.

4.3 Calibration Functions

In analytical spectroscopic applications, the degree to which the recorded spectral line intensity of the neutral or ionized species scales with the corresponding concentration of the parent atom is of primary importance. Figures 4.6 and 4.7 illustrate some examples of the increasing relative emission intensity with the carbon content for the spectral lines 45.96, 90.41 and 97.70 nm. Similar relationships were obtained with the other carbon spectral lines under investigation. Each spectrum was obtained by integrating the emission signal (at 1.5 mm from the target surface) from 20 laser shots as mentioned earlier. All of the spectra, obtained from different target concentrations, were taken in a random order to reduce the effect of any fluctuation in the laser energy.

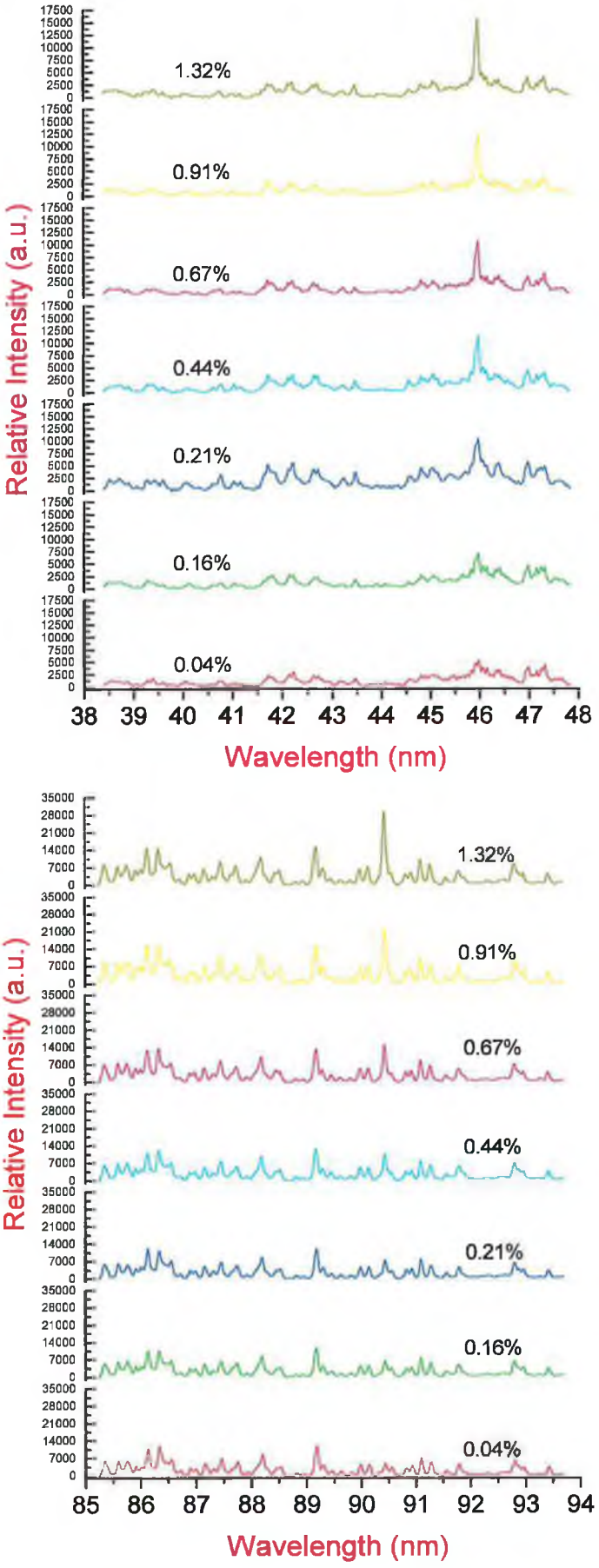

Fig 4.6 Variation of the relative line intensity for the C III 45.96 nm (A) and C II 90.41 nm (B) spectral lines with the carbon content in the samples under investigation. For more details see text.

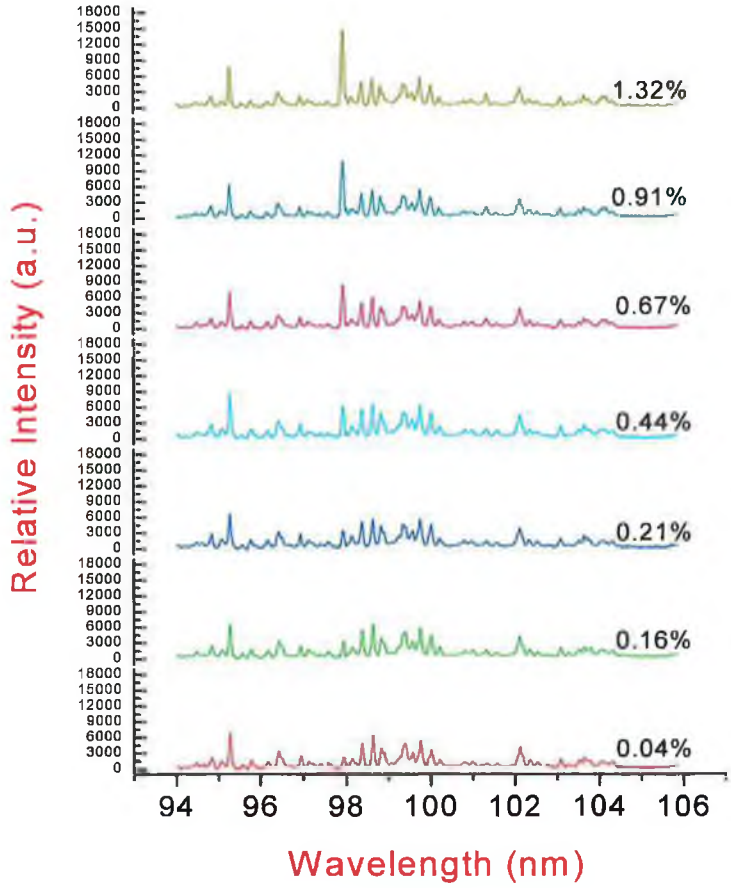

Fig 4.7 Variation of the relative line intensity for the C III 97.70 nm spectral line with the carbon content in the samples under investigation. For more details see text.

According to the spectra obtained in Figs. 4.6 and 4.7, analytical calibration curves (see § 2.5.2 in chapter II) can therefore be constructed between the relative emission intensities representing a relevant spectral line and their corresponding concentrations belonging to various samples under consideration. Figures 4.8 and 4.9 show the calibration curves obtained with the different carbon spectral lines under investigation (see Table 4.1). In all cases, linear calibration functions were obtained with correlation coefficients (R^2) between 0.994 (for the C II 68.73 nm line) and 0.999 (for the C III 97.70 nm line). Each calibration point in the graphs represents the average emission intensity obtained from plasmas produced by firing the laser 20 times at 5 Hz onto at least three different positions of each target surface, in order to eliminate the effect of possible non-homogeneity, if any, in the individual samples. The emission intensities were measured by integrating the area under the spectral line profiles obtained for each target. Care was taken to ensure constant experimental conditions for each calibration.

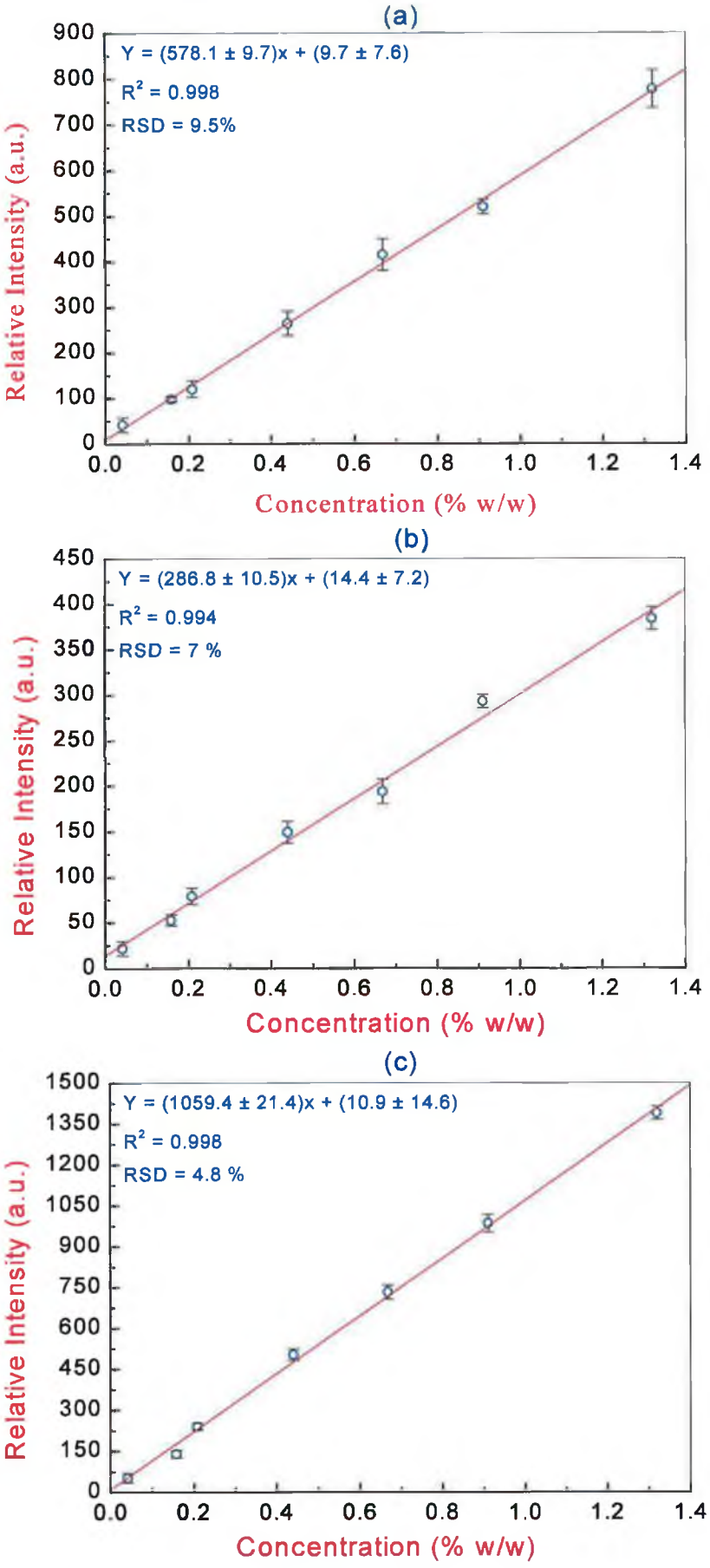

Fig. 4.8 Calibration curves for the C III 45.96 nm (a), C II 68.73 nm (b) and C II 90.41 nm spectral lines. See text for more details.

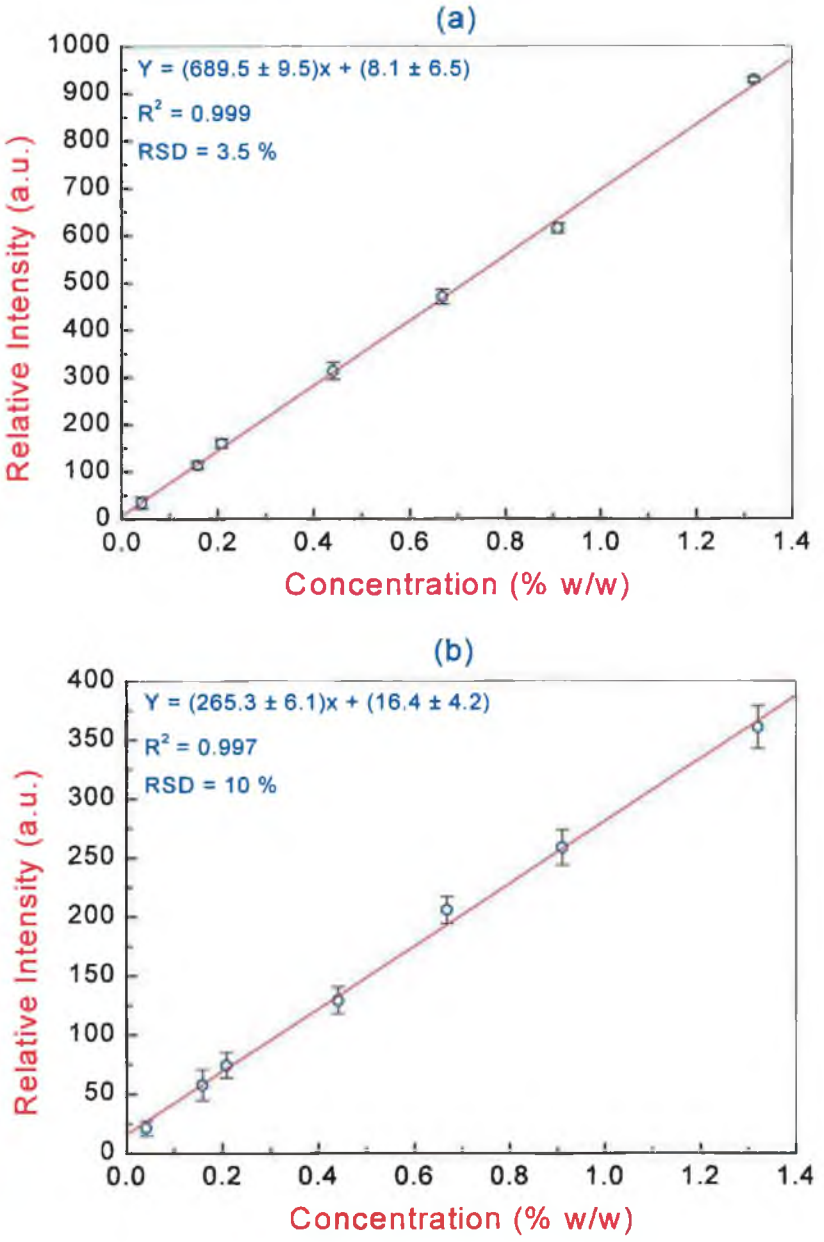

Fig. 4.9 Calibration curves for the C III 97.70 nm (a) and C III 117.57 nm (b) spectral lines. See text for more details.

It should be mentioned here that the analytical calibration curve for the C IV 154.82 nm spectral line could not be constructed due to the fact that the quantum efficiency of the CEMA detector is very low in this spectral region compared to the other spectral regions studied. This was confirmed in Fig. 4.5 in which the relative emission intensity of this line, obtained from the target containing the highest carbon concentration (1.32%), was very low compared to those produced from the other spectral lines at the same carbon concentration. Also note the relatively high noise and background levels at the position of the spectral line, which will definitely prevent proper intensity measurements for lower carbon concentrations.

Of the five spectral lines shown in Figs. 4.8 and 4.9, the C II 90.41 nm, C III 97.70 nm, and C III 45.96 nm spectral lines have the highest SNRs (the noise signal is represented here by the intercept with the intensity axis). Also, the calibration curves for these lines have the best fitting functions (correlation coefficients) and the highest slopes, hence the best sensitivities. Moreover, the standard errors in the 'noise' signal for these lines are relatively high. Accordingly, the three mentioned spectral lines should demonstrate the best limits of detection among all lines studied. In conclusion, these three lines are the best carbon lines to use when carrying out elemental characterization of metals and alloys in the VUV region, providing that they are interference-free with respect to neighbouring spectral lines of elements constituting the corresponding matrix.

As indicated by the individual error bars in Figs. 4.8 and 4.9, determined from the spread of the three measurements for each concentration, the overall precision (relative standard deviation or RSD) of intensity measurements (concentration determination) from different samples under investigation was between 3.5% for the C III 97.70 nm spectral line and 10% for the C III 117.57 nm spectral line. Despite the relatively modest precision of some calibration points in some figures, the overall precision and correlation coefficients of the corresponding spectral lines are quite satisfactory.

4.4 Limits of Detection

The relative limit of detection (c_L) for an element in a composite matrix is an extremely important figure of merit for any analytical technique. It is basically defined as the smallest concentration of the relevant element that can be detected by an analytical technique, with a certain level of confidence. It is also a characteristic quantity that can be used for comparing the power of detection of two techniques for a particular element, or the power of detection of one and the same technique for different elements.

At a very low concentration of an element, it becomes uncertain whether an observed value of the spectral emission intensity is due to the presence of that element in the corresponding sample or to an uncontrolled chance of perturbation, which is often termed analytical noise. In practice, the magnitude of these statistical fluctuations can be found by making a sufficiently large number of background measurements (in the neighbourhood of the spectral line) from which the average and standard deviation

values can be calculated. On the other hand, the analytical signal, in order to be accepted as valid, must amount to a multiple (k) of the standard deviation of the background signal. Therefore, the spectral emission intensity (I_x) that corresponds to the limit of detection of an element is the product of the factor (k) and the standard deviation of the background measurements [234]:

$$I_x = k\sigma(I_b) \qquad [4.1]$$

where I_b is the intensity of the background emission and $\sigma(I_b)$ is the standard deviation of measurements of the background intensity. The carbon limits of detection measured in the present work for the five spectral lines under investigation are shown in Table 4.2. These values were determined from the well-known expression [234]:

$$c_L = 3\left(\frac{\sigma(I_b)}{S}\right) \qquad [4.2]$$

where S is the slope of the analytical calibration curve for each relevant spectral line. The number '3' in equation 4.2 was chosen to correspond to the desired level of confidence as mentioned earlier; other values such as $2\sqrt{2}$ and $3\sqrt{2}$ are also acceptable [234].

Table 4.2 Limits of detection for the five spectral lines used. ppm is an abbreviation for the term parts per million; alternatively, the term μg/g (microgram per gram) is sometimes used.

Spectral line (nm)	Limit of detection (ppm)
CIII 45.96	148 ± 19
CII 68.73	208 ± 28
CII 90.41	130 ± 12
CIII 97.70	87 ± 10
CIII 117.57	154 ± 31

As the table indicates, the limits of detection obtained for the different spectral lines range from values between 87 ppm for the C III 97.70 nm line and 208 ppm for the C II 68.73 nm line. As might be expected, and as mentioned in the previous section, the best limits of detection were obtained from the spectral lines with the steepest slope of the calibration curves shown in the previous section (see Figs. 4.8 and 4.9). These lines are the C III 97.70 nm, C II 90.41 nm and C III 45.96 nm. The corresponding detection limits were 87 ± 10, 130 ± 12 and 148 ± 19 ppm, respectively. Generally speaking, the doubly-ionized spectral lines have lower (better) limits of detection in comparison with those obtained from singly-ionized carbon lines. The only exception is the C II 90.41 nm line, since that the background continuum in this spectral region is very low and the emission intensity of this line is relatively high (see Fig. 4.4).

The lowest detection limit of 87 ppm obtained from the C III 97.70 nm spectral line (compared to 100 ppm obtained by Balloffet and Romand [199] from the same spectral line, using the sliding vacuum spark source) indicates that this line is the most sensitive carbon line in the VUV region, and therefore is the most suitable for performing quantitative composition analyses of metals and alloys for their carbon content. Carrying out detailed optimization studies on different experimental parameters (see the next chapter) and using a charge-coupled device (CCD) detector (see the next section) should further improve the detection limit achieved in this part of the work.

4.5 Accuracy of Measurements

Generally speaking, the accuracy of any measuring or analytical technique is defined as the percentage differences between the experimental and actual values. For analytical spectroscopic applications, including the LIPS technique, there are a number of methods to characterize the accuracy of determining an element's content in a sample provided by the calibrated technique. The most common, and indeed simplest, way to access the accuracy is to calculate the residual error between values obtained from the analytical calibration curve and the actual values. From the linear regression fit formula obtained for each calibration curve in Figs. 4.8 and 4.9, the percentage carbon content was 'back' calculated from the experimental data. The results are shown in Table 4.3 together with the magnitude of the error for each value for the C III 97.70 nm spectral line, as an example.

As can be inferred from the table, the overall average accuracy of the LIPS data for determination of carbon in the steel samples under consideration is approximately 5%. The relatively large error (~ 22%) of determining the concentration from the target having 0.041% carbon is likely due to the poor precision in the intensity measurements at this low concentration (see Fig. 4.8).

Table 4.3 Calculated carbon concentrations (wt%) for the C III 97.70 nm spectral line. The ± standard deviations of the certified concentrations in the first column were taken from the manufacturers' certificate.

Certified % carbon	Calculated % carbon	Magnitude error
0.041 ± 0.0011	0.032	-0.009
0.158 ± 0.0043	0.150	-0.008
0.208 ± 0.0036	0.219	+0.011
0.44 ± 0.0062	0.448	+0.008
0.668 ± 0.0052	0.682	+0.014
0.91 ± 0.0033	0.89	-0.018
1.32 ± 0.0015	1.322	+0.002

4.6 Comparison between CEMA / PDA and CCD Detectors

In this section, a comparison between the performance of CEMA / PDA and CCD detectors in the VUV is carried out. The CEMA / PDA detector combination, as well as the Photometrics™ CCD array were fully described in the previous chapter (§ 3.4.3), therefore only the results obtained from this study are presented here.

With the CEMA / PDA detector in position, the best spectral resolution was ~ 0.1 nm at 100 nm (maximum $\lambda / \Delta\lambda \cong 1000$). Through deconvolution of the instrumental function from the raw spectrum, this figure was improved to better than 0.05 nm. The results are shown in Fig. 4.10, with the C III 45.96 nm spectral line taken as an example. As can be seen from the figure, the resolution as well as the emission intensity of the spectral line

is significantly improved by the deconvolution procedure. Figure 4.10(c) shows the

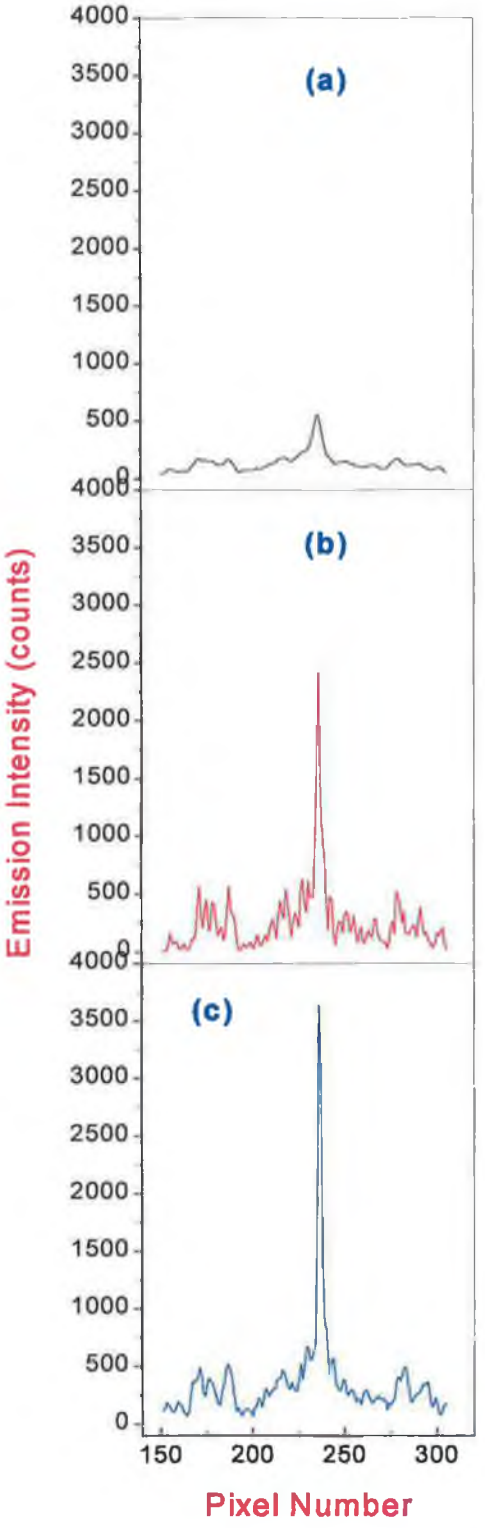

Fig 4.10 Spectral performance comparison between the CCD and CEMA / PDA detector systems for the C III 45.96 nm spectral line under the same experimental conditions. (a) CEMA / PDA raw spectrum; (b) CEMA / PDA deconvoluted spectrum and (c) CCD spectrum.

spectrum obtained under exactly the same experimental conditions, when the CEMA / PDA detector system was replaced by the CCD array. The spectral resolution produced directly by the CCD detector compares very favourably with that obtained from the deconvoluted spectrum of the CEMA / PDA combination. In addition, the signal-to-noise ratio (SNR) in case of the CCD is significantly better.

A further advantage of the CCD array proved to be its sensitivity. Figure 4.10(c) shows that the emission counts (from the same number of laser shots, and under similar other conditions) for the C III 45.96 nm spectral line with the CCD detector was significantly higher than that recorded with the CEMA / PDA system at the maximum operating voltages of 950 / 3000 V. Another example of the superior sensitivity of the CCD array is illustrated in Fig. 4.11. The emission intensity, signal-to-background ratio, as well as signal-to-noise ratio for the C IV 154.82 nm spectral line (recorded from only 10 laser shots) were all significantly better than those obtained with the CEMA / PDA detector (see Fig. 4.5). This allowed the construction of the analytical calibration curve for this spectral line down to the lowest carbon concentration used here, i.e. 0.041%, which was not possible with the CEMA / PDA as mentioned earlier; Fig. 4.12 provides this calibration curve using the CCD detector.

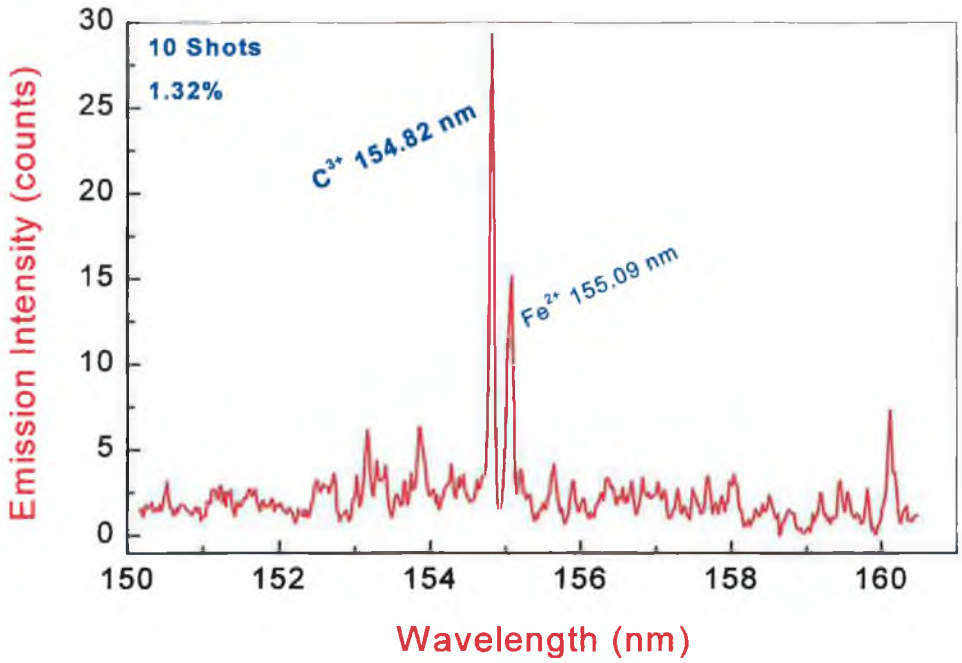

Fig. 4.11 Laser-produced steel plasma emission spectrum showing the superior sensitivity of the CCD array compared to that of the CEMA / PDA for the C IV 154.82 nm spectral line.

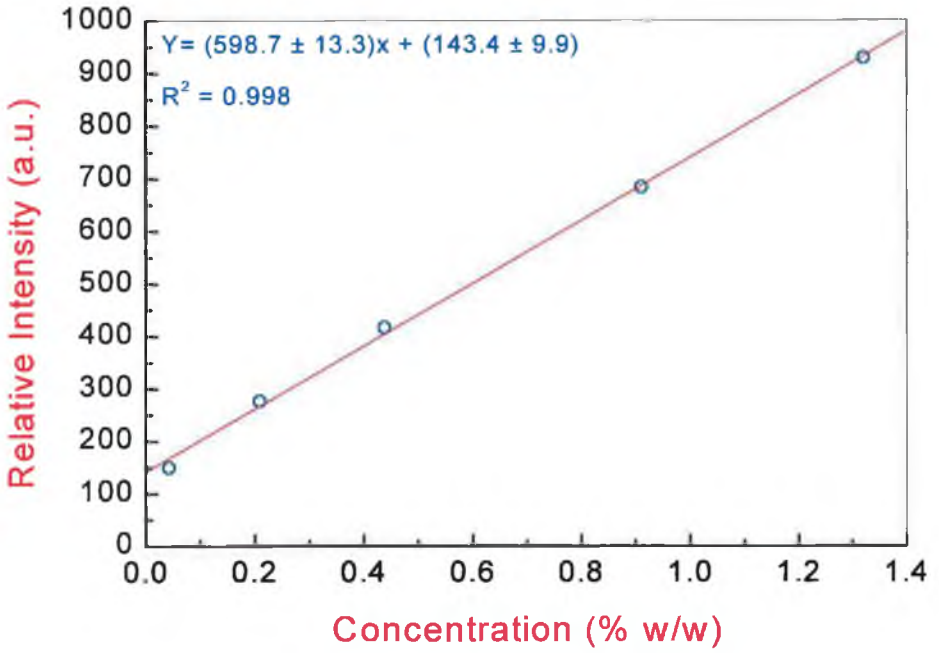

Fig. 4.12 Analytical calibration curve for the C IV 154.82 nm spectral line using the CCD array. No background correction was applied to the calibration points. 20 laser shots were used to integrate the emission intensity for each concentration.

The advantages of the CCD array of better spectral resolution and sensitivity are important particularly when measurements of low carbon concentrations are considered. Deconvolution procedures can introduce uncertainties into data, through amplification of high spatial frequency components in the spectral image, with a concomitant deleterious effect on the signal-to-noise ratio.

A notable advantage of the spatially resolved approach to discriminating against the background continuum emission is that it allows the replacement of the CEMA / PDA combination array with the CCD detector. This option would not have been possible if the spectral measurements were relying on temporal resolution due to the fact that it is difficult (and indeed expensive) to achieve high temporal resolution, combined with Nyquist limited spatial resolution, with a CCD array in the VUV region (30–160 nm).

Figure 4.13 illustrates calibration curves obtained with both detectors under comparison for the C III 97.70 nm spectral line. Each calibration point represents the average of 20 laser shots onto at least three different positions of each target surface, and in a random

order. As before, the relative emission intensities were measured by integrating the area under the spectral line profile.

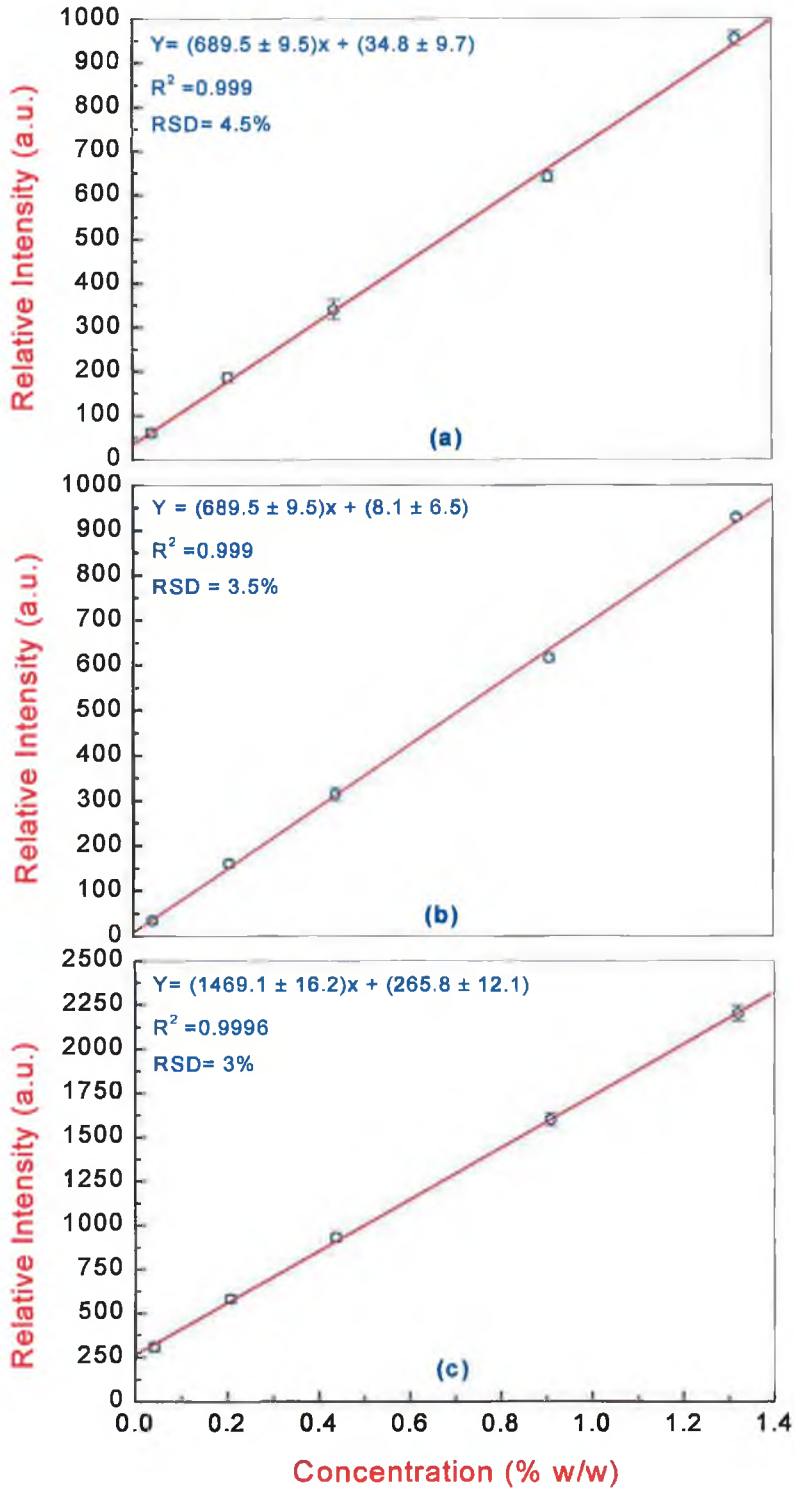

Fig. 4.13 Calibration curves comparison for the C III 97.70 nm spectral line. (a) CEMA / PDA without background correction; (b) CEMA / PDA with background correction and (c) CCD without background correction. See text for more details.

Figures 4.13(a) and 4.13(b) show the calibration curves obtained with the CEMA / PDA detector before and after background correction, respectively. On the other hand, background correction was not applied to the CCD data. As can be seen from the figure, linear curves with correlation coefficients not less than 0.999 were obtained in all three situations. For the CEMA / PDA detector, the slopes of both calibration curves, as expected, are the same. The calibration curve obtained with the CCD demonstrates a significantly higher slope than that obtained with the CEMA / PDA, again suggesting that a lower limit of detection can be expected with the former detector. Furthermore, the relative standard deviation (RSD) of the CCD results is lower indicating a higher level of precision in the data.

To summarize, the results obtained in this section showed that the CCD array affords significant advantages in terms of spectral resolution, relative intensity, as well as sensitivity compared to the more common CEMA / PDA detector system. On the basis of these results, detailed optimization procedures for different experimental parameters and conditions using the CCD detector is needed in order to further improve the detection sensitivity of the LIPS technique obtained in this chapter. This will be the subject of the next chapter.

CHAPTER V

VUV Optimization of Experimental Parameters and Conditions for Laser-Produced Steel Plasmas: Analytical Results

This chapter represents the main bulk of the present work. Several experimental parameters including the laser focusing lens types (spherical versus cylindrical) and conditions, laser power density, various ambient atmospheres (air, argon and helium) and pressures, laser harmonics, laser energy, spatial distribution of emitting species in the plasma, as well as entrance slit-width of the spectrometer used are all investigated and optimized. The optimum values of these parameters are then used to construct analytical calibration curves for the C III 97.70 nm spectral line. This spectral line has proved to be the best among other VUV carbon spectral lines selected in terms of sensitivity, as well as reproducibility. Then, the performance characteristics of the LIPS technique developed in this work including limits of detection and precision are determined and compared to those obtained in previous works.

5.1 Introduction

In the previous chapter, it was demonstrated that time-integrated, space-resolved laser-induced plasma spectroscopy (TISR-LIPS) technique developed for the first time in our laboratory, in conjunction with vacuum ultraviolet spectroscopy is a useful, relatively easy-to-use and effective technique for the quantitative elemental characterization of steel alloys. It was shown that by using simple spatial resolved measures to sample the emitted radiation from further out regions of the laser-produced plasmas under investigation, it is possible to enhance the spectral line contrast with respect to the very high levels of background continuum emitted from regions very close to the target surface (~ 0–1 mm). Six ionic spectral lines of carbon, representing three ionization stages (II, III, and IV) and covering a relatively wide wavelength range from 40 nm to 160 nm, were employed. Linear calibration curves, with coefficients of deviation (COD) better than 0.994, were constructed and a detection limit of 87 (± 10) μg/g was obtained from the C III 97.70 nm spectral line. These preliminary results were obtained using a series of standard calibrated samples of relatively high carbon concentrations, and a channel electron multiplier array / photodiode array (CEMA / PDA) detection system.

It is a well-known fact that the interaction of pulsed, high-powered lasers with solid materials and the subsequent generation of optically induced plasmas are complex processes [62, 97]. The spectral emission characteristics of these plasmas are greatly influenced by a number of experimental conditions and parameters [8–9, 41–49, 50–61]. In the present chapter, the CEMA / PDA detector is replaced by a modern, VUV-sensitive, backside-illuminated CCD array (Andor Technology™) and a series of optimization studies on several experimental parameters and conditions are performed. The influence of the focusing lens types and conditions, laser energy and power density, laser harmonics, ambient atmospheres and pressures, calibration method and spatial position of emitting species on the plasma emission characteristics are studied and discussed. The objective of this work was to further increase the sensitivity of the VUV-based, LIPS technique previously developed in the last chapter. The results obtained in this chapter should demonstrate a typical set of optimum conditions for the maximum emission intensity and signal-to-background ratio obtained from laser produced-plasmas for the direct quantitative determination of light elements in the VUV spectral region.

5.2 Optimization of Laser Beam Focusing Conditions

The objectives of this part of the work were to optimize the choice of lens type, and to measure the different carbon ionic spectral lines signal-to-background ratios as functions of the laser beam focusing conditions. The Q-switched laser used (Continuum, Model Surelite III–10) was working at its fundamental wavelength only (1064 nm), and produced a typical pulse energy of ~ 800 mJ in 5–7 ns duration. For the results reported in this part, the fore-slit, mounted within the target chamber to provide the required spatial discrimination in the plasma, was located so that a plasma region 2 mm from the sample surface (see Fig. 3.2) was observed by the spectrometer. The steel plasmas were created in an aluminium cube chamber under vacuum environment (~ 2×10^{-5} mbar). Except when otherwise stated, 20 laser shots (10 additional pre-shots were used for cleaning the target surface) were used to produce the recorded emission spectra. The 'vertical' entrance slit-width of the spectrometer was fixed at 50 μm; this value provided a compromise in terms of both spectral intensity and resolution. For all the experiments reported in this chapter, vertical binning (1 pixel × 1 column) of the CCD pixels was used in order to integrate along the spectrum line heights. Other experimental conditions are kept as mentioned before in chapter III.

Both plano-convex spherical and cylindrical lenses, with nominal focal lengths of 125 mm and 150 mm (PK7 glass type), respectively, were used in turn to focus the laser beam onto the surface of the relevant steel target. As mentioned in chapter III, the focusing lens was mounted on a translation stage in order to precisely change the lens-to-sample distance (LTSD) and so the focused spot size of the laser beam on the steel sample. Figure 5.1 illustrates the dependence of the dimensions of the craters formed onto the target surface on the lens defocusing distance for both lens types. The latter parameter is defined as the axial distance displaced by the lens from its best focusing position towards (or away from) the target surface. As expected, a linear relationship between the crater diameter formed by the spherical lens, or the crater width in case of the cylindrical lens, and the lens defocusing distance was obtained in each case. Also shown in Fig. 5.1 is the variation in the laser power density deposited on the target surface as a function of the lens defocusing distance for each lens type. The power densities were estimated in terms of the measured laser pulse energy, pulse duration and

the dimensions of the laser beam-induced craters on the target surface (using an optical

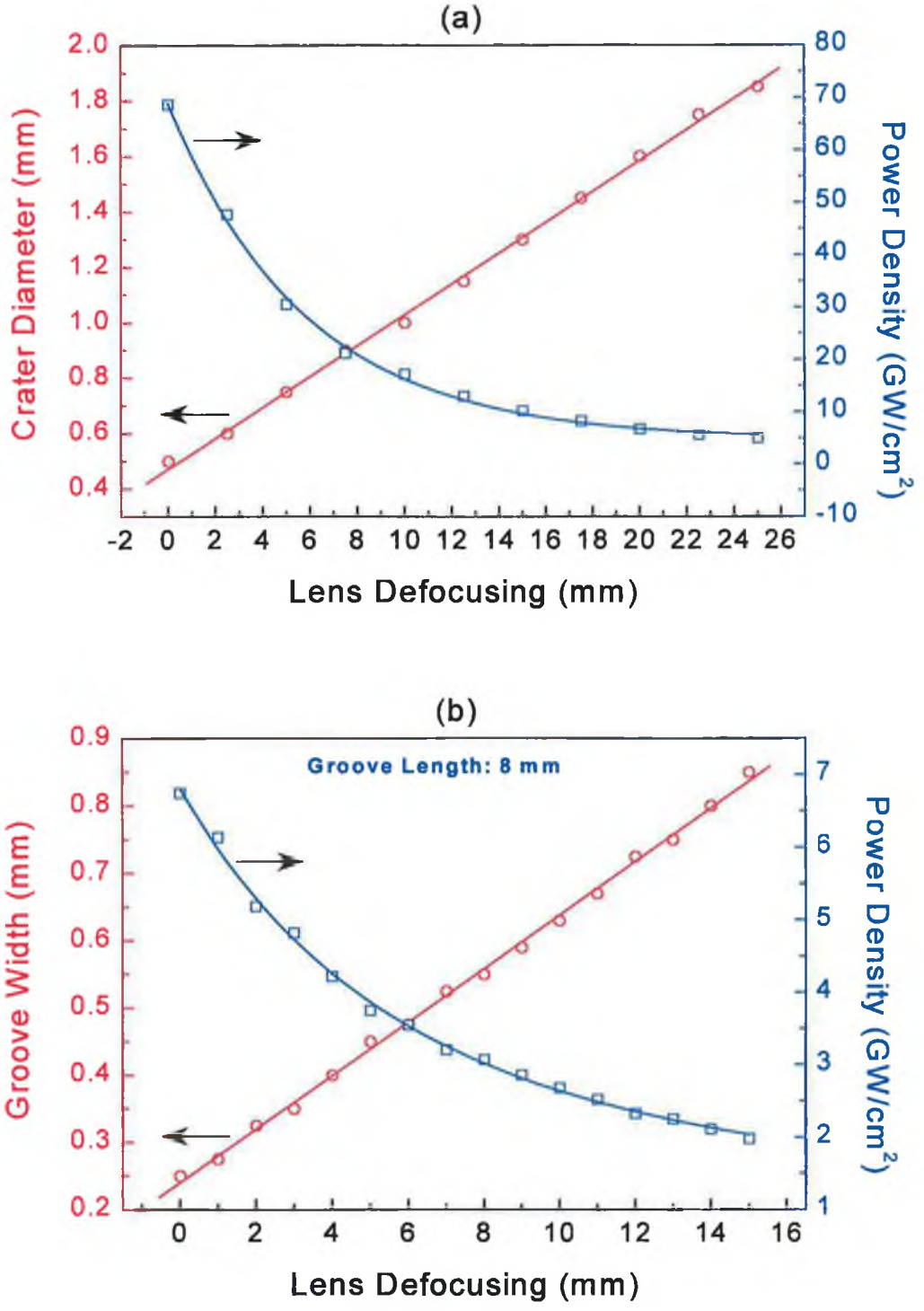

Fig. 5.1 Craters diameters and widths (red curves), as well as laser power densities (blue curves) as functions of lens defocusing distances for (a) spherical and (b) cylindrical lenses.

microscope). Since the incident laser beam was properly aligned with respect to the target surface, it is expected to obtain similar power density values to those shown in Fig. 5.1 if the lens was displaced in the opposite direction, i.e. away from the target surface.

In the case of the spherical lens, the laser pulse created circle-like craters of the target surface. Diameters of the craters formed varied from ~ 0.5 mm, corresponding to a highest power density of about 70 GW/cm^2 to ~ 2 mm, corresponding to an irradiance of approximately 5 GW/cm^2. Figure 5.2 shows the influence of varying the spherical lens defocusing distance on both the relative emission intensity, as well as the signal-to-background ratio for the C II 90.41 nm, C III 97.70 nm and C IV 154.82 nm spectral lines. Selection of these spectral lines for display in Fig. 5.2 was based on the fact that they represent three different ionization stages (II, III and IV), so that the behaviour of their emission characteristics in the plasma should provide useful information to be

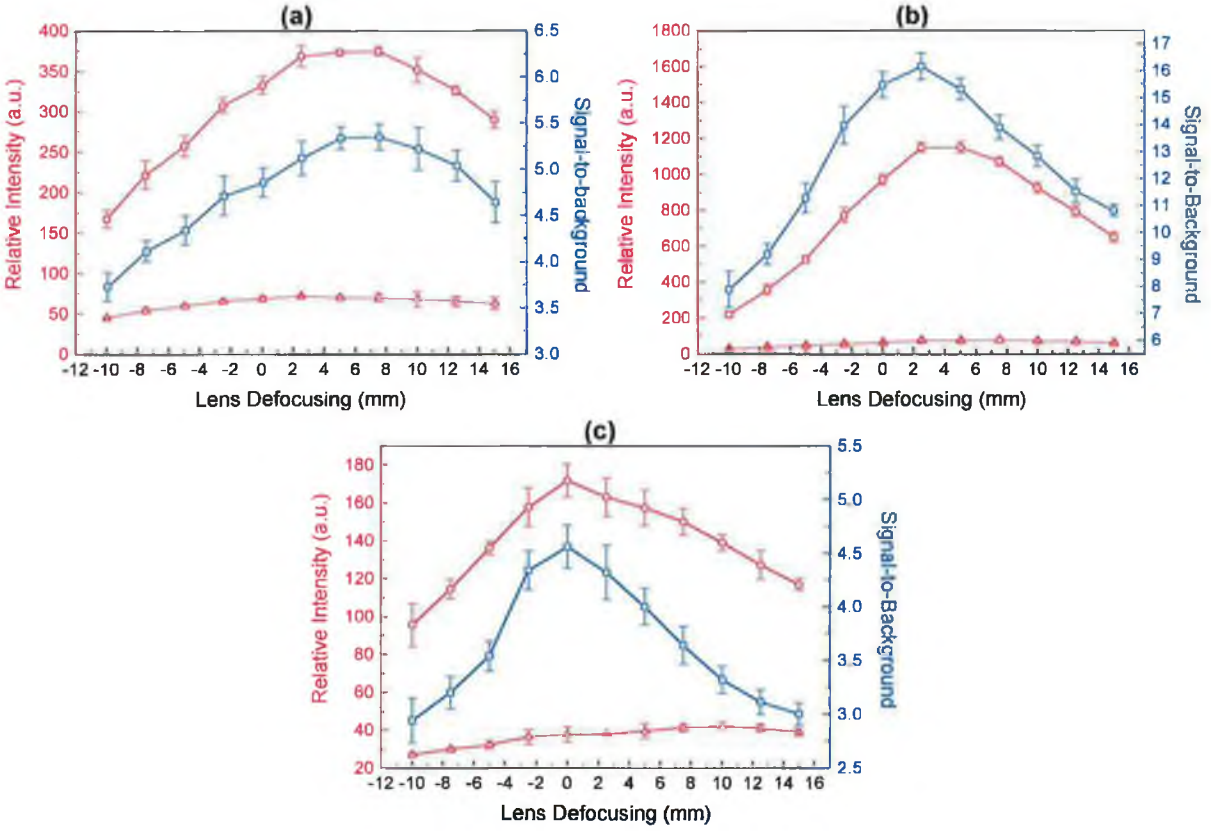

Fig. 5.2 Influence of the spherical lens defocusing distance on the emission intensity (spectral line intensity (O); background intensity (Δ)); as well as signal-to-background ratio (□) for the C II 90.41 nm (a), C III 97.70 nm (b) and C IV 154.82 nm (c) spectral lines.

drawn for similar ion stages under the same operating conditions. The plano-convex spherical lens was moved from its best focus position (determined by the smallest crater size formed on the surface of the target from a few laser shots) either towards the target surface or away from it, thus decreasing the laser power density deposited onto the target, with approximately the same amount in either direction (see Fig. 5.1). For each spectral line illustrated in Fig. 5.2, the target surface was positioned in such a way to provide the highest signal-to-background ratios for these lines when the lens was placed at its nominal focal length (125 mm). In other words, VUV radiation emitted from regions in the plasma located 2.25 mm, 3 mm and 2 mm from the target surface were selected in turn to be viewed by the spectrometer for the C II 90.41 nm, C III 97.70 nm and C IV 154.82 nm spectral lines, respectively. Finally, all data shown in Fig. 5.2 were produced by accumulating light from plasmas formed by 10 (10 pre-shots for cleaning)

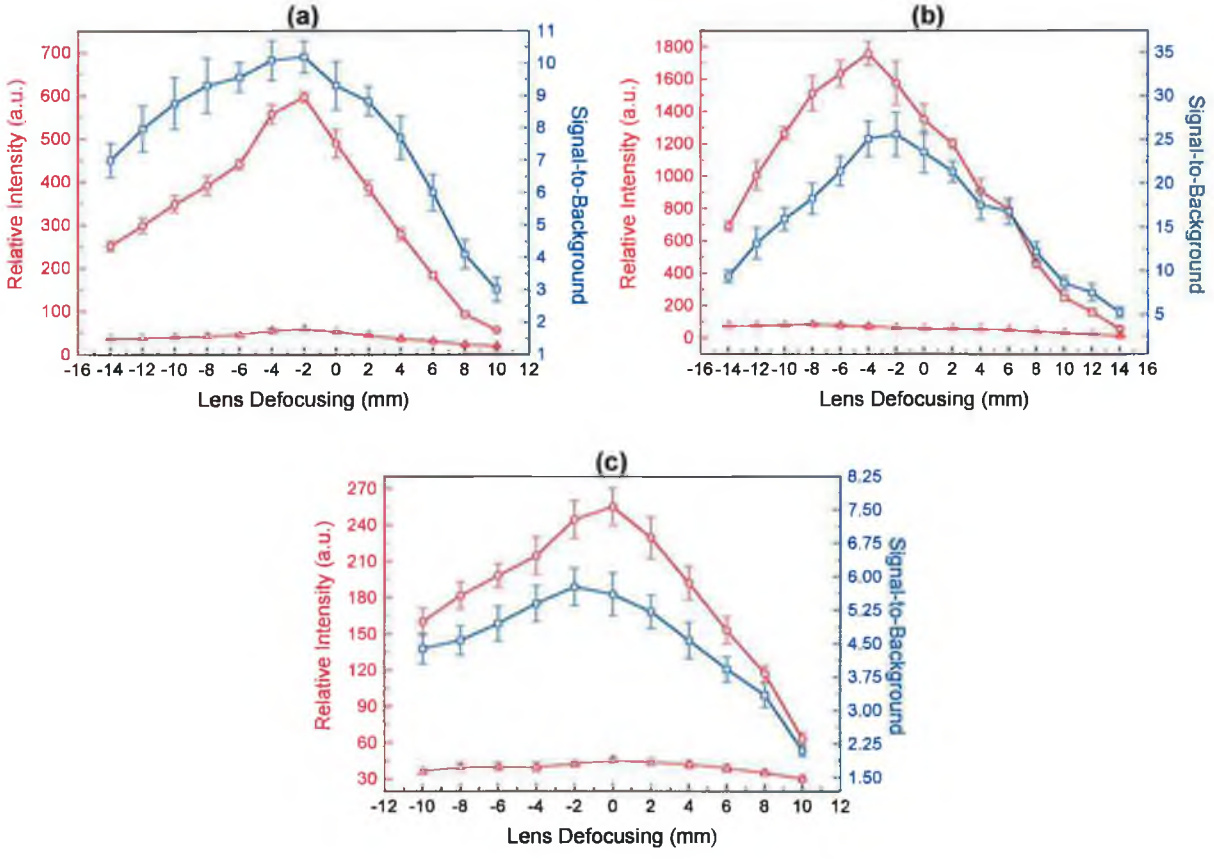

Fig. 5.3 Influence of the cylindrical lens defocusing distance on the emission intensity (spectral line intensity (O); background intensity (Δ)); as well as signal-to-background ratio (□) for the C II 90.41 nm (a), C III 97.70 nm (b) and C IV 154.82 nm (c) spectral lines.

consequent laser shots at 5 Hz. When the laser beam was focused using the cylindrical lens, vertical line plasmas (parallel to both the fore- and spectrometer entrance-slits) were formed on the target. The length of these relatively long plasmas was about 8 mm, as indicated by the imprint left on the sample surface, which was approximately equivalent to the diameter of the unfocused incident laser beam. The highest power density, obtained at the best focus position, was ~ 7 GW/cm^2 whereas at about 15 mm away from this position the irradiance reduced to only 2 GW/cm^2 (see Fig. 5.1(b)).

Figure 5.3 shows the dependence of the emission characteristics of the three spectral lines investigated in Fig. 5.2 on the lens defocusing distance when the cylindrical lens replaced the spherical lens. Similar experimental conditions to those used in case of the spherical lens (Fig. 5.2), were also applied for Fig. 5.3. The only difference was the axial spatial position of the target surface, with respect to the position of the fixed fore-slit within the target chamber, at which the highest signal-to-background ratios for the various species in the plasma were obtained. These locations were 2 mm, 2 mm and 1.5 mm for the C II 90.41 nm, C III 97.70 nm and C IV 154.82 nm spectral lines, respectively. Table 5.1 compares between the spherical and cylindrical lenses used in the present work in terms of the maximum spatial limit in the plasma at which the VUV emission intensities of the spectral lines under investigation can still be detected. For all spectral lines, maximum spatial positions were higher in case of the spherical lens due to the fact that plasmas created using this lens are greater in size than those formed by the cylindrical lens.

Table 5.1 Maximum spatial (axial) extent for various carbon ionic species in the plasma for the spherical and cylindrical lenses used.

Spectral line (nm)	Maximum spatial distance (mm)	
	Spherical lens	Cylindrical lens
(1) C III 45.96	4.5	3.0
(2) C II 68.73	5.0	4.0
(3) C II 90.41	5.0	4.0
(4) C III 97.70	5.0	4.0
(5) C III 117.57	3.5	2.5
(6) C IV 154.82	3.5	2.5

For the spherical lens (Fig. 5.2), emission intensities as well as signal-to-background ratios are maximized at different locations of the lens with respect to the target surface, for the three spectral lines under investigation. For example, the maximum emission intensities for the C II 90.41 nm and C III 97.70 nm spectral lines took place when the focus of the spherical lens was located 2–8 mm and 2–5 mm behind the target surface, respectively; on the other hand, tight focusing of the spherical lens onto the target surface provided the highest emission intensity for the C IV 154.82 nm spectral line. Moreover, the highest signal-to-background ratios were obtained when the lens was focused 4–8 mm, 2 mm and 0 mm behind the target surface for the C II 90.41 nm, C III 97.70 nm and C IV 154.82 nm spectral lines, respectively.

The situation has significantly improved when the cylindrical lens replaced the spherical lens in focusing the laser beam (Fig. 5.3). Emission intensities, as well as signal-to-background ratios for all spectral lines under consideration occurred within almost the same lens defocusing distance, i.e. when the focus of the cylindrical lens was positioned 0–5 mm in front of the target surface (see Fig. 5.3). Unlike when the spherical lens is used as the focusing element, the emission characteristics of various ionic stages have a common spectral behaviour when the cylindrical lens is employed. This is important when the analytical performance characteristics of various spectral lines having different ionic stages are to be compared.

Careful observation of Figs. 5.2 and 5.3 reveals another extremely important advantage of the cylindrical lens over the spherical one. Under exactly the same experimental parameters and conditions, emission intensities as well as signal-to-background ratios for all spectral lines investigated are much higher than their corresponding values in case of the spherical lens. Figure 5.4 compares the spectral line intensities, background intensities and signal-to-background ratios monitored from plasmas produced by both lenses for the six carbon lines employed in the present work. Each data point in Fig. 5.4 was reproduced from its corresponding 'highest' value recorded in Figs. 5.2 and 5.3. In other words, the data shown in Fig. 5.4 represent the highest recorded emission intensity, corresponding background intensity as well as signal-to-background ratio for the six spectral lines under investigation, and for each lens used.

Although the cylindrical lens delivered significantly lower power densities, Fig. 5.4

illustrates that higher intensities for all spectral lines were recorded from plasmas created using this lens (Fig. 5.4a). More significantly, the signal-to-background ratios were also greatly improved (Fig. 5.4c). The enhancement of the signal-to-background ratios for all spectral lines was partly due to the slight decrease of background intensities for all spectral lines (Fig. 5.4b).

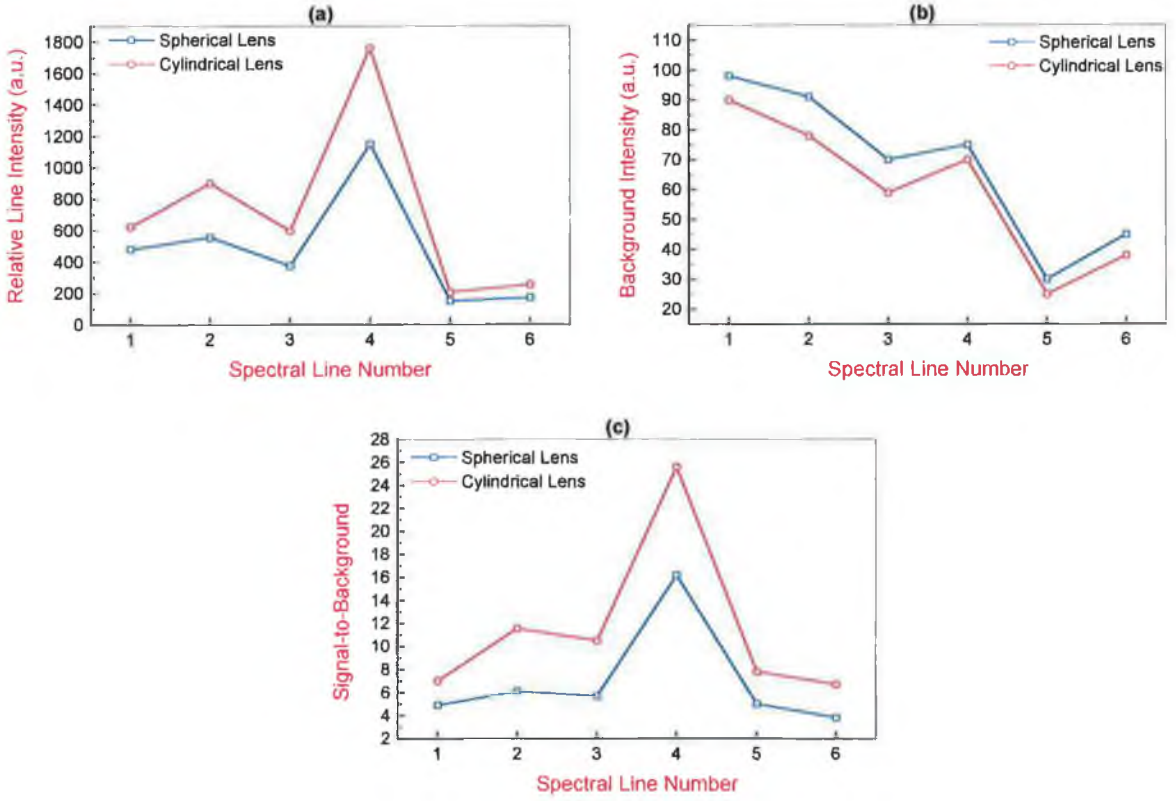

Fig. 5.4 Emission characteristics comparison between the spherical and cylindrical lenses used for the six carbon spectral lines employed in the present work (Table 5.1).

Because of the particular geometry used in the experiments, in which the line plasmas formed, fore-slit and spectrometer entrance-slit are all parallel to each other and lie in the same vertical plane (see Fig. 3.2), the overall amount of light admitted to the spectrometer in case of the cylindrical lens is higher than that obtained using the spherical lens. Furthermore, since lower laser power densities were used to create the plasmas, the background continuum levels were also lower in this case. Results obtained in Fig. 5.4 confirm that the C III 97.70 nm spectral line provides the best performance figures in terms of both spectral line intensity (Fig. 5.4a) and signal-to-background ratio

(Fig. 5.4c), and so should produce the best limit of detection among spectral lines studied in this work. Accordingly, the focus will be mostly on this spectral line for the rest of experiments described in this chapter.

The results achieved in this section compare very favourably with those previously obtained by Multari and co-authors [235]. They investigated the effect of some sampling geometry parameters used in LIPS, such as the focusing lens types and the lens-to-sample distance (LTSD), on analytical results for field-based applications with soil and metal samples. The authors employed time-resolved imaging and spectroscopic techniques to study such effects in air at atmospheric pressure. They firstly concluded that the use of spherical and cylindrical lenses with relatively long focal lengths (around 150 mm) minimizes some effects of changes in the sample geometry, without degrading the analytical performance. The sensitivity of analyte emissions, as well as the mass ablated from the sample was found to be maximum and less sensitive to changes in LTSD parameter when the cylindrical lens was used. In addition, detection limits and precision of measurements were, in general, better in the case of the cylindrical lens.

On the basis of the results obtained in this section, and since the aim of the present work is to achieve the best signal-to-background ratios (and hence the highest analytical sensitivity), it was decided to use the cylindrical lens as the laser focusing element for the rest of the experiments including the construction of analytical calibration curves.

5.3 Influence of Ambient Atmospheres and Pressures: Preliminary Investigations

The significant effect of introducing gases (mostly inert) into the plasma environment in analytical plasma spectrochemical applications has been well known for a long time. For example, the use of inert gases in spark discharges increases the sensitivity, precision and accuracy of the analytical method [50]. In the case of laser-produced plasmas, several spectroscopic studies, all carried out in the visible and UV spectral regions, reported on the influence of various ambient atmospheres and pressures on the emission and plasma characteristics, as well as on different excitation mechanisms using several laser systems covering a wide range of output energies [50–61]. For example, Sdorra and Niemax [54] observed a 30–fold increase of the emission intensity for

neutral spectral lines on reducing an argon gas pressure from 1000 mbar to 140 mbar. Also, Lee and co-workers [56] reported an 11–fold enhancement in the emission intensity of atomic copper spectral lines in an argon atmosphere upon reducing its pressure from atmospheric to about 10 Torr (~ 13 mbar). However, these studies were carried out for considerably longer wavelengths than those used in the present work.

For the first time, the VUV spectral lines employed (Table 5.1) were examined whether or not they are subjected to the significant enhancement in the emission characteristics of UV / visible spectral lines previously observed. The influence of introducing the inert gases argon and helium, at various pressures, on the emission characteristics of VUV spectral lines emitted by the laser-produced steel plasmas is preliminary investigated. Later in this chapter, this effect will be thoroughly studied as a function of both the laser energy and axial distance from the target surface.

In the experiments, the laser (Continuum, Model Surelite III–10) operated at its fundamental wavelength (1064 nm), delivering energetic pulses of 800 mJ (the largest possible energy that could be obtained with the present system) in about 6 ns duration. The plano-convex cylindrical lens was used as the laser focusing lens, and was positioned at distances from the target surface that provided the highest signal-to-background ratios for the six spectral lines (see Table 5.1 and Fig. 5.4c) under investigation. The plasma emission intensity was integrated from firing the laser 20 times (at 5 Hz) onto the steel target containing 1.32% carbon (Appendix E).

Fig. 5.5 illustrates the influence of changing the pressure of argon and helium atmospheres on the line, as well as background emission intensities for the C II 90.41 nm, C III 97.70 nm, C III 117.57 nm and C IV 154.82 nm spectral lines. The pressures were varied from essentially complete vacuum, at about 2×10^{-5} mbar, up to about 10 mbar and 1000 mbar (atmospheric pressure) of argon and helium gases, respectively. For all spectral lines shown in the figure, the emission intensities (both line and background) significantly increased, in both atmospheres, on raising the pressure from complete vacuum environment. The emission intensities were initially constant up to certain pressure values, before they started a gradual increase with pressures; these pressures values were significantly lower in the argon than in helium atmosphere due to differences in densities of both gases: the density of argon is 0.0018 g/cm^3, while that

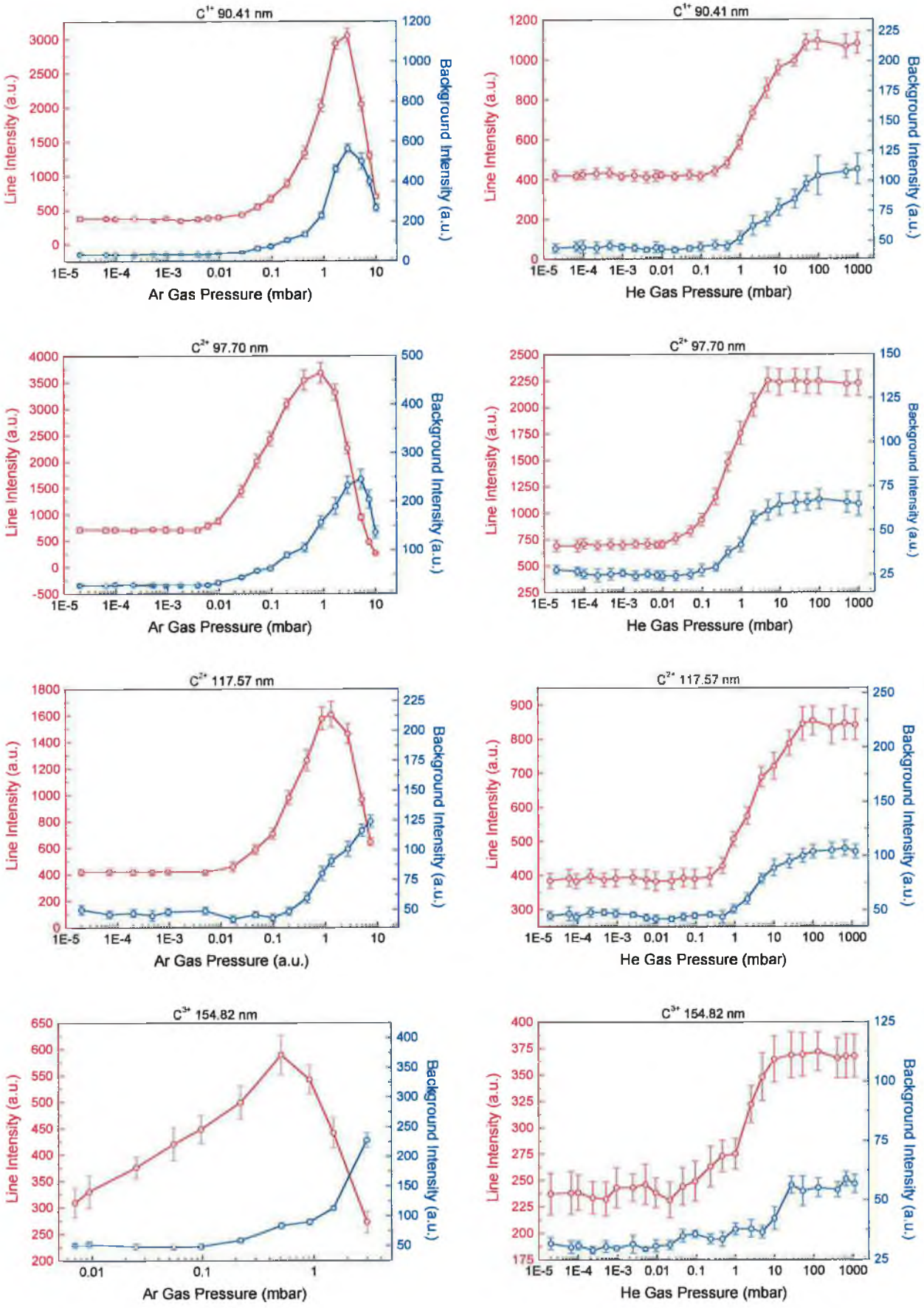

Fig. 5.5 Effect of Ar (left) and He (right) gas pressures on line (red) and background (blue) emission intensities for the spectral lines under investigation. See text for more details.

of helium is about an order of magnitude less, i.e. 0.00018 g/cm^3. The flow rate of each gas was controlled by needle valves in the gas supply as well as in the pumping line, and the pressure in the target chamber was measured using a Pirani gauge. Spectra of the four spectral lines under consideration for three selected pressures of both gases

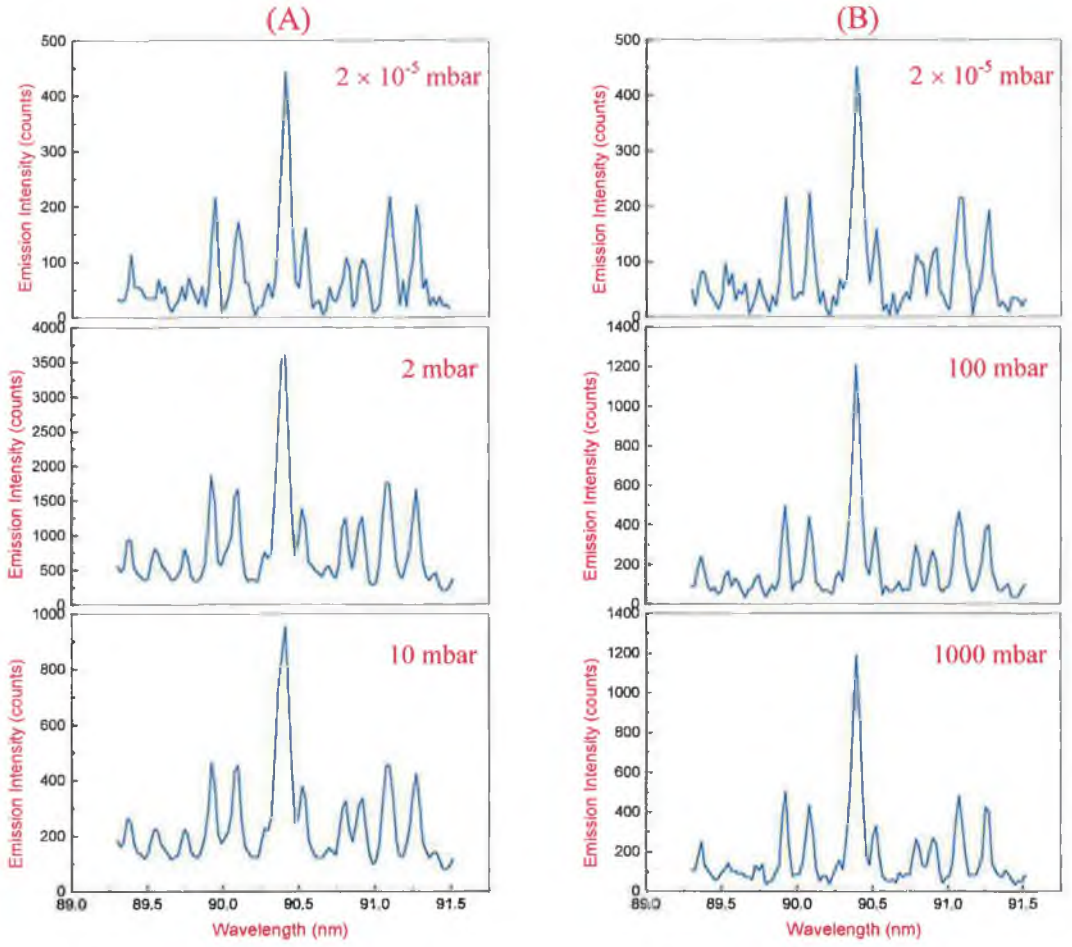

Fig. 5.6 Emission intensities for the C II 90.41 nm spectral line at different three pressures of Ar (A) and He (B) atmospheres.

are shown in Figs. 5.6–5.9. Note that the middle spectrum in each figure represents the pressure value of either argon or helium atmosphere at which the emission intensity of the corresponding spectral line reached its highest value.

In the argon atmosphere, the emission intensities initially dramatically increased with pressure, maximizing at low pressure values between 0.5 and 2 mbar and then sharply decreasing for higher pressures. The increases were 8-, 5-, 4- and 2-folds for the C II 90.41 nm, C III 97.70 nm, C III 117.57 nm and C IV 154.82 nm spectral lines, respectively (see Figs. 5.5–5.9).

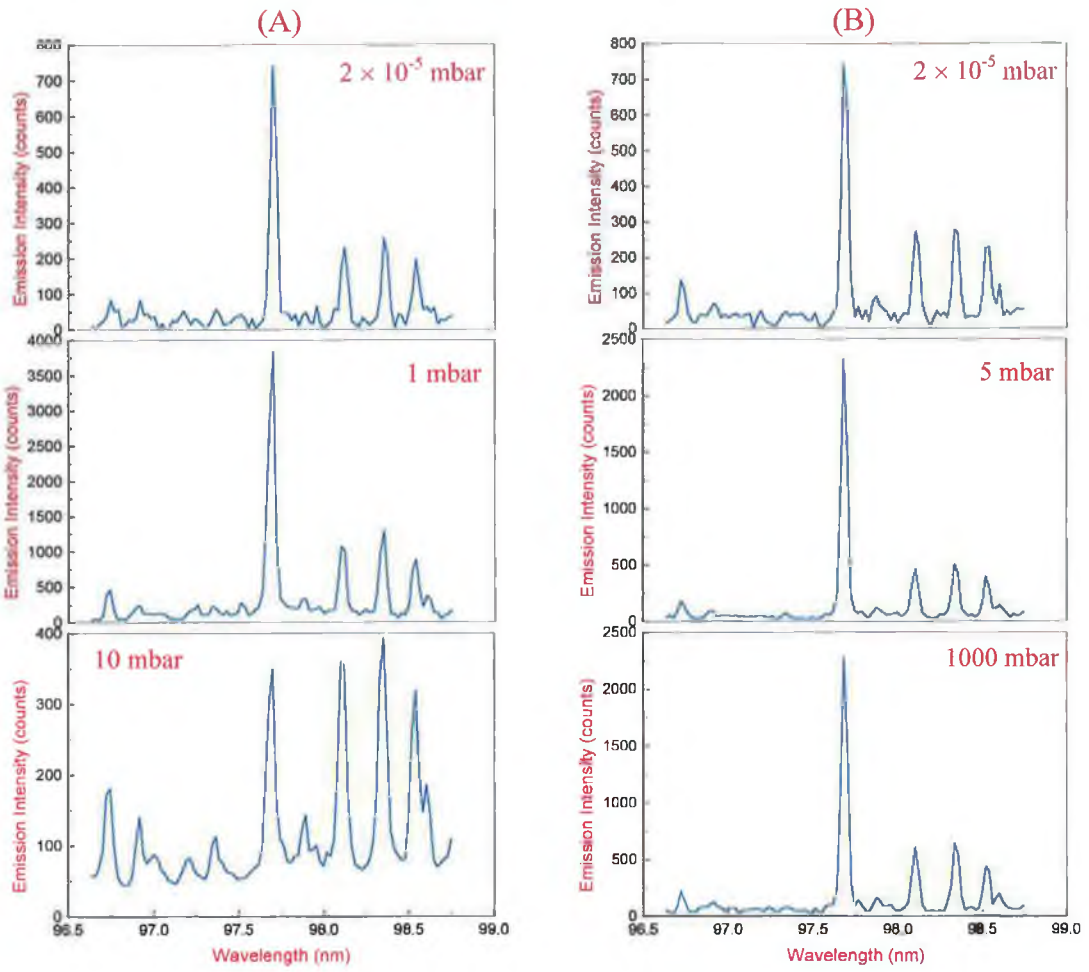

Fig. 5.7 Emission intensities for the C III 97.70 nm spectral line at different three pressures of Ar (A) and He (B) atmospheres.

In the case of helium atmosphere, the emission intensities also significantly increased with pressure, and maximized at relatively low pressure values of 5–100 mbar before they leveled off, remaining approximately constant up to atmospheric pressure (see Figs. 5.5–5.9). However, the enhancements of the line emission intensities were lower than those achieved in the argon atmosphere and valued at 3-, 3-, 2- and 1.5-folds for the C II 90.41 nm, C III 97.70 nm, C III 117.57 nm and C IV 154.82 nm spectral lines, respectively. Except for the C III 117.57 nm spectral line, the background intensities of the other three spectral lines were significantly lower in the helium environment.

The significant spectral line intensity gains in both atmospheres may be qualitatively explained in the following terms. For relatively low argon and helium pressures, there is a plasma breakdown in the sample layer as well as in the 'buffer' gas. The ablated

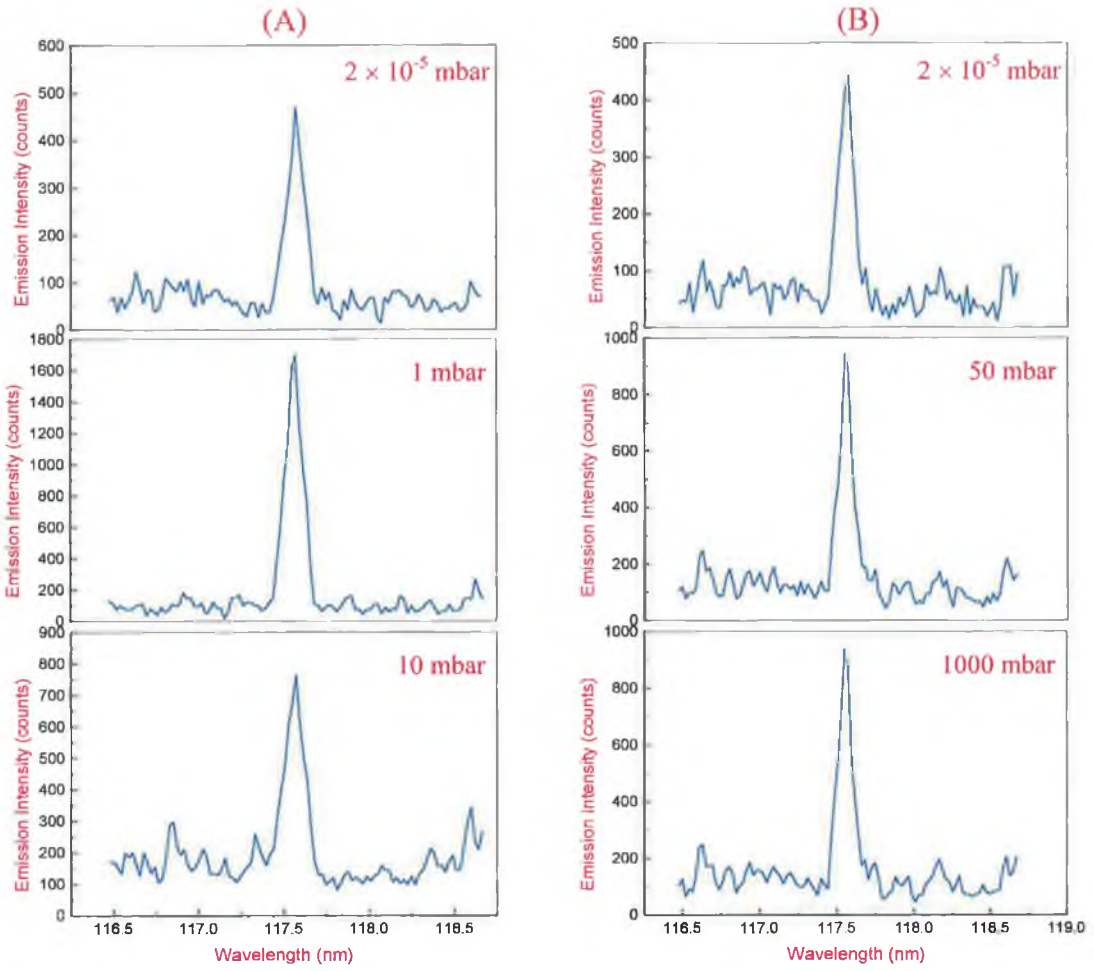

Fig. 5.8 Emission intensities for the C III 117.57 nm spectral line at different three pressures of Ar (A) and He (B) atmospheres.

sample droplets and particles therefore penetrate into the hot buffer gas, and subsequent additional atomization, excitation and ionization processes can take place (see § 2.1.4.2, chapter II). The metastable energy states that become significantly populated in the plasma environment can transfer large amounts of energy to the ablated atoms / ions not only sufficient for ionization, but also to produce significantly populated excited ionic levels, thus enhancing their corresponding transitions. In other words, the buffer gas plasma formed serves as an energy reservoir for the ablated sample material. In comparison with laser ablation in vacuum, these important atomization / excitation processes are absent, and so the analytical efficiency is considerably lower.

Since the amount of sample vaporized at reduced pressures of Ar and He atmospheres does not almost change [53], the efficiency of atomization / excitation processes must

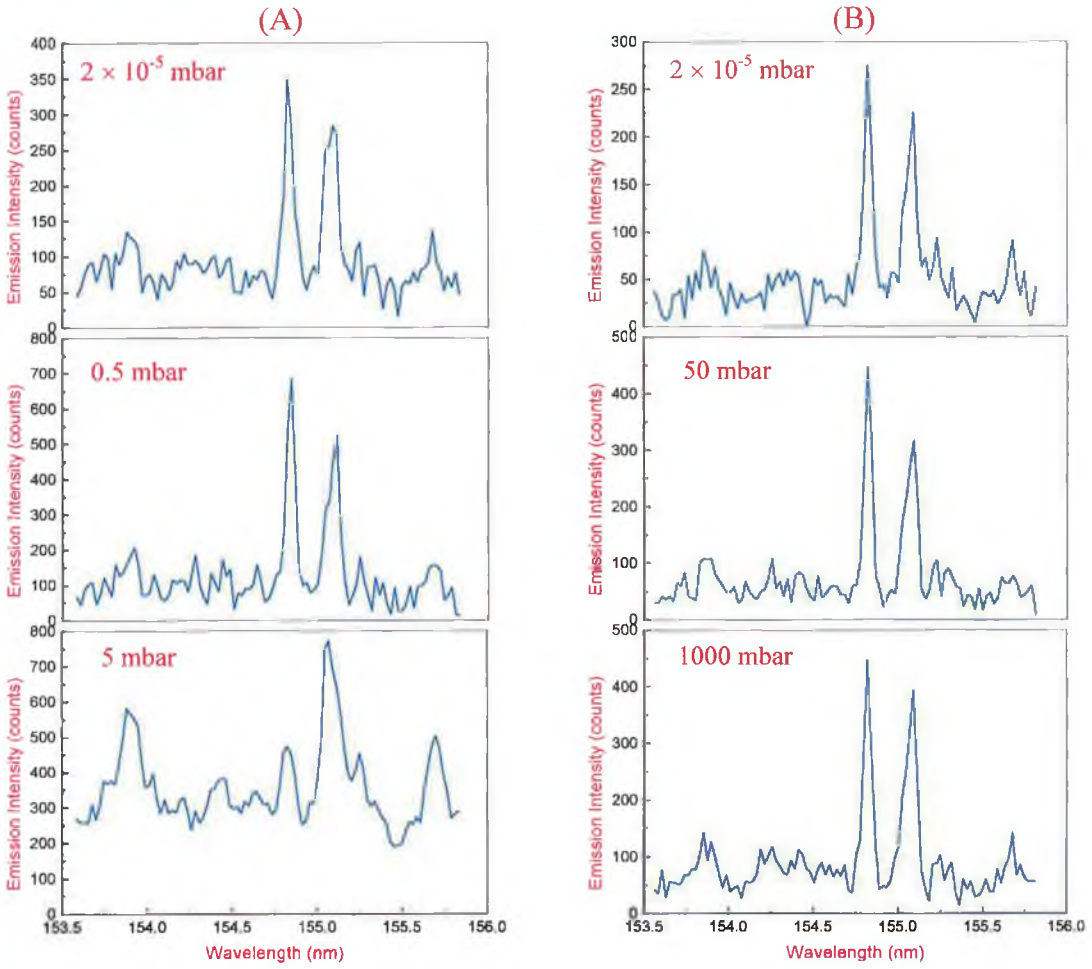

Fig. 5.9 Emission intensities for the C IV 154.82 nm spectral line at different three pressures of Ar (A) and He (B) atmospheres.

be higher in argon compared to helium, leading to the significantly higher emission intensities of all spectral lines shown in Figs. 5.5–5.9.

It should be mentioned at this stage that almost no effect was observed on the emission intensity of the C III 45.96 nm and C II 68.73 nm spectral lines in the argon atmosphere. Figure 5.10 depicts the behaviour of the emission intensity of both spectral lines as a function of the argon gas pressure. The spectral line, as well as background intensities remained almost unchanged as the pressure was increased from essentially complete vacuum up to about 0.0075 mbar of argon, when a sharp decrease occurred for higher pressures. This behaviour can be interpreted by the absence of argon metastable states that are responsible for the significant enhancements observed with the other spectral lines. Figure 5.11 shows spectra of the C III 45.96 nm and C II 68.73 nm spectral lines at three selected argon pressures, demonstrating the behaviour just described.

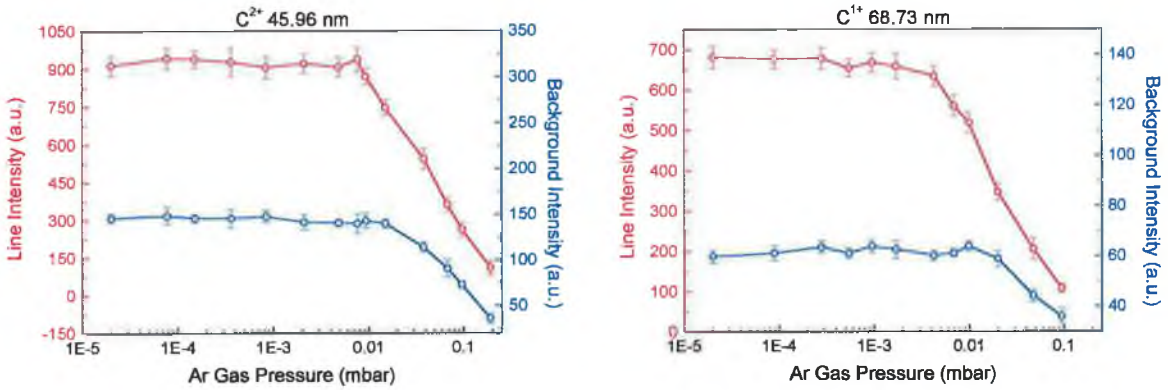

Fig. 5.10 Emission intensities for the C III 45.96 nm (left) and C II 68.73 nm (right) spectral lines as a function of argon gas pressure.

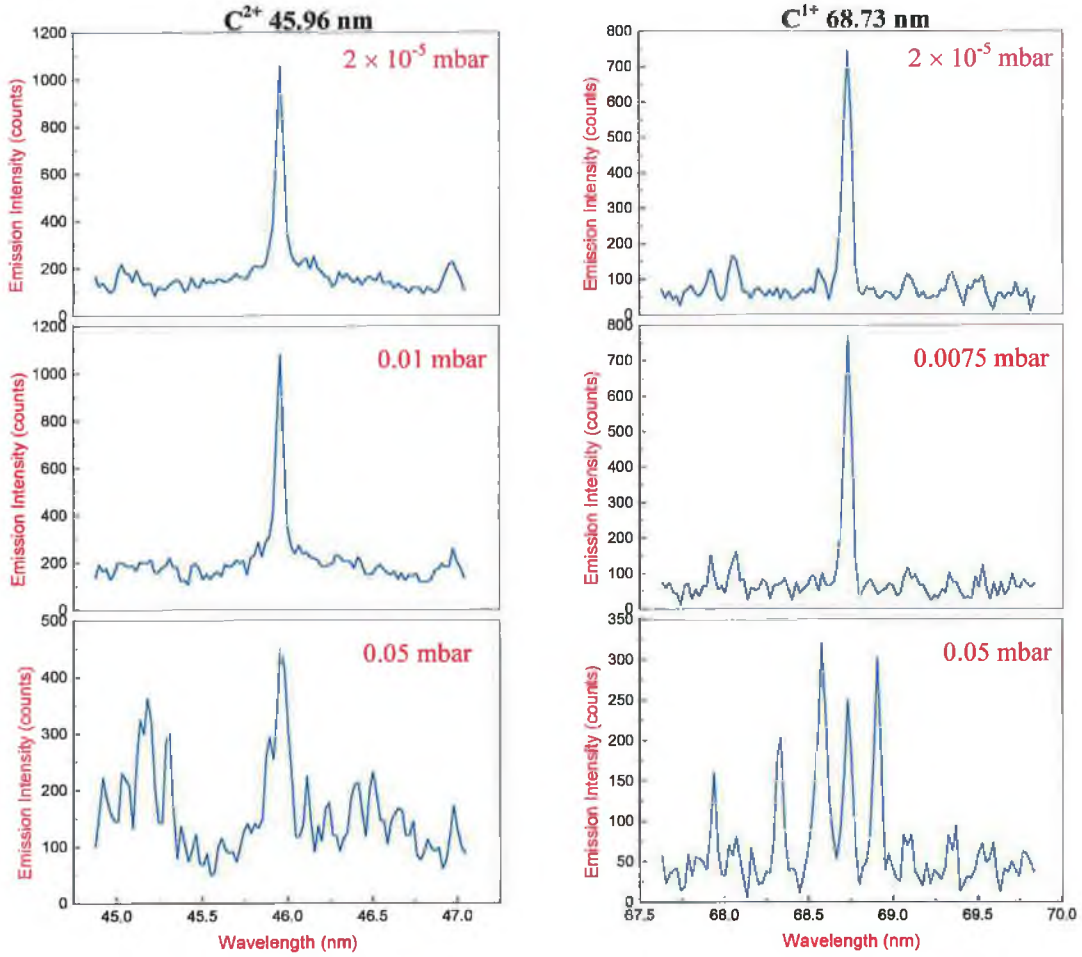

Fig. 5.11 Emission intensities for the C III 45.96 nm (left) and C II 68.73 nm (right) spectral lines in an argon atmosphere at three different pressures.

The dramatic decrease in the spectral line intensities at higher argon pressures (with respect to those shown in the middle spectra of Figs. 5.6–5.9 and 5.11) can be explained by the shielding effect [50, 210]. Laser-induced argon breakdown plasmas can be formed in front of the solid target surface leading to a lowering of the laser-target coupling efficiency, and a consequent reduction in the amount of material ablated from the sample. The power density threshold required to induce a breakdown in argon at those pressure values is usually on the order of 1×10^{12} W/cm^2; however, the presence of the solid target significantly decreases the gas breakdown threshold and the probability of gas breakdown considerably increases, even at power densities in the order of 1×10^6 W/cm^2 [236]. Furthermore, the onset of gas breakdown was visually observed through laser-safety goggles.

On the other hand, because of the higher ionization potential of helium compared to argon (24.6 eV for the former and 15.8 eV for the latter), gas breakdown in helium does not take place, even at atmospheric pressure, keeping the laser-target coupling efficiency high and leading to the approximately constant emission intensity behaviour seen in Fig. 5.5. The above explanations are in a firm agreement with the experiments carried out by Iida [52–53], in which the amount vapourized from the solid target significantly decreased above a certain argon pressure (0.01–1 mbar) in comparison to that in the helium atmosphere.

The condition necessary for the development of a cascade-like growth in the electron number density of laser-induced gas breakdown plasmas is given by the following formula [236]:

$$\frac{d\varepsilon}{dt} = \left(\frac{4\pi e^2 I \nu_{eff.}}{m_e c \omega^2} \right) - \left(\frac{2 m_e \nu_{eff.} \mathrm{E}}{M} \right) > 0 \qquad [5.1]$$

where ε is the energy of the free electron with charge e and mass m_e, M is the mass of the neutral gas particles, E is the energy of the first ionization stage of the gas atoms, $\nu_{eff.}$ is the effective frequency of electron collisions with the gas particles, and I and ω are the laser power density and angular frequency, respectively. The first term in equation 5.1 expresses the rate of growth of the energy of free electrons as a result of

the inverse Bremsstrahlung effect (see § 2.1.2 in chapter II and Appendix A), while the second term represents the maximum rate of energy loss due to elastic collisions with the neutral particles of the gas.

In comparing argon and helium gases, the cascade condition expressed in equation 5.1 is more favoured by argon (M = 40, and E = 15.8 eV) rather than helium (M = 4, and E = 24.6 eV). The result is that plasmas developed in an argon atmosphere are more absorptive than those in a helium atmosphere, due to their higher electron number densities and degree of ionization. Accordingly, the absorption of laser radiation by argon plasmas is more significant than in helium plasmas, and increases with pressure.

Figure 5.12 depicts the signal-to-background ratios for the C II 90.41 nm and C III 97.70 nm spectral lines as functions of argon and helium pressures. The different signal-to- background ratio values were reproduced from the data presented in Fig. 5.5.

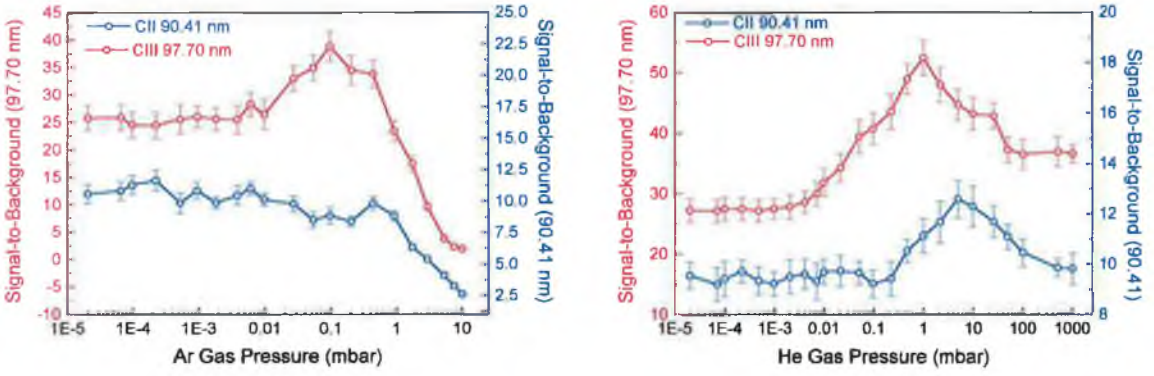

Fig. 5.12 Signal-to-background ratios for the C II 90.41 nm and C III 97.70 nm spectral lines as functions of argon (left) and helium (right) gas pressures.

The figure shows that the highest signal-to-background ratios were obtained in the helium atmosphere at relatively low pressures of 1–5 mbar. For the C III 97.70 nm spectral line, the enhancement in the signal-to-background was 2- and 1.5-folds higher than those produced in vacuum (2×10^{-5} mbar) and argon (0.1 mbar) atmospheres, respectively. Although the emission intensity of the C II 90.41 nm spectral line was 8-times higher in argon compared to vacuum (see Figs. 5.5 and 5.6), the signal-to-background ratio did not change much, mainly due to the significantly higher

background intensity. In the helium atmosphere (5 mbar), on the other hand, the signal-to-background ratio of this spectral line was only 1.3 times higher than that in vacuum (2×10^{-5} mbar), although the spectral line intensity was about 3 times larger. The enhancement of signal-to-background ratios in the helium atmosphere for both spectral lines was mainly due to the cooling effect introduced by the higher thermal conductivity helium gas (0.14 W/m.K, compared to 0.016 W/m.K for argon), which can considerably suppress the background intensity compared to the case of an argon gas [56].

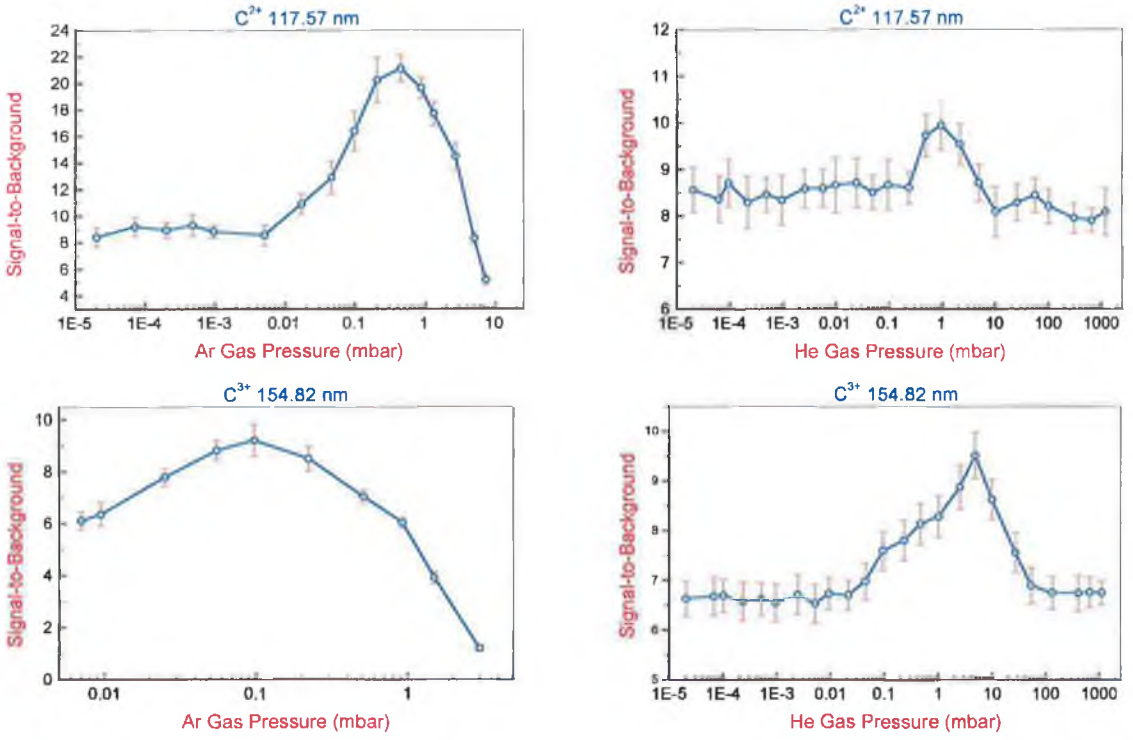

Fig. 5.13 Effect of changing the pressure of argon and helium atmospheres on the signal-to-background ratios for the C III 117.57 nm and C IV 154.82 nm spectral lines.

The dependence of signal-to-background ratios for the C III 117.57 nm and C IV 154.82 nm spectral lines on Ar and He pressures are shown in Fig. 5.13.

As can be noticed from the figure, the highest signal-to-background ratio for the C III 117.57 nm spectral line was obtained in the argon atmosphere (0.5 mbar), and valued at 2.5 times with respect to that obtained in vacuum; in helium (1 mbar), this value reduced to only 1.2 times. This was due to the fact that levels of the background intensity in argon and helium were almost the same, while the line intensity in the argon

atmosphere was abut 2-times higher than that in the helium atmosphere. In case of the C IV 154.82 nm spectral line, the signal-to-background ratios were almost equivalent in the argon (0.1 mbar) as well as in the helium (5 mbar) atmospheres, and valued at 1.5 times with respect to that in complete vacuum environment.

5.4 Effect of Laser Harmonics

The influence of the laser wavelength on ablation of metallic solid materials, as well as on emission characteristics of the subsequent plasmas produced has been investigated by several authors in the near UV / visible region of the electromagnetic spectrum [see 41–43, for example]. Different types of laser systems, including Nd:YAG (1064 nm, 532 nm, 355 nm and 266 nm), CO_2 (10.6 μm) and excimers (XeCl at 308 nm, KrF at 248 nm and ArF at 193 nm) were employed. The highest sensitivities for different elements, obtained from their neutral spectral lines, in a variety of matrices were obtained from plasmas created by lasers working in the visible range, i.e. the ruby and second harmonic of Nd:YAG lasers [see Ref. 7 and references therein].

In the present work, the third Nd:YAG laser system (Continuum, Model Surelite I-10) was employed (see chapter III). It can generate radiation at the fundamental wavelength (1064 nm) its second, third or fourth harmonic (532, 355 or 266 nm, respectively). The generation of the three harmonics was achieved via passing the fundamental radiation through harmonic crystals, which were placed at the end of the laser bench and could be adjusted by external knobs. The energies recorded at the exit port of the laser aperture were 400, 250, 100 and 55 mJ for the four wavelengths, respectively. Four sets of dielectric steering mirrors (each set is specified to one laser wavelength and consists of three mirrors) were used to guide the output laser pulses to the target chamber. Accordingly, the laser energies measured just before the focusing lenses were 360, 200, 65 and 40 mJ for the above mentioned wavelengths, respectively. Plano-convex spherical lenses with 125 mm nominal focal length and anti-reflection coatings to provide the highest transmission at each specified wavelength, were used to focus the laser beam. Each lens was sequentially placed at its best focus position, delivering the largest possible power density for each particular energy value. The pulse duration was between 5–7 ns for the fundamental and its second harmonic, and 4–6 ns for the third and fourth harmonics (see chapter III for more details).

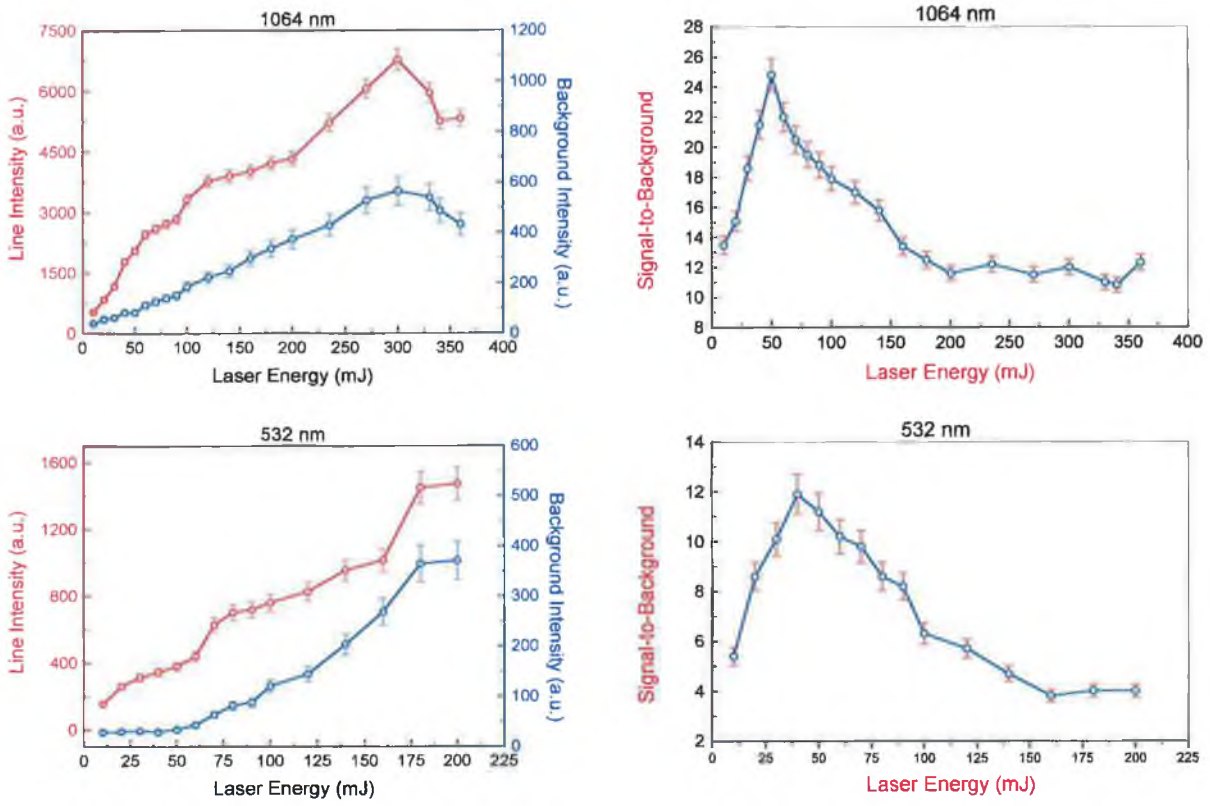

Fig 5.14 Influence of the fundamental (top) and second harmonic (bottom) Nd:YAG wavelengths on the emission intensities and signal-to-background ratios for the C III 97.70 nm spectral line, at different laser output energies.

The aim of this part was to study the influence of the Nd:YAG harmonics at 532, 355 and 266 nm, with respect to the fundamental wavelength at 1064 nm, on the emission characteristics of the laser-produced steel plasmas investigated. Figure 5.14 illustrates the dependence of the emission intensities, as well as signal-to-background ratios for the C III 97.7 nm spectral line on the laser energy for both the Nd:YAG fundamental and second harmonic wavelengths. Each data point shown in the figure was the result of integrating the light produced from the plasma over consequent 50 laser shots at 5 Hz. The steel plasmas were formed under vacuum environment (2×10^{-5} mbar) from the target containing 1.32% carbon.

As can be seen from Fig. 5.14 the emission intensity is significantly higher (in the laser energy interval 10–200 mJ) in the case of the fundamental radiation compared to the second harmonic wavelength. The signal-to-background ratios are also noticeably much higher for the 1064 nm radiation. They maximized at much lower energies for both wavelengths, indicating the importance of having lower background intensity in spectral measurements.

The considerable enhancement in emission intensities is basically due to the fact that the fundamental wavelength at 1064 nm produces plasmas with higher electron temperatures [222]. Colombant and Tonon [222], derived a formula relating the temperature (in eV) of laser-produced plasmas and the laser wavelength as follows:

$$T(eV) \approx 5.2 \times 10^{-6} A^{1/5} \left[\lambda^2 \phi\right]^{3/5} \qquad [5.2]$$

where A is the atomic number of the element considered (26 for Fe, in this case), λ (μm) is the laser wavelength and ϕ is the power density (W/cm^2). Accordingly, equation 5.2 suggests that for approximately the same laser power density, steel plasmas produced by the Nd:YAG fundamental wavelength at 1.06 μm will have higher electron temperatures than those produced by the 0.532 μm laser radiation. In addition, as mentioned earlier, at longer laser wavelengths the predominant physical mechanism of plasma formation is the thermal avalanche ionization (*inverse Bremsstrahlung*) which is responsible for heating the plasma via production of fast growth in the number of free electrons [94] (see § 2.1.3 in chapter II, and Appendix A).

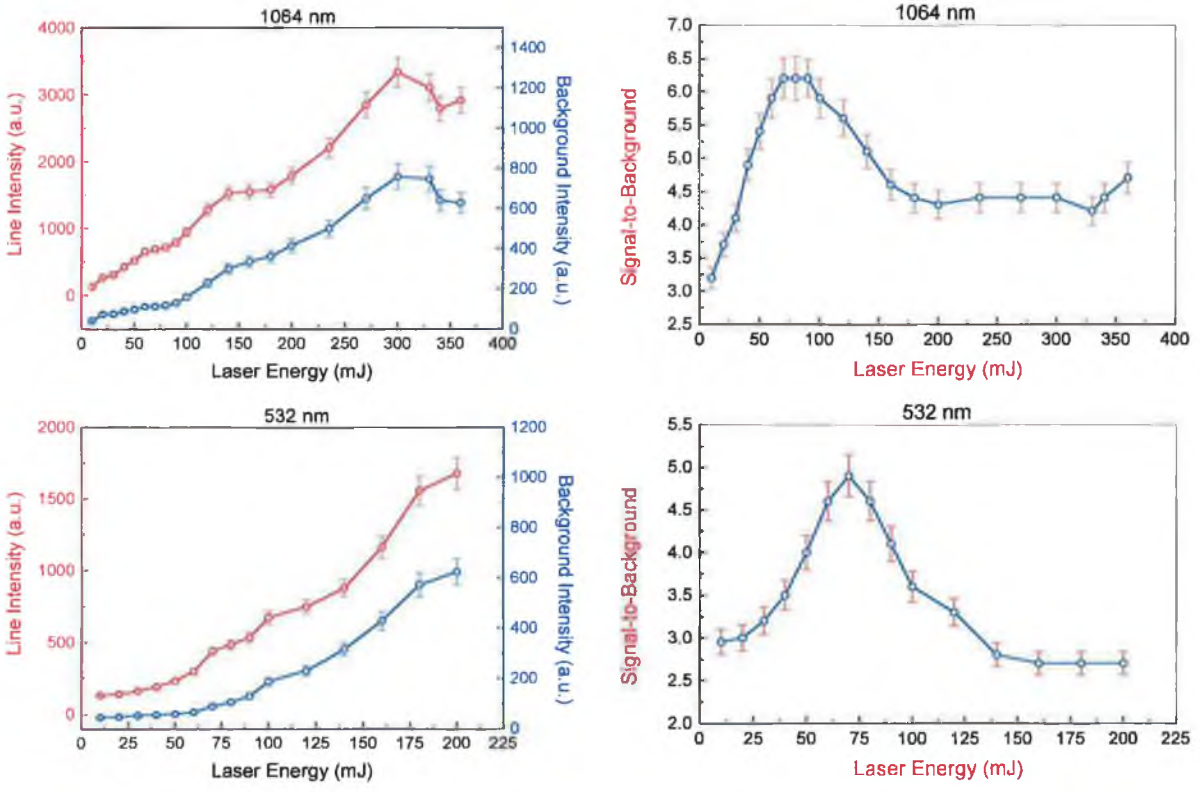

Fig 5.15 Influence of the fundamental (top) and second harmonic (bottom) Nd:YAG wavelengths on the emission intensities and signal-to-background ratios for the C II 90.41 nm spectral line, at different laser output energies.

Similar results to those obtained for the C III 97.70 nm spectral line in Fig. 5.14 were also obtained for the C II 90.41 nm spectral line, and are presented in Fig. 5.15. For the 1064 nm laser radiation, the emission intensity for both spectral lines was maximized at the same laser energy, i.e. 300 mJ. On the other hand, the highest signal-to-background ratio for the singly-ionized spectral line occurred at higher energy values (70–90 mJ) in comparison with those for the doubly-ionized spectral line (40–60 mJ). The same behaviour was observed in the case of the 532 nm laser radiation, where the signal-to-background ratios for the C II 90.41 nm and C III 97.70 nm spectral lines maximized at 70 mJ and 40 mJ, respectively.

At 200 mJ of laser energy, the emission intensity for the singly-ionized carbon spectral line at 90.41 nm was approximately the same when either the 1064 nm, or 532 nm laser radiation was employed (see Fig. 5.15). The signal-to-background ratio, however, was a little higher in the case of the fundamental radiation (1.3-folds). On the other hand, the emission intensity for the doubly-ionized carbon spectral line at 97.70 nm for the 1064 nm wavelength was 3-times higher than that at the 532 nm radiation, at the same energy (200 mJ). The signal-to-background ratio was also considerably improved, and was 2 times bigger than that obtained with the second harmonic (see Fig. 5.14).

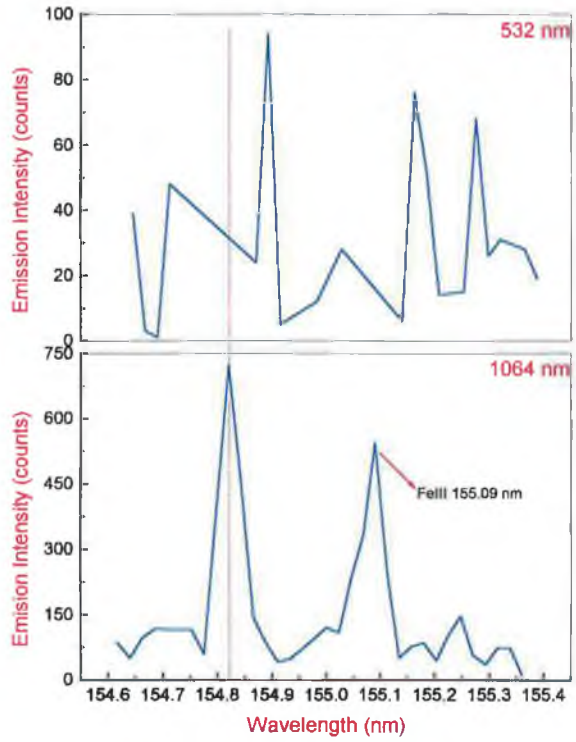

Fig. 5.16 Effect of the 532 nm (top) and 1064 nm (bottom) laser wavelengths on the emission characteristics for the C IV 154.82 nm spectral line. The red-dotted line indicates the exact position of the carbon spectral line.

It should be mentioned here that, no measurable emission intensity was detected from the trebly-ionized carbon spectral line at 154.82 nm when the laser second harmonic wavelength at 532 nm was used to create the steel plasmas under investigation. Figure 5.16 shows a comparison between two spectra, recorded from plasmas created using the Nd:YAG fundamental and second harmonic wavelengths. As can be seen from the figure, the spectrum recorded by the 532 nm laser radiation is dominated by spectral noise, and no spectral lines (even from iron, the major constituent of the steel samples) were observed. This result confirms that plasmas produced by shorter laser wavelengths have lower electron temperatures in comparison with those formed by the fundamental wavelength at 1064 nm.

As might be expected, no detectable emission intensities were recorded for the six carbon spectral lines under investigation from plasmas generated by the third and fourth harmonics at 355 nm and 266 nm, respectively. Again, electron temperatures of these plasmas were too low to efficiently excite the VUV carbon transitions under consideration, even when measurements were taken from plasma regions very close to the target surface. Although the mass ablated from metallic targets is significantly higher in the case of UV wavelengths, due to their high optical coupling efficiency, they provide much poorer analytical results [41]. The dependence of the mass ablation rate, m (kg s^{-1} cm^{-2}), on the laser wavelength can be represented by the following formula [7]:

$$m = 110\left(\frac{\phi_a}{10^{14}}\right)^{1/3}\lambda^{-4/3} \qquad [5.3]$$

Here, ϕ_a is the absorbed power density (W cm^{-2}) and λ (μm) is the laser wavelength used. Therefore, the mass ablation rate significantly increases with shorter laser wavelengths. For this reason, almost all commercial systems, consisting of a laser as the ablation (atomizer) unit and a second plasma (such as ICP, for example) as the excitation / ionization source, make use of UV lasers (mostly the Nd:YAG fourth harmonic at 266 nm and KrF excimer at 248 nm) to increase the amount of materials introduced into the subsequent plasma source, and hence the sensitivity of the instrument [69].

5.5 Effect of Laser Energy

It has been long recognized that the emission characteristics of laser-produced plasmas are greatly influenced by the incident laser energy [see 44–46, and 50–51, for example]. For instance, Kuzuya and co-authors [44] investigated the effects of varying both the laser energy and surrounding atmosphere pressure on the emission characteristics of laser-induced plasmas created by Q-switched Nd:YAG laser over the energy range 20–95 mJ. Argon, helium and air were used as the background atmospheres, and their pressures were changed from atmospheric down to about 1 Torr (~ 1.3 mbar). These studies have successfully demonstrated the general behaviour of the emission characteristics of laser-produced plasmas as spectrochemical excitation sources in terms of their dependence on both the laser pulse energy and the nature as well as pressure of the surrounding atmospheres. However, all studies were limited to spectral lines of neutral and / or singly-charged species in the UV / visible range. Furthermore, the laser energy values were relatively low (2–100 mJ), and the pressure of background gases was restricted to variations between atmospheric pressure and approximately 5 mbar.

In the present section, the influence of laser energy on spectral line intensities as well as signal-to-background ratios, in the presence of air, argon and helium atmospheres at different pressures, is investigated. The focus of the experiments will be towards the doubly-ionized carbon spectral line at 97.70 nm, as it proved to be the most sensitive carbon line in the VUV regime. The plano-convex cylindrical lens (150 mm nominal focal lens) was located at the position that produced the best signal-to-background ratio for the mentioned spectral line, i.e. 0–4 mm behind the best focus position (see section 5.2 above). Moreover, the laser energy was varied from 200 mJ to 800 mJ by simply changing the delay time between flash lamps and Q-switch onsets. In addition, the pressure of the background atmospheres was changed between 0.005 mbar to 5.0 mbar, depending on the composition of the gas used.

Figure 5.17 illustrates the dependence of the emission intensities on the laser energy at different pressure values of the three atmospheres under investigation, for the C III 97.70 nm spectral line. Each data point in the figure represents the average light integrated from firing the laser 100 times at 5 Hz onto the target containing 0.91% carbon.

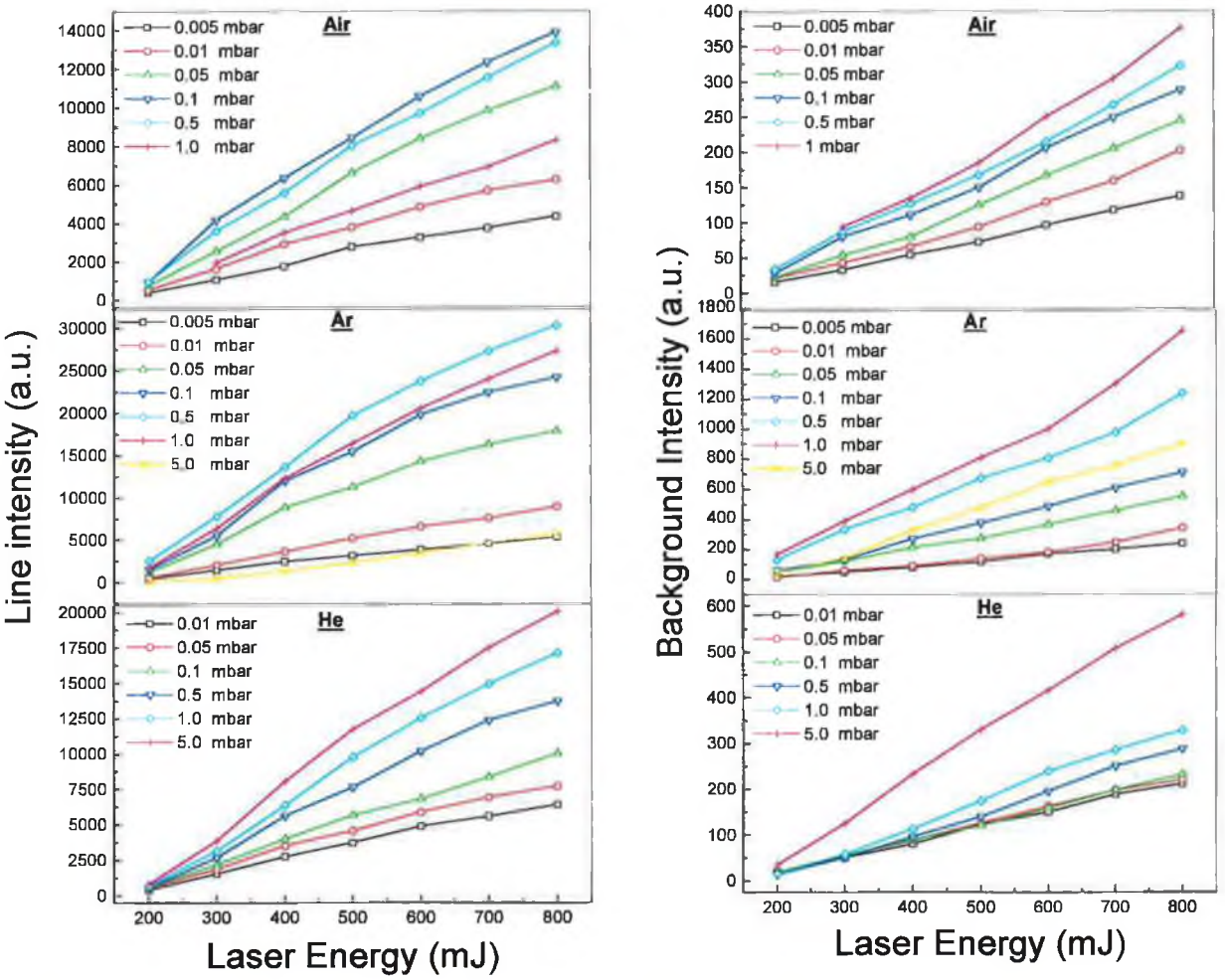

Fig. 5.17 Influence of laser energy on line (left), as well as background (right) emission intensities in air, argon and helium atmospheres at different pressures for the C III 97.70 nm spectral line.

As can be seen from the figure, the line as well as background emission intensities significantly increased with laser energy for all three atmospheres under consideration. As may be expected, the highest emission intensities were produced in argon at a pressure of 0.5–1.0 mbar and for all laser energy values used. On the other hand, the lowest emission intensities recorded occurred in air at a pressure of about 0.1 mbar.

For each particular laser energy value, the spectral line intensity in both air and argon atmospheres showed a gradual increase with the pressure up to a certain value. Depending on the composition of the gas, this specific pressure was around 0.1 mbar in air and between 0.5 mbar and 1 mbar in argon. Raising the pressure beyond these values resulted in a significant reduction in the line emission intensities. This intensity decrease was much more pronounced in argon than in air atmosphere. The same result for argon

was obtained earlier in this chapter (see section 5.3). In the case of helium, however, the line intensity kept increasing with pressure up to the maximum value employed in this experiment, i.e. 5.0 mbar. In section 5.3 (Fig. 5.5), the spectral line intensity for the C III 97.70 nm line in helium atmosphere increased with pressure, maximized around 5–10 mbar, and then levelled off up to atmospheric pressure. Accordingly, it is expected that the spectral line intensity will be almost constant after 5.0 mbar.

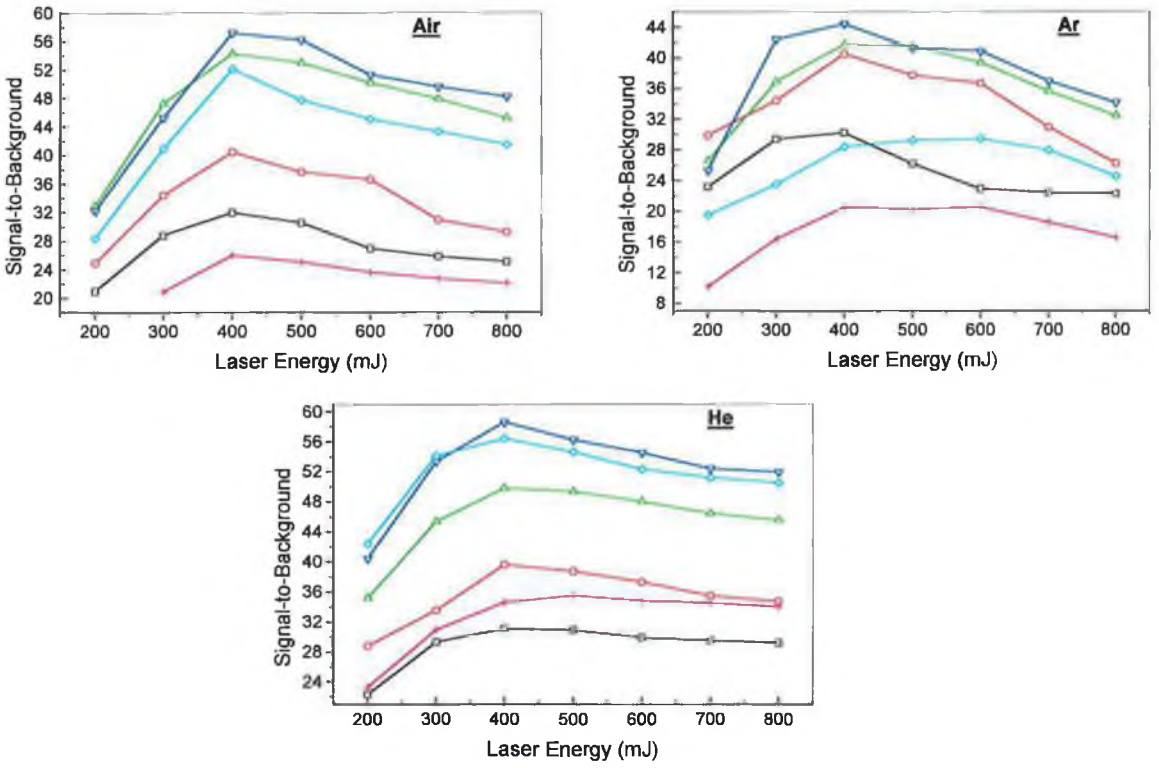

Fig. 5.18 Signal-to-background ratios for the C III 97.70 nm spectral line as functions of laser energy, as well as pressure of the three atmospheres under study. See Fig. 5.17 for definition of different data symbols and colour schemes.

The background emission intensity, on the other hand, also monotonically increased with the laser energy for all three atmospheres used. The argon atmosphere produced the highest background intensities, while much smaller levels were obtained in air and helium, and they were approximately identical for a particular laser energy and pressure. Also, in the case of helium and at low pressures the background intensity is less sensitive to changes in laser energy than argon and air atmospheres. However, at higher pressures of helium the rate of increase in the background intensity is greater compared

to the other two gases. Beyond 1 mbar pressure in argon, the background intensity dramatically decreased with laser energy. On the other hand, reduction of the background intensity with increasing the pressure of helium was not observed up to 5 mbar, and it is highly likely to level off up to atmospheric pressure (see Fig. 5.5). The approximate similarities in the spectral emission characteristics of plasmas created in air and argon atmospheres, compared to helium, in the pressure range studied can be described, to some extent, on the basis of differences in the mass density of the respective gas [44]. As mentioned in section 5.3, The density of helium is about one order of magnitude lower than that of argon, while the density between argon and air is negligibly small.

Figure 5.18 shows the dependence of the signal-to-background ratios for the C III 97.70 nm spectral line on both the laser energy and pressure of the three atmospheres investigated. The data in the figure were derived from those obtained in Fig. 5.17. For each atmosphere under study, signal-to-background ratios considerably increased with the laser energy and pressure. However, at a particular pressure value (and 400 mJ of laser energy) the signal-to-background ratios started a gradual decrease, the nature of which strongly depends on the composition of the filled gas (see Fig. 5.18). This specific pressure valued at about 0.1 mbar in air and argon, and between 0.1 mbar and 1 mbar for helium (note the corresponding pressure values in Fig. 5.17).

The signal-to-background ratios maximized at an intermediate laser energy of 400 mJ, for all three atmospheres and at each particular pressure. However, in the argon atmosphere the signal-to-background ratios levelled off at relatively higher pressures (0.5–1 mbar) in the energy range 400–600 mJ, before it slowly decreased for higher energy values. The same tendency was observed in the helium atmosphere at a pressure of 5 mbar. It is also seen from the figure that the highest signal-to-background ratios were obtained in both air and helium atmospheres, at relatively high pressures of 0.1 mbar and 0.5 mbar, respectively.

Figures 5.19 and 5.20 were reproduced from the data presented in Figs. 5.17 and 5.18, in which the emission intensities, as well as signal-to-background ratios are plotted against pressure of the three atmospheres under study, for different laser energies.

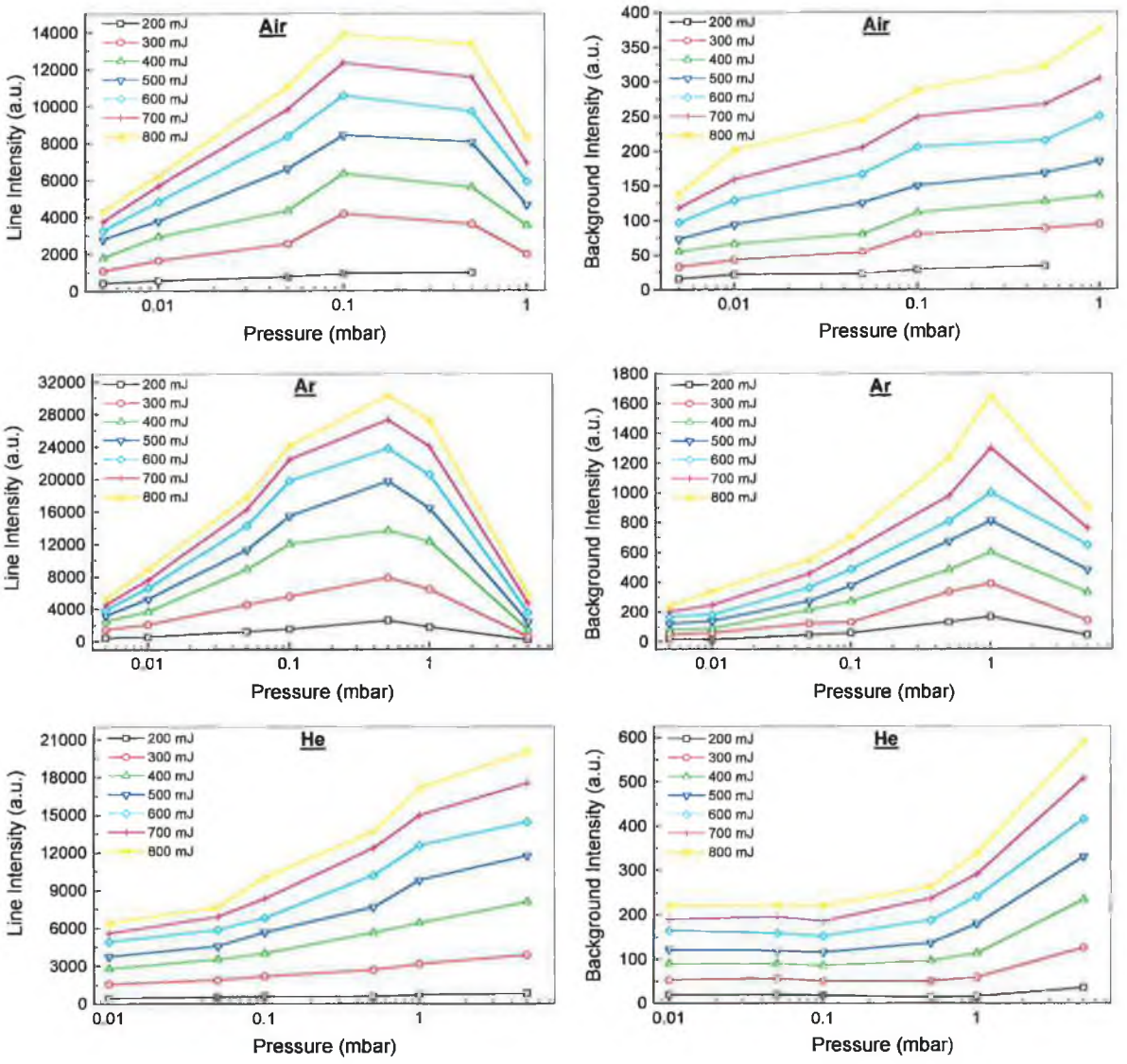

Fig. 5.19 Dependence of line (left) and background (right) emission intensities on the pressure and laser energy (Reproduced from Fig. 5.17).

In this way, the behaviour of the three spectral quantities described above is more obvious and can be directly easily seen from the figures. For more clarity, signal-to-background ratios at laser energies of 300, 500 and 700 mJ were omitted from Fig. 5.20.

The significant enhancement of spectral line intensities at low pressures of air, argon and helium atmospheres, seen in Figs. 5.17 and 5.19, can be explained, again, by the fact that additional excitation / ionization processes of the ablated sample material, which is an increasing function of laser energy, can take place in the buffer gas plasma formed in front of the target surface.

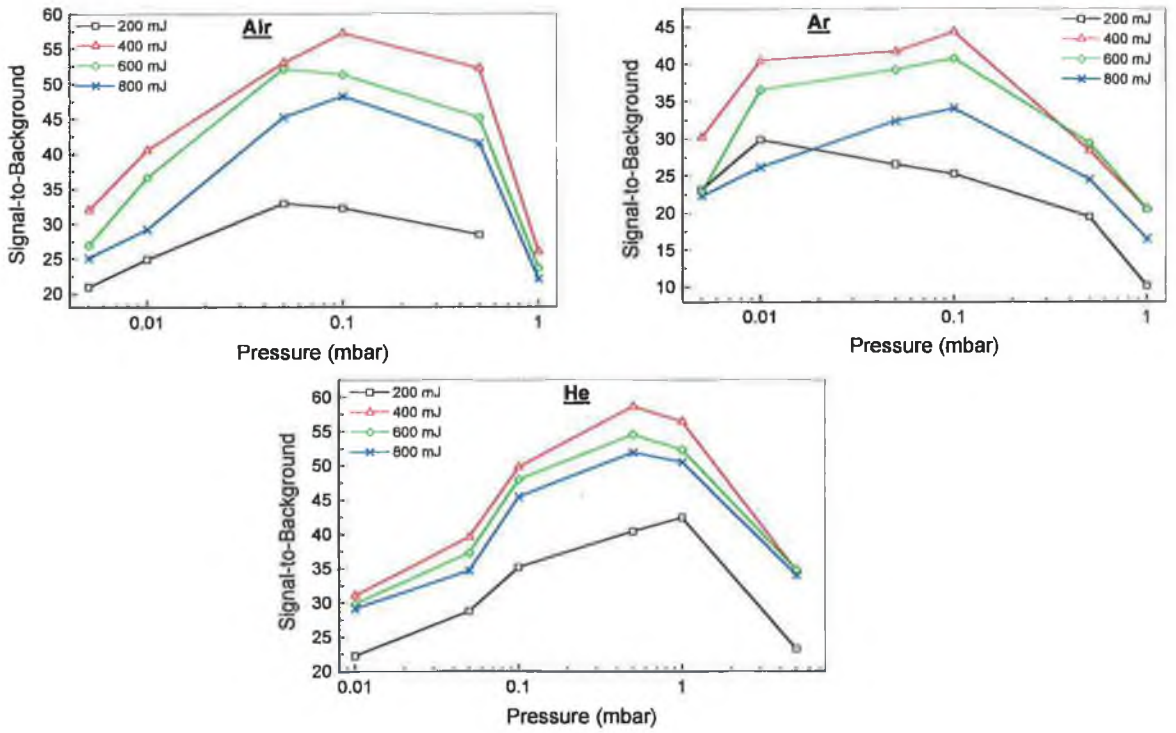

Fig. 5.20 Dependence of signal-to-background ratios on the pressure and laser energy (Reproduced from Fig. 5.18).

The efficiency of these processes are higher in the argon atmosphere, as mentioned earlier in section 5.3, compared to air and helium atmospheres due to the fact that plasmas created in argon have the highest electron temperatures [54], which was justified by the higher emission intensities achieved in Figs. 5.17 and 5.19. The dramatic decrease of the spectral line intensities observed at higher pressures of air and argon atmospheres can be interpreted by the shielding effect (see section 5.3). On the other hand, due to the higher ionization potential of helium compared to air and argon (24.6 eV for helium; 15.8 eV for argon; 15.6 eV for nitrogen and 12.1 eV for oxygen) gas breakdown in helium does not take place, keeping the laser-target coupling efficiency high, and leading to the behaviour observed in the figures.

Sdorra and Niemax [54] measured the crater diameter and depth, amount of material ablated, line emission intensity (for Mg I at 285.2 nm spectral line), electron density and temperature of laser-produced copper plasmas as a function of laser energy and pressure of several ambient atmospheres. The authors found out that plasmas generated in argon have the highest electron densities (see equation 5.1), compared to those produced in air

or helium atmospheres. As mentioned earlier (section 5.3), the heating of the gas plasma by inverse Bremsstrahlung (IB) mechanism is most effective if argon is used as the surrounding buffer gas. In this case, the electron density is so high that the surface of the target becomes optically shielded. As a result, the crater diameters and depths, and hence the amount of materials ablated, were much smaller in the case of argon with respect to the other two gases; the materials ablated, however, was sufficient to provide the highest emission intensities observed in the figures.

5.6 Spatial Distribution of the Plasma Emission

In chapter IV, the dependence of the emission intensity for the six different carbon species under investigation on the spatial position (the axial distance from the target surface) in the plasma was studied. The experiments were carried out in vacuum (2×10^{-5} mbar), and the plano-convex spherical lens was used to focus the laser. Emission intensities, as well as signal-to-background ratios for all spectral lines were maximized at a distance of 1.5–2 mm from the target surface (see section 4.2 for more details).

In the present section, the variation of emission intensities and signal-to-background ratios for the C III 97.70nm spectral line with the axial distance from the target surface is investigated. The plano-convex cylindrical lens was instead used as the laser focusing element, and the laser-produced steel plasmas were generated in different ambient atmospheres of air, argon and helium at various pressures. The laser energy was set at 400 mJ, the value that produced the best signal-to-background ratio for the C III 97.70 nm spectral line in the previous section.

Figure 5.21 displays the line, as well as background emission intensities for the C III 97.70 nm spectral line as a function of the spatial distance from the target surface, in the three atmospheres employed and at various pressures. As expected, the spectral line intensity gradually decreased with the axial distance in the plasma in the three atmospheres, and at various pressures up to 5.0 mm from the target surface. In air atmosphere and at distances above 1 mm from the target surface, the spectral line intensities significantly decreased for both the highest and lowest pressure values used (0.01 and 1.0 mbar).

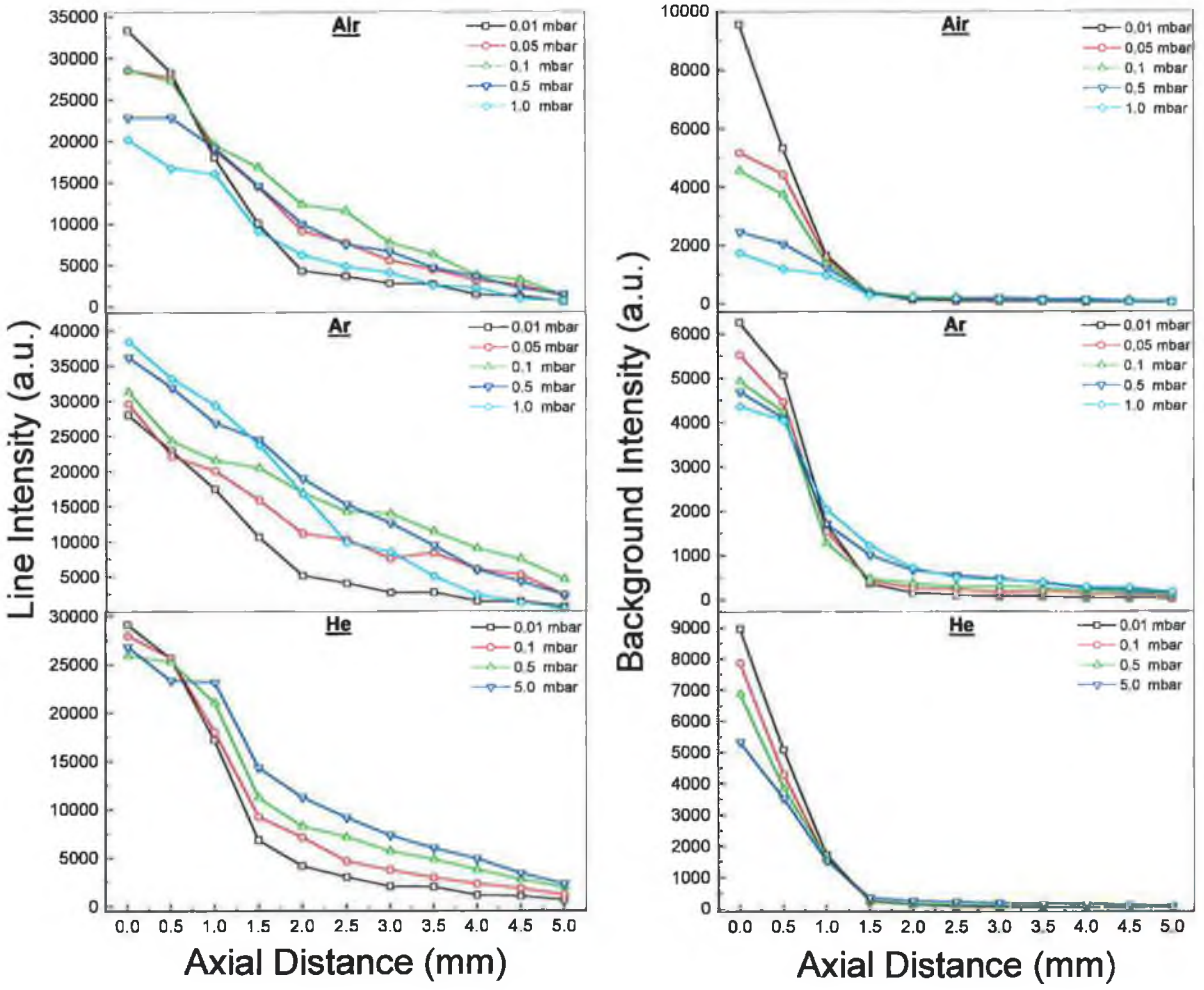

Fig. 5.21 Line (left) and background (right) emission intensities as functions of the axial distance from the target surface for the C III 97.70 nm spectral line, in air, argon and helium atmospheres at different pressures.

The highest emission intensities were obtained at 0.1 mbar within the region 1 to 5 mm from the target surface. For argon, the highest emission intensities were obtained at 0.5 mbar in the distance range 1.5 to 2.5 mm, and at 0.1 mbar afterwards. Note the difference in the behaviour of the line intensity at the target surface (0 mm) between air and argon atmospheres; the spectral line intensity decreased with increasing the pressure in air, while it increased with pressure in the case of argon atmosphere (see Fig. 5.21).

In the helium atmosphere, The emission intensity was initially slightly higher at lower pressures than at higher pressures. However, above about 1.25 mm from the target

surface the spectral intensity behaviour was reversed in such a way that the higher pressure produced the larger emission intensity. The highest spectral line intensities were obtained at 5.0 mbar at subsequent distances (see the figure). Note the agreement between the pressure values of the three atmospheres at which the highest spectral line intensities occurred and those obtained from the previous section.

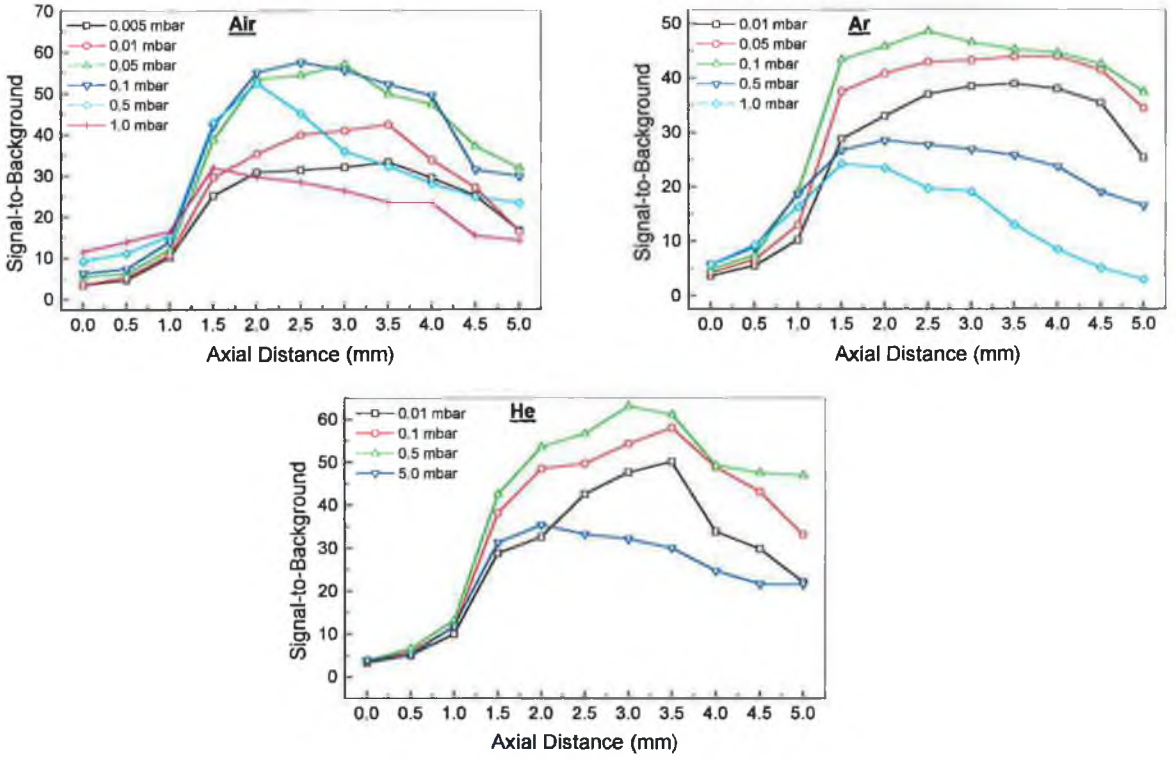

Fig. 5.22 Signal-to-background ratios for the C III 97.70 nm spectral line as functions of the axial distance from the target surface, in air, argon and helium atmospheres at various pressures.

The behaviour of the background emission intensity for the C III 97.70 nm spectral line displayed in Fig. 5.21 was more systematic and less complicated than that obtained for the line emission intensity. The background intensity decreased with distance for all three atmospheres at different pressures. The decrease was dramatic in the range between 0 mm and 1.5 mm; above this point in the plasma, the rate of decline was much less up to the maximum position studied of 5.0 mm.

Figure 5.22 illustrates the dependence on the spatial distance, composition, as well as pressure of ambient atmospheres of the signal-to-background ratios for the C III 97.70

nm spectral line. As can be seen from the figure, the signal-to-background ratios increased with distance for all three atmospheres and at all pressure values. However, depending on the composition of the background gas used, the signal-to-background ratio maximized at a particular distance from the target surface and pressure of the gas.

The highest signal-to-background ratio was produced in air at 0.1 mbar, and 2.5 mm from the target surface. This was followed by helium at 0.5 mbar and 3.0 mm, and finally by argon at 0.1 mbar and 2.5 mm spatial distance in the plasma. It is of great interest to observe that, for the three atmospheres under study, the spatial point in the plasma at which the signal-to-background ratio was maximized moved closer to the target surface as the pressure of the surrounding gas increased (see Fig. 5.22, and refer to § 2.1.4.2, chapter II). This observation was also reported by Lee and co-authors [56], for neutral carbon spectral lines in the UV / visible range.

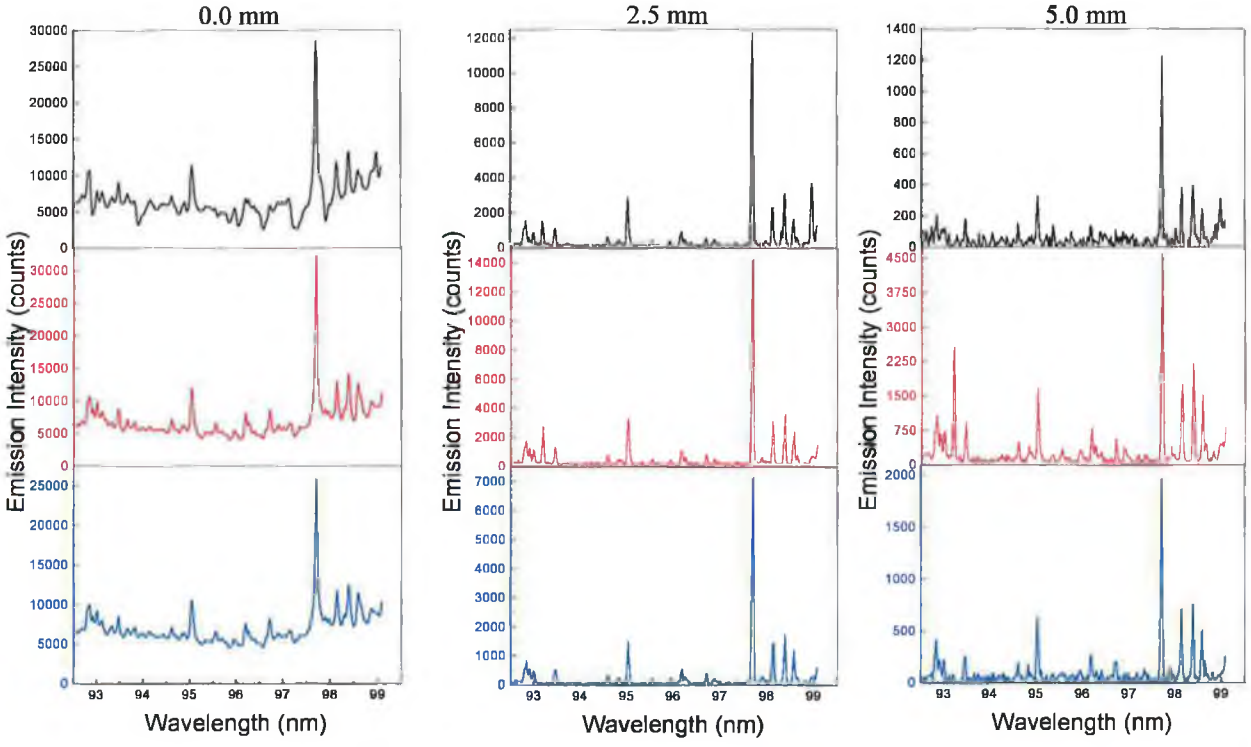

Fig. 5.23 Laser-produced steel plasma emission spectra recorded at three different positions in the plasma (0, 2.5 and 5 mm) with respect to the target surface, in air at 0.1 mbar (black), argon at 0.1 mbar (red) and helium at 0.5 mbar (blue). Note the effect on the C III 97.70 nm spectral line.

Figure 5.23 shows some parts of the plasma emission spectrum containing the C III 97.70 nm spectral line at three different axial positions in the plasma, and at pressure values that provided the highest signal-to-background ratios (Fig. 5.22). These were 0.1 mbar for air and argon and 0.5 mbar for helium. As can be seen in the figure, both the composition and pressure of the surrounding atmosphere, as well as the spatial position of the emitting species in the plasma strongly influence the emission characteristics of the spectral line under investigation.

The results obtained in Figs. 5.21–5.23 can be explained by the plasma confinement [52]. At higher pressures of air and argon atmospheres the expansion of the plasma is greatly confined by the surrounding gas, resulting in a very hot plasma which not only emits significantly weak spectral line signal but also an intense background continuum. On the contrary, at lower pressures the fast expansion of the plasma plume may cause a deterioration of the spectral line intensity by the prompt escape of the emitting species from the observation zone. At an intermediate pressure value, therefore, the moderate confinement of the plasma would produce an intense emission signal without increasing the background continuum emission, hence maximizing the signal-to-background ratio.

As mentioned earlier, the highest signal-to-background ratios for the C III 97.70 nm spectral line were obtained in air (0.1 mbar and 2.5 mm) and helium (0.5 mbar and 3.0 mm) atmospheres. In order to obtain the best sensitivity from this spectral line, a comparison between these two atmospheres were made around the pressure range that provided the highest signal-to-background ratio observed in Fig. 5.22. The results are shown in Fig. 5.24, where both the line and background emission intensities, as well signal-to-background ratios for the C III 97.70 nm spectral line are plotted against the pressure of air and helium atmospheres in the pressure ranges 0.05–0.5 mbar, and 0.1–1.0 mbar, respectively.

As can be seen from the figure, signal-to-background ratios for the C III 97.70 nm spectral line produced in air (0.2–0.3 mbar, and 2.5 mm) and helium (0.6–0.8 mbar, and 3.0 mm) atmospheres were almost equivalent. However, the air atmosphere was chosen to construct the analytical calibration curves for the present work, since it produced a slightly better line emission intensity (see Fig. 5.24) and it is also cost-effective.

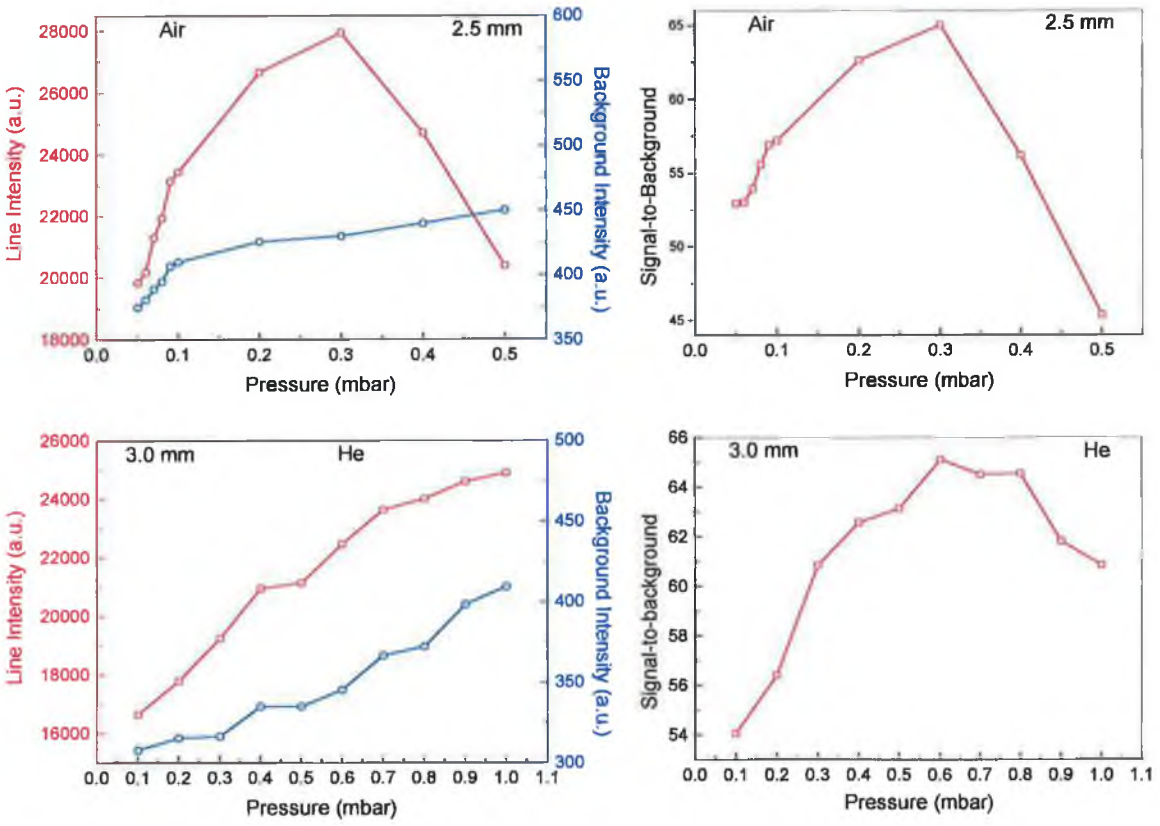

Fig. 5.24 Emission characteristics for the C III 97.70 nm spectral line as functions of pressure in air (top), as well as in helium (bottom). The laser energy was 400 mJ, and the axial distances in the plasma were 2.5 mm and 3.0 mm for air and helium, respectively.

5.7 Influence of the Spectrometer Slit-Width

In all experiments that carried out so far, the spectrometer entrance slit-width was fixed at 50 μm. The aim of this section of the work is to investigate whether the plasma emission characteristics can be further improved by varying the width of the entrance slit. The slit-width in this section is varied from 10 μm to 250 μm, while its height was kept constant at 10 mm. The laser energy was set at 400 mJ, and the plasma was created in air atmosphere at a pressure of about 0.3 mbar. In addition, spectra were recorded from a region in the plasma located 2.5 mm from the target surface.

The results obtained are shown in Fig. 5.25, which illustrates the variation of line and

background emission intensities, as well as signal-to-background ratios for the C III 97.70 nm spectral line with the entrance slit-width. The line intensity demonstrated a significant enhancement with the slit-width up to 80 μm, and then levelled off up to the 250 μm width employed. The background intensity, on the other hand, kept increasing with the slit-width in the 10–250 μm range (see Fig. 5.25).

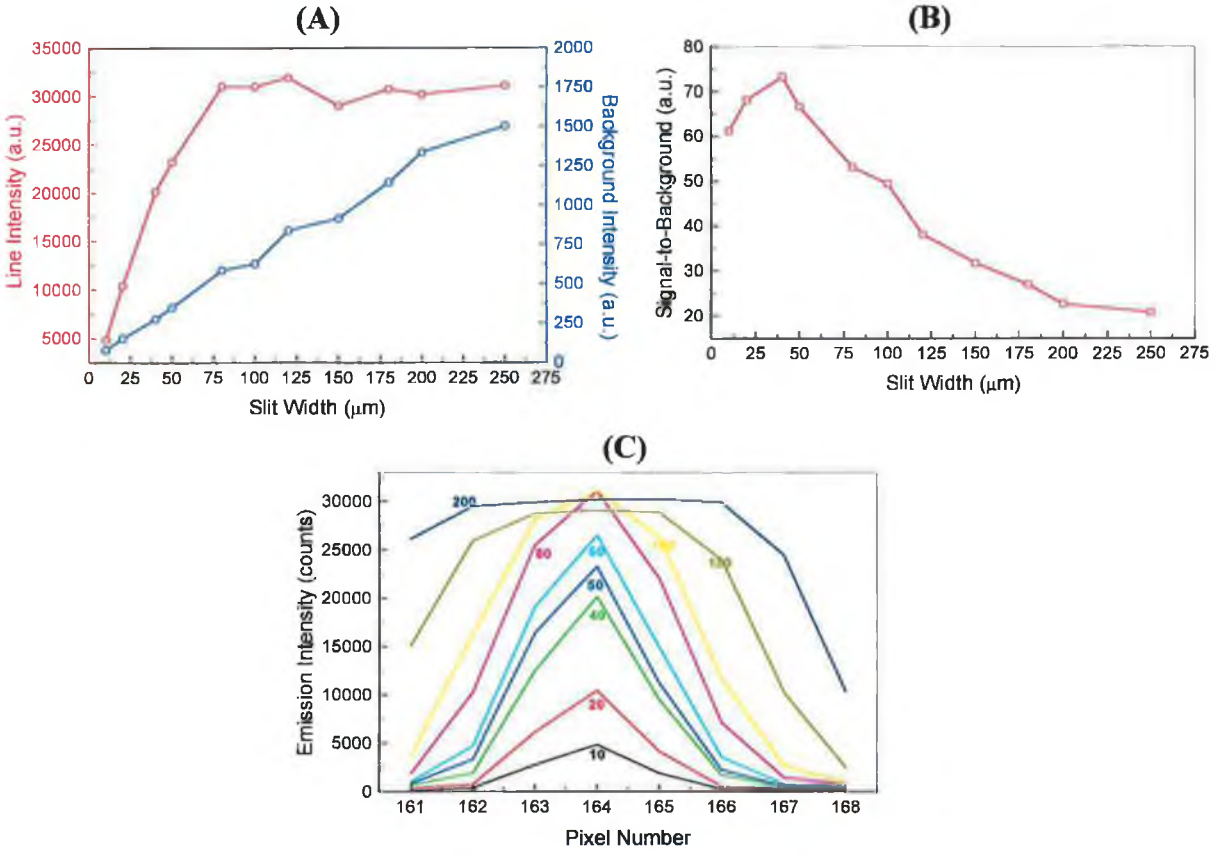

Fig. 5.25 Influence of the entrance slit-width on the emission characteristics for the C III 97.70 nm spectral line. Numbers inside (C) indicate the slit-width in μm, at which the corresponding line intensity was recorded.

The signal-to-background ratio shown in Fig. 5.25 (B) increased with the slit-width, maximized at 40 μm, before it dramatically decreased for larger widths. It can be noted that the difference between signal-to-background ratios recorded at 40 μm and 50 μm is not too significant, although it could make a distinct improvement in the overall result.

In Fig. 5.25 (C), the actual C III 97.70 nm spectral line profiles were plotted at different slit-widths. The highest emission intensity was obtained at a relatively wide slit of 80

μm, with no remarkable deformation of the spectral line shape. However, as depicted from Fig. 5.25 (B), the signal-to-background ratio at 80 μm was approximately 1.4 times than that recorded at 40 μm.

Table 5.2 summarizes the different experimental parameters and conditions investigated in this work, along with their optimized values that are to be used for constructing analytical calibration curves in the following final section.

Table 5.2 Summary of optimum values for various experimental parameters and conditions investigated in the present work.

Parameter	Optimum condition
Laser	1064 nm; 5.0 Hz; 400 mJ
Focusing lens	Cylindrical; defocused 0–4 mm
Ambient atmosphere	Air at 0.2–0.3 mbar
Axial distance	2.0–3.0 mm from the target surface
Slit-width	40 μm

5.8 Analytical Results: Calibration Curves and Limit of Detection

In chapter IV, preliminary analytical calibration curves were constructed for carbon in the steels samples under investigation. The emission intensities of the spectral lines under investigation were linear functions of concentration in the range 0.041–1.32%, with coefficients of deviation (R^2) better than 0.994. A limit of detection of 87 ppm (parts per million) for carbon in steels was deduced for the C III 97.70 nm spectral line, which proved to be the best carbon line in the VUV region in terms of sensitivity, as well as precision.

In the present section, analytical calibration curves for the C III 97.70 nm spectral line are constructed using experimental parameters and conditions that have been optimized

in the previous sections (see Table 5.2). Two different methods for construction of the analytical calibration curves are used (and compared). The first method is based on the direct measurement of relative spectral line intensities (see equations 2.25 and 2.36 of chapter II), and the other method uses the internal referencing procedure (see equation 2.37 of chapter II). In the latter approach, a plot of the intensity ratio of a spectral line emitted by a trace element (the C III 97.70 nm in this case) to that emitted by the major constituent in the sample (Fe) against the fractional concentration of the trace element should demonstrate a linear relationship.

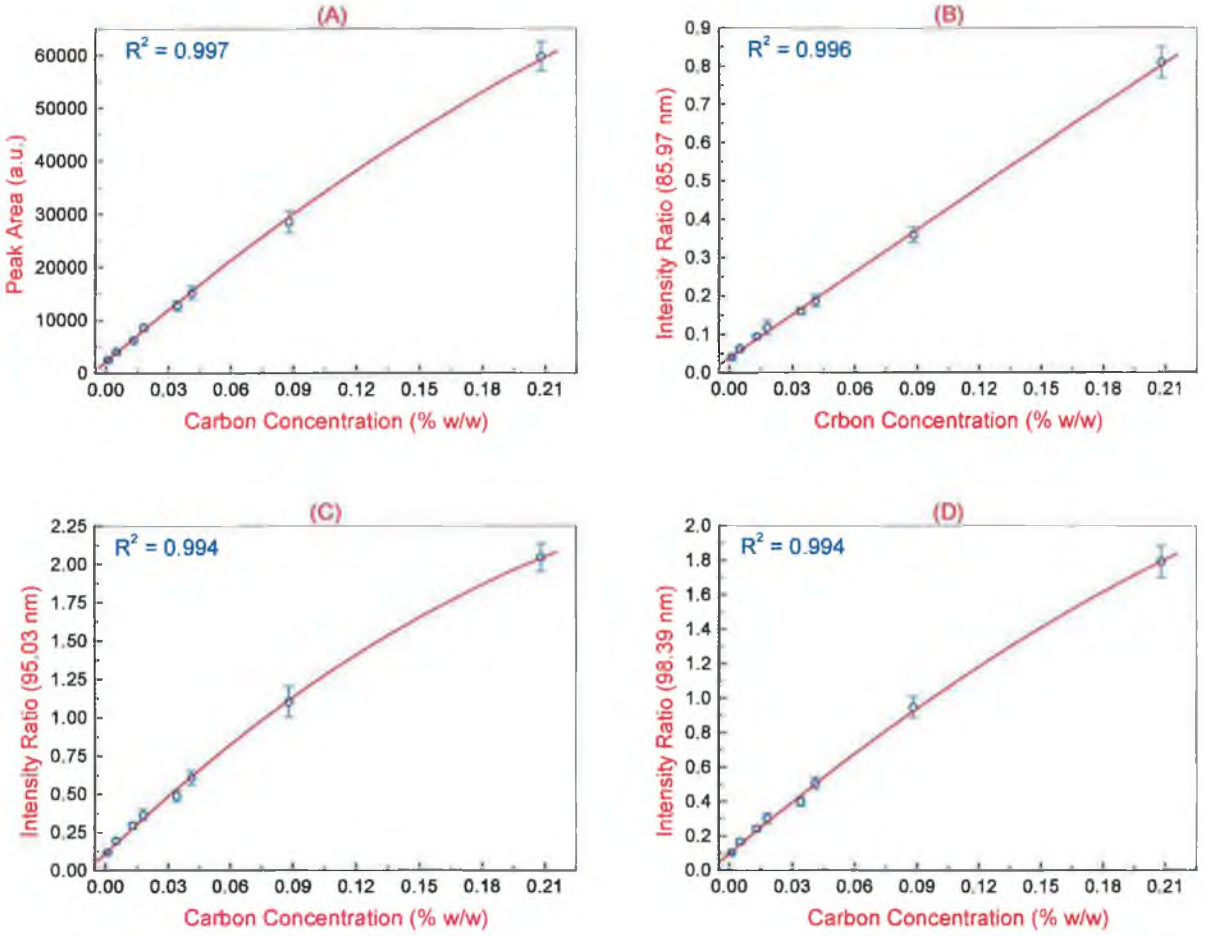

Fig. 5.26 Analytical calibration curves for the C III 97.70 nm spectral lines using two different methods. (A) Relative line intensities, and (B), (C) and (D) internal standardization method. See text for more details.

Three iron spectral lines were tested as possible internal standards for the C III 97.70 nm spectral lines. These are Fe III 85.97 nm (0.00–14.42 eV), Fe III 95.03 nm (3.76–16.81 eV) and Fe III 98.39 nm (2.52–15.12 eV). Figure 5.26A illustrates the

calibration curve obtained by plotting the integrated emission intensity for the C III 97.70 nm spectral line versus the corresponding carbon concentration. Also shown [Figs. 5.26B–5.26D], are the calibration curves, for the same spectral line, constructed using the internal standardization method, employing the three iron spectral lines previously mentioned. Note that, lower carbon concentration samples (Appendix E) than those used previously in chapter IV were employed to create the calibration curves.

Each data point in the figures represents the average of 250 laser shots recorded from five different positions on each sample, and in a random order. In addition, 50 laser shots were fired onto a fresh area of each sample prior to any measurements in order to remove any surface contaminants. At the 5 Hz laser repetition rate used, the time required to complete measurements for all the 12 samples under investigation (Appendix E) was about an hour, including the time taken to change the samples (see § 3.3.1 of chapter III). Relative line intensities were measured by integrating the area under the profile of the carbon, as well as the iron spectral lines. Finally, a second order polynomial regression function was used to fit the data in all the figures.

As can be seen from Fig. 5.26, the calibration curve obtained with the direct measurement of relative line intensities (Fig. 5.26A) compares very well with those obtained using the internal referencing iron spectral lines (Figs. 5.26B–5.26C). This result is usually taken as an evidence of complete atomization (evaporation) of the sample material penetrating into the hot centre of the plasma formed in the buffer gas used (0.3 mbar air) [81].

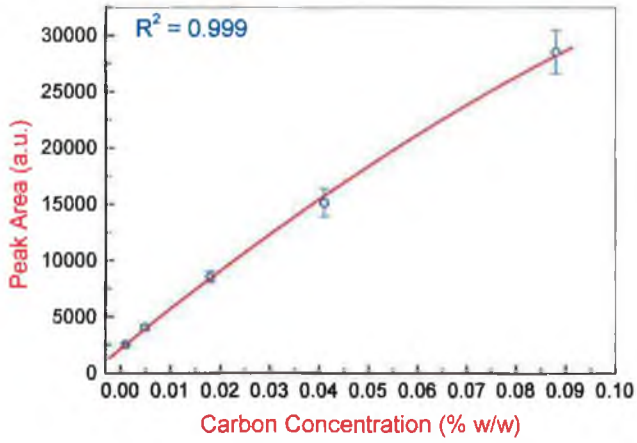

Fig. 5.27 Calibration curve for the C III 97.70 nm spectral line constructed from the lowest carbon concentrations employed in the present work.

As might be expected, the Fe III 85.97 nm spectral line proved to be the best internal standard for the C III 97.70 nm spectral line as testified by its fitting function, which more clearly represents a near linear fit (see Fig. 5.26B). Among the three iron spectral lines studied, the upper energy level for the Fe III 85.97 nm spectral line (14.42 eV) has the closest gap to that for the C III 97.70 nm spectral line (12.69 eV), and hence their intensity ratio has the highest probability to be independent on the variation in the plasma temperature. It should be mentioned at this stage that relative line intensities and line ratios in the present work were plotted against the carbon concentration and not the fractional concentration. This was due the fact that the iron concentrations in all samples were quite similar, and virtually 100%. Also noted in the figures that the spread of the five measurements for each concentration indicates reproducibility (RSD) between 3% and 5% for the analytical method. Fig. 5.27 is a reproduction of Fig. 5.26A for some of the lowest carbon concentrations used. As can be seen, the coefficient of deviation (COD) was improved, which indicates more linearity between the data points plotted. This curve was used for calculation of the detection limit.

Limits of detection were calculated using the 3σ criterion (see section 4.4 of chapter IV), where σ is the standard deviation of the background intensity for the target with the lowest carbon concentration (10 μg/g, or alternatively 0.001%). Accordingly, the limit of detection of carbon in steel obtained from the present work was estimated to be as low as 1 μg/g. The relative standard deviation of these measurements was valued at 15%. Finally, Table 5.3 presents limits of detection of carbon in steels obtained from different direct analytical techniques.

Table 5.3 Detection limits for carbon in steels measured using various direct techniques.

Author	Reference [Year]	Detection limit, μg/g
Balloffet	199 [1955]	100
Aguilera et al.	200 [1992]	65
Khater et al.	93 [2000]	87 ± 10
Sturm et al.	203 [2000]	7
Hemmerlin et al.	193 [2001]	5 (LIPS); 1 (Spark)
Khater et al.	237 [2001]	1.2 ± 0.18

CHAPTER VI

Development of Spectroscopic Diagnostic Techniques in The VUV for the Determination of Laser-Produced Steel Plasma Physical Parameters

Spectroscopic diagnostic techniques in the VUV spectral range are used for the determination of the physical parameters of laser-produced steel plasmas under consideration. The plasma electron density is estimated using the Stark broadening approach; the excitation temperature is measured by the Boltzmann's plot method for relevant spectral lines belonging to the same element and ionization stage, while the ionization temperature is evaluated by using the relative emission intensities ratio of two lines from the same element and successive ionization stages. The validity of the local thermal equilibrium (LTE) condition in the plasmas investigated is discussed, based upon the results obtained.

6.1 Introduction

There have been several diagnostic techniques employed for determining the electron densities and temperatures for a wide range of plasmas. These include emission spectroscopy [226, 238], Langmuir probes [239–240], microwave [241–242] and laser [243–244] interferometry, and Thomson scattering by microwave or laser irradiation [244]. Knowledge of the plasma physical parameters is vital for understanding the various processes taking place in the plasma such as vaporization, excitation as well as ionization, resulting in better performance and figures of merit for the relevant application. Among the above mentioned techniques, emission spectroscopy is preferred since that there is no disturbing effect on the plasma during measurements, as is the case with probes, for example, so that the data of the unperturbed plasma are obtained. In addition, the information content of a calibrated emission spectrum is very large, and the instrumentation required is relatively simple.

Laser-produced plasmas have a relatively short temporal existence and are transient in their nature, with a fast evolution of the characteristic physical parameters that are strongly dependent on different experimental conditions such as the laser energy, wavelength, pulse duration, as well as ambient gas composition and pressure. Furthermore, the plasma physical parameters significantly vary with the axial distance from the solid target surface under the same irradiation conditions. Detailed investigation of optical emission spectra emitted from a laser-produced plasma plume provides valuable information on the spatial, as well as temporal evolution of the various species produced during laser-target interaction.

In this chapter, emission spectroscopic techniques are developed in the VUV region for the determination of laser-produced steel plasma physical parameters, namely the electron number density (n_e), the excitation (Boltzmann), as well as ionization (Saha) temperatures (T_{exc} and T_{ion}, respectively) as functions of the axial distance from the target surface. The measurements reported in this chapter were produced from the same spectra recorded under the optimized operating conditions achieved in the previous chapter (see Table 5.2, chapter V). In the absence of time-gated detection, it was not possible to temporally resolve the spectral lines. Nevertheless, the time-integrated measurements provide useful data on the average values in the plasma in the different

plasma spatial zones. Whenever possible, comparisons with previous work carried out in the UV / visible spectral range, under similar as well as different experimental conditions, will be made.

6.2 Electron Density (n_e)

Electron number density (n_e) is an important physical parameter used to describe a plasma environment, and is crucial for establishing its thermodynamic equilibrium status. Although a variety of spectroscopic methods are known for the determination of n_e, the most common, precise and indeed widely used technique is based on Stark broadening of suitable and well-isolated spectral lines [225–226]. Examples of relevant spectral lines used include Si I 250.7 and 288.2 nm [97, 248], Al II 281.6 nm [248], Mg II 280.3 nm [248], C II 392 nm [137], Li I 610.3 nm [252] and various Ti II lines [139].

Stark broadening (see § 2.6.2, chapter II) is the perturbation of the energy levels of the individual atoms / ions by the changing electric fields occurring in collisions with the charged particles (electrons / ions) in the plasma, which results in broadening the corresponding spectral lines originating from these excited levels. The method is considered as a direct and reliable evaluation of electron number density of a particular plasma source in the density range $10^{14} \leq n_e \leq 10^{19}$ cm^{-3}. The most important advantage of this method is the fact that it yields electron densities that are largely independent of the temperature in the plasma, and also of any assumption about the existence of local thermodynamic equilibrium (LTE) state [226].

As previously mentioned in chapter II, the overall spectral line shape emitted from plasmas is the result of the interaction between different broadening mechanisms. Accordingly, the effective spectral line profile is a convolution of the Gaussian and Lorentzian components, and can be represented by the Voight function. However, for laser-produced plasmas investigated in the present work, other broadening mechanisms including natural, Doppler (see § 2.6.1, chapter II), resonance and Van der Waals [245–246] can be safely neglected, because relatively low-temperature (~ 0.7–few eV), high electron density (10^{17}–10^{19} cm^{-3}) plasmas are generated. The spectral line profile can therefore be represented by an approximate Lorentzian function, which is corrected by simply subtracting the contribution from the instrumental function with the use of

[128, 137, 189]:

$$\Delta\lambda_{true} = \Delta\lambda_{observed} - \Delta\lambda_{instrument} \qquad [6.1]$$

The FWHM (Full Width at Half Maximum) exhibited by an isolated spectral line due to the Stark effect is related to the electron number density in the plasma by the following expression [221]:

$$\Delta\lambda_{1/2} = 2W\left(\frac{n_e}{10^{16}}\right) + 3.5A\left(\frac{n_e}{10^{16}}\right)^{1/4}\left[1 - \frac{3}{4}N_D^{-1/3}\right]W\left(\frac{n_e}{10^{16}}\right) \qquad [6.2]$$

where $\Delta\lambda_{1/2}$ is the FWHM (Å) due to Stark broadening; n_e (cm^{-3}) is the electron number density; W and A (Å) are the electron impact and ion broadening parameters, respectively, which are independent of the electron density and slowly varying (weak) functions of the electron temperature and N_D is the number of particles in the Debye sphere. Equation 6.2 applies for neutrals; however, to make it applicable also for singly-charged atoms the numerical coefficient ¾ is replaced by 1.2 [221].

The first term on the right side of equation 6.2 represents the broadening due to electrons, while the second term is the ion correction factor. For nonhydrogenic ions, Stark broadening of spectral lines is predominantly by electron impact, and the perturbations caused by ions is negligible compared to electrons [137]. Accordingly, equation 6.2 reduces to:

$$\Delta\lambda_{1/2} = 2W\left(\frac{n_e}{10^{16}}\right) \qquad [6.3]$$

Following this approach in the present work, the electron number densities of the steel plasmas investigated were inferred from the Stark-broadened C II 68.73 nm spectral line. The electron impact parameter (W) values for this spectral line, calculated in the temperature range 0.25×10^4–8×10^4 K, are available and were taken from Griem's tables [226]. The spectral profiles of the C II 68.73 nm line emitted from three different locations in the plasma are shown in Fig. 6.1. As mentioned earlier, these measurements were performed under the same experimental conditions produced in chapter V (see

Table 5.2).

Figure 6.2 illustrates the full-width at half maximum (FWHM) for the spectral line studied as a function of the axial distance from the target surface. The corresponding electron number densities calculated through equation 6.3 from the experimental results plotted in Fig. 6.2 are shown in Fig. 6.3, for three different plasma temperatures of 10^4, 2×10^4 and 4×10^4 K; the electron impact parameters equivalent to these temperatures are 9.30×10^{-5}, 1.40×10^{-4} and 1.91×10^{-4} Å, respectively, as documented by Griem [226]. As can be seen from the figure, the electron number density decreased fairly rapidly, for all temperatures, with increasing the distance from the target surface, in the

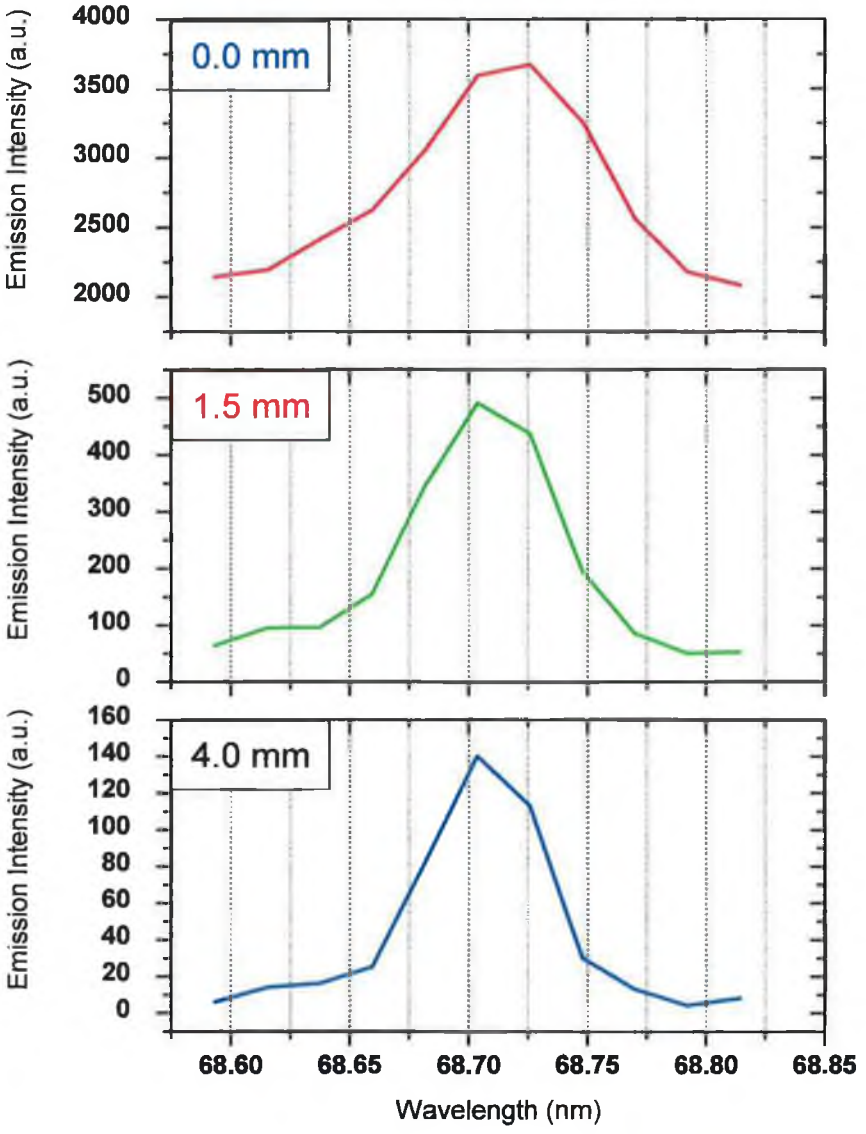

Fig. 6.1 Stark-broadened profiles for the C II 68.73 nm spectral line at three different axial distances from the target surface.

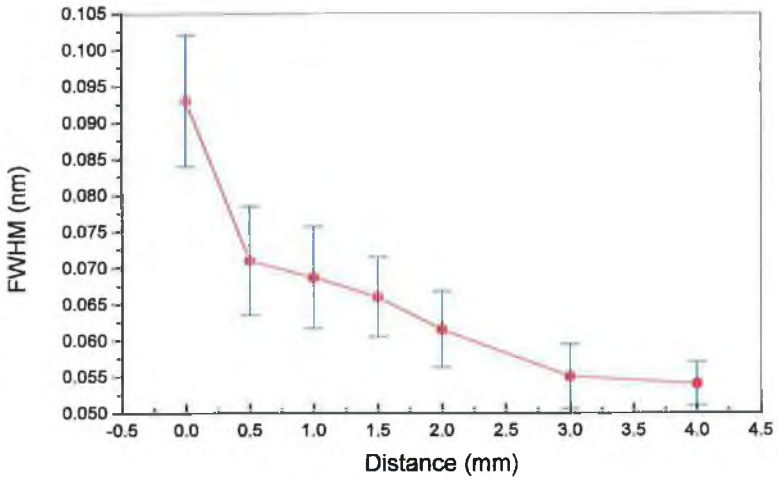

Fig. 6.2 Full width at half maximum (FWHM) for the C II 68.73 nm spectral line as a function of the axial distance from the target surface.

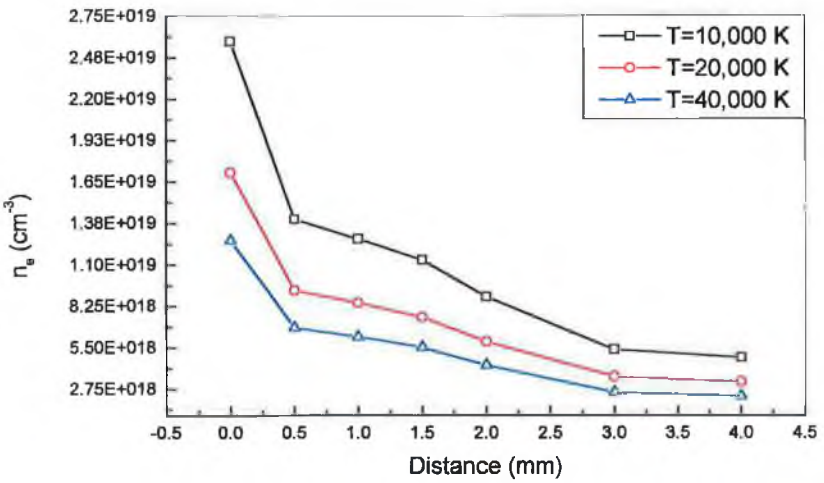

Fig. 6.3 Evolution of the electron number density as a function of the axial distance from the target surface, at different three plasma temperatures.

range 0–0.5 mm. At larger distances, the electron density slowly declined up to the maximum distance studied of 4.0 mm.

Similar space-dependent measurements of the plasma electron density observed in Fig. 6.3 were reported in previous experimental studies of laser-ablated solid targets, with almost similar [137, 185], as well as much smaller [252] laser power densities. The fall off with distance of the electron number density is related to the expansion of the

initially point source plasma plume into a large volume [251]. In fact, other studies employing time-resolved measurements at various power density levels also confirm the trend seen in Fig. 6.3, in which the rapid decrease of the electron number density takes place within about 300 ns after the termination of the laser pulse, after which the density slowly decreases for the rest of the plasma lifetime [139, 144, 248, 253].

For plasma temperatures of about 2×10^4 K, the time-integrated electron density obtained in the present work ranged from 2.58×10^{19} cm^{-3} very close to the target surface to 2.36×10^{18} cm^{-3} at 4.0 mm away from the target surface. In a similar laser-produced plasma investigation carried out in the VUV range [254], electron densities larger than 10^{18} cm^{-3} at 0.5 mm, of the order of 10^{18} cm^{-3} at 1 mm and around 7×10^{17} cm^{-3} at 1.5 mm from the target surface were estimated, though using much less laser power densities (~ 0.13 GW/cm^2, compared to ~ 5 GW/cm^2 used in the present work).

6.3 Excitation Temperature (T_{exc})

The excitation (Boltzmann) temperature (T_{exc}) is an equally important plasma physical parameter. T_{exc} can be spectroscopically determined in a variety of ways: from the ratio of integrated relative line intensities of the same atom or ion [254–255], from the integrated relative spectral line intensities of the same atom or ion (Boltzmann plot) [131, 144, 185, 248, 256–258], from the ratio of line intensity to underlying background continuum [253] or from the relative intensity and shape of the continuum spectrum [238]. The plasma excitation temperature determined in any of these ways is sometimes referred to as the spectroscopic temperature. Among the mentioned methods, the first two approaches are the most popular and widely used.

In determining the plasma excitation temperature using the spectral line ratio technique, the following assumptions are followed:

- The plasma source volume under consideration is in local thermodynamic equilibrium (LTE), has a homogenous distribution of emitters and remains in a steady state during the time (space) interval of interrogation.

- The spectral lines selected are optically thin, and their relevant oscillator strengths must be well known.
- The population distribution amongst the internal energy levels is described by the Boltzmann distribution function.

The excitation temperature, T_{exc}, is given by the following equation [247]:

$$T_{exc} = \frac{E_j - E_i}{k} \ln\left(\frac{I_j g_i A_i \lambda_j}{I_i g_j A_j \lambda_i}\right) \qquad [6.4]$$

where I represents the relative integrated intensity recorded for the two spectral lines (indexed i and j) of the same element and ionization stage; k is the Boltzmann constant; E is the excitation energy for the upper level; g is the statistical weight (degeneracy) of the upper level; A is the transition probability of the upper level and λ is the wavelength. The two-line method has the advantage in comparison with a single-line radiance method (absolute measurements) in that one eliminates the need for knowing the value for the effective pathlength through the source, the total particle number density, the partition function and the need for an absolute radiance calibration of the detection system, as well as the absolute transition probabilities. In practice, the spectral line pair should have almost identical wavelengths and the difference in the upper energies of the two transitions as large as possible. The first criterion is useful in the sense that relative intensity calibration is easier and more accurate, and the second criterion assures that the temperature calculated is more reproducible and not sensitive to small fluctuations in the intensity ratio measurements.

The two-line ratio technique usually, however, suffers from relatively poor accuracy (even if LTE exists), mainly because the relative emission intensity ratio is fairly insensitive to changes in temperature. An obvious solution to this problem is to extend the observations to a larger number of spectral lines from the same element and ionization stage. This is similar to applying a least-squares linear regression to a larger number of points to determine the slope and intercept instead of determining the linear relationship from just two points; some improvement in accuracy is certainly achieved in this way. Recalling the equation for the intensity of a spectral line emitted from LTE plasmas (Equation 2.35, chapter II):

$$I = \frac{h\nu_{pq}}{4\pi} A_{qp} \frac{N_T g_q}{Q(T_{exc})} \exp\left(-\frac{E_q}{k_B T_{exc}}\right) \qquad [6.5]$$

The relationship between the oscillator strength, *f*, and the transition probability, A, for the same transition can be represented by the Ladenburg formula [234]:

$$f = \frac{\lambda^2 mc}{8\pi^2 e^2} A \qquad [6.6]$$

where e and m are the electronic charge and mass, respectively. Now substituting for the oscillator strength from equation 6.6 into equation 6.5 one obtains:

$$I = \frac{2\pi he^2}{m\lambda^3} \frac{N_T(gf)}{Q(T_{exc})} \exp\left[-\frac{E}{kT_{exc}}\right] \qquad [6.7]$$

Rearranging equation 6.7, and taking the logarithm we get:

$$\log\left(\frac{I\lambda^3}{gf}\right) = \log\left(\frac{2\pi N_T he^2}{Q(T_{exc})m}\right) - \frac{E}{kT_{exc}} \qquad [6.8]$$

In the application of the foregoing equation for the determination of the excitation temperature, a number of spectral lines of one and the same species are selected and their relative integrated intensities are measured; since these lines belong to the same element, the partition function, Q, and total number of particles, N_T, are the same for all spectral lines. If the population of the excited states follows the Boltzmann distribution law, then the plot of log ($I\lambda^3/gf$) versus the excitation energy, E, should provide a straight line with a slope equals to ($-1 / kT_{exc}$). This plot is usually called the Boltzmann plot. It is worth mentioning here that relative intensities and *gf* values for the measured spectral lines, as opposed to absolute values, will not affect the calculated temperature, and will only result in a change of the intercept. Also, the same practical considerations regarding closely matched wavelengths for accurate relative intensity calibration, and large differences in upper energies from which the transitions originate to give better precision in the calculated temperature, apply similarly to both the two-line ratio and the

Boltzmann plot techniques.

After testing many lines in the VUV range, five Fe III spectral lines located in the wavelength region 89.9–93.2 nm were selected for the determination of the steel plasmas excitation temperatures, using the Boltzmann's plot method; these spectral lines proved to be satisfactory for the general criteria described above. Table 6.1 lists the wavelengths, *gf* values, as well as the lower and upper energy levels for the Fe III spectral lines employed [259]. Moreover, Fig. 6.4 illustrates a portion of the steel plasma emission spectrum in the mentioned wavelength range, showing the Fe III spectral lines under investigation.

Table 6.1 Wavelengths, *gf* values and energy levels for the Fe III spectral lines selected for the determination of the excitation temperature using Boltzmann's plot [Ref. 259].

λ, nm	*gf*	E_{lower}, cm^{-1} (eV)	E_{upper}, cm^{-1} (eV)
89.960	8.32×10^{-5}	30886.4 (3.83)	142047.0 (17.61)
91.122	3.00×10^{-3}	50295.2 (6.24)	160037.9 (19.84)
91.814	0.1012	82001.7 (10.17)	190918.2 (23.67)
91.939	6.6×10^{-5}	30857.8 (3.83)	139625.2 (17.31)
93.195	2.5×10^{-5}	30886.4 (3.83)	138187.9 (17.13)

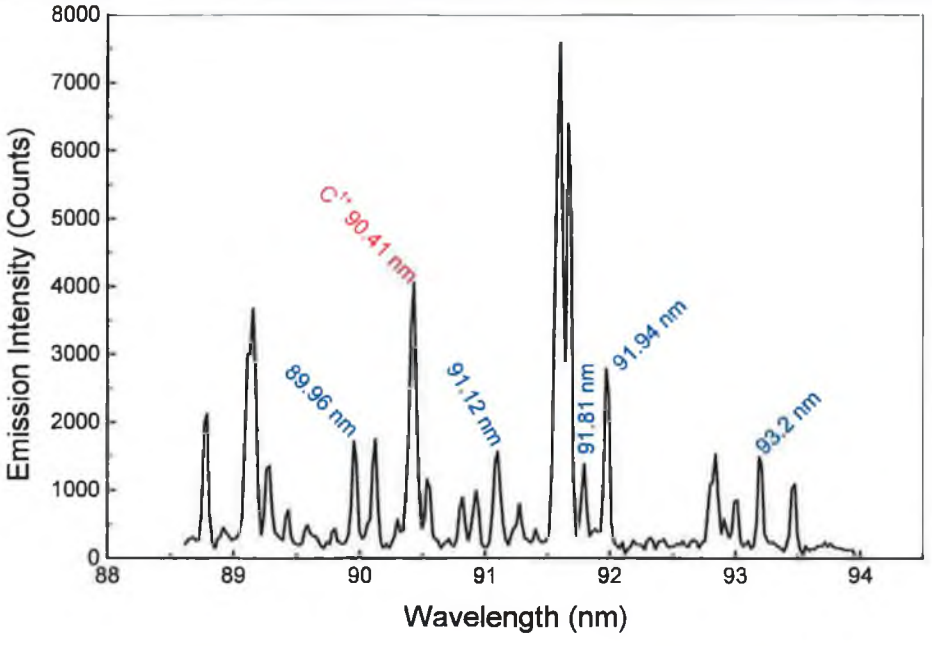

Fig. 6.4 Fe III spectral lines (in blue) used for constructing Boltzmann's plot. Also shown is the C II 90.41 nm (in red) spectral line.

The maximum energy difference between the upper excited levels of these spectral lines is 6.54 eV (52748.4 cm^{-1}). Using equation 6.8 along with parameters shown in Table 6.4 and the integrated line emission intensities recorded, Boltzmann plots for the different Fe III spectral lines studied were constructed as a function of the axial distance from the target surface. Examples of these plots are shown in Fig. 6.5 for the distances 1.5, 2.0 and 2.5 mm with respect to the target surface.

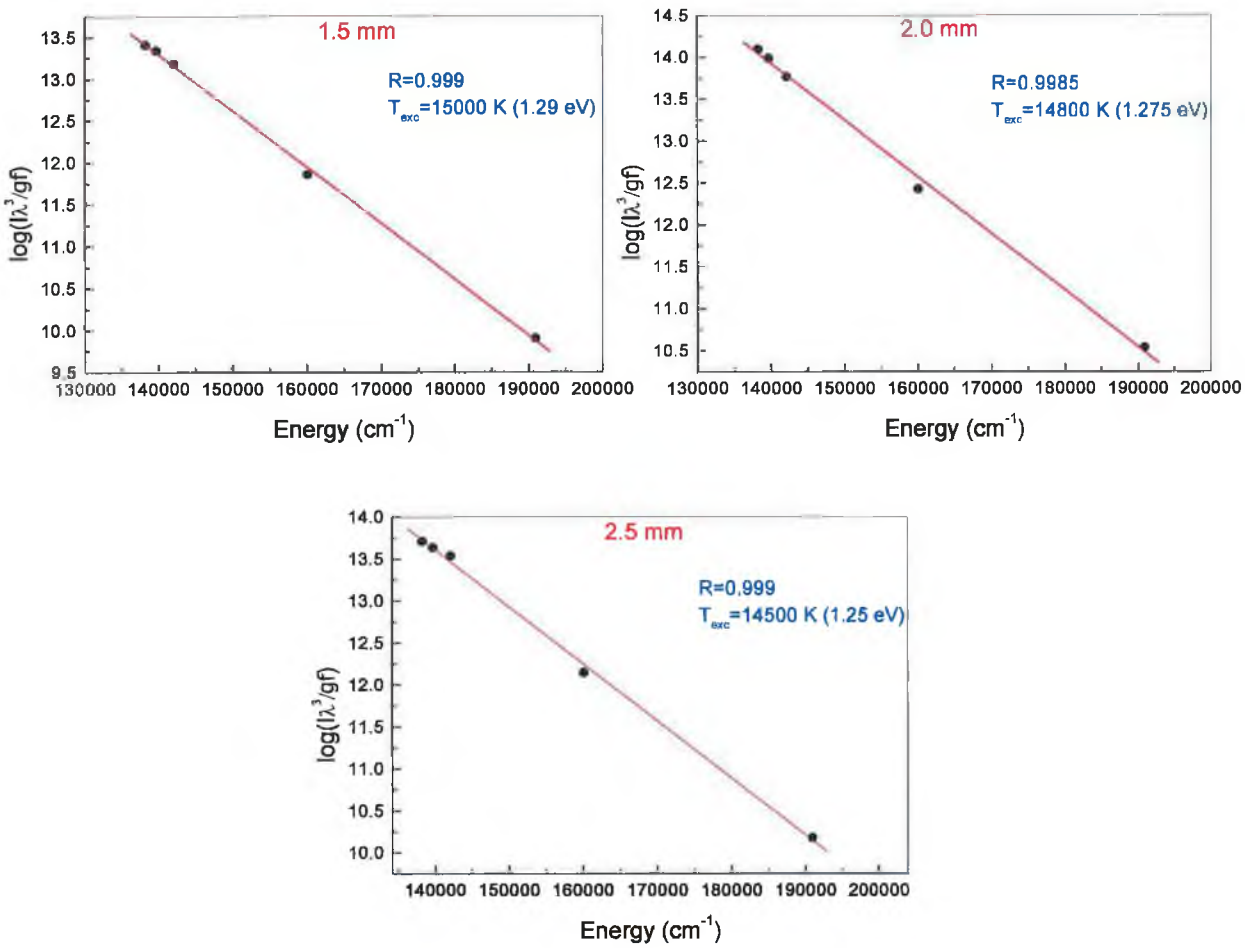

Fig. 6.5 Examples of Boltzmann plots for the VUV Fe III spectral lines selected (see Table 6.1) at different distances from the target surface of 1.5, 2.0 and 3.0 mm. Also shown are the corresponding excitation temperatures calculated from the slopes of the fitted lines.

As can be noted from Fig. 6.5, the excitation temperatures measured are slowly varying functions of the location in the plasma, at relatively large distances (1.5–3.0 mm) from the target surface; they varied between 15000 K (1.29 eV) at 1.5 mm, and 14300 K

(1.23 eV) at 3.0 mm. Due to the strong emission signal from the background continuum at distances smaller than 1.5 mm, the measurement of the Fe III spectral line intensities was virtually impossible, and hence the corresponding excitation temperatures could not be evaluated in this range (0.0–1.5 mm). The spatial zone stretching between 1.5 mm and 3.0 mm is, however, the most important for analytical applications utilizing laser-produced plasmas, as demonstrated in the previous two chapters.

6.4 Ionization Temperature (T_{ion})

The plasma ionization temperature is usually determined by the relative intensity ratio of two suitable spectral lines representing *successive* ionization stages of the same element. The relevant energy difference is now enhanced by the ionization energy, which is often much larger than kT. In LTE plasmas, the ratio of such spectral lines is given by the combined Saha-Boltzmann equation [238, 248]:

$$\frac{I_{ion}}{I_{atom}} = 4.83\times10^{15}\left(\frac{gA}{\lambda}\right)_{ion}\left(\frac{\lambda}{gA}\right)_{atom}\left(\frac{1}{n_e}\right) \times T_{ion}^{\,3/2}\exp\left[-\frac{E_\infty + E_{ion} - E_{atom} - \Delta E_\infty}{kT_{ion}}\right] \qquad [6.9]$$

where n_e is the electron number density (cm^{-3}); I is the integrated spectral line emission intensity (arbitrary unit); gA is the product of the statistical weight and Einstein coefficient for spontaneous emission of the upper level (s^{-1}); λ is the wavelength (nm); T_{ion} is the ionization temperature (eV); E_∞ is the ionization energy of the lower energy stage (eV); E_{ion} and E_{atom} are the excitation energies of the higher and lower ion stages, respectively (eV); k is Boltzmann's constant (8.617×10^{-5} eV K^{-1}) and ΔE_∞ is the correction to the ionization energy E_∞ of the lower ionization stage due to plasma interactions, and can be estimated using the following formula [137]:

$$\Delta E_\infty(eV) = 3zb\frac{e^2}{4\pi\varepsilon_0}\left[\frac{4\pi\times10^6 n_e}{3}\right]^{1/3} \qquad [6.10]$$

where z = 2 for the lowest ionization stage, e is the electron charge (C), ε_0 is the

permittivity of the free space (F m^{-1}), n_e is the electron number density (cm^{-3}), and b = 6.2414×10^{18} is the energy conversion factor from joules to eV.

Spectral lines used for the determination of the ionization temperature should be simultaneously detected, i.e. located in the same spectral window. In addition, relative emission intensities with large signal-to-background ratios and no overlapped lines are required to increase the precision, as well as the accuracy of the measurements. In order to satisfy these conditions for the present work, the C II 90.41 nm and C III 97.70 nm spectral lines were selected for measuring the ionization temperature of the steel

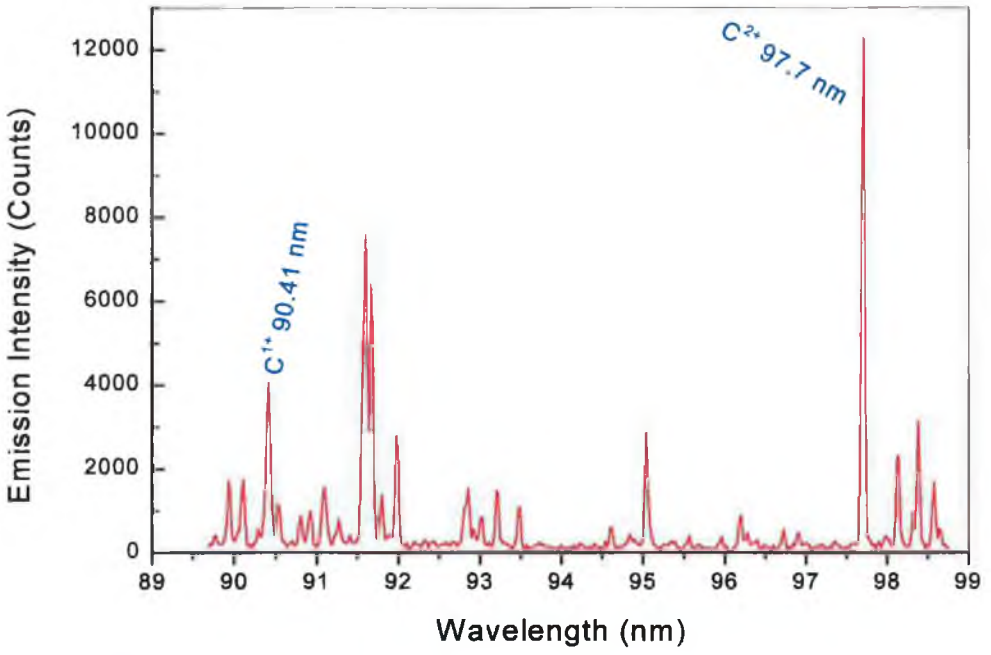

Fig. 6.6 Emission intensities for the C II 90.41 nm and C III 97.70 nm spectral lines used for estimating the plasma ionization temperature in the present work.

plasmas investigated, as a function of the distance from the target surface. The atomic constants for both spectral lines needed for equation 6.9 were taken from Table 4.1 and Ref. 233. Figure 6.6 shows a part of the steel plasma VUV emission spectrum in the 89–99 nm wavelength range, illustrating the carbon spectral lines employed.

The electron number density values determined earlier (section 6.2), along with the recorded integrated emission intensities for the two carbon lines, as well as other atomic

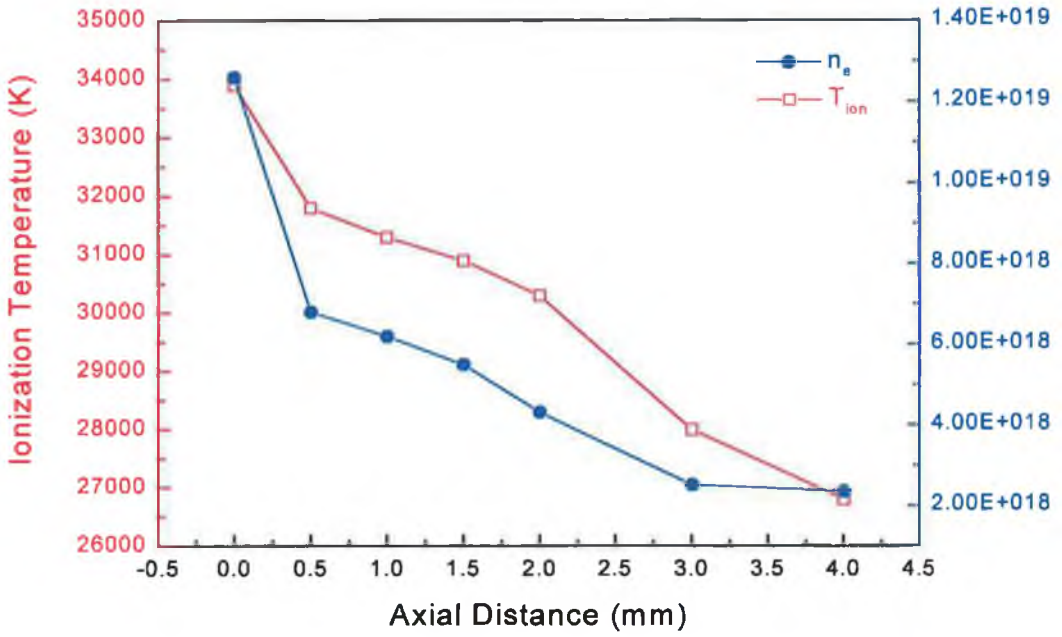

Fig. 6.7 Plasma ionization temperatures (red) obtained in the present work as functions of the axial distance from the target surface. For comparison purposes, the corresponding electron densities (blue) are also shown.

data and constants were introduced into equation 6.9. Then a simple iterative code [Appendix F], written in Qbasic language, was used to calculate the corresponding ionization temperature at each particular distance from the target surface.

Table 6.2 Plasma electron number densities, as well as excitation and ionization temperatures obtained in the present work at various distances from the target surface.

Distance (mm)	n_e (cm^{-3})	T_{exc} (K)	T_{ion} (K)
0.0	1.3×10^{19}	-	33900
0.5	6.8×10^{18}	-	31800
1.0	6.2×10^{18}	-	31300
1.5	5.5×10^{18}	15000	30900
2.0	4.3×10^{18}	14800	30300
3.0	2.5×10^{18}	14300	28000
4.0	2.3×10^{18}	-	26800

The results obtained indicate ionization temperatures ranging from 33900 K (2.92 eV) very close to the target surface to 26800 K (2.41 eV) at 4.0 mm away from it. Figure 6.7. illustrates the ionization temperatures obtained as functions of the distance from the target surface; the electron densities corresponding to these temperatures are also shown in the figure. Furthermore, Table 6.2 presents a comparison between electron densities, excitation as well as ionization temperatures obtained in the present work at various axial distances from the target surface. It is interesting to note that, like the excitation temperature, the plasma ionization temperature is a slowly decreasing function of location in the plasma at relatively larger distances from the target surface.

The behaviour of the plasma ionization temperature seen in Fig. 6.7 was also observed in other previous studies employing spectral lines in the visible range [137, 260]. In the first study [137], the ionization temperature, of plasmas generated by the fundamental radiation from a Nd:YAG laser focused onto a graphite target under vacuum (~ 10^{-4} mbar), varied between 2.46 eV (28540 K) at 1.5 mm to 1.66 eV (19260 K) at about 12 mm away from the target surface. However, the laser power density was about 10 times higher than that employed in the present work, and the plasma electron density was almost an order of magnitude lower than that obtained here.

In the second investigation [260], the spatial as well as temporal evolution of electron density and ionization temperature for both neutral and singly-ionized lithium atoms was investigated under vacuum. The on-target power density was estimated to be very close to 1 GW/cm^{-2}, which is about 5 times lower with respect to that used in the present work. The ionization temperatures measured using the combined Saha-Boltzmann equation (equation 6.9) ranged between 2.82 eV (32712 K) at 2.5 mm away from the target surface and 2.65 eV (30740 K) at a distance of 7.5 mm; The corresponding electron densities were 1.3×10^{18} and 0.2×10^{18} cm^{-3}, respectively.

In another relevant publication [256], the temporal variation of temperature and electron density in a CO_2 laser-induced air plasma was investigated. The ionization temperature ranged from 175000 K (15.1 eV) at 5 μs to less than 10000 K (0.86 eV) at 25 μs, while the excitation temperature varied from 19000 K (1.64 eV) at 1 μs to above 11000 K (0.95 eV) at 25 μs. The study showed that at delay times greater than 20 μs, the two temperatures converge, implying thermodynamic equilibration between the species.

6.5 Thermodynamic Equilibrium Considerations

For the purposes of determining the plasma temperatures, it was necessary to assume that the laser-produced steel plasmas under consideration reached a state of LTE soon after the termination of the laser pulse. In LTE plasmas, it is essential that the velocity distribution of the free electrons be Maxwellian. Griem [249] stated that in relatively dense, low-temperature plasmas ($n_e > 10^{16}$ cm^{-3}, kT < 5 eV), the electron velocity distribution is almost always Maxwellian. In the spatial region investigated in the present work, i.e. 0–4 mm, the steel plasmas produced have electron densities ranging from 1.3×10^{19} to 2.3×10^{18} cm^{-3}, with corresponding ionization temperatures of 2.92–2.31 eV (see Table 6.2). Accordingly, one expects that the free-electron velocity distribution will be Maxwellian.

Furthermore, in LTE plasmas the populations of atomic and ionic excited states are mostly maintained by electron collisional excitation and deexcitation processes, as opposed to radiative processes. Moreover, the populations of bound energy states must follow Boltzmann distribution, which implies a state of thermodynamic equilibrium between electron and atom / ion distributions. The minimum electron density (in cm^{-3}) required for LTE between two states separated in energy by ΔE (in eV) is a function of the plasma temperature (in K), and is given by the following expression [221]:

$$n_e = 1.6 \times 10^{12} \sqrt{T_{exc}} (\Delta E)^3 \qquad [6.11]$$

For ΔE = 9.58 eV, which corresponds to the largest energy gap investigated, i.e. the energy of the shortest wavelength transition used in the excitation temperature determination, i.e. 89.96 nm (see Table 6.1), and an excitation temperature of 15,000 K, n_e should be at least 1.7×10^{17} cm^{-3}. For the steel plasmas studied, n_e is in excess of 10^{18} cm^{-3} for the spatial range investigated of 0–4 mm. This suggests that LTE is likely to exist throughout the excited states in the plasma.

An important, but not necessary, requirement for LTE plasmas is close agreement of measurements of the different energy distributions, i.e. kinetic, ionization (Saha), and excitation (Boltzmann) temperatures (in the plasmas investigated in the present work,

however, the concept of kinetic temperature, which describes the velocity distribution of atoms / ions, has no thermal equilibrium significance because the electron number density is high enough so that both electron-atom and electron-ion collisions are more important than atom-ion or ion-ion interactions). Such a "single" plasma temperature was not observed in the present investigations, which might suggest non-thermal equilibrium conditions. Differences in the ionization and excitation temperatures are clearly observed in Table 6.2.

The apparent discrepancy between excitation and ionization temperatures is not believed to be significant, however, because of the relatively high degree of uncertainty associated with the line ratio method used for determination of the ionization temperature [255, 258]. The accuracy of this method is usually limited by the uncertainty of the oscillator strengths for the observed VUV carbon transitions. Furthermore, the time-integrated technique followed in the present work for recording the relative intensities and widths of spectral lines under consideration may significantly contribute to the relatively large temperature differences observed. However, it is expected that both temperatures will converge at larger distances from the target surface (> 5 mm), assuming that the VUV iron and carbon spectral lines are still emitting, with good records of signal-to-background ratios, at such distances. The convergence between excitation and ionization temperatures has been previously observed, employing time-resolved laser-produced plasma measurements, for visible transitions at relatively long delay times after the termination of the exciting laser pulse [248, 256, 258].

The results suggest that detailed time-, as well as space-resolved measurements of the plasma physical parameters in the VUV spectral range are required, particularly in the power density range 10^{8}–10^{11} W/cm^{2}, where many important practical applications of laser-produced plasmas have been developed. For example, the influence of the laser parameters (energy, wavelength and pulse width) and surrounding ambient atmospheres on the electron densities as well as on excitation and ionization temperatures, as functions of space and time, will definitely improve the current understanding of the way lasers interact with various solid materials, leading to a more efficient use of many relevant techniques in current applications, as well as developing novel methods and applications utilizing laser-produced plasmas.

CHAPTER VII

Summary, Conclusions, Future Work and Technique Developments

In this final chapter, a summary of the present work, including the set-ups employed, as well as conclusions of the main results obtained are presented. Also, the feasibility of further developments for the laser-induced plasma spectroscopy (LIPS) technique developed in the present work, either alone or in combination with other recently developed laser-based techniques, are briefly suggested and discussed as possible future lines of research.

7.1 Summary and Conclusions

In the present work, the analytical feasibility of laser-produced plasmas in the deep *vacuum ultraviolet* (VUV) region (40 nm to 160 nm) for the quantitative determination of the element *carbon* in standard reference samples of low-alloy steels (carbon steels) has been investigated by optical emission spectroscopy (OES). Carbon was chosen as a test element, because it, along with other light (low-atomic number) elements such as N, P, O and S, plays an extremely important role in determining some of the mechanical and physical properties, e.g. stiffness and ductility, of almost all steel products. The carbon concentration range studied extends from 0.001% up to 1.32%; many important industrial and technological products are being manufactured from various steel alloys containing carbon in this concentration range. Prior to this work, the laser-induced plasma spectroscopy (LIPS) technique has only been employed in the UV / visible spectral region. It has been used in carrying out various on-line and in-situ analytical applications, particularly those involved in hostile and harsh environments. However, because of the well-known fact that the strongest spectral lines of light elements are emitted from their ions in the vacuum ultraviolet, it was decided from the beginning to employ a VUV-LIPS set-up for the quantitative characterization of the steel alloys, in order to get the best analytical figures of merit, i.e. sensitivity, precision, etc.

To achieve the above-mentioned aim, a VUV-based laser-induced plasma spectroscopic technique has been developed, using time-integrated spatially-resolved optical emission spectroscopy. For the first time, the effectiveness of employing this technique in the deep VUV in eliminating the need for more expensive time-gated detector systems has been explored. Six prominent VUV ionic spectral lines of carbon, representing three ionization stages of II, III and IV, have been carefully chosen and proved to be spectral-interference free. These are C III 45.96 nm, C II 68.73 nm, C II 90.41 nm, C III 97.70 nm, C III 117.57 nm and C IV 154.82 nm.

Three modern, high-peak power Nd:YAG lasers, operating at the fundamental wavelength 1064 nm as well as at the second, third and fourth harmonics, i.e. 532, 355 and 266 nm, respectively, have been used to produce the steel plasmas under investigation. The laser pulses were focused onto the surface of the steel samples by using either a plano-convex spherical or cylindrical lens, with relatively long focal

lengths (125 mm and 150 mm, respectively). The plasmas were produced inside an aluminum cube chamber, under vacuum (~ 2×10^{-5} mbar). A vertical fore-slit, of approximately 250 μm width, mounted within the target chamber on the spectrometer side of the sample, provided the required spatial discrimination in the plasma viewed by the vertical spectrometer entrance slit. The fore-slit was fixed in position with respect to the optical axis of the spectrometer, while the sample holder could be moved horizontally to access different spatial regions in the plasma plume. The VUV radiation emitted from the plasma was dispersed using a 1-m, Rowland mount-based, normal incidence vacuum spectrometer (Acton, Model VM-521), equipped with a concave reflective holographic grating (Al + MgF_2 coating); the grating had 1200 grooves/mm and a reciprocal linear dispersion of 0.83 nm/mm in the first order. A combination of rotary and turbo-molecular pumps was used to pump the spectrometer chamber down to about 2×10^{-6} mbar.

The dispersed radiation was detected using two VUV-sensitive, non-gated multichannel detectors. The first detector used was a combination between a channel electron multiplier array / photodiode array (CEMA / PDA). The second detector was a backside-illuminated, and anti-reflection coated charge-coupled device (CCD) array. A set of 12 certified steel reference samples with carbon concentrations in the range 0.001% to 1.32% were used to construct analytical calibration curves. Each sample was turned down to 15 mm diameter, and the 12 samples were fitted into two circular target holders of 60 mm in diameter. The turn-round time between mounting a target holder in the vacuum chamber and resuming measurements was less than 15 minutes.

The following conclusions can be drawn from the results obtained in the present work.

It is a well known fact that laser-produced plasmas emit a strong background continuum radiation stretching throughout the visible and VUV spectral ranges. For emission spectroscopic studies, therefore, it is essential that this continuum radiation is in some way screened out in order to maximize the contrast of the overlying spectral lines. Fortunately, an inherent characteristic feature of the plasma background continuum is that it lasts for a much shorter time than the spectral line emission. Accordingly, almost all studies on applications of laser-produced plasmas to the elemental characterization of solid materials discriminate against this continuum emission by using time-gated

detectors to monitor spectral lines after decay of the strong background radiation. Nevertheless, this option is usually relatively expensive, is not easily extended to the VUV spectral regime and its suitability depends on the relevant application and experimental conditions.

Spatially-resolved technique:

In the present work, it has been demonstrated that an alternative, simple, inexpensive and effective method of discriminating against the continuum emission is to exploit the space dependence of the laser-produced plasma emission. In the VUV spectral range, the very high level of background continuum is mostly emitted from a region of about 0–1 mm above the target surface, after which it starts a dramatic decrease permitting the overlying spectral line intensities of various species in the plasma to maximize. The fore-slit, of approximately 250 μm wide and ~ 1.5 cm high, vertically mounted in the target chamber on the spectrometer side of the target, provided the required spatial discrimination in the plasma viewed by the vertical spectrometer entrance slit. In this way, the emission was selected from a narrow 'slice' of the plasma parallel to the target surface.

Different spatial regions of the plasma could be sequentially examined by carefully moving the backside target holder, while the fore-slit was kept fixed in position with respect to the optical axis of the vacuum spectrometer used. The best results were obtained at distances of 1–3 mm from the target surface for all six carbon spectral lines under investigation, where the background continuum radiation is low and the spectral lines emitted are relatively strong and narrow. This resulted in a significant enhancement of the spectral line-to-background intensity ratios. Due to the rapid expansion and cooling, as well as different recombination processes, the spectral intensities of these lines dramatically decreased at distances greater than 3 mm above the target surface.

Linear analytical calibration curves, with correlation coefficients (R^2) better than 0.994, were constructed for the carbon spectral lines under study in the concentration range between 0.041% and 1.32%. The overall precision of measurements was between 3.5% for the 97.70 nm and 10% for the 117.57 nm doubly-ionized spectral lines. Preliminary limits of detection were determined for all carbon spectral lines under investigation, and

the best detection limit of 87 ± 10 ppm (parts per million) was obtained from the 97.70 nm C^{2+} spectral line. The use of this spectral line also provided a best overall accuracy of 5.5% for the quantitative determination of carbon in steel alloys.

In order to further improve the sensitivity of the VUV-based LIPS technique developed in the present work, the CEMA / PDA detector was replaced by a modern CCD array and measurements were performed using steel samples with lower carbon concentrations. Moreover, an extensive series of optimization studies for various experimental parameters and conditions was carried out. These included the laser focusing lens types (spherical *versus* cylindrical), laser power density, laser harmonics, laser pulse energy, ambient atmospheres and pressures, as well as spatial distribution of the emitting species in the plasma.

Laser-beam focusing lens types:

In the case of focusing the laser pulse with the spherical lens, circle-like craters of the target surface were created, with diameters varied from 0.5 mm (70 GW/cm^2) and 2 mm (5 GW/cm^2). When the laser beam was focused using the cylindrical lens, vertical line plasmas were formed at the target surface; the length of these relatively long plasmas was about 8 mm, as indicated by the imprint left on the sample surface. The highest power density, obtained at the best focus position, was about 7 GW/cm^2, whereas at about 15 mm away from this position the irradiance reduced to ~ 2 GW/cm^2.

For the spherical lens, the spectral line intensities as well as signal-to-background ratios for the different six wavelengths under investigation were maximized when the focus of the lens located 2–5 mm and 2 mm behind the target surface, respectively. In the case of the cylindrical lens, the highest spectral line intensity was obtained when the lens was slightly displaced behind the best focus position, i.e. the position of the laser beam focus was 3–5 mm in front of the target surface. The signal-to-background ratio, on the other hand, was maximized in such a way that the laser focus is located either on the target surface or up to 4 mm away from it, which indicates that the maximum signal-to-background ratios are insensitive to the location of the focus of the cylindrical lens within this range. When the cylindrical lens was employed, the positions at which the emission intensities, as well as signal-to-background ratios maximized were approximately the same for various carbon ionic stages investigated.

Another important advantage of the cylindrical lens over the spherical lens was that spectral line intensities, as well as signal-to-background ratios were much higher, under the same operating conditions, for all spectral lines under study. This can be explained by the fact that the amount of light admitted to the spectrometer in case of the cylindrical lens was higher than that obtained by using the spherical lens as the laser focusing element.

Laser parameters and ambient atmospheres:

The fundamental radiation at 1064 nm proved to be the most effective wavelength for steel analysis by the LIPS technique in the VUV spectral range, when compared to the Nd:YAG harmonics at 532 nm, 355 nm and 266 nm. The results obtained in the present work demonstrated the strong dependence of the laser-produced steel plasmas spectral emission characteristics (line intensities, background intensities and signal-to-background ratios) on the laser pulse energy, various ambient atmospheres and pressures, as well as on the position of the relevant species in the plasma.

The spectral line intensities significantly increased with increasing both the laser energy and pressure of the three surrounding atmospheres (air, argon and helium) under consideration. The highest emission intensities were produced in argon within the pressure range 0.5–1.0 mbar, and at the largest laser energy deposited onto the target surface (800 mJ). Similarities in the spectral emission characteristics of plasmas created in air and argon atmospheres, compared to helium, can be explained, to some extent, on the basis of differences in the mass density of the respective gas. The mass density of helium is about one order of magnitude lower than that of argon, while the density difference between argon and air is negligibly small.

The significant enhancements observed in the spectral line intensities for the various atmospheres may be explained in terms of additional excitation / ionization processes of the ablated sample material, taking place in the buffer gas plasma formed in front of the target surface. For laser ablation in vacuum, these important processes are absent and so the resultant analytical efficiency is considerably lower. Also, due to the fact that plasmas generated in argon have higher electron temperatures, the efficiencies of atomization, excitation, as well as ionization processes are higher compared to air and helium atmospheres. The dramatic decrease in the spectral line intensities observed at

higher pressures of air and argon atmospheres can be interpreted by the *shielding effect*. Because of the higher ionization potential of helium compared to air and argon (24.6 eV for helium, 15.8 eV for argon, 5.6 eV for nitrogen and 12.1 eV for oxygen), gas breakdown in helium did not take place, even at pressures ranging up to atmospheric, keeping the laser-target coupling efficiency high and leading to the constant intensity behaviour recorded.

Signal-to-background ratios obtained in the present work maximized at an intermediate laser pulse energy of 400 mJ, for all three atmospheres studied, and at each particular pressure value. The highest recorded values were produced in both air and helium atmospheres, at relatively high pressures of 0.1 mbar, and 0.5 mbar, respectively.

For all three atmospheres studied, the spectral line intensity gradually decreased with increasing the distance from the target surface. The signal-to-background ratios, on the other hand, initially increased with the distance from the surface for all three atmospheres, and at all pressure values. Depending on the composition of the background used, however, the signal-to-background ratio maximized at a particular distance from the target surface, and for a specific pressure of the respective gas. The highest signal-to-background ratio was produced in air at 0.1 mbar, and at 2.5 mm from the target surface. The next best case was that of helium at 0.5 mbar and 3.0 mm and finally argon at 0.1 mbar and 2.5 mm spatial distance in the plasma. It is interesting to observe that, for the three ambient gases under study, the spatial point in the plasma at which the signal-to-background ratio was maximized moved closer to the target surface as the pressure of the surrounding gas increased. This result may be explained in terms of plasma confinement.

Analytical calibration functions obtained with the direct measurement of relative spectral line intensities compared very favourably with those constructed using the internal standardization method. This result is usually taken as evidence of complete atomization of the sample material that penetrates into the relatively hot center of the plasma formed in the buffer gas used. An unprecedented limit of detection for carbon in steels of 1.2 μg/g ± 15% was measured with the C III 97.70 nm spectral line.

Plasma diagnostics:

Spectroscopic diagnostic techniques were developed in the VUV spectral range for the determination of the laser-produced steel plasma physical parameters, as functions of the axial distance from the target surface. The electron number density was estimated from measurements of the FWHM of the Stark-broadened C II 90.41 spectral line. The measured electron densities ranged between 1.3×10^{19} cm^{-3} on the target surface and 2.3×10^{18} cm^{-3} at 4.0 mm away from it. The excitation temperature of the plasma was evaluated by the Boltzmann's plot method for five selected Fe III spectral lines in the wavelength range 89–93 nm. The excitation temperatures varied from 14920 K at 1.5 mm to 14270 K at 3.0 mm with respect to the target surface. Finally, the ionization temperature was determined using the relative line intensities ratio of C II 90.41 nm and C III 97.7 nm spectral lines, applied to the Saha-Boltzmann equation. Ionization temperatures determined in this way changed from 33900 K at the target surface to 26800 K at 4.0 mm away from it.

Criteria for the existence of local thermodynamic equilibration (LTE) between the excited energy states in the steel plasmas investigated in the present work, were established. However, large differences between the measured excitation and ionization temperatures suggest non-thermal equilibrium conditions between electrons and heavier ionic species. The time-integrated technique employed, along with the relatively high uncertainty in the oscillator strengths of the VUV carbon transitions used largely contribute to this discrepancy. Nevertheless, it is expected that both temperatures will converge at larger distances from the target surface (> 5 mm), assuming that the VUV iron and carbon spectral lines are still emitting, with good records of signal-to-background ratios, at such distances.

7.2 Future Work

In analytical spectroscopic applications, a continuing challenge is to improve the figures of merit of the respective analytical method. One approach to achieve this aim is to further optimize the different experimental parameters and conditions involved in the technique. This indeed results in better understanding and control of the resultant output parameters required. In fact, further improvements in the sensitivity and reproducibility

of the LIPS technique developed for the quantitative elemental characterization of solid materials were achieved through controlling the laser parameters, as well as the environment in which the interaction of the laser beam with the solid target takes place. Some suggestions for further raising the analytical performance of the LIPS technique are briefly outlined in the following paragraphs.

In virtually all previous LIPS applications, including the present work, single pulses, i.e. one laser pulse per pump pulse, of Q-switched lasers were used to ablate and evaporate various materials, as well as for the production of the plasma required. In this case, the ablation and plasma excitation processes can not be optimized independently, in contrast to two-step techniques, such as laser ablation with subsequent excitation by electrical sparks, microwaves or inductively coupled plasmas. The combination of laser ablation with either of these techniques may result in significant improvements in the overall analytical performance of the relevant method. These two-step techniques, however, require additional equipment close to the interaction area, which considerably reduces the flexibility of the analytical method and, may well interfere with the analysis.

Two-step laser pulses:

The use of Q-switched ***dual-laser pulses*** separated by a short delay time, can lead to lower detection limits, significant enhancement in emission line intensities, as well as much improved signal-to-background ratios. The introduction of a second laser pulse may take several forms with respect to the geometry of the interaction between the laser and the solid material. In one set-up [264], in which two separate Q-switched Nd:YAG lasers in an orthogonal configuration may be used, the first laser pulse is incident and focused onto the target surface at right angles, leading to the formation of a plasma plume above the surface. After some selected delay time, the second laser pulse is directed perpendicular to the first laser pulse (parallel to the target surface), which results in creating another plasma plume, at some distance from the target surface, and reheating of the original laser-induced target plasma.

In the pre-ablation spark set-up [265], the first laser pulse is brought in parallel to the target surface and focused above it (1–2 mm) to form an "air" plasma. After some delay time (~ 2.5–25 μs), the second laser pulse is launched in a direction normal to the first pulse, i.e. normal to the target surface, and focused onto the sample surface creating the

laser-induced plasma from which the line emission signals are recorded. Although the plasma generated by the pre-ablation spark heats the sample, it is sufficiently far from the surface to ensure that ablation and emission are not occurred.

In a third configuration [174, 266], a single Q-switched laser system is modified in such a way as to produce two equal-energy Q-switched pulses, separated by some microseconds. In this case, both laser pulses are incident on the same spot of the target surface, resulting in producing the plasma plume. The significant enhancements observed in the spectral line intensities may be generally explained by a combination of increased material ablation, better atomization and bigger plasma volume. Such observations are similar to those dealing with ultrashort plasmas used as soft X-ray sources, where it has been shown that forming the main plasma in an expanding preplasma improves the X-ray yield [266]. The modelling of such plasmas is indeed fairly advanced, and one could benefit from it. For laser-produced plasmas applied to spectrochemical analysis, however, a deeper understanding of the laser-plasma interaction taking place at the arrival of the second pulse of a double-pulse burst would be gained from detailed experimental data, as well as modelling.

Besides improving the measurement sensitivity, the higher line emission intensities obtained with the different dual-laser pulse techniques also significantly reduce the statistical error. Furthermore, the use of a single laser in a double-pulse mode provides a more compact, reliable and less expensive system than can be achieved by using two separate lasers. In addition, a single laser system eliminates the problem of aligning two discrete laser beams, and the deleterious effect of a small deviation in this alignment could have on the emission signals. On the other hand, some limitations are inherent in the commercially available lasers generating dual pulses, such as insufficient independent control of the energy and duration of the two pulses. In fact, the use of two separate laser sources would provide better flexibility and control in terms of energy, duration and also wavelength for each individual pulse.

Ultra-short laser pulses:

Ultrashort laser pulses in the ***picosecond / femtosecond*** regimes have become available in recent years. At such pulse durations, the physical mechanisms involved during the laser ablation process noticeably differ from those taking place with nanosecond lasers.

Because of its very short pulse duration, the laser beam does not interact with the resulting plasma. The part of the laser pulse energy absorbed is thus fully deposited into the material at the solid density with only a little thermal diffusion while the pulse is on. The short duration of the laser pulse therefore yields a shrinking of the heat-zone, which prevents an uncontrollable and often undesirable material modification and removal [47]. Accordingly, lower ablation thresholds and larger efficiency of material ablation can be obtained with high precision and minimal damage.

With ultrashort laser pulses the plasma is formed by direct photoionization (PI) of the ablated material through a multiphoton process, in contrast to the case of nanosecond laser excitation where the ablated material is largely ionized by electron-ion collisions (through IB process) [47–48]. Accordingly, an obvious advantage of plasmas produced by ultrashort laser pulses is the significantly lower background emission in comparison to those created by nanosecond laser excitation [49]. This would result in considerable higher signal-to-background ratios.

Échelle Spectrometer:

One major advantage of LIPS is its capability for multi-element detection. Also, in plasma diagnostics the simultaneous detection of several atomic and / or ionic spectral lines distributed over a relatively wide spectral range may be crucial. Accordingly, simultaneous detection of a wide spectral interval with an adequate spectral resolution can be considered as satisfactory for numerous analytical tasks. One way to achieve this aim is the coupling of a two-dimensional CCD detector with an echelle spectrograph. ***Échelle spectrographs*** with internal cross-dispersion generate two-dimensional spectra, thus fully exploiting the capabilities of the two-dimensional CCD array [248]. The high dispersion of the echelle grating produces a highly resolved spectrum in one direction, which consists of many overlapping spectral orders. A cross-dispersing element, either a second grating or a prism, separates the different orders by shifting them orthogonally with respect to the echelle dispersion. By changing the grating, the cross-dispersing prism and the focal length of the camera mirror, either the spectral resolution or the wavelength interval can be chosen in the range from IR to VUV [267–268].

Experiments showed that the spectrometer entrance slit-width of 50 μm, which was employed for the bulk of the present work, is close to optimum, although some further

gain in the signal-to-background ratios could be obtained at the optimum value of 40 μm. Regarding on-line and in-situ applications of LIPS in harsh and / or hostile environments, where problems of available space are frequently encountered, the size of the present instrument could be largely reduced, and keeping its current analytical performance such as sensitivity and spectral resolution unchanged, by simply replacing the 1200 grooves/mm grating employed here by a higher grooves density grating.

Finally, it is anticipated that the analytical methodology followed in the present work will also be applicable to the quantitative determination of other industrially important low atomic number elements, in a variety of solid matrices, such as Li, Be, B, N, O, F S, P and Cl, which similarly have their strongest spectral lines in the deep VUV region.

7.3 Technique Developments

In the following, a brief account of the possibility of combining LIPS with two other laser-based spectroscopic techniques for the quantitative determination of trace and ultra-trace elements in a variety of matrices is given. These are laser-induced fluorescence spectroscopy (LIFS), and diode laser atomic absorption spectroscopy (DLAAS). I strongly believe that these techniques, i.e. LIPS-LIFS and LIPS-DLAAS, will represent an important contribution to the applied research activities taking place in the National Center for Plasma Science and Technology (NCPST), at Dublin City University.

Many LIPS applications generally experience considerable restrictions for the accurate determination of specific elements in some matrices. These elements typically do not have spectral lines that are free from interference emission from other, more abundant, matrix elements, or their spectral lines are in wavelength regions not accessible to a particular spectrometric system. This would definitely lead to substantial errors when performing quantitative analysis. To partially overcome this problem, it has been recently proposed and investigated to combine the primary technique of LIPS with a secondary probe, namely ***laser-induced fluorescence spectroscopy (LIFS)*** [64]. In this hyphenated technique, the pulse of a second laser source, which is tuned to an optical transition of the species of interest, is directed into the plasma plume generated. The fluorescence radiation induced by this second laser pulse is then evaluated for

quantitative analysis. It was demonstrated that the combination between LIPS and LIFS is more effective than LIPS alone in terms of almost all analytical figures of merit, i.e. sensitivity, selectivity, dynamic range, precision and accuracy, as well as freedom from matrix effect. A higher degree of the system set-up's complexity and alignment required is, however, frequently encountered [65, 269–271].

The application of laser atomic absorption spectroscopy (LAAS) for the detection of free analyte atoms in a laser-produced plasma is less popular as compared to laser-induced fluorescence measurements. An obvious reason for this popularity is the fact that the newly developed diode laser-induced fluorescence (DLIFS) techniques are highly selective and characterized by a wide dynamic concentration range. However, the main limitation of the DLIFS technique is the strong broadband emission of the laser plasma. In order to minimize this background emission one has to delay the fluorescence sampling time and to select the probe volume at a certain distance from the sample surface, where the plasma is relatively cold. In this way, the best signal-to-background ratios and the lowest limits of detection for the LIPS-DLIF technique have been obtained [272], but at the price of dramatic decrease of the number density of free atoms / ions in the plasma volume observed. The highest concentrations of the ablated ions and neutrals of an analyte of interest are definitely located at relatively early stages of the plasma evolution, and close to the sample surface.

The technique of ***diode laser atomic absorption spectroscopy (DLAAS)***, on the other hand, has some serious advantages over LIPS or LIPS-DLIFS techniques [273]. First, DLAAS does not need a large solid angle of light collection — a laser beam of low divergence (typically < 2.5 mrad) contains all information about the absorption signal. Therefore, the total intensity of plasma emission collected by the detector is highly reduced, and does not seriously affect the absorption measurement and in particular the achievable limit of detection. As a consequence, hotter and more dense zones of the laser plume at an early stage of the plasma evolution can be probed by DLAAS. In fact, from the analytical point of view, DLAAS applied to a laser plume with high analyte concentrations can provide higher sensitivity in comparison with LIFS detection in the cooler parts of the plasma plume. Furthermore, the current research efforts aiming at the development of "high-power" diode lasers emitting in the blue / violet spectral range will have a significant influence on many applications utilizing both techniques.

THESIS REFERENCES

[1] Brech F and Cross L (1962). Optical Microemission Stimulated by a Ruby Maser, *Appl. Spectrosc.* **16,** 59.

[2] Carroll P K and Kennedy E T (1981). Laser-Produced Plasmas, *Contemp. Phys.* **22,** 61–96.

[3] Scott R H and Strasheim A (1970). Laser Induced Plasmas for Analytical Spectroscopy, *Spectrochim. Acta* Part B **25,** 311–32.

[4] Scott R H and Strasheim A (1978). Laser Emission Excitation and Spectroscopy, in *Applied Atomic Spectroscopy* (Grove E L, ed.), Plenum Press, New York.

[5] Laqua K (1979). Analytical Spectroscopy Using Laser Atomizers, in *Analytical Laser Spectroscopy* (Omenetto N, ed.), Wiley, New York.

[6] Adrian R S and Watson J (1984). Laser Microspectral Analysis: Review of Principles and Applications, *J. Phys. D: Appl. Phys.* **17,** 1915–40.

[7] Dittrich K and Wennrich R (1984). Laser Vaporization in Atomic Spectroscopy, in *Progress in Analytical Atomic Spectroscopy* (Chakrabarti C L, ed.), Pergamon, New York.

[8] Piepmeier E H (1986). Laser Ablation for Atomic Spectroscopy, in *Analytical Applications of Lasers* (Piepmeier E H, ed.), Wiley, New York.

[9] Blankenburg M-B L (1989). *Laser Micro-Analysis*, Wiley, New York.

[10] Majidi V and Joseph M R (1992). Spectroscopic Applications of Laser-Induced Plasmas, *Crit. Rev. Anal. Chem.* **23,** 143–62.

[11] Darke S A and Tyson J F (1993). Interaction of Laser Radiation with Solid Materials and its Significance to Analytical Spectroscopy: A Review, *J. Anal. At. Spectrom.* **8,** 145–209.

[12] Radziemski L J (1994). Review of Selected Analytical Applications of Laser Plasmas and Laser Ablation, *Microchem. J.* **50,** 218–34.

[13] Russo R E (1995). Laser Ablation, *Appl. Spectrosc.* **49,** 14A–28A.

[14] Song K, Lee Y-I and Sneddon J (1997). Applications of Laser-Induced Breakdown Spectrometry, *Appl. Spectrosc. Rev.* **32,** 183–235.

[15] Russo R E and Mao X (1998). Chemical Analysis by Laser Ablation, *Exp. Meth. Phys. Sci.* **30,** 375–412.

[16] Haisch C and Panne U (1997). Laser-Induced Plasma Spectroscopy (LIPS) in Action, *Spectrosc. Europe* **9,** 8–14.

[17] Chrisey D B and Hubler G K (eds.) (1994). Pulsed Laser Deposition of Thin Films, Wiley, New York.

[18] Von Allmen M and Blatter A (1995). Laser Beam Interactions with Materials: Physical Principles and Applications, Springer, Berlin.

[19] Torok T, Mika J and Gegus E (1978). *Emission Spectrochemical Analysis*, Crane Russak, New York.

[20] Nemet B and Kozma L (1995). Basic Investigations of Nanosecond Laser-Induced Plasma Emission Kinetics for Quantitative Elemental Microanalysis of High Alloys, *J. Anal. At. Spectrom.* **10,** 631–6.

[21] Anglos D, Couris S and Fotakis C (1997). Laser Diagnostics of Painted Artworks: Laser-Induced Breakdown Spectroscopy in Pigment Identification, *Appl. Spectrosc.* **51,** 1025–30.

[22] Salimbeni R, Pini R and Siano S (2001). Achievement of Optimum Laser Cleaning in the Restoration of Artworks: Expected Improvements by on-Line Optical Diagnostics, *Spectrochim. Acta* Part B **56,** 877–85.

[23] Cremers D A (1987). The Analysis of Metals at a Distance Using Laser-Induced Breakdown Spectroscopy, *Appl. Spectrosc.* **41,** 572–9.

[24] Wisbrun R, Niessner R and Schroder H (1993). Laser-Induced Breakdown Spectrometry as a Fast Screening Sensor for Environmental Analysis of Trace Amounts of Heavy Metals in Soils, *Anal. Meth. Instrum.* **1,** 17–22.

[25] Davies C M et al. (1995). Quantitative Analysis Using Remote Laser-Induced Breakdown Spectroscopy (LIBS), *Spectrochim. Acta* Part B **50,** 1059–75.

[26] Paksy L et al. (1996). Production Control of Metal Alloys by Laser Spectroscopy of the Molten Metals. Part 1. Preliminary Investigations, *Spectrochim. Acta* Part B **51,** 279–90.

[27] Yamamoto K Y et al. (1996). Detection of Metals in the Environment Using a Portable Laser-Induced Breakdown Spectroscopy Instrument, *Appl. Spectrosc.* **50,** 222–33.

[28] Ciucci A et al. (1996). Trace Pollutants Analysis in Soil by a Time-Resolved Laser-Induced Breakdown Spectroscopy Technique, *Appl. Phys. B* **63,** 185–90.

[29] Pakhomov A V, Nichols W and Borysow J (1996). Laser-Induced Breakdown Spectroscopy for Detection of Lead in Concrete, *Appl. Spectrosc.* **50,** 880–4.

[30] Davies C M, Telle H H and Williams A W (1996). Remote in Situ Analytical Spectroscopy and its Applications in the Nuclear Industry, *Fresenius J. Anal. Chem.* **355,** 895–9.

[31] Pichahchy A E, Cremers D A and Ferris M J (1997). Elemental Analysis of Metals under Water Using Laser-Induced Breakdown Spectroscopy, *Spectrochim. Acta* Part B **52,** 25–39.

[32] Pietsch W, Petit A and Briand A (1998). Isotope Ratio Determination of Uranium by Optical Emission Spectroscopy on a Laser-Produced Plasma – Basic Investigations and Analytical Results, *Spectrochim. Acta* Part B **53,** 751–61.

[33] Castle B C et al. (1998). Battery Powered Laser-Induced Plasma Spectrometer for Elemental Determinations, *J. Anal. At. Spectrom.* **13,** 589–95.

[34] Kurniawan H et al. (2000). Laser-Induced Shock Wave Plasma Spectrometry Using a Small Chamber Designed for in Situ Analysis, *Spectrochim. Acta* Part B **55,** 839–48.

[35] Palanco S and Laserna J J (2000). Full Automation of a Laser-Induced Breakdown Spectrometer for Quality Assessment in the Steel Industry with Sample Handling, Surface Preparation and Quantitative Analysis Capabilities, *J. Anal. At. Spectrom.* **15,** 1321–7.

[36] Gruber J et al. (2001). Rapid in-Situ Analysis of Liquid Steel by Laser-Induced Breakdown Spectroscopy, *Spectrochim. Acta* Part B **56,** 685–93.

[37] Rosenwasser S et al. (2001). Development of a Method for Automated Quantitative Analysis of Ores using LIBS, *Spectrochim. Acta* Part B **56,** 707–14.

[38] Wainner R T et al. (2001). Analysis of Environmental Lead Contamination: Comarison of LIBS field and Laboratory Instruments, *Spectrochim. Acta* Part B **56,** 777–93.

[39] Whitehouse A I et al. (2001). Remote Material Analysis of Nuclear Power Station Steam Generator Tubes by Laser-Induced Breakdown Spectroscopy, *Spectrochim. Acta* Part B **56,** 821–30.

[40] Castle B C et al. (1998). Variables Influencing the Precision of Laser-Induced Breakdown Spectroscopy Measurements, *Appl. Spectrosc.* **52,** 649–57.

[41] Sdorra W, Brust J and Niemax K (1992). Basic Investigations for Laser Microanalysis: IV. The Dependence on the Laser Wavelength in Laser Ablation, *Mikrochim. Acta* **108,** 1–10.

[42] Kagawa K et al. (1994). XeCl Excimer Laser Induced Wave Plasma and Its Applications to Emission Spectrochemical Analysis, *Appl. Spectrosc.* **48,** 198–205.

[43] Cabalin L M and Laserna J J (1998). Experimental Determination of Laser Induced Breakdown Thresholds of Metals under Nanosecond Q-Switched Laser Operation, *Spectrochim. Acta* Part B **53,** 723–30.

[44] Kuzuya M et al. (1993). Effect of Laser Energy and Atmosphere on the Emission Characteristics of Laser-Induced Plasmas, *Appl. Spectrosc.* **47,** 1659–64.

[45] Aguilera J A, Aragon C and Penalba F (1998). Plasma Shielding in Laser Ablation of Metallic Samples and its Influence on LIBS Analysis, *Appl. Surf. Sci.* **127-129,** 309–14.

[46] Eland K L et al. (2001). Energy Dependence of Emission Intensity and Temperature in a LIBS Plasma Using Femtosecond Excitation, *Appl. Spectrosc.* **55,** 286–91.

[47] Margetic V et al. (2000). A Comparison of Nanosecond and Femtosecond Laser-Induced Plasma Spectroscopy of Brass Samples, *Spectrochim. Acta* Part B **55,** 1771–85.

[48] Eland K L et al. (2001). Some Comparisons of LIBS Measurements Using Nanosecond and Picosecond Laser Pulses, *Appl. Spectrosc.* **55,** 279–85.

[49] Drogoff B L et al. (2001). Temporal Characterization of Femtosecond Laser Pulses induced Plasma for Spectrochemical Analysis of Aluminum Alloys, *Spectrochim. Acta* Part B **56,** 987–1002.

[50] Piepmeier E H and Osten D E (1971). Atmospheric Influence on Q-Switched Laser Sampling and Resulting Plumes, *Appl. Spectrosc.* **25,** 642–52.

[51] Treytl W J et al. (1971). Effect of Atmosphere on Spectral Emission from Plasmas Generated by the Laser Microprobe, *Anal. Chem.* **43,** 1452–6.

[52] Iida Yasuo (1989). Atomic Emission Characteristics of Laser-Induced Plasmas in an Argon Atmosphere at Reduced Pressure, *Appl. Spectrosc.* **43,** 229–34.

[53] Iida Y (1990). Effects of Atmosphere on Laser Vaporization and Excitation Processes of Solid Samples, *Spectrochim. Acta* Part B **45,** 1353–67.

[54] Sdorra W and Niemax K (1992). Basic Investigations for Laser Microanalysis: III. Applications of Different Buffer Gases for Laser-Produced Sample Plumes, *Mikrochim. Acta* **107,** 319–27.

[55] Kurniawan H, Kobayashi T and Kagawa K (1992). Effect of Different Atmospheres on the Excitation Process of TEA-CO_2 Laser-Induced Shock Wave Plasma, *Appl. Spectrosc.* **46,** 581–6.

[56] Lee Y I et al. (1992). Interaction of an Excimer-Laser with Metals. Part III: The Effect of a Controlled Atmosphere in Laser-Ablated Plasma Emission, *Appl. Spectrosc.* **46,** 1597–1604.

[57] Kuzuya M and Mikami O (1992). Effect of Argon Pressure on Spectral Emission of a Plasma Produced by a Laser Microprobe, *J. Anal. At. Spectrom.* **7,** 493–7.

[58] Thiem T L et al. (1994). Quantitative Simultaneous Elemental Determination in Alloys Using Laser-Induced Breakdown Spectroscopy (LIBS) in an Ultra-High Vacuum, *Appl. Spectrosc.* **48,** 58–64.

[59] Man B Y, Wang X T and Wang G T (1997). Effect of Ambient Pressure on the Generation and the Propagation of Plasmas Produced by Pulsed Laser Ablation of Metal Al in Air, *Appl. Spectrosc.* **51,** 1910–15.

[60] Lee Y-I et al. (1997). Influence of Atmosphere and Irradiance Wavelength on Copper Plasma Emission Induced by Excimer and Q-Switched Nd:YAG Laser Ablation, *Appl. Spectrosc.* **51,** 959–64.

[61] Marpaung A M et al. (2001). Comprehensive Study on the Pressure Dependence of Shock Wave Plasma Generation under TEA CO_2 Laser Bombardment on Metal Sample, *J. Phys. D: Appl. Phys.* **34,** 758–71.

[62] Amoruso S et al. (1999). Characterization of Laser-Ablation Plasmas, *J. Phys. B: At. Mol. Opt. Phys.* **32,** R131–72.

[63] Manabe R M and Piepmeier E H (1979). Time and Spatially Resolved Atomic Absorption Measurements with a Dye Laser Plume Atomizer and Pulsed Hollow Cathode Lamps, *Anal. Chem.* **51,** 2066–70.

[64] Sdorra W, Quentmeier A and Niemax K (1989). Basic Investigations for Laser Microanalysis: II. Laser-Induced Fluorescence in Laser-Produced Sample Plumes, *Mikrochim. Acta [Wien]* **II,** 201–18.

[65] Telle H H et al. (2001). Sensitive and Selective Spectrochemical Analysis of Metallic Samples: The Combination of Laser-Induced Breakdown Spectroscopy and Laser-Induced Fluorescence Spectroscopy, *Spectrochim. Acta* Part B **56,** 947–60.

[66] Leis F et al. (2001). Investigations on Laser Ablation-Microwave Induced Plasma-Atomic Emission Spectrometry using Polymer Samples, *Spectrochim. Acta* Part B **56,** 27–35.

[67] Mao X L et al. (1998). Laser Ablation Processes Investigated using Inductively Coupled Plasma-Atomic Emission Spectroscopy (ICP-AES), *Appl. Surf. Sci.* **127-129,** 262–8.

[68] Gagean M and Mermet J M (1998). Study of Laser Ablation of Brass Materials using inductively Coupled Plasma Atomic Emission Spectrometric Detection, *Spectrochim. Acta* Part B **53,** 581–91.

[69] Lim J M et al. (2000). Development and Characterization of Directly Connected Laser Ablation/Low-Pressure Inductively Coupled Plasma Atomic Emission Spectrometry for Solid Sample Analysis, *Appl. Spectrosc.* **54,** 1253–60.

[70] Baker S A, Smith B W and Winefordner J D (1997). Laser Ablation Inductively Coupled Plasma Mass Spectrometry with a Compact Laser Source, *Appl. Spectrosc.* **51,** 1918–21.

[71] Günther D, Jackson S E and Longerich H P (1999). Laser Ablation and Arc/Spark Solid Sample Introduction into Inductively Coupled Plasma Mass Spectrometers: A Review, *Spectrochim. Acta* Part B **54,** 381–409.

[72] Ehler A W (1966). Vacuum Ultraviolet Radiation from Plasmas Formed by A Laser on Metal Surfaces, *Appl. Phys. Lett.* **8,** 89–91.

[73] XU N and Majidi V (1993). Wavelength- and Time-Resolved Investigation of Laser-Induced Plasma as a Continuum Source, *Appl. Spectrosc.* **47,** 1134–9.

[74] Meighan O et al. (1997). Short-Pulse, Extreme-Ultraviolet Continuum Emission from a Table-Top Laser Plasma Light Source, *Appl. Phys. Lett.* **70,** 1497–9.

[75] Carroll P K, Kennedy E T and Sullivan G O (1980). Laser-Produced Continua for Absorption Spectroscopy in the VUV and XUV, *Appl. Opt.* **19,** 1454–62.

[76] Costello J T et al. (1991). X-UV Absorption Spectroscopy with Laser-Produced Plasmas: A Review, *Phys. Scri.* **T34,** 77–92.

[77] Hirsch J S et al. (2000). Vacuum-Ultraviolet Resonant Photoabsorption Imaging of Laser Produced Plasmas, *J. Appl. Phys.* **88,** 4953–60.

[78] Archbold E, Harper D W and Hughes T P (1964). Time-Resolved Spectroscopy of Laser-Generated Microplasmas, *Brit. J. Appl. Phys.* **15,** 1321–6.

[79] Millard J A, Dalling R H and Radziemski L J (1986). Time-Resolved Laser-Induced Breakdown Spectrometry for the Rapid Determination of Beryllium in Beryllium-Copper Alloys, *Appl. Spectrosc.* **40,** 491–4.

[80] Grant K J, Paul G L and O'Neill J A (1990). Time-Resolved Laser-Induced Breakdown Spectroscopy of Iron Ore, *Appl. Spectrosc.* **44,** 1711–4.

[81] Sdorra W and Niemax K (1990). Temporal and Spatial Distribution of Analyte Atoms and Ions in Microplasmas Produced by Laser Ablation of Solid Samples, *Spectrochim. Acta* Part B **45,** 917–26.

[82] Joseph M R, Xu N and Majidi V (1994). Time-Resolved Emission Characteristics and Temperature Profiles of Laser-Induced Plasmas in Helium, *Spectrochim. Acta* Part B **49,** 89–103.

[83] Nemet B and Kozma L (1995). Time-Resolved Optical Emission Spectrometry of Q-Switched Nd:YAG Laser-Induced Plasmas from Copper Targets in Air at Atmospheric Pressure, *Spectrochim. Acta* Part B **50,** 1869–88.

[84] Gornushkin I B et al. (1997). Time-Resolved Resonance Shadow Imaging of Laser-Produced Lead and Tin Plasmas, *Spectrochim. Acta* Part B **52,** 1617–25.

[85] Carroll P K and Kennedy E T (1977). Doubly Excited Autoionization Resonances in the Absorption Spectrum of Li^+ Formed in a Laser-Produced Plasma, *Phys. Rev. Lett.* **38,** 1068–71.

[86] Laserna J J, Calvo N and Cabalin L M (1993). Imaging and Space-Resolved Spectroscopy in the Xe-Cl Laser Ablation of Noble Metals with Charge-Coupled Device Detection, *Analyt. Chim. Acta* **289,** 113–20.

[87] Kennedy E T et al. (1994). Extreme Ultraviolet Studies with Laser-Produced Plasmas, *Opt. Eng.* **33,** 3984–92.

[88] Kennedy E T, Costello J T, and Mosnier J P (1996). New Experiments in Photoabsorption Studies of Singly and Multiply Charged Ions, *J. Electron. Spectrosc.* **79,** 283–8.

[89] Lee Y I and Sneddon J (1996). Spatial and Temporal Characteristics of an Excimer Laser-Induced Lead Plasma Emission, *Spectrosc. Lett.* **29,** 1157–71.

[90] Castle B C et al. (1997). Spatial and Temporal Dependence of Lead Emission in Laser-Induced Breakdown Spectroscopy, *Appl. Spectrosc.* **51,** 1017–24.

[91] Whitty W et al. (1998). Absorption Spectroscopy of an Expanding Laser Produced Lithium Plasma in the Extreme Ultraviolet Using the Dual Laser Plasma Technique, *Appl. Surf. Sci.* **127-129,** 686–91.

[92] Kennedy E T et al. (1999). New Dual Laser Plasma Investigations of Inner-Shell Excitations, *J. Electron. Spectrosc.* **101-103,** 161–6.

[93] Khater M A et al. (2000). Time-Integrated Laser-Induced Plasma Spectroscopy in the Vacuum Ultraviolet for the Quantitative Elemental Characterization of Steel Alloys, *J. Phys. D: Appl. Phys.* **33,** 2252–62.

[94] Kim Y W (1989). Fundamentals of Analysis of Solids by Laser-Produced Plasmas, in *Laser-Induced Plasmas and Applications* (Radziemski L J and Cremers D A, eds.), Dekker, New York.

[95] Gibson A F, Hughes T P and Ireland C L M (1971). CO_2 Laser Generation of Plasma for Spectroscopy and Spectrochemical Analysis, *J. Phys. D: Appl. Phys.* **4,** 1527–34.

[96] Chichkov B N et al. (1996). Femtosecond, Picosecond and Nanosecond Laser Ablation of Solids, *Appl. Phys. A* **63,** 109–15.

[97] Milán M and Laserna J J (2001). Diagnostics of Silicon Plasmas Produced by Visible Nanosecond Laser Ablation, *Spectrochim. Acta* Part B **56,** 275–88.

[98] Singh R K and Viatella (1994). Estimation of Plasma Absorption Effects during Pulsed Laser Ablation of High-Critical-Temperature Superconductors, *J. Appl. Phys.* **75,** 1204–6.

[99] Tokarev V N et al. (1995). Analytical Thermal Model of Ultraviolet Laser Ablation with Single-Photon Absorption in the Plume, *J. Appl. Phys.* **78,** 1241–6.

[100] Ho J R, Grigoropoulos C P and Humphrey J A C (1996). Gas Dynamics and Radiation Heat Transfer in the Vapor Plume Produced by Pulsed Laser Irradiation of Aluminum, *J. Appl. Phys.* **79,** 7205–15.

[101] Chang J J and Warner B E (1996). Laser-Plasma Interaction during Visible-Laser Ablation of Metals, *Appl. Phys. Lett.* **69,** 473–5.

[102] Leboeuf J N et al. (1996). Modeling of Dynamical Processes in Laser Ablation, *Appl. Surf. Sci.* **96-98,** 14–23.

[103] Boardman A D, Cresswell B and Anderson J (1996). An Analytical Model for the Laser Ablation of Materials, *Appl. Surf. Sci.* **96-98,** 55–60.

[104] Fähler S and Krebs H-U (1996). Calculations and Experiments of Material Removal and Kinetic Energy during Pulsed Laser Ablation of Metals, *Appl. Surf. Sci.* **96-98,** 61–5.

[105] Mazhukin V I, Smurov I and Flamant G (1996). 2D-Simulation of the System: Laser Beam + Laser Plasma + Target, *Appl. Surf. Sci.* **96-98,** 89–96.

[106] Mao X et al. (1996). Preferential Vaporization and Plasma Shielding during Nano-Second Laser Ablation, *Appl. Surf. Sci.* **96-98,** 126–30.

[107] Jeong S H, Greif R and Russo R E (1998). Numerical Modeling of Pulsed Laser Evaporation of Aluminum Targets, *Appl. Surf. Sci.* **127-129,** 177–83.

[108] Arnold N, Luk'yanchuk B and Bityurin N (1998). A Fast Quantitative Modelling of ns Laser Ablation Based on Non-Stationary Averaging Technique, *Appl. Surf. Sci.* **127-129,** 184–92.

[109] Lunney J G and Jordan R (1998). Pulsed Laser Ablation of Metals, *Appl. Surf. Sci.* **127-129,** 941–6.

[110] Neamtu J et al. (1999). Theoretical Modelling of Phenomena in the Pulsed-Laser Deposition Process: Application to Ti Targets Ablation in Low-Pressure N_2, *J. Appl. Phys.* **86,** 6096–106.

[111] Amoruso S (1999). Modelling of Laser Produced Plasma and Time-of-Flight Experiments in UV Laser Ablation of Aluminum Targets, *Appl. Surf. Sci.* **138-139,** 292–8.

[112] Sankaranarayanan S and Kar A (1999). Nonlinear Effects of Laser-Plasma Interaction on Melt-Surface Temperature, *J. Phys. D: Appl. Phys.* **32,** 777–84.

[113] Kools J C S et al. (1992). Gas Flow Dynamics in Laser Ablation Deposition, *J. Appl. Phys.* **71,** 4547–56.

[114] Anisimov S I, Luk'yanchuk B S and Luches A (1996). An Analytical Model for Three-Dimensional Laser Plume Expansion into Vacuum in Hydrodynamic Regime, *Appl. Surf. Sci.* **96-98,** 24–32.

[115] Chen K R et al. (1996). Laser-Solid Interaction and Dynamics of Laser-Ablated Materials, *Appl. Surf. Sci.* **96-98,** 45–9.

[116] Wood R F et al. (1998). Dynamics of Plume Propagation, Splitting, and Nanoparticle Formation during Pulsed-Laser Ablation, *Appl. Surf. Sci.* **127-129,** 151–8.

[117] Mao S S et al. (2000). Simulation of a Picosecond Laser Ablation Plasma, *Appl. Phys. Lett.* **76,** 3370–2.

[118] Gusarov A V and Gnedovets A G (2000). Gas Dynamics of Laser Ablation: Influence of Ambient Atmosphere, *J. Appl. Phys.* **88,** 4352–64.

[119] Le H C et al. (2000). Modelling of Gas Dynamics for a Laser-Generated Plasma: Propagation into Low-Pressure Gases, *Phys. Rev. E* **62,** 4152–61.

[120] Colonna G, Casavola A and Capitelli M (2001). Modelling of LIBS Plasma Expansion, *Spectrochim. Acta* Part B **56,** 567–86.

[121] Vidal F et al. (2001). Numerical Simulations of Ultrashort Laser Pulse Ablation and Plasma Expansion in Ambient Air, *Spectrochim. Acta* Part B **56,** 973–86.

[122] Riley D et al. (2000). Spectral Simulation of Laser Ablated Magnesium Plasmas, *Plasm. Sourc. Techn.* **9,** 270–8.

[123] Capitelli M, Capitelli F and Eletskii A (2000). Non-equilibrium Problems in Laser-Induced Plasmas, *Spectrochim. Acta* Part B **55,** 559–74.

[124] De Giacomo A, Shakhatov V A and De Pascale O (2001). Optical Emission Spectroscopy and Modeling of Plasma Produced by Laser Ablation of Titanium Oxides, *Spectrochim. Acta* Part B **56,** 753–76.

[125] Garrelie F, Aubreton J and Catherinot A (1998). Monte Carlo Simulation of the Laser-Induced Plasma Plume Expansion under Vacuum: Comparison with Experiments, *J Appl. Phys.* **83,** 5075–82.

[126] Itina T E et al. (1998). Numerical Study of the Role of a Background Gas and System Geometry in Pulsed Laser Deposition, *J. Appl. Phys.* **83,** 6050–4.

[127] Dyer P E and Sidhu J (1988). Spectroscopic and Fast Photographic Studies of Excimer Laser Polymer Ablation, *J. Appl. Phys.* **64,** 4657–63.

[128] Tambay R, Singh R and Thareja R K (1992). Studies on Recombining Al-Plasma Using 1.06, 0.532, 0.355, and 0.266 μm Laser Radiation, *J. Appl. Phys.* **72,** 1197–9.

[129] Iida Y and Yeung E S (1994). Optical Monitoring of Laser-Induced Plasma Derived from Graphite and Characterization of the Deposited Carbon Film, *Appl. Spectrosc.* **48,** 945–50.

[130] Sakeek H F et al. (1994). Emission Studies of the Plume Produced during $YBa_2Cu_3O_7$ Film Production by Laser Ablation, *J. Appl. Phys.* **75,** 1138–44.

[131] Hermann J et al. (1995). Plasma Diagnostics in Pulsed Laser TiN Layer Deposition, *J. Appl. Phys.* **77,** 2928–36.

[132] El-Astal A H et al. (1995). A Quantitative Investigation of Emission from Low Temperature Laser-Induced $YBa_2Cu_3O_x$ Plasma Plumes, *J. Appl. Phys.* **77,** 6572–80.

[133] Geohegan D B and Puretzky A A (1996). Laser Ablation Plume Thermalization Dynamics in Background Gases: Combined Imaging, Optical Absorption and Emission Spectroscopy, and Ion Probe Measurements, *Appl. Surf. Sci.* **96-98,** 131–8.

[134] Al-Wazzan R A, Hendron J M and Morrow T (1996). Spatially and Temporally Resolved Emission Intensities and Number Densities in Low Temperature Laser-Induced Plasmas in Vacuum and in Ambient Gases, *Appl. Surf. Sci.* **96-98,** 170–4.

[135] Fuso F et al. (1996). Optical Diagnostics of the Laser-Target and Laser-Plume Interaction in Pulsed Laser Ablation, *Appl. Surf. Sci.* **96-98,** 181–5.

[136] Lenk A, Witke Th and Granse G (1996). Density and Electron Temperature of Laser Induced Plasma: A Comparison of Different Investigations Methods, *Appl. Surf. Sci.* **96-98,** 195–8.

[137] Harilal S S et al. (1997). Electron Density and Temperature Measurements in a Laser Produced Carbon Plasma, *J. Appl. Phys.* **82,** 2140–6.

[138] Rusak D A et al. (1997). Excitation, Vibrational, and Rotational Temperatures in Nd:YAG and XeCl Laser-Induced Plasmas, *Spectrochim. Acta* Part B **52,** 1929–35.

[139] Hermann J, Boulmer-Leborgne C and Hong D (1998). Diagnostics of the Early Phase of an Ultraviolet Laser Induced Plasma by Spectral Line Analysis Considering Self-Absorption, *J. Appl. Phys.* **83,** 691–6.

[140] Harilal S S, Bindhu C V, Nampoori V P N and Vallabhan C P G (1998). Temporal and Spatial Behaviour of Electron Density and Temperature in a Laser-Produced Plasma from $YBa_2Cu_3O_7$, *Appl. Spectrosc.* **52,** 449–55.

[141] Li M, Duffey T P and Mazumder J (1998). Spatially and Temporally Resolved Temperature Measurements of Plasma Generated in Percussion Drilling with a Diode-Pumped Nd:YAG Laser, *J. Appl. Phys.* **84,** 4122–7.

[142] Atwee T, Aschke L and Kunze H-J (2000). Investigation of Laser-Produced Plasmas from Boron Nitride Targets, *J. Phys. D: Appl. Phys.* **33,** 2263–7.

[143] Atwee T, Harilal S S and Kunze H-J (2001). XUV Spectroscopic Studies of Plasma Plumes Produced from Boron, Boron Carbide and Boron Nitride Targets by a Laser, *J. Phys. D: Appl. Phys.* **34,** 1–6.

[144] Milán M and Laserna J J (2001). Diagnostics of Silicon Plasmas Produced by Visible Nanosecond Laser Ablation, *Spectrochim. Acta* Part B **56,** 275–88.

[145] Martin G W et al. (1998). Three-Dimensional Number Density Mapping in the Plume of a Low-Temperature Laser-Ablated Magnesium Plasma, *Appl. Surf. Sci.* **127-129,** 710–5.

[146] Le H C et al. (1996). Temperature Measurements during Laser Ablation of Si into He, Ar and O_2, *Appl. Surf. Sci.* **96-98,** 164–9.

[147] Kozolov B N et al. (1995). Particle Number Density and Velocity Distributions in Laser Plumes, *Mikrochim. Acta* **120,** 111–9.

[148] Neogi A and Thareja R K (1999). Laser-Produced Carbon Plasma Expanding in Vacuum, Low Pressure Ambient Gas and Nonuniform Magnetic Field, *Phys. Plasm.* **6,** 365–71.

[149] Varier G K et al. (1997). Investigations on Nanosecond Laser Produced Plasma in Air from the Multi-Component Material $YBa_2Cu_3O_7$, *Spectrochim. Acta* Part B **52,** 657–66.

[150] Doyle L A et al. (1998). Electron Number Density Measurements in magnesium Laser Produced Plumes, *Appl. Surf. Sci.* **127-129,** 716–20.

[151] Hendron J M et al. (1997). Langmuir Probe Measurements of Plasma Parameters in the Late Stage of a Laser Ablated Plume, *J. Appl. Phys.* **81,** 2131–4.

[152] Hansen T N, Schou J and Lunney J G (1999). Langmuir Probe Study of Plasma Expansion in Pulsed Laser Ablation, *Appl. Phys. A* **69,** S601–4.

[153] Wisbrun R et al. (1994). Detector for Trace Elemental Analysis of Solid Environmental Samples by Laser-Plasma Spectroscopy, *Anal. Chem.* **66,** 2964–75.

[154] Wainner R T et al. (2001). Analysis of Environmental Lead Contamination: Comparison of LIBS Field and Laboratory Instruments, *Spectrochim. Acta* Part B **56,** 777–93.

[155] Hardjoutomo W et al. (1992). A Compact TEA CO_2 Laser for Field-Based Spectrochemical Analysis of Geological Samples, *Opt. Laser Technol.* **24,** 273–7.

[156] Franzke D, Klos H and Wokaun A (1992). Element Identification on the Surface of Inorganic Solids by Excimer Laser-Induced Emission Spectroscopy, *Appl. Spectrosc.* **46,** 587–92.

[157] Thiem T L and Wolf J (1994). Analysis of National Institute of Standards and Technology Ore and United States Geological Survey Samples by Inductively Coupled Plasma Spectroscopy/Laser-Induced Breakdown Spectroscopy, *Microchem. J.* **50,** 244–52.

[158] Sun Q, Tran M and Winefordner J D (2000). Determination of Mn and Si in Iron Ore by Laser-Induced Plasma Spectroscopy, *Anal. Chim. Acta* **413,** 187–95.

[159] Rosenwasser S et al. (2001). Development of a Method for Automated Quantitative Analysis of Ores using LIBS, *Spectrochim. Acta* Part B **56,** 707–14.

[160] Lee Y I and Sneddon J (1994). Direct and Rapid Determination of Potassium in Standard Solid Glasses by Excimer Laser Ablation Plasma Atomic Emission Spectrometry, *Analyst* **119,** 1441–3.

[161] Kurniawan H et al. (1995). Laser-Induced Shock Wave Plasma in Glass and Its Application to Elemental Analysis, *Appl. Spectrosc.* **49,** 1067–72.

[162] Kurniawan H et al. (1996). Emission Spectrochemical Analysis of Glass Containing Li and K in High Concentration using a XeCl Excimer Laser-Induced Shock Wave Plasma, *Appl. Spectrosc.* **50,** 299–305.

[163] Marpaung A M et al. (2000). Shock Wave Plasma Induced by TEA CO_2 Laser Bombardment on Glass Samples at High Pressures, *Spectrochim. Acta* Part B **55,** 1591–9.

[164] Vadillo J M, Milán M and Laserna J J (1996). Space and Time-Resolved Laser-Induced Breakdown Spectroscopy Using Charge-Coupled Device Detection, *Fresenius J. Anal. Chem.* **355,** 10–15.

[165] Romero D and Laserna J J (1997). Multielemental Chemical Imaging Using Laser-Induced Breakdown Spectrometry, *Anal. Chem.* **69,** 2871–6.

[166] Milán M et al. (1998). Depth Profiling of Phosphorus in Photonic-Grade Silicon Using Laser-Induced Breakdown Spectrometry, *Appl. Spectrosc.* **52,** 444–8.

[167] Romero D and Laserna J J (2000). A Microanalytical Study of Aluminum Diffusion in Photovolatic Cells Using Imaging-Mode Laser-Induced Breakdown Spectrometry, *Spectrochim. Acta* Part B **55,** 1241–8.

[168] Sattmann R et al. (1998). Laser-Induced Breakdown Spectroscopy for Polymer Identification, *Appl. Spectrosc.* **52,** 456–61.

[169] Pietsch W, Petit A and Briand A (1998). Isotope Ratio Determination of Uranium by Optical Emission Spectroscopy on a Laser-Produced Plasma — Basic Investigations and Analytical Results, *Spectrochim. Acta* Part B **53,** 751–61.

[170] Sun Q et al. (2000). Zinc Analysis in Human Skin by Laser Induced-Breakdown Spectroscopy, *Talanta* **52,** 293–300.

[171] Ohls K D (1996). A Personal View of the Development of Solid Sampling Emission Spectrochemical Analysis, *Spectrochim. Acta* Part B **51,** 245–52.

[172] Adrian R S et al. (1980). Laser Microspectral Analysis of Steels, *Opt. Laser Technol.* **June,** 137–43.

[173] Kagawa K and Yokoi S (1982). Application of the N_2 Laser to Laser Microprobe Spectrochemical Analysis, *Spectrochim. Acta* Part B **37,** 789–95.

[174] Sattmann R and Noll R (1995). Laser-Induced Breakdown Spectroscopy of Steel Samples Using Multiple Q-Switch Nd:YAG Laser Pulses, *J. Phys. D: Appl. Phys.* **28,** 2181–7.

[175] Kagawa K et al. (1995). Atomic Emission Spectrometric Analysis of Steel and Glass using a TEA CO_2 Laser-Induced Shock Wave Plasma, *Anal. Chim. Acta* **299,** 393–9.

[176] Ernst W E, Farson D F and Sames D J (1996). Determination of Copper in A533b Steel for the Assessment of Radiation Embrittlement Using Laser-Induced Breakdown Spectroscopy, *Appl. Spectrosc.* **50,** 306–9.

[177] Palanco S et al. (1999). Infrared Laser Ablation and Atomic Emission Spectrometry of Stainless Steel at High Temperatures, *J. Anal. At. Spectrom.* **14,** 1883–7.

[178] Bassiotis I et al. (2001). Effects of Experimental Parameters in Quantitative Analysis of Steel Alloy by Laser-Induced Breakdown Spectroscopy, *Spectrochim. Acta* Part B **56,** 671–83.

[179] Baldwin J M (1970). Q-Switched Laser Sampling of Copper-Zinc Alloys, *Appl. Spectrosc.* **24,** 429–35.

[180] Autin M et al. (1993). Characterization by Emission Spectrometry of a Laser-Produced Plasma from a Copper Target in Air at Atmospheric Pressure, *Spectrochim. Acta* Part B **48,** 851–62.

[181] Sabsabi M and Cielo P (1995). Quantitative Analysis of Copper Alloys by Laser-Produced Plasma Spectrometry, *J. Anal. At. Spectrom.* **10,** 643–7.

[182] Kurniawan H et al. (1997). Characteristics of the Secondary Plasma Induced by Focusing a 10-mJ XeCl Laser Pulse at Low Pressure, *Appl. Spectrosc.* **51,** 1769–80.

[183] André N et al. (1994). UV Laser Ablation Optical Emission Spectrometry on Aluminum Alloy in Air at Atmospheric Pressure, *Spectrochim. Acta* Part B **49,** 1363–72.

[184] Bescós B et al. (1995). Laser-Induced Breakdown Spectroscopy of Al-Samples: Applications to Chemical Analysis of Metallic Elements, *Laser Chem.* **16,** 75–82.

[185] Sabsabi M and Cielo P (1995). Quantitative Analysis of Aluminum Alloys by Laser-Induced Breakdown Spectroscopy and Plasma Characterization, *Appl. Spectrosc.* **49,** 499–507.

[186] Geertsen C et al. (1996). Evaluation of Laser Ablation Optical Emission Spectrometry for Microanalysis in Aluminum Samples, *Spectrochim. Acta* Part B **51,** 1403–16.

[187] Gomba J M et al. (2001). Spectroscopic Characterization of Laser Induced Breakdown in Aluminum-Lithium Alloy Samples for Quantitative Determination of Traces, *Spectrochim. Acta* Part B **56,** 695–705.

[188] Song K et al. (1997). Determination of Trace Elements in Zinc-Base Alloy and Rock Samples Using Laser-Induced Breakdown Spectroscopy (LIBS), *J. Korean Phys. Soc.* **30,** 463–9.

[189] St-Onge L, Sabsabi M and Cielo P (1997). Quantitative Analysis of Additives in Solid Zinc Alloys by Laser-Induced Plasma Spectrometry, *J. Anal. At. Spectrom.* **12,** 997–1004.

[190] Kim D E et al. (1997). Quantitative Analysis of Aluminum Impurities in Zinc Alloy by Laser-Induced Breakdown Spectroscopy, *Appl. Spectrosc.* **51,** 22–9.

[191] Lorenzen C J et al. (1992). Applications of Laser-Induced Emission Spectral Analysis for Industrial Process and Quality Control, *J. Anal. At. Spectrom.* **7,** 1029–35.

[192] Noll R et al. (2001). Laser-Induced Breakdown Spectrometry — Applications for Production Control and Quality Assurance in the Steel Industry, *Spectrochim. Acta* Part B **56,** 637–49.

[193] Hemmerlin M et al. (2001). Application of Vacuum Ultraviolet Laser-Induced Breakdown Spectrometry for Steel Analysis — Comparison with Spark-Optical Emission Spectrometry Figures of Merit, *Spectrochim. Acta* Part B **56,** 661–9.

[194] Jakubowski N et al. (1992). Analysis of Conducting Solids by Inductively Coupled Plasma Mass-Spectrometry with Spark Ablation, *J. Anal. At. Spectrom.* **7,** 121–5.

[195] Jakubowski N, Feldmann I and Stuewer D (1995). Comparison of ICP-MS with Spark Ablation and GDMS for Direct Element Analysis of Conducting Solids, *Spectrochim. Acta* Part B **50,** 639–54.

[196] Coedo A G, Dorado M T and Fernandez B (1995). Spark Ablation as Sampling Device for Inductively-Coupled Plasma-Mass Spectrometric Analysis of Low-Alloyed Steels, *J. Anal. At. Spectrom.* **10,** 859–63.

[197] Maibusch R et al. (1999). Spark Ablation Inductively Coupled Plasma Mass Spectrometry Analysis of Minor and Trace Elements in Low and High Alloy Steels Using Single Calibration Curves, *J. Anal. Atom. Spectrom.* **14,** 1155–62.

[198] Ishibashi Y (1997). Rapid Analysis of Steel by Inductively Coupled Plasma-Atomic Emission Spectrometry and –Mass Spectrometry with Laser Ablation Solid Sampling, *ISIJ Int.* **37,** 885–91.

[199] Balloffet G and Romand M J (1955). Utilisation Des Etincelles Glissantes Pour L'Analyse Spectrale Dans L'Ultraviolet Lointain. Possibilite De Detection Et Dosage Du Soufre, Du Phosphore Et Du Carbone Dans Les Aciers, *J. Physique Radium* **16,** 490–1.

[200] Aguilera J A, Aragon C and Campos J (1992). Determination of Carbon Content in Steel using Laser-Induced Breakdown Spectroscopy, *Appl. Spectrosc.* **46,** 1382–7.

[201] Aragon C, Aguilera J A and Campos J (1993). Determination of Carbon Content in Molten Steel Using Laser-Induced Breakdown Spectroscopy, *Appl. Spectrosc.* **47,** 606–8.

[202] González A et al. (1995). Determination of Sulfur Content in Steel by Laser-Produced Plasma Atomic Emission Spectroscopy, *Appl. Spectrosc.* **49,** 1632–5.

[203] Sturm V, Peter L and Noll R (2000). Steal Analysis with Laser-Induced Breakdown Spectrometry in the Vacuum Ultraviolet, *Appl. Spectrosc.* **54,** 1275–8.

[204] Hughes T P (1975). Plasmas and Laser Light, *Adam Hilger*, UK.

[205] Ready J F (1971). Effects of High-Power Laser Radiation, *Academic Press Inc.*, London, UK.

[206] Svanberg S, L'Huillier L and Wahlström C-G (1997). Atomic Physics Using Short-Wavelength Coherent Radiation, *Nucl. Instrum. Meth. Phys. Res.* **398,** 55–64.

[207] Zel'dovich Y B and Raizer Y P (1967). Physics of Shock Waves and High Temperature Hydrodynamic Phenomena, *Academic Press Inc.*, New York.

[208] Cremers D A and Radziemski L J (1987), in *Laser Spectroscopy and Its Applications* (Radziemski L J, Solarz R W and Paisner J A, Eds.), Dekker, New York p. 361.

[209] Root R G (1989). Modeling of Post-Breakdown Phenomena, in *Laser-Induced Plasmas and Applications* (Radziemski L J and Cremers D A, Eds.), Marcel Dekker Inc., New York.

[210] Kim Y W (1989). Fundamental of Analysis of Solids by Laser-Produced Plasmas, in *Laser-Induced Plasmas and Applications* (Radziemski L J and Cremers D A, Eds.), Marcel Dekker Inc., New York.

[211] Irons F E, McWhirter R W P and Peacock N J (1972). The Ion and Velocity Structure in a Laser Produced Plasma, *J. Phys. B: At. Mol. Phys.* **5** ,1975–87.

[212] Boland B C, Irons F E and McWhirter W P (1968). A Spectroscopic Study of the Plasma Generated by a Laser From Polyethylene, *J. Phys. B (Proc. Phys. Soc.)* **1,** 1180–91.

[213] Sedov L I (1959). Similarity and Dimensional Methods in Mechanics, *Academic Press Inc.*, New York, p. 213.

[214] Zucrow M J and Hoffman J D (1976). Gas Dynamics, *Wiley, Chichester, New York*, p. 346.

[215] Budi W S et al. (1999). Shock Excitation and Cooling Stage in Laser Plasma Induced by a Q-Switched Nd:YAG Laser at low Pressures, *Appl. Spectrosc.* **53,** 719–30.

[216] Cooper J (1966). Plasma Spectroscopy, *Rep. Prog. Phys.* **29,** 35–130.

[217] Offenberger A A and Fedosejevs R (1989). KrF Laser Produced Plasmas, *Laser Part. Beams* **7,** 393–403.

[218] Richter J (1995). Radiation of Hot Gases, in *Plasma Diagnostics* (Lochte-Holtgreven W, Ed.), American Institute of Physics Press.

[219] Mcwhirter R W P (1965). Spectral Intensities, in *Plasma Diagnostic Techniques* (Huddlestone R H and Leonard S L, Eds.), Academic Press, New York.

[220] Sandin T R (1989). *Essentials of Modern Physics*, Addison-Wesley Publishing Company, Reading, Massachusetts.

[221] Bekefi G, Deutsch C and Yaakobi B (1976). Spectroscopic Diagnostics of Laser Plasmas, in *Principles of Laser Plasmas* (Bekefi G, Ed.), John Wiley & Sons, Inc.

[222] Colombant D and Tonon G F (1973). X-Ray Emission in Laser-Produced Plasmas, *J. Appl. Phys.* **44,** 3524–37.

[223] Chandrasekhar S (1960). *Radiative Transfer*, Dober Publication, New York.

[224] Corney A (1977). Atomic and laser Spectroscopy, Clarendon Press, Oxford.

[225] Wiese W L (1965). Line Broadening, in *Plasma Diagnostic Techniques* (Huddlestone R H and Leonard S L, Eds.), Academic Press, New York.

[226] Griem H R (1974). *Spectral Line Broadening by Plasmas*, Academic Press, New York.

[227] Samson J A (1967). Techniques of Vacuum Ultraviolet Spectroscopy, John Wiley & Sons Inc., New York.

[228] Namioka T (1961). Theory of the Concave Grating, *J. Opt. Soc. Amer.* **49,** 446–60.

[229] Talmi Y (1983). *Multichannel Image Detectors,* American Chemical Society, Washington, D.C., USA.

[230] Morrissey P F, McCandliss S R and Feldman P D (1995). Vacuum Ultraviolet Quantum Efficiency of a Thinned, Backside-Illuminated Charge-Coupled Device, *Appl. Opt.* **34,** 4640–4650.

[231] Sims G R (1994). Principles of Charge-Transfer Devices, in *Charge-Transfer Devices in Spectroscopy* (Sweedler J V, Ratzlaff K L and Denton M B, Eds.), VCH Publications, Inc., New York.

[232] Poletto L, Boscolo A and Tondello G (1999). Characterization of a Charge-Coupled Device Detector in the 1100–0.14 nm (1 eV to 9 keV) Spectral Region, *Appl. Opt.* **38,** 29–36.

[233] Kelly R L (1987). Atomic and Ionic Spectrum Lines below 2000 Angstroms: Hydrogen through Krypton Part I (H-Cr), *J. Phys. Chem. Ref. Data* **16,** 35–50.

[234] Boumans P W J M (1987). Inductively Coupled Plasma Emission Spectroscopy Part I, Wiley, New York.

[235] Multari R A et al. (1996). Effect of Sampling Geometry on Elemental Emissions in Laser-Induced Breakdown Spectroscopy, Appl. Spectrosc. **50,** 1483–99.

[236] Weyl G W (1989). Physics of Laser-Induced Breakdown: An Update, in *Laser-Induced Plasmas and Applications* (Radziemski L J and Cremers D A, Eds.), Dekker, New York.

[237] Khater M A et al. (2002). Optimization of the Emission Characteristics of Laser-Produced Steel Plasmas in the Vacuum Ultraviolet: Significant Improvements in Carbon Detection Limits, Appl. Spectroscopy. Submitted for Publication.

[238] Griem H R (1997). Principles of Plasma Spectroscopy, Cambridge University Press, Cambridge, UK.

[239] Chen F F (1965). Electric Probes, in *Plasma Diagnostic Techniques* (Huddlestone R H and Leonard S L, Eds.), Academic Press, New York.

[240] Schott L (1995). Electrical Probes, in *Plasma Diagnostics* (Lochte-Holtgreven W, Ed.), American Institute of Physics Press.

[241] Wharton C B (1965). Microwave Techniques, in *Plasma Diagnostic Techniques* (Huddlestone R H and Leonard S L, Eds.), Academic Press, New York.

[242] Hermansdorfer H (1995), Microwave Diagnostic Techniques, in *Plasma Diagnostics* (Lochte-Holtgreven W, Ed.), American Institute of Physics Press.

[243] Alpher R A and White D R (1965). Optical Interferometry, in *Plasma Diagnostic Techniques* (Huddlestone R H and Leonard S L, Eds.), Academic Press, New York.

[244] Kunze H J (1995). The Laser as a Tool for Plasma Diagnostics, in *Plasma Diagnostics* (Lochte-Holtgreven W, Ed.), American Institute of Physics Press.

[245] Colón C et al. (1993). Measurement of the Stark Broadening and Shift Parameters for Several Ultraviolet Lines of Singly Ionized Aluminum, *J. Appl. Phys.* **73,** 4752–8.

[246] Gornushkin I B et al. (1999). Line Broadening Mechanisms in the Low-Pressure Laser-Induced Plasma, *Spectrochim. Acta* Part B **54,** 1207–17.

[247] Boumans P W J M (1966). Theory of Spectrochemical Excitation, Plenum Press, New York.

[248] Detalle V et al. (2001). An Evaluation of a Commercial Echelle Spectrometer with Intensified Charge-Coupled Device Detector for Materials Analysis by Laser-Induced Plasma Spectroscopy, *Spectrochim. Acta* Part B **56,** 1011–25.

[249] Griem H R (1963). Validity of Local Thermal Equilibrium in Plasma Spectroscopy, *Phys. Rev.* **131,** 1170–1176.

[250] Lochte-Holtgreven W (1995). Evaluation of Plasma Parameters, in *Plasma Diagnostics* (Lochte-Holtgreven W, Ed.), American Institute of Physics Press.

[251] Singh R K and Narayan J (1990). Pulsed-Laser Evaporation Technique for Deposition of Thin Films: Physics and Theoretical Models, *Phys. Rev. B* **41,** 8843–59.

[252] Gordillo-Vazquez et al. (2001). Temporal and Spatial Evolution of the Electronic Density and Temperature of the Plasma Produced by Laser Ablation of LiNbO3, *Appl. Phys. Lett.* **78,** 7–9.

[253] Liu H C et al. (1999). Early Phase Laser Induced Plasma Diagnostics and Mass Removal During Single-Pulse Laser Ablation of Silicon, *Spectrochim. Acta Part B* **54,** 1607–24.

[254] Mehlman G et al. (1993). Vacuum Ultraviolet Spectroscopy Study of Excimer-Laser-Generated Plasmas, *J. Appl. Phys.* **74,** 53–61.

[255] Simeonsson J B and Miziolek A W (1993). Time-Resolved Emission Studies of ArF-Laser-Produced Microplasmas, *Appl. Opt.* **32,** 939–47.

[256] Radziemski L J, Cremers D A and Niemczyk T M (1985). Measurement of the Properties of a CO_2 Laser Induced Air-Plasma by Double Floating Probe and Spectroscopic Techniques, *Spectrochim. Acta Part B* **40,** 517–25.

[257] De Giacomo A et al. (2001). Spectroscopic Investigation of the Technique of Plasma Assisted Pulsed Laser Deposition of Titanium Dioxide, *Spectrochim. Acta Part B* **56,** 1459–72.

[258] Simeonsson J B and Miziolek A W (1994). Spectroscopic Studies of Laser-Produced Plasmas Formed in CO and CO_2 using 193, 266, 355, 532 and 1064 nm Laser Radiation, *Appl. Phys. B* **59,** 1–9.

[259] Kurucz Atomic Line Database:
http://cfawww.harvard.edu/amdata/ampdata/kurucz23/sekur.html

[260] Bowe P et al. (1999). Effects of Resonant Pumping on the Temporal and Spatial Evolution of a Laser Produced Lithium Plasma, *J. Appl. Phys.* **86,** 3002–9.

[261] Harvey P D (Ed.) (1982). Engineering properties of steel, *American Society for Metals*, Metals Park, Ohio, USA.

[262] Whitty W (1998). A Study of the Expansion of a Laser Produced Lithium Plasma Using Spatially and Temporally Resolved Imaging and Spectroscopic Techniques, *PhD Thesis*, Dublin City University, Dublin, Ireland.

[263] Meighan O E (2000). XUV and VUV Photoabsorption and Emission Studies in Thorium and Other High-Z Laser Plasmas, *PhD Thesis*, Dublin City University, Dublin, Ireland.

[264] Uebbing J et al. (1991). Reheating of a Laser-Produced Plasma by a Second Pulse Laser, *Appl. Spectrosc.* **45,** 1419–23.

[265] Stratis D N, Eland K L and Angel M (2000). Dual-Pulse LIBS Using a Pre-Ablation Spark for Enhanced Ablation and Emission, *Appl. Spectrosc.* **54,** 1270–74.

[266] St-Onge L, Sabsabi M and Cielo P (1998). Analysis of Solids Using Laser-Induced Plasma Spectroscopy in Double-Pulse Mode, *Spectrochim. Acta Part B* **53,** 407–15.

[267] Luan S et al. (2001). An Échelle Polychromator for Inductively Coupled Plasma Optical Emission Spectroscopy with Vacuum Ultraviolet Wavelength Coverage and Charge Injection Device Detection, *Spectrochim. Acta Part B* **56,** 1143–57.

[268] Florek S et al. (2001). A New, Versatile Échelle Spectrometer Relevant to Laser Induced Plasma Applications, *Spectrochim. Acta Part B* **56,** 1027–34.

[269] Niemax K and Sdorra W (1990). Optical Emission Spectroscopy and Laser-Induced Fluorescence of Laser Produced Sample Plumes, *Appl. Opt.* **29,** 5000–6.

[270] Gornushkin I B et al. (1997). Determination of Cobalt in Soil, Steel, and Graphite Using Excited-State Laser Fluorescence Induced in a Laser Spark, *Appl. Spectrosc.* **51,** 1055–59.

[271] Hilbk-Kortenbruck F et al. (2001). Analysis of Heavy Metals in Soils Using Laser-Induced Breakdown Spectrometry Combined with Laser-Induced Fluorescence, *Spectrochim. Acta Part B* **56,** 933–45.

[272] Smith B W et al. (1999). Measurement of Uranium Isotope Ratios in Solid Samples Using Laser Ablation and Diode Laser-Excited Atomic Fluorescence Spectrometry, *Spectrochim. Acta Part B* **54,** 943–58.

[273] Quentmeier A, Bolshov M and Niemax K (2001). Measurement of Uranium Isotope Ratios in Solid Samples Using Laser Ablation and Diode Laser-Atomic Absorption Spectrometry, *Spectrochim. Acta Part B* **56,** 45–55.

APPENDICES

Appendix A

A short note on absorption mechanisms in laser-produced plasmas

The IB absorption coefficient (cm^{-1}), α_{IB}, of an ionized gas with a Maxwellian electron velocity distribution and a kinetic temperature, T_k, due to electron-ion collisions is expressed as [205]:

$$\alpha_{IB} = \sigma_{IB} n_e = \frac{4}{3}\left(\frac{2\pi}{3k_B T_k}\right)^{1/2} \frac{Z^2 e^6}{hcm_e^{3/2}\nu^3} n_i n_e \left(1 - \exp\left(\frac{h\nu}{k_B T_k}\right)\right) \qquad [A.1]$$

where σ_{IB} is the IB absorption cross section; n_i and n_e are the number density of ions and electrons, respectively; k_B is Boltzmann's constant; z, e and m_e are the ionic charge, electronic charge and mass, respectively; h is Planck's constant; c is the speed of light and ν is the laser frequency.

Equation A.1 shows that the IB process is less efficient for UV than visible and IR laser wavelengths. In IR laser-ablation processes, primary electrons coming from the early vapourization of the target are able to strongly absorb laser photons by IB even at very low electron density (through IB absorption during electron-neutral collisions).

For UV laser-ablation processes at relatively low power densities (on the order of 10^8 W cm^{-2}), IB mechanism becomes less efficient. Here, direct photoionizaton (PI) of excited atoms in the weakly ionized vapour plays a significant role [101, 109, 111]. The absorption coefficient, α_{PI}, of this process is given approximately by [207]:

$$\alpha_{PI} = \sigma_{PI} n_n \approx \sum_n 2.9\times10^{-17} \frac{(E_n)^{5/2}}{(h\nu)^3} n_n \qquad [A.2]$$

where σ_{PI} is the PI absorption cross section; $h\nu$ is the photon energy (eV); E_n (eV) and n_n (cm^{-3}) are the ionization energy and number density of the excited state n, respectively and the summation is performed over the energy levels that satisfy the condition $h\nu > E_n$. In UV laser-ablation of metals, the photon energy is almost always

comparable with the typical ionization energy of excited atoms, making σ_{PI} of the order of 10^{-17} cm^2 in most cases. In addition, electron impact (EI) excitation and ionization time constants (relaxation times) are much shorter (in the order of 10^{-13} s) than the nanosecond duration laser pulses, producing an effective enhancement of the excited and ionized species [207]. The subsequent increase of the electron and ion number densities strongly enhances the probability of UV photon absorption by IB due to electron-ion collisions.

Recombination processes, on the other hand, can counterbalance the electron generation by PI and EI, thus reducing charged particles number densities in the plasma. The rate of recombination can be estimated by considering the relaxation times of three-body recombination (τ_{tbr}) and photo-recombination (τ_{phr}) processes [205]:

$$\tau_{tbr} \approx 1.1\times10^{26} Z^{-3} T^{9/2} n_e^{-2} \qquad [A.3]$$

$$\tau_{phr} \approx 3.7\times10^{12} Z^{-2} T^{3/4} n_e^{-1} \qquad [A.4]$$

with T and n_e in eV and cm^{-3}, respectively. For a typical plasma electron density and temperature of 10^{18}–10^{20} cm^{-3} and several eV, respectively, τ_{tbr} values are comparable with the excitation and ionization time constants, thus significantly influencing the plasma dynamics during the laser pulse. τ_{phr}, on the other hand, results are much larger than the laser pulse. This situation holds true until the plasma expands to a size of ≈ 100 μm and its density decreases to about 10^{17} cm^{-3}, where τ_{tbr} reaches values higher than ≈ 1 μs at this low-density value.

For a degree of ionization larger than 0.005, the heat transfer relaxation time, τ_{ht}, is mainly determined by electron-ion collisions, and can be approximately estimated by [205]:

$$\tau_{ht} \approx 3\times10^{8} \frac{A T^{3/2}}{Z^2 n_e \ln\Lambda} \qquad [A.5]$$

where A is the surface absorbance and Λ is a plasma parameter given by $\Lambda=1.55\times10^{10}T^{3/2}n_e^{-1/2}$; T is in eV and n_e in cm^{-3}. With $n_e \approx 10^{18}$–10^{20} cm^{-3}, and T ≈ 1–5 eV, the relaxation time τ_{ht} is almost always less than 1 ns and the excitation and ionization temperatures can be assumed to be approximately equal (LTE condition). Experimental studies involving nanosecond visible and UV laser ablation of metallic targets showed that under moderate irradiation (10^8–10^{10} W cm^{-2}), the laser-produced plasma has typically temperatures of several eV [128, 136].

Appendix B

Radiation Distribution Relations

1- Velocity of particles / Maxwell distribution

$$dn_v = 4\pi N\left(\frac{m}{2\pi k_B T_k}\right)^{3/2} \exp\left(\frac{-mv^2}{2k_B T_k}\right) v^2 dv \qquad [B.1]$$

where dn_v is the number of particles (of mass m) having velocities between v and v + dv; N is the total number density of particles at all velocities; k_B is Boltzmann's constant and T_k is the kinetic temperature [219].

2- Population distribution of bound states / Boltzmann distribution

The ratio of number densities of atoms / ions in two different bound states is given by [219]:

$$\frac{N_i}{N_k} = \frac{g_i}{g_k} \exp\left(-\frac{\chi(i,k)}{k_B T_{exc}}\right) \qquad [B.2]$$

where i and k denote the lower and upper energy levels, respectively; g is the statistical weight of the level, and calculated as: $g_1 = 2J_1 + 1$, where J is the total angular momentum quantum number for the species under consideration; χ(i, k) is the energy difference between the two levels and T_{exc} is the excitation (population) temperature of the species under consideration. Another form of the Boltzmann distribution can be obtained by relating the number density of atoms / ions in the excited state k, N_k, to the total number density of the corresponding species (in the same state of ionization), N_T [216]:

$$\frac{N_k}{N_T} = \frac{g_k}{Q(T_{exc})} \exp\left(-\frac{E_k}{k_B T_{exc}}\right) \qquad [B.3]$$

where E_k is the excitation energy of the state k as measured in reference to the ground-energy level of the species in the same state of ionization and $Q(T_{exc})$ is the partition function of the atoms / ions under consideration and is given by [216]:

$$Q(T_{exc}) = \sum_k g_k \exp\left(-\frac{E_k}{k_B T_{exc}}\right) \qquad [B.4]$$

The sum is over all allowed electronic energy levels. At low temperatures, the partition function may be approximated by the degeneracy (statistical weight) of the ground state if the first excited state energy is very large compared with kT.

3- Population distribution of ionization stages / Saha distribution

The ratio of population densities, N_z and N_{z-1}, in two successive ionization stages, z and z-1, is governed by the Saha equation [218]:

$$\frac{N_z n_e}{N_{z-1}} = 2\left(\frac{2\pi m_e k_B T_{ion}}{h^2}\right)^{3/2} \frac{Q_z(T_{ion})}{Q_{z-1}(T_{ion})} \exp\left(-\frac{E_{z-1}(\infty)}{k_B T_{ion}}\right) \qquad [B.5]$$

where z = 1, 2, 3, ...; n_e and T_{ion} are the electron number density and ionization temperature, respectively; h is Planck's constant and $E_{z-1}(\infty)$ is the ionization energy of the z-1 ionization stage.

4- Black body radiation / Planck distribution law

For a solid or gas in a closed system, the intensity of the black body radiation field in vacuum is given by Planck as:

$$I_\nu = B_\nu(T) = \frac{2h\nu^3}{c^2}\left[\exp\left(\frac{h\nu}{k_B T}\right) - 1\right]^{-1} \qquad [B.6]$$

The corresponding expression for the wavelength is given by:

$$I_\lambda = B_\lambda(T) = \frac{2hc^2}{\lambda^5}\left[\exp\left(\frac{hc}{\lambda k_B T}\right) - 1\right]^{-1} \qquad [B.7]$$

In terms of the specific (spectral) radiation energy densities, u_ν and u_λ, the above two formula become [220]:

$$u_\nu = \frac{8\pi h\nu^3}{c^3}\left[\exp\left(\frac{h\nu}{k_B T}\right) - 1\right]^{-1} \qquad [B.7]$$

where T is the absolute temperature of the system. For wavelength:

$$u_\lambda = \frac{8\pi hc}{\lambda^5}\left[\exp\left(\frac{hc}{\lambda k_B T}\right) - 1\right]^{-1} \qquad [B.8]$$

At short wavelengths ($hc / \lambda k_B T >> 1$), Wien's approximation nay be applied:

$$B_\lambda(T) \approx \frac{2hc^2}{\lambda^5}\exp\left[-\frac{hc}{\lambda k_B T}\right] \qquad [B.9]$$

For long wavelengths, i.e. $hc / \lambda k_B T << 1$, the Rayleigh-Jeans radiation law holds:

$$B_\lambda(T) \approx \frac{2k_B c}{\lambda^4}T \qquad [B.10]$$

Appendix C

Some Remarks on Emission and Absorption of Spectral Lines

1- Radiation intensity

The total radiation intensity, I_T, from any source is defined as the energy, ΔE, emitted per unit time, Δt, from an area, ΔA, per unit solid angle, $\Delta\Omega$, and is given by:

$$I_T = \lim \frac{\Delta E}{\Delta t \Delta A \Delta \Omega} \qquad \text{for } \Delta t, \Delta A \text{ and } \Delta\Omega \to 0 \qquad [C.1]$$

In spectroscopic applications, however, it is of great interest to refer to the intensity in units of frequency or wavelength. Considering this, the above formula becomes:

$$I_{\nu(\lambda)} = \lim \frac{\Delta E}{\Delta t \Delta A \Delta \Omega \Delta \nu (\Delta \lambda)} \quad \text{for } \Delta t, \Delta A, \Delta\Omega \text{ and } \Delta\nu\ (\Delta\lambda) \to 0 \qquad [C.2]$$

I_ν or I_λ refer to as the specific (spectral) intensity. If the specific radiation involves spectral lines, then the line intensity, I_L, may be introduced. Accordingly, in the vicinity of the spectral line, the spectral intensity I_ν or I_λ can be resolved into two parts: a continuous function, $I_{\nu,C}$, and a discrete function, $I_{\nu,L}$. For spectroscopic applications concerning with observations on discrete spectral lines only, the continuous part must be subtracted from the specific intensity. Therefore, the spectral line intensity is simply produced by integration over the discrete function to give:

$$I_L = \int_{Line} I_{\nu,L} d\nu = \int_{Line} I_{\lambda,L} d\lambda \qquad [C.3]$$

2- Radiation density

The spectral energy density, u_ν or u_λ, is closely related to the corresponding intensity and is more important when the interaction of electromagnetic radiation and matter is

concerned. It can be calculated from the specific intensity when the latter is known for all directions, i.e.:

$$u_\nu = \frac{1}{c}\int I_\nu(\vartheta,\varphi)d\Omega \quad ; \quad u_\lambda = \frac{1}{c}\int I_\lambda(\vartheta,\varphi)d\Omega \qquad [C.4]$$

The relation between u_ν and u_λ is similar to that between the corresponding specific radiation intensities, I_ν and I_λ, that is to say:

$$u_\nu = \frac{\lambda^2}{c}u_\lambda \qquad [C.5]$$

and the energy density of the total radiation is given by:

$$u = \int_0^\infty u_\nu d\nu = \int_0^\infty u_\lambda d\lambda \qquad [C.6]$$

3- Transition probabilities

The emission and absorption of a spectral line are determined by the population of the lower and upper energy levels of the relevant transition, respectively, as well as by Einstein's transition probabilities. Corresponding to the three processes spontaneous emission, absorption and stimulated emission, there are three transition probabilities that describe the mechanisms of emission and absorption of light photons. For a system of atoms / ions enclosed in a black body cavity in complete thermodynamic equilibrium at temperature T, the principle of detailed balance holds for transitions to and from all individual energy levels and also for collisional and radiative processes:

$$A_{qp}N_q + B_{qp}u(\nu_{pq})N_q = B_{pq}u(\nu_{pq})N_p \qquad [C.7]$$

where A_{qp}, B_{qp} and B_{pq} are Einstein coefficients of spontaneous emission, stimulated emission and absorption, respectively; N_q and N_p are the atomic / ionic populations of the upper, q, and lower, p, energy levels, respectively and $u(\nu_{pq})$ is the radiation energy

density of the corresponding transition. Using the above equality, Einstein derived the well-known relationships between the three transition probabilities as follows:

$$A_{qp} = \frac{g_p}{g_q} B_{pq} \frac{8\pi h \nu_{pq}^{\ 3}}{c^3} \qquad \text{and} \qquad g_q B_{qp} = g_p B_{pq} \qquad [C.8]$$

where g_q and g_p are the statistical weights of the upper and lower levels, respectively.

4- Kirchhoff's law of radiation

For plasmas in CTE or LTE, Kirchhoff's law of radiation can be stated as:

$$\varepsilon_\nu = k(\nu) B_\nu(T) \qquad \text{and} \qquad \varepsilon_\lambda = k(\lambda) B_\lambda(T) \qquad [C.9]$$

where ε and k are the coefficients for emission and absorption, respectively. For LTE plasmas, the energy emitted from a unit volume, per second and per unit solid angle can be expressed by the emission coefficient of the spectral line, ε. Integration over the spectral line profile gives:

$$\varepsilon_L = \int_{Line} \varepsilon_{\nu,L} d\nu = \frac{h\nu_{pq}}{4\pi} A_{qp} N_q \qquad [C.10]$$

This equality is known as the fundamental relation of emission spectroscopy, and it shows the dependence of the spectral line intensity on the population of the excited state, N_q. Recalling Boltzmann equation (Appendix B) and substituting for Nq, one obtains:

$$I = \frac{h\nu_{pq}}{4\pi} A_{qp} \frac{N_T g_q}{Q(T_{exc})} \exp\left(-\frac{E_q}{k_B T_{exc}}\right) \qquad [C.11]$$

This equation is usually used to determine the excitation temperature, T_{exc}, in LTE plasmas. The absorption coefficient of a spectral line, $k_L(\nu)$, on the other hand, can be represented in terms of the atomic cross section of the line, $\sigma_L(\nu)$, as follows:

$$k_L(\nu) = \sigma_L(\nu) N_p l \qquad \text{[C.12]}$$

where N_p is the number density of atoms / ions in the lower energy level p and l is the length of the plasma over which the absorption takes place. Both $k_L(\nu)$ and $\sigma_L(\nu)$ strongly depend on the frequency because spectral line absorption is a typical resonance phenomenon. This dependency can be described by the spectral line profile, $P(\nu)$, which is normalized so that:

$$\int_{Line} P(\nu) d\nu = 1 \qquad \text{[C.13]}$$

In the case where the upper energy level, q, is not populated then the absolute value of $k_L(\nu)$ results directly from Ladenburg's formula [218]:

$$\int_{Line} k_L(\nu) d\nu = \frac{h\nu}{c} N_p B_{pq} \qquad \text{[C.14]}$$

where B_{pq} is the Einstein's coefficient for absorption. Combining C.13 and C.14, one obtains:

$$k_L(\nu) = \frac{h\nu}{c} N_p B_{pq} P(\nu) \qquad \text{[C.15]}$$

On the other hand, if a certain number of atoms / ions are promoted to the upper energy level q, then the contribution of induced emission must be included in equation C.15. This is an appropriate modification since the induced emission has the same frequency and direction as the incident radiation, and thus may be considered as "negative" absorption signal. Accordingly, the absorption coefficient of the spectral line can be written as:

$$\begin{aligned} K_L(\nu) &= \frac{h\nu}{c} P(\nu)\left(N_p B_{pq} - N_q B_{qp}\right) \\ &= k_L(\nu)\left(1 - N_q B_{qp} / N_p B_{pq}\right) \end{aligned} \qquad \text{[C.16]}$$

For collision-dominated LTE plasmas, the ratio of particle densities can be replaced by Boltzmann's factor, $\exp(-h\nu / k_B T_{exc})$, then:

$$K_L(\nu) = k_L(\nu)\left(1 - \exp\left(-\frac{h\nu}{k_B T_e}\right)\right) \qquad [C.17]$$

Appendix D

Voigt Profiles

Voigt profiles are the result of folding Doppler (Gaussian) and Stark (Lorentzian) spectral line shapes. They are available in tabular, as well as graphical form for a wide range of conditions. The half-widths of Voigt profiles are reproduced in the following table (after Ref. 225). The observed half-width is denoted by $\Delta\lambda_{1/2}$, and the half-widths from pure Doppler and pure Lorentzian broadening are denoted by $\Delta\lambda_{1/2}^{D}$, and $\Delta\lambda_{1/2}^{L}$, respectively.

$\Delta\lambda_{1/2}^{L}/\Delta\lambda_{1/2}^{D}$	$\Delta\lambda_{1/2}^{L}/\Delta\lambda_{1/2}$	$\Delta\lambda_{1/2}^{D}/\Delta\lambda_{1/2}$
∞	*1*	*0*
12.01	*0.993*	*0.083*
6.01	*0.972*	*0.162*
4.00	*0.941*	*0.235*
3.00	*0.904*	*0.301*
2.70	*0.886*	*0.327*
2.40	*0.863*	*0.359*
1.80	*0.794*	*0.441*
1.50	*0.742*	*0.494*
1.20	*0.672*	*0.559*
1.14	*0.655*	*0.574*
1.08	*0.637*	*0.589*
1.02	*0.618*	*0.605*
0.96	*0.597*	*0.622*
0.90	*0.575*	*0.639*
0.84	*0.552*	*0.656*
0.78	*0.527*	*0.675*
0.72	*0.500*	*0.694*
0.66	*0.472*	*0.715*
0.60	*0.442*	*0.736*
0.54	*0.410*	*0.758*
0.48	*0.375*	*0.780*
0.42	*0.338*	*0.804*
0.36	*0.299*	*0.829*
0.30	*0.257*	*0.855*
0.24	*0.212*	*0.882*
0.18	*0.164*	*0.910*
0.12	*0.113*	*0.939*
0.05	*0.050*	*0.984*
0	*0*	*1*

Appendix E

In this appendix, some technical characteristics and specifications of various parts in the set-ups employed in the present work are tabulated.

1- Lasers

Characteristic	Laser Model		
	SL803	Surelite III-10	Surelite I-10
Manufacturer	Spectron, UK	Continuum, USA	Continuum, USA
Laser Type	Q-switched, Double-Stage Nd:YAG	Q-switched, Oscillator-Only Nd:YAG	Q-switched, Oscillator-Only Nd:YAG
Wavelength (nm)	1064	1064	1064; 532; 355 and 266
Max. O/P Energy (mJ)	850	800	400; 250; 100 and 55
Pulse Width (ns)	12–15	5–7	5–7; 5–7; 4–6 and 4–6
Rep. Rate (Hz)	10	10	10
Divergence (mrad)	~ 1.2	0.6	0.6

2- Samples

Sample Number	Concentration (weight %)	
	C	Fe
361-50E	0.001	99.83
084-CRMFE1	0.005	99.75
15704a-2	0.013	99.81
15704a-3	0.018	99.62
15704a-1	0.034	99.35
361-XAAS	0.041	99.41
15704a-4	0.087	99.17
361-2932	0.208	98.14
361-XCCV	0.44	97.35
361-54D	0.668	97.09
351-215/3	0.91	98.00
371-229/1	1.32	97.71

3- The spectrometric system

(1) Spectrometer

Model	ARC™ VM-521
Optical system	Normal incidence, 15°
Focal length (m)	0.9954 (Diameter of Rowland circle)
f-number	*f* / 10.4 with the grating used
Grating type	Concave reflective (Al + MgF_2 coated)
Grooves/mm	1200
Ruled area (mm^2)	96 × 56 (height × width)
Blaze wavelength (nm)	80 in the first order
Wavelength range (nm)	30–325
Wavelength coverage (nm)	~ 21 (used either the PDA or CCD detector)
Reciprocal linear dispersion	0.83 nm/mm

(2) Detection systems

(a) CEMA / PDA

Model	Galileo™ 6025-FM
MCP dimensions (mm^2)	40 × 0.5 (diameter × thickness)
Minimum electron gain	3.3×10^4
Wavelength range (nm)	20–180
Detection efficiency	10–20%
OMA Model	EG&G™ 1471A detector controller interface
PDA Model	EG&G™ 1453A silicon linear array
Array pixel number	1024
Array size (mm^2)	25.6 × 2.5 (length × height)
Wavelength range (nm)	180–1100
Quantum efficiency	70% at 650nm

(b) Photometrics™ CCD

Model	Model SI003-AB
Format	Thinned (~ 10 μm), backside illuminated
Array pixel number	1024 × 1024 (height × width)

Imaging area (mm^2)	24.6 × 24.6
Readout frequency (kHz)	200
Quantum efficiency	15–40% over the range 20–220 nm

(c) Andor™ CCD

Model	DV420-BN
Format	Thinned (~ 10 μm), backside illuminated
Array pixel number	1024 × 256 (width × height)
Imaging area (mm^2)	26.6 × 6.7
Readout frequency (MHz)	1
Dark current	0.01 counts/pixel/sec
Minimum temperature	-45° C with Peltier cooler (no water circulation)

Appendix F

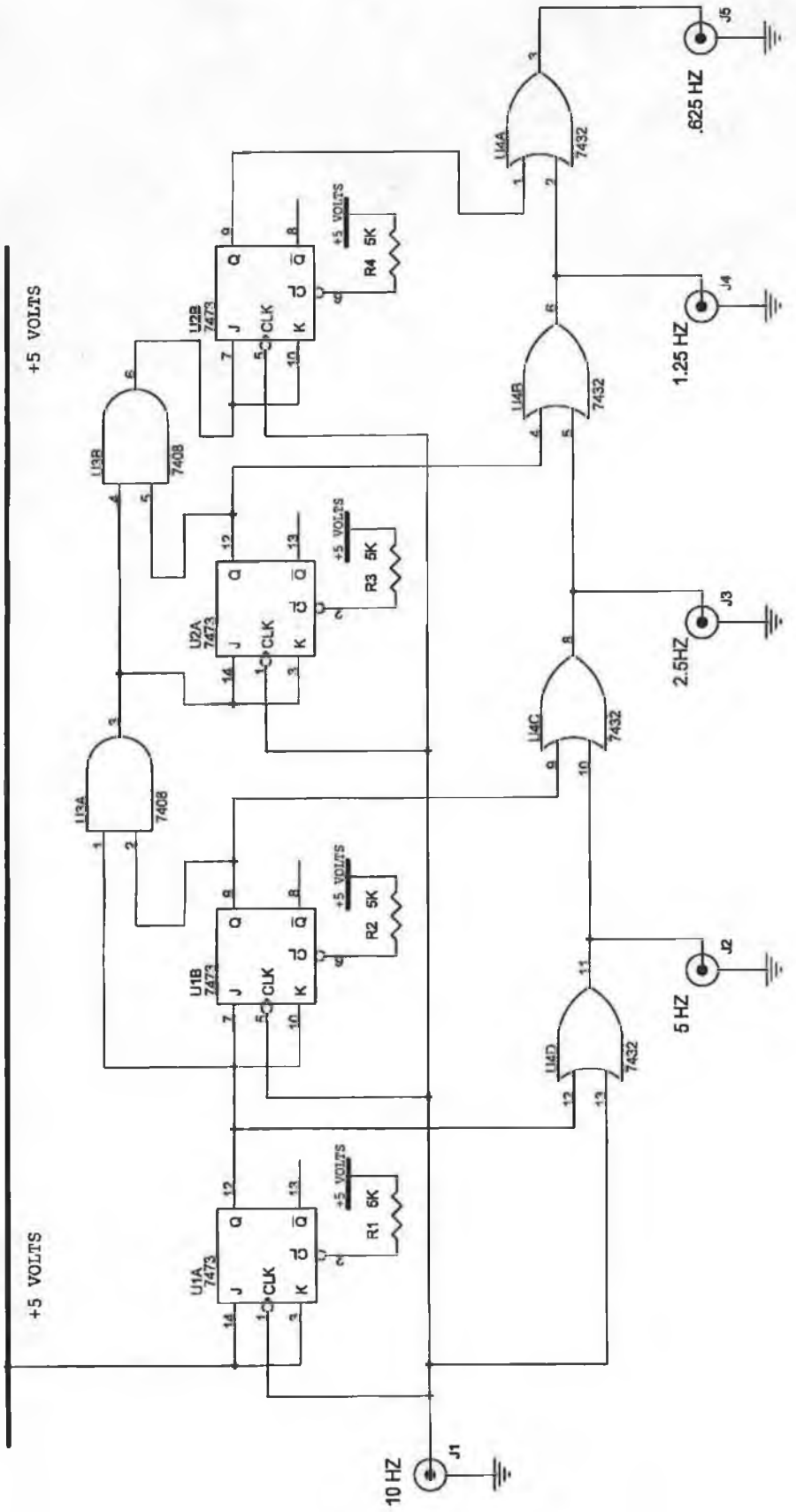
FREQUENCY DIVIDER / 4 BIT COUNTER
+5 VOLTS
+5 VOLTS
+5 VOLTS
+5 VOLTS
+5 VOLTS
+5 VOLTS
R1 5K
R2 5K
R3 5K
R4 5K
U1A 7473
U1B 7473
U2A 7473
U2B 7473
U3A 7408
U3B 7408
U4A 7432
U4B 7432
U4C 7432
U4D 7432
J1
J2
J3
J4
J5
10 HZ
5 HZ
2.5HZ
1.25 HZ
.625 HZ

Appendix G

A short note on establishment of LTE state in laser-produced plasmas

In the case of a transient plasma, such as a laser-produced plasma, knowledge of the electron number density is important because it indicates not only if LTE is possible but also how quickly the plasma will proceed towards the LTE state, once it is formed. The time for establishing a kinetic equilibrium between electrons and heavier ions and neutrals is inversely proportional to the electron number density, and can be estimated from the following formula [250]:

$$t_{kin} = \left[7.5\times10^{-7} \left(\frac{X_H}{kT} \right)^{3/2} n_e \right]^{-1} \frac{nm}{n^+ m_e} \qquad [G.1]$$

where X_H is the ionization energy of hydrogen (J), n^+ is the number density of neutral or charged species (cm^{-3}), m is the atomic mass of the species under study (g) and m_e is the electron mass (g). For a laser-produced plasma that is approximately 10% ionized, where $n_e = 10^{18}$ cm^{-3} and kT = 1.5 eV, t_{kin} = 10 ns for particles up to m = 50 amu.

Another consideration in a transient plasma environment is the time necessary for Boltzmann equilibration to take place once the plasma is created. This can be estimated using the following expression [250]:

$$t_B = 1.1\times10^{7} \frac{z^3}{f_{1,2} n_e} \frac{n_z}{n_z + n_{z-1}} \left(\frac{E_{z-1,2}}{z^2 X_H} \right) \left(\frac{kT}{z^2 X_H} \right) \exp\left(\frac{E_{z-1,2}}{kT} \right) \qquad [G.2]$$

where z is the stage of ionization (1 = neutrals, 2 = singly-charged atoms, etc.), f is the oscillator strength, n_z is the number density of the particles under investigation (in cm^{-3}), E_i is the energy of the state i (in J) and the rest quantities were previously defined. Under similar plasma conditions as described above, i.e. $n_e = 10^{18}$ cm^{-3} and kT = 1.5 eV, a Boltzmann equilibrium among the excited states of the different particles is expected within approximately 1 ns.

Appendix H

An iterative Qbasic code for calculation of the plasma ionization temperature (T_{ion})

```
REM Iterative code to fit temperature to Saha eqn.
CLS
PRINT
INPUT "Enter electron density (cm-3)"; density
PRINT
INPUT "Enter alpha coefficient"; alpha
PRINT
INPUT "Enter beta coefficient"; beta
PRINT
INPUT "Enter Tmin, Tmax and Tinc (in K)"; Tmin, Tmax, Tinc
PRINT
INPUT "Enter tolerance in ne (%)"; tolerance
PRINT
tolerance = 0.01 * tolerance * density
REM Compute number of temperature point
n = INT((Tmax - Tmin) / Tinc)
REM Loop, compute residuals and stop when residual <
tolerance
REM
REM open output file for residuals
REM
OPEN "resid" FOR OUTPUT AS #1
FOR i = 0 TO n
T = Tmin + i * Tinc
rhs = alpha * (T ^ 1.5) * EXP(-beta / T)
residual = density - rhs
PRINT #1, T; rhs; density; residual
REM PRINT T; rhs; density; ABS(residual)
IF ABS(residual) < tolerance THEN GOTO loop2
NEXT i
loop2:
PRINT "temp="; T, "residual ="; ABS(residual)
CLOSE #1
END
```

List of Figures and Photographs

List of Tables